Manipulation of electronic properties in strongly correlated Cerium-based surface alloys

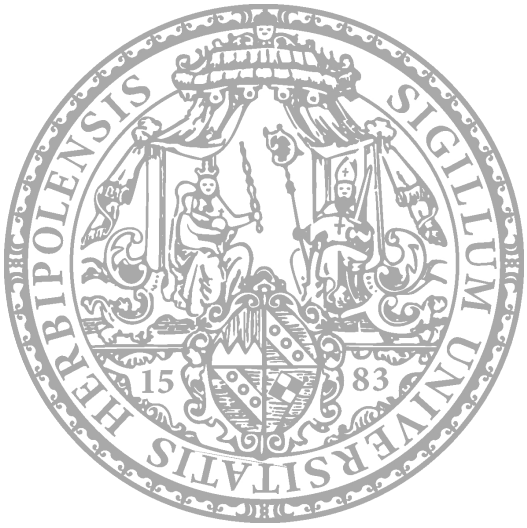

Dissertation zur Erlangung des naturwissenschaftlichen Doktorgrades
der Julius-Maximilians-Universität Würzburg

vorgelegt von

Katharina Kißner
aus Weißenburg i. Bay.

Würzburg, 2021

Eingereicht am: 18.08.2021
bei der Fakultät für Physik und Astronomie

1. Gutachter: Prof. Dr. Friedrich Reinert
2. Gutachter: Prof. Dr. Vladimir Hinkov
3. Gutachter: .....
der Dissertation

Vorsitzende(r): Prof. Dr. Karl Brunner
1. Prüfer: Prof. Dr. Friedrich Reinert
2. Prüfer: Prof. Dr. Vladimir Hinkov
3. Prüfer: Prof. Dr. Fakher Assaad
im Promotionskolloquium

Tag des Promotionskolloquiums: 29.04.2022

Doktorurkunde ausgehändigt am: .....

Zusammenfassung

Photoelektronenspektroskopie eignet sich auf vielerlei Weise verschiedenste Aspekte der elektronischen Struktur stark korrelierter Elektronensysteme zu untersuchen. Die vorliegende Arbeit zeigt, wie gezielt Einfluss auf die Ausprägung starker Korrelation in Cer-basierten Oberflächenlegierungen genommen werden kann. Die Photoemission ermöglicht es dabei zum einen Zugang zu den niedrigen Energieskalen starker Korrelation im Kondo-Regime zu erhalten, zum anderen auch Veränderungen auf dieser Energieskala zu erfassen. Diese Arbeit zeigt, dass die Ausbildung des Kondo-Grundzustandes durch eine Vielzahl von Parametern beeinflusst werden kann. Diese sind beispielsweise die Wahl des metallischen Bindungspartners in binären Cer-Verbindungen, die Schichtdicke der Oberflächenlegierung und die damit einhergehenden Änderungen der Gitterstruktur sowie die Grenzschichten zu Substrat oder Vakuum. Durch Kontrolle dieser Parameter erhält man die Möglichkeit, entscheidende Zustandsgrößen des Systems, wie die effektive Besetzung des f-Niveaus n_f oder die Kondo-Temperatur T_K, maßgeblich zu beeinflussen.

Cer-basierte Oberflächenlegierungen stellen ein ideales Modellsystem für die Untersuchung starker Korrelation im Kondo-Regime dar. Zum einen besitzt Cer genau ein $4f$-Elektron, was die Beschreibung möglicher Grundzustandskonfigurationen vereinfacht, zum anderen erhält man über das epitaktische Wachstum der Dünnfilme Kontrolle über die oben aufgeführten Einflussgrößen. Daher stehen dünne Filme der intermetallischen Verbindungen $CePt_5$/Pt(111) und $CeAg_x$/Ag(111) im Zentrum der vorliegenden Arbeit.

Durch den Einsatz verschiedener Anregungsenergien bietet die Photoemission Zugang zu den Merkmalen des Kondo-Effekts im Valenzband, aber auch in den Rumpfniveauspektren. Diese sind die Kondo-Resonanz und ihr Spin-

Bahn-Partner nahe der Fermienergie sowie die Multiplettstruktur der Ce 3*d*-Rumpfniveaus. Die Auswertung verschiedener Ce 3*d*-Rumpfniveauspektren ergibt eine erhöhte Delokalisation der *f*-Elektronen für dünne Filme von $CePt_5$/Pt(111). Dies ist auf Änderungen der Gitterstruktur bei dünnen Filmen sowie den erhöhten Einfluss des Pt-Substrates zurückzuführen. Bei höheren Filmdicken ergibt sich eine Zunahme der Lokalisation der *f*-Elektronen und das System zeigt seine charakteristischen Volumeneigenschaften. An der Oberfläche der $CePt_5$-Legierung deuten die Ce 3*d*-Spektren auf eine Erhöhung der Hybridisierung zwischen Leitungsband- und *f*-Elektronen hin, die auf die Pt-Terminierung der Oberfläche zurückzuführen ist. Die Auswertung der Ce 3*d*-Spektren in Abhängigkeit der Probentemperatur ermöglicht die Bestimmung der Kondo-Temperatur des Systems. Für dünne Schichten $CePt_5$/Pt(111) ergibt sich diese zu $T_K \approx 200-270\,K$, für dickere Schichten zu $T_K > 280\,K$. Diese Ergebnisse wurden durch Simulation der Spektren auf Basis des Gunnarsson-Schönhammer-Formalismus für Rumpfniveauspektren sowie durch Analyse der Kondo-Resonanz im Valenzband bestätigt. Die Anpassung der Ce 3*d*-Spektren durch das Gunnarsson-Schönhammer-Modell ermöglicht zudem die Bestimmung der Coulomb-Anziehung U_{fc} zwischen Rumpfloch und *f*-Level und der $f-f$ Coulomb-Abstoßung U_{ff} zu $U_{fc} = 12\,eV$ und $U_{ff} = 8.5-9.5\,eV$.

Durch Variation der Schichtdicke des $CeAg_x$-Films, wurde auch im Materialsystem $CeAg_x$/Ag(111) Einfluss auf die elektronische Struktur genommen. Zudem wird die Oberflächenlegierung mit dem schweren Element Bismut versetzt, um das Zusammenspiel von Spin-Bahn-Kopplung und starker Korrelation zu untersuchen. Obwohl sich Änderungen sowohl bei verschiedenen Schichtdicken, als auch durch die Zugabe von Bismut ergeben, konnten keine Anzeichen des Kondo-Grundzustandes, wie beispielsweise die Kondo-Resonanz an der Fermienergie oder die Multiplettstruktur der Ce 3*d*-Rumpfniveaus, beobachtet werden.

Abstract

Photoelectron spectroscopy proves as a versatile tool for investigating various aspects of the electronic structure in strongly correlated electron systems. Influencing the manifestation of strong correlation in cerium-based surface alloys is the main task of this work. Photoemission is able to access the small energy scales of electron correlation in the Kondo regime and even capture variations upon that scale. It is shown, that the manifestation of the Kondo ground state is influenced by a multitude of parameters such as the choice of the metal binding partner in binary cerium compounds, the surface alloy layer thickness and accompanying variations in the lattice structure as well as the interfaces to substrate or vacuum. Gaining access to these parameters allows to directly influence essential state variables of the system, such as the f level occupancy n_f or the Kondo temperature T_K.

Cerium-based surface alloys serve as a suitable model system for the purpose of this work. On the one hand, cerium provides exactly one f electron, rendering the possible ground state configurations of the f multiplet manageable. On the other hand, the epitaxial growth of surface alloy thin films allows for great control over the desired tuning parameters. Therefore the intermetallic thin films of $CePt_5$/Pt(111) and $CeAg_x$/Ag(111) are the center of this work.

By utilizing different excitation energies, photoemission spectroscopy provides access to characteristic features of Kondo physics in the valence band, such as the Kondo resonance and its spin-orbit partner at the Fermi level, as well as the multiplet structure of the Ce $3d$ core levels. In this work both approaches are applied to $CePt_5$/Pt(111) to determine n_f and T_K for a variety of surface alloy layer thicknesses. The analysis of the Ce $3d$ core level multiplet reveals an enhancement of the f level delocalization for thinner layer

thicknesses, caused by variations in the lattice structure and an increased influence of the Pt(111) substrate. At larger layer thicknesses the f electron delocalization decreases and the bulk characteristics of the material dominate. However, at the intermetallic's surface, the Ce $3d$ spectra suggest a larger hybridization between conduction band and f electrons as compared to the bulk, which is attributed to the Pt termination of the surface. A temperature dependent study of the Ce $3d$ core levels allows to determine the systems Kondo temperature for the different layer thicknesses. This leads to $T_{\mathrm{K}} \approx 200-270\,\mathrm{K}$ in the thin layer thickness regime and $T_{\mathrm{K}} > 280\,\mathrm{K}$ for larger layer thicknesses. These results are confirmed by fitting the Ce $3d$ multiplet based on the Gunnarsson-Schönhammer formalism for core level spectroscopy and additionally by valence band photoemission spectra of the respective Kondo resonances. The Gunnarsson-Schönhammer models, furthermore, allow for the determination of the core hole$-f$ level Coulomb attraction U_{fc} and the $f-f$ Coulomb repulsion U_{ff} as $U_{fc} = 12\,\mathrm{eV}$ and $U_{ff} = 8.5-9.5\,\mathrm{eV}$. The influence of varying layer thickness on the manifestation of strong correlation is subsequently studied for the surface alloy $\mathrm{CeAg}_x/\mathrm{Ag}(111)$. Furthermore, the heavy element bismuth is added, to investigate the effects of strong spin-orbit coupling on the electronic structure of the surface alloy. Although changes are observed both upon varying the layer thickness and adding bismuth, characteristic Kondo ground state features, like the Kondo resonance at the Fermi level or the multiplet structure of the Ce $3d$ core levels, are not observed for $\mathrm{CeAg}_x/\mathrm{Ag}(111)$.

Table of contents

1

Introduction

The wide field of strongly correlated electron systems steped into focus again very recently by the discovery of topologically non trivial materials. The interplay of strong electron correlation and spin-orbit coupling brought forth a new class of materials – topological Kondo insulators [1–3]. The discovery of topological insulators lead to a new classification of insulators based on their intrinsic band order [3]. One of the driving forces for non-trivial topology is the strong spin-orbit coupling of heavy elements like bismuth [4–8]. The inverted, topological band order cannot be adiabatically connected to a tivial band order, without closing the insulating gap. This gives rise to metallic, spin-polarized surface states, at the interface between topologically trivial and non-trivial insulators.

In 2010, *Dzero et al.* showed, that this classification of insulators can be transferred to the material class of heavy fermion systems and in particular to Kondo insulators [1–3]. The energy gap in Kondo insulators emerges due to the hybridization of itinerant conduction band electrons and a flat heavy fermion band [1]. The heavy fermions constitute of a strongly localized f electron, surrounded by a screening cloud of conduction band electrons [9]. The basic screening mechanism is known since the early 1960ies as the Kondo effect [10–13]. The localized magnetic moment of the f electron polarizes

the surrounding conduction band electrons, until the local moment is entirley screened below a material specific temperature T_K, the Kondo temperature [13–15]. If the local moments are packed densly in a regular crystalline lattice, the screening clouds might overlap, forming a heavy fermion band [9]. This band inherits the odd parity of the f electrons. Thus, a hybridization between heavy fermion and conduction band leads to an energy gap between bands of inverted parity. This energy gap is topologically non-trivial, giving rise to the class of topological Kondo insulators hosting topological surface states in the correlation energy gap [1, 3].

Kondo insulators emerge both in intermediate valent systems, like SmB_6, where the f level occupation is strongly reduced and the valence assumes non integer, intermediate values [16], as well as Kondo systems like $Ce_3Bi_4Pt_3$, where the f electron count is reduced only little and the occupation is close to one [17–19]. While theoretical works as well as transport measurement on both compounds report a residual low temperature conductivity [1,16,20,21], a direct observation of a topological surface state, causing this low temperature behaviour, is still controversial [22–25].

This work sets out on a different approach to study the interplay of strong correlation and spin-orbit coupling. The focus lies on epitaxially grown thin film surface alloys rather than bulk single crystalline topological insulator candidates. The *in situ* growth of thin films of Ce-based surface alloys produces well and long range ordered films [26–30]. Furthermore one gains access to a variety of tuning parameters like the surface alloy layer thickness and lattice structure, the choice of substrate material and additional dopants.

The two suface alloys $CePt_5$/Pt(111) and $CeAg_x$/Ag(111) constitude the heart of this work. Ce-based compounds often serve as model systems for the investigation of strong correlation. As the second element of the Lanthanide series, Ce features exactelly one $4f$ electron, rendering the understanding and thoeretical description of its spectral function manageable. Futhermore thin films of $CePt_5$/Pt(111) exhibit a variety of different surface reconstructions depending on the $CePt_5$ layer thickness, which creates the opportunity to study the correlated ground state in relation to surface, bulk and interface effects as well as changes in the lattice structure. X-ray and angle-resolved

photoemission provide access to the energy scale of strong correlation in the core levels as well as in the valence band and even to variations upon that scale caused by the parameters listed above [26, 31–33].
The influence of spin-orbit coupling is investigated by changing the metal substrate from Pt to Ag and thus reducing the spin-orbit coupling of the involved conduction band electrons. Additionally the effects of adding Bi, a heavy element featuring strong spin-orbit coupling, on the electronic structure of $CeAg_x$ are investigated by photoemission spectroscopy.
This work sets out to establish a variety of tuning parameters for the elecetronic structure in strongly correlated electron systems. Especially epitaxially grown thin films of Ce-based surface alloys proof as an elaborate playground to influence the manifestation of strong correlation and study the effects of strong spin-orbit coupling. Furthermore it is shown that photoemission spectroscopy is a powerful tool to address the spectral function of strongly correlated electron systems and trace variations upon it throughout a wide parameter range. The large parameter control in epitaxially grown films of strongly correlated materials under the influence of strong spin-orbit coupling, constitutes a promising approach to finally realize and proof topologically protected surface states in Kondo insulating systems.

⁂

The basic principles of strong electron correlation in the Kondo and heavy fermion limit as well as spin-orbit coupling are discussed in section 2. Section 3 outlines the main aspects of angle-resolved and X-ray photoelectron spectroscopy as well as of the spectral features representing strong correlation in these respective energy regimes. Details of the experimental setup, sample preparation as well as data processing and evaluation are described as well in section 3. An overview over the known material properties of binary Ce – Pt and Ce – Ag compounds is presented in section 4. Section 5 extensively treats the manifestation of strong correlation in various layer thicknesses of $CePt_5$/Pt(111). Material properties like the $c-f$ hybridization or the effective occupancy of the f level are determined via Ce $3d$ core level spectra

and simulations of the latter with the Gunnarsson-Schönhammer model for core level spectroscopy. Additionally the Kondo temperature of selected layer thicknesses is determined via X-ray and angle-resolved photoelectron spectroscopy. Section 6, first discusses the influence of the surface alloy layer thickness on the electronic structure of $CeAg_x$ and in particular on the manifestation of strong correlation and second the respective effects observed upon Bi deposition. The main results of sections 5 and 6 are summarized in section 7 and discussed concerning future works in the area of strongly correlated electron systems under the influence of strong spin-orbit coupling.

2

Theoretical concepts

2.1 Strongly correlated electron systems

Describing and predicting the physical properties of solids such as electric conductivity, heat capacity and heat conductance as well as optical properties for example the absorption and emission of light, is one of the major tasks in modern solid state physics. All of these properties are determined by the entirety of the electronic states in the solid and are therefore subject to a complex many-body problem that cannot be solved analytically.
Nevertheless there are appropriate assumptions to simplify the necessary calculations and still reach satisfactory agreement with experimental results. Two of the most fundamental assumptions are incorporated in the nearly free electron (NFE) and the tight binding (TB) model. The electronic states are thereby either derived from itinerant, nearly free electrons subject only to a small perturbative potential, or strongly localized electrons from atomic states [34–37]. The NFE model, for example, is suitable for describing the physical properties of electrons in metals like Ag, Cu or Au, where they are able to travel almost freely within the crystalline lattice, only disturbed by the weak periodic potential of the ionic cores.

However, both models already loose their validity when elements with filled d shells in the transition metal group are considered. Whereas d electrons in principle can be understood as itinerant, local Coulomb repulsion can adopt very high values on the order of several electron volts. This largely suppresses any hopping of charge carriers between lattice sites and therefore strongly limits electric conductance.
This mechanism is described in the Hubbard model that is essentially based on a tight binding approach [38, 39]. Every lattice site is hereby occupied by one electron. This amounts to half filled bands and should therefore result in metallic behaviour. The Hamilton operator of the Hubbard model is given in equation 2.1 [40]

$$H = -t_{i,j} \sum_{i,j,\sigma} a^{\dagger}_{i,\sigma} a_{j,\sigma} + U \sum_{i} n_{i,\uparrow} n_{i,\downarrow}, \tag{2.1}$$

where $a^{\dagger}_{i,\sigma}$ and $a_{j,\sigma}$ describe the creation of an electron at site i while simultaneously annihiliating an electron at site j. The movement of electrons through the lattice from site i to j is described by a hopping matrix element t_{ij}. However, for the hopping to be possible, the system has to overcome the local Coulomb repulsion U between two d electrons on the same lattice site n_i. At a sufficiently large Coulomb repulsion $U \gg t_{ij}$, hopping and therefore conductance in the system is suppressed.
Photoemission spectroscopy was substantially involved in understanding a material system that is now known as a prototype Mott-Insulator [40]. In Nickel(II)-oxide (NiO) the Ni d shell is filled with eight out of ten potential d electrons. This amounts to a partially filled band, rendering NiO to behave like a normal metal. However, there is a strong local Coulomb repulsion between the d electrons that largely suppresses hopping between lattice sites. This leads to the opening of a band gap of $E_{\mathrm{gap}} \approx 4\,\mathrm{eV}$, whereby NiO becomes an insulator [41].
Besides insulating behaviour, there are other possible consequences of strongly localized electronic states. In rare earth metals for example, the $4f$ or $5f$ electrons have a probability density very close to the atomic core as opposed to the more extended $5s$, $5p$, $5d$ and $6s$ levels. This is schematically shown in

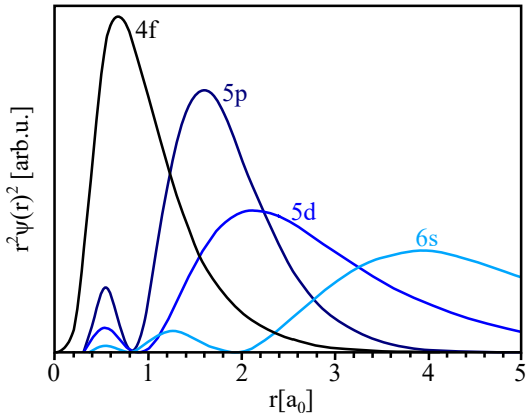

Figure 2.1: Radial probability density for Ce valence and core states. The $4f$, $5d$, and $6s$ valence state, as well as the $5p$ core level probability densities are depicted in units of the Bohr radius a_0 for Ce with an electronic configuration of $[\mathrm{Xe}]4f^1 5d^1 6s^2$. The $4f$ level is situated close to the atomic core and is screened by the more extended $5p$, $5d$ and $6s$ levels. Graphic adapted from [42].

figure 2.1 for metallic Ce.

Thus, the f electrons are effectively screened by the valence electrons, which renders direct exchange between neighbouring f electrons highly unlikely. The system features strongly localized $4f$ or $5f$ electrons on the one hand, whereas on the other hand, conduction is still provided by more delocalized s and p states. The Coulomb repulsion between two f electrons on the same lattice site exceeds typical values of the Hubbard U by far, which is why the Hubbard model is no longer suitable for describing these material systems. They are referred to as *strongly correlated electron systems*.

Due to the strongly localized $4f$ or $5f$ electrons, these compounds exhibit interesting physical properties. If embedded in a metallic host the localized spin of these electrons might polarize the magnetic moment of the surrounding conduction band electrons. This particularly gains importance at low temperatures where conductivity, specific heat as well as suszeptibility of rare earth – metal compounds strongly deviates from that of other metals. These characteristics are summarized by the term *Kondo effect*. The occurence and tunability of electronic structure in the Kondo limit is the central question in

the material systems investigated in this work. Therefore, the Kondo effect will be considered in more detail in the following sections.

2.1.1 The Kondo effect

In 1934, *de Haas et al.* performed transport experiments on simple metals like Cu, Au or Pb and thus reported the first experimental observations of what should later be known as the Kondo effect [10]. The resistance of a metal usually decreases upon lowering the temperature, due to a reduction of lattice vibrations that allow for a higher charge carrier mobility. At temperatures of about $T = 10 - 20\,\mathrm{K}$ the resistance either saturates in consequence of residual scattering of charge carriers on static defects, or drops to zero as the material becomes superconducting [43].
This, however, was not observed in *de Haas'* transport measurements on Au wires [10]. Upon lowering the temperature further to $T \approx 1\,\mathrm{K}$ an increase of the electric resistance is observed, causing a minimum in its temperature dependence. Deviations from the linear T^2-dependence of the specific heat C/T, as well as a Curie-Weiss term in the magnetic suszeptibility at low temperatures, suggested localized magnetic moments to lie at the heart of this novel behaviour [11, 12]. In *de Haas'* experiments those magnetic moments were present due to a contamination of the Au wire with magnetic impurities.
Nevertheless, it was not until 1964 until Jun Kondo could provide a theoretical explanation of the observed effects [13]. On the basis of the $s-d$ model, he considered a spin scattering of conduction electrons with a local spin density $\mathbf{s}(0)$ at the site of the impurity, on a localized moment with spin $\mathbf{S}$ of the form

$$H_K = \sum_{\mathbf{k}\sigma} \epsilon_{\mathbf{k}} n_{\mathbf{k}\sigma} - 2J\mathbf{S} \cdot \mathbf{s}(0) \tag{2.2}$$

[44–47]. The sum describes the conduction band electrons with energy $\epsilon_{\mathbf{k}}$ and $n_{\mathbf{k}\sigma} = a^\dagger_{\mathbf{k}\sigma} a_{\mathbf{k}\sigma}$ as the creation and annihilation operator of a conduction band electron [48].

To determine the electrical resistivity he performed perturbation theory calculations on the $s-d$ model up to third order in J, where J is the exchange constant. For $J<0$, representing antiferromagnetic coupling, he showed that an interaction between the spin of the scatterer and the spin density of the conduction electrons causes an increase of the second order resistance term over the first, causing a logarithmic increase of the resistance at low temperatures.
Though correctly describing the upturn of the electric resistance at low temperatures, Kondo's appoach also predicts an unphysical divergence of the resistance as $T \to 0\,\mathrm{K}$.
These shortcomings of the Kondo model are solved by treating the Kondo problem in the framework of the *Single Impurity Anderson Model* (SIAM), established in 1961 by *P.W. Anderson* [14]. The SIAM implies a "scaling" of the Kondo problem, reducing the system's degrees of freedom as the temperature is lowered. This hypothesis was later confirmed by *K. Wilson* in 1974, whose work shows, that the magnetic impurity gets completely screened by conduction band electrons below a certain, material specific temperature T_K, the Kondo temperature [15, 43]. The SIAM is a powerful approach to the Kondo problem as it provides the theoretical basis for calculating photoemission spectra of rare earth systems in the framework of the Gunnarsson-Schönhammer formalism [49].
The $s-d$ model as well as the Hubbard model are derived for two extremums of the SIAM. If the local Coulomb interaction U between two electrons on the same lattice site $U \to \infty$, one obtains rigorously the spin interaction of the $s-d$ model at a single lattice site. This is extended to the whole lattice by applying the same interaction at every lattice site. Thus the $s-d$ model is often referred to as the *Kondo lattice model* [50, 51].
On the other hand if the hybridization matrix element V between the impurity site and the conduction band electrons $V \to 0$, one obtains the localized electrons as featured in the Hubbard model. Hopping between sites is described by t_{ij} at the expense of the Coulomb repulsion U [51, 52].
Within the SIAM, the macroscopic properties of a material are governed by a competition between localized and kinetic behaviour of the electrons. The

SIAM therefore constitutes the framework for describing a variety of strongly correlated electron systems.

2.1.2 The single-impurity Anderson model

The single-impurity Anderson model (SIAM) describes the interaction of a single magnetic moment with a sea of itinerant conduction band electrons [14]. It expands the Kondo $s-d$ model in a way, that it not only considers the spin interaction between magnetic moments and conduction band electrons but also takes into account the strong Coulomb correlation U_{ff} between electrons on the same impurity site as well as the hybridization matrix element $V_{\boldsymbol{k}\sigma}$ between local moments and conduction band electrons [48]. This is summarized in the SIAM-Hamiltonian in equation 2.3 for the case of a single f electron acting as the magnetic moment according to [49, 53]:

$$H_{SIAM} = \underbrace{\sum_{\boldsymbol{k}\sigma} \epsilon_{\boldsymbol{k}\sigma} a^{\dagger}_{\boldsymbol{k}\sigma} a_{\boldsymbol{k}\sigma}}_{\substack{\text{creation and annihilation} \\ \text{of a conduction band electron}}} + \underbrace{\epsilon_f \sum_{m\sigma} f^{\dagger}_{m\sigma} f_{m\sigma}}_{\substack{\text{creation and annihilation} \\ \text{of an } f \text{ electron}}} + \underbrace{U_{ff} \sum_{m\sigma \neq m`\sigma`} n^{\dagger}_{m\sigma} n_{m`\sigma`}}_{\substack{\text{Coulomb repulsion} \\ \text{between } f \text{ electrons}}}$$
$$+ \underbrace{\sum_{\boldsymbol{k}m\sigma} (V_{\boldsymbol{k}\sigma} f^{\dagger}_{m\sigma} a_{\boldsymbol{k}\sigma} + h.c.)}_{\substack{\text{hopping between} \\ \text{conduction and } f \text{ level}}} + \underbrace{[\epsilon_c n_c + U_{fc}(1 - n_c) \sum_{m\sigma} f^{\dagger}_{m\sigma} f_{m\sigma}]}_{\text{core hole excitation}}. \quad (2.3)$$

The first and second term describe the conduction band electrons as well as the localized f electron. Hereby $\epsilon_{\boldsymbol{k}\sigma}$ is the energy of the conduction band electrons with momentum $\boldsymbol{k}$ and spin σ whereas ϵ_f describes the energy of the f electron. $a^{\dagger}_{\boldsymbol{k}\sigma}$ and $a_{\boldsymbol{k}\sigma}$ are creation and annihilation operators for a conduction band electron with momentum $\boldsymbol{k}$ and spin σ whereas $f^{\dagger}_{m\sigma}$ and $f_{m\sigma}$ are creation and annihilation operators for an f electron in the state $m\sigma$.
The third term describes the Coulomb repulsion U_{ff} between two f electrons on the same impurity site. The fourth term allows for hybridization between conduction band states and local moments via the hybridization

matrix element $V_{\boldsymbol{k}\sigma}$. Note that in this representation $V_{\boldsymbol{k}\sigma}$ is considered to be $\boldsymbol{k}$-dependent.

The last term in equation 2.3 is not initially included in the SIAM-Hamiltonian in the works of *P. W. Anderson* but has been added by *O. Gunnarsson* and *K. Schönhammer* to allow for the calculation of core level photoemission spectra [14, 49]. It describes the creation of a core hole at energy ϵ_c with $n_c = a_c^\dagger a_c$. Due to their probability density close to the core the f electrons experience an attractive potential U_{fc} of the core hole leading to a drastic reordering of the energy levels in the photoemission final state. This causes significant satellite peaks in the core level photoemission spectra of strongly correlated materials. This core level multiplet structure enables direct access to the low energy Kondo physics in the valence band. Therefore the spectroscopy of core levels in correlated materials with for example X-ray photoelectron spectroscopy, provides valuable access to the many-body ground state in these systems. This mechanism will be exploited in great detail by an extensive study of the Ce $3d$ core levels in $CePt_5$/Pt(111) and will be discussed in more detail in section 3.1.3. n_c, in equation 2.3 denotes the electron occupation of the core level, which is $n_c = 1$ in the initial state prior to the photoemission process and $n_c = 0$ afterwards.

As a result the intensity of a photoemission experiment is determined by the transition matrix element $\langle \Phi_f | H_{\mathrm{SIAM}} | \Phi_i \rangle$ with Φ_f and Φ_i being final and initial state of the system. Due to the hybridization of conduction band and f electrons ($c-f$ hybridization) the initial state $|\Phi_i\rangle$ of Ce, that features exactly one f electron in its atomic configuration, is composed of a mixture of zero (f^0), single (f^1) and double (f^2) occupancy of the f level. The respective spectroscopic weights are given by c_0, c_1 and c_2. In summary the initial state is given by $|\Phi_i\rangle = c_0|f^0\rangle + c_0|f^1\rangle + c_0|f^2\rangle$.

This partial delocalization of the f electrons leads to a reduction of the effective occupancy n_f of the f level. For the case of Ce this means $n_f < 1$ and the valence v of the f level decreases to non integer values $v = 4 - n_f$. The new state formed by hybridized f and conduction band electrons is lowered in energy with respect to the non hybridized state by $\delta_{\mathrm{K}} = k_{\mathrm{B}} T_{\mathrm{K}}$ where k_{B} is the Boltzmann constant and T_{K} is the Kondo temperature.

The influence of $c-f$ hybridization on photoemission spectra of different energy regimes is exemplarily shown in figure 2.2. Subfigure a) and b) each show Ce $4f$ valence spectra calculated with the Gunnarsson-Schönhammer formalism. Graph i) corresponds to a poorly hybridized case with n_f close to one ($n_f = 0.96$), whereas ii) shows a strongly hybridized case with $n_f = 0.88$. Subfigure b) thereby depicts a smaller energy range as compared to a) to allow for a more detailed analysis of the apparent structures close to the Fermi level. Note that both spectra in a) are broadened by a Gaussian–function with a full width at half maximum (FWHM) of 500 meV whereas the spectra in b) are broadened less [33].

The wide energy range of figure 2.2 a) shows two distinguishable features. One is a peak close to the Fermi level at $E - E_\mathrm{F} = 0\,\mathrm{eV}$ that becomes stronger as n_f is lowered. This is the Kondo resonance (KR) with the spectroscopic notation f^1. The second peak is located at higher binding energies of $E - E_\mathrm{F} = -2 - -5\,\mathrm{eV}$ and results from direct photoemission of an electron from the f level, leaving the f level empty. It is called the ionization peak (IP) and labeled with the spectroscopic notation f^0. The ionisation peak becomes less intense and shifts to higher binding energies as n_f is lowered between i) and ii) and weight is transferred to the Kondo resonance at the Fermi level [33, 54]. Hence, the intensity of the IP is a first indicator of the manifestation of strong correlation in Ce-based systems, where large spectroscopic weight in the IP points towards little $c-f$ hybridization.
Figure 2.2 b) presents a more detailed view of the energy range close to the Fermi level. Here a second structure close to the Kondo resonance becomes apparent: the spin-orbit partner (SOP) of the Kondo resonance. The $4f$ level is 14-fold degenerate and has two spin-orbit branches with $j = \frac{5}{2}$ and $j = \frac{7}{2}$. Those are seperated by $\Delta E_\mathrm{SO} \approx 280\,\mathrm{meV}$. The $j = \frac{5}{2}$ state is sixfold degenerate and represents the ground state, whereas the $j = \frac{7}{2}$ state is eightfold degenerate and constitutes the excited state. The Kondo resonance at $E - E_\mathrm{F} \approx 0\,\mathrm{eV}$ is the spectroscopic representation of an excitation between the hybridized Kondo singlet with reduced f occupancy $n_f < 1$ ($f^{1-\delta}$, $\delta \lessapprox 0.2$) and a set of low lying triplet states with f^1 character. Both Kondo singlet and triplet lie within the $j = \frac{5}{2}$ multiplet. This is schematically shown in figure 2.3 a),

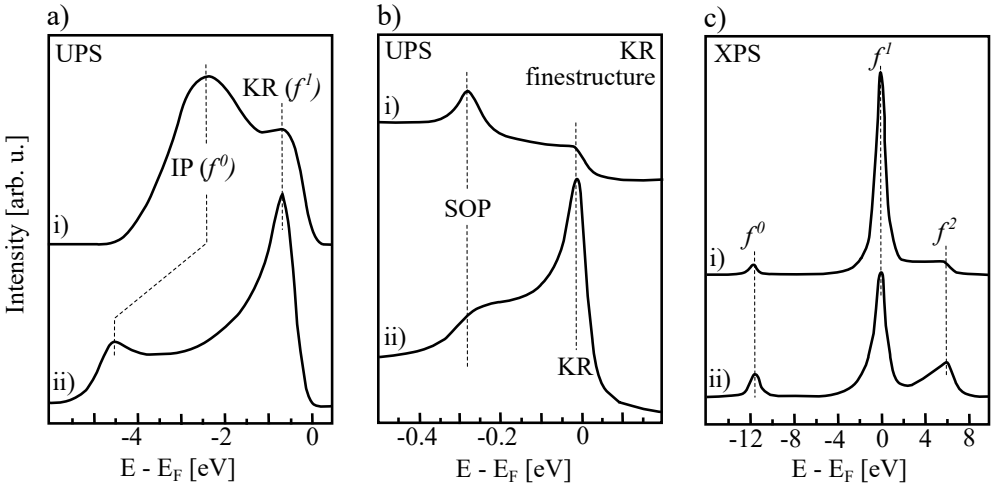

Figure 2.2: Calculated valence band and core level spectral functions of atomic Ce. a) and b) show Ce $4f$ spectral functions, whereas c) depicts a core level spectrum of one Ce $3d$ spin-orbit channel. All spectra are calculated with the Gunnarsson-Schönhammer formalism [33]. In each case, graph i) depicts a poorly hybridized case with $n_f = 0.96$, whereas ii) corresponds to a strongly hybridized case with $n_f = 0.88$. The Kondo resonance (KR) with predominantly f^1 character and its spin orbit partner (SOP) are clearly visible in the strongly hybridized case ii) in b) whereas the ionisation peak (IP) appears only in the wider energy range in a). The Ce $3d$ core level in c) is split into three components, representing the respective proportions of zero (f^0), single (f^1) and double (f^2) occupation of the Ce $4f$ initial state.

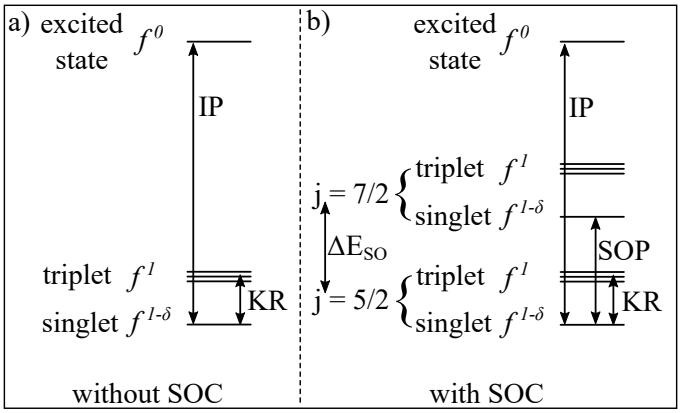

Figure 2.3: Kondo resonance with and without spin and orbital degeneracy. Schematic illustrartion of the excitation processes in the valence states in Ce compounds when spin-orbit coupling of the $4f$ level is neglected in a) and when it is taken into account in b). The lowering of the degeneracy of the $4f$ level due to spin-orbit coupling results in an additional set of singlet and triplet levels lifted by ΔE_{SO}. Additional excitations are enabeled between the $j = \frac{5}{2}$ ground state and the first $j = \frac{7}{2}$ excited state, resulting in the SOP of the Kondo resonance [33, 48, 55]. Figure based on [48]

where SOC is neglected. The reduction of n_f, however, is not limited to the $j = \frac{5}{2}$ ground state. It also appears in the $j = \frac{7}{2}$ excited state, causing this state to split into a hybridized singlet state with a reduced f occupancy and a set of low lying triplet states with f^1 character as well. This is schematically shown in figure 2.3 b), where SOC is taken into account. The spectral feature, that is denoted as SOP corresponds to an excitation between the hybridized excited state singlet ($j = \frac{7}{2}$, $f^{1-\delta}$) and the Kondo ground state singlet within the $j = \frac{5}{2}$ multiplet [48].

The calculated valence band spectra in figure 2.2 b) show, that the weight of the SOP is less affected by the decreasing hybridization between ii) and i) as is the Kondo resonance at E_{F}. The appearance of the KR is determined by the energetic separation between the $j = \frac{5}{2}$ Kondo singlet and the low lying $j = \frac{5}{2}$ triplet states. It vanishes quickly as this splitting becomes less defined due to a broadening of the involved states for example by increasing temper-

atures. The excitation resulting in the SOP, however, is governed mainly by the energy scale of the spin-orbit splitting $\Delta E_{\mathrm{SO}} \approx 280\,\mathrm{meV}$ and is therefore still distinct, when the singlet – triplet separation is small, or starts to vanish with rising temperatures [54].
An even more detailed spectrum of the energy range close to E_{F} would exhibit another structure next to the Kondo resonance. Due to the crystal electric field, the f level degeneracy is lifted further to $N_f = 2$ for the $j = \frac{5}{2}$ ground state and the Kondo resonance exhibits a crystal-field partner at an energy of $\Delta E_{\mathrm{CF}} \approx 30\,\mathrm{meV}$. This however is hardly ever resolved in photoemission measurements [54].
The Full Width at Half Maximum (FWHM) of the Kondo resonance is strongly temperature dependent. Therefore its width at a given sample temperature T_s is used for determining T_{K}. The occupied part of the Kondo resonance is fitted by a Lorentzian function, whose position is determined by the Kondo energy $\delta_{\mathrm{K}} = k_{\mathrm{B}} T_{\mathrm{K}}$ and FWHM by equation 2.4 [56]. A detailed explanation of the applied fitting procedure is given in subsection 3.4.

$$\mathrm{FWHM} = 2\sqrt{(\pi k_B T_s)^2 \,+\, 2(k_B T_K)^2} \tag{2.4}$$

Finally, figure 2.2 c) illustrates the effects of $c-f$ hybridization on Ce $3d$ core level spectra. The poorly hybridized case is again plotted in i) whereas the strongly hybridized case can be seen in ii). Only one spin-orbit branch of the Ce $3d$ core levels is shown. However, one clearly observes not one but three distinct peaks, that can all be assigned to the Ce $3d$ core level. Due to its probability density close to the core the occupancy of the Ce $4f$ level influences the screening of the $3d$ core hole, that is produced in the process of photoemission. Therefore, the multiplet splitting of the Ce $3d$ core level reflects the differnt occupancies f^0, f^1 and f^2 of the Ce $4f$ level.
The lower n_f the more weight gets transfered to the f^0 and f^2 peaks in the spectrum whereas the f^1 peak diminishes. It should be mentioned, that in a measured core level spectrum one observes both spin-orbit partners of the Ce $3d$ core level with $j = \frac{3}{2}$ and $j = \frac{5}{2}$ with a separation of about $\Delta E_{\mathrm{SO}}(\mathrm{Ce}\ 3d) \approx 18\,\mathrm{eV}$. Therefore, the three peak structure in the calcula-

tion in figure 2.2 c) gets doubled and one observes six peaks in total. A thorough explanation of the underlying processes causing the complex Ce $3d$ core level spectra will be given in section 3.1.3, whereas the Gunnarsson-Schönhammer formalism used in this work for calculating Ce $3d$ XPS spectra of $CePt_5$/Pt(111) will be introduced in more detail in section 3.1.4.
In summary, figure 2.2 shows that the SIA model within the Gunnarsson-Schönhammer formalism is able to correctly describe the features expected for a single impurity Kondo system. That is, in the valence band, the Kondo resonance as a sharp peak at the Fermi level, its spin-orbit and crystal-field partner, as well as the ionisation peak at higher binding energies. For the Ce $3d$ core level it correctly predicts a splitting of each spin-orbit channel into three components of f^0, f^1 and f^2 character. The material systems presented in this work, however, do not solely belong to the single impurity regime. In fact the deposited Ce atoms alloy with the metallic host and form a regular impurity lattice. This might have severe consequences for the observed valence band structure which will be discussed in the next section.

2.1.3 Heavy fermions in a Kondo lattice

When a single magnetic impurity is embedded in a metallic host the magnetic moment of the impurity polarizes the surrounding conduction band electrons until, below a certain temperature, the magnetic moment gets screened entirely. Similar to the Landau Fermi liquid picture, the screened magnetic impurity can be described as a quasiparticle, consisting of a single magnetic moment and its surrounding screening cloud. In the single magnetic impurity regime, the quasiparticles are well separated, experiencing no influence of other quasiparticles in the vicinity.
However, by increasing the impurity concentration up to a point where the impurities form a regular lattice with the metallic host, this picture is no longer valid. Whereas there is no direct interaction between the f magnetic moments themselves due to their high degree of localization, there is a coupling between the quasiparticles, mediated by the electrons in the screening

cloud. Depending on the coupling strength J between impurity spin and conduction band electrons the systems ground state is subject to two competing coupling mechanisms.

In the exchange Hamiltonian $H = -J\mathbf{S} \cdot \mathbf{s}(0)$, J is the coupling strength between impurity spin $\mathbf{S}$ and conduction band electrons $\mathbf{s}(0)$, as described in section 2.1.1. The Kondo temperature T_K, describing the formation of a Kondo singlet ground state, is proportional to $T_\mathrm{K} \propto \exp(-1/|J\rho|)$ whereas the Néel temperature T_N, favouring a magnetically ordered ground state, scales with $T_\mathrm{N} \propto |J\rho|^2$. Here ρ ist the density of conduction band states at the Fermi level.

Hence, for small J the magnetically ordered ground state is preferred. Since there is no direct exchange between the strongly localized magnetic moments, the magnetic order is established by the weaker Ruderman-Kittel-Kasuya-Yosida (RKKY) interaction [45, 46, 57]. The magnetic moment of the impurity polarizes the surrounding conduction band electrons leading to a long range oscillation of magnetic moments. This oscialltion indirectly couples different impurity spins establishing ferromagnetic or antiferromagnetic order, depending on the inter-impurity distance.

In contrast, for large J the system tends to demagnetize and the ground state properties are governed by non-interacting Kondo singlets with partially delocalized f electrons. This competing behaviour between magnetic order and Kondo screening was first described by *S. Doniach* and is summarized in the *Doniach-diagram* [58, 59].

However, there are materials, in particular Ce, Yb and U compounds, that exhibit properties at temperatures far below T_K that cannot be described in a single impurity picture. Below a certain coherence temperature $T^* \ll T_\mathrm{K}$ the screening clouds of the magnetic impurities begin to overlap, forming coherent Bloch waves in the periodic impurity lattice. This leads to the emergence of a new electronic quasiparticle band, that inherits the impurities' f character.

The effective mass of the quasiparticles, consisting of magnetic impurity and screening cloud, is very high, up to a thousand times the effective mass of a free electron. Therefore, they are called *heavy fermions* and the quasi-

particle band a *heavy fermion band*. Due to the high effective mass of the quasiparticles this band is very flat. In case of Ce compounds it is located slightly above the Fermi level since the effective occupancy of the Ce $4f$ level is reduced to $n_f < 1$ [9].
The heavy fermion band might also interact with the conduction band leading to a renormalization of the overall band structre around the Fermi level. In $CePt_5$/Pt(111), for example, for temperatures $T_s \leq 13\,\mathrm{K}$ a hybridization gap of $\Delta \mathrm{E}_{\mathrm{gap}} \approx 5\,\mathrm{meV}$ has been observed as a result of an avoided crossing between the flat f- and conduction band [60, 61].

In summary, if the coupling J between impurity spin and conduction band electrons is sufficiently large, establishing Kondo screening as the dominating effect at low temperatures, an ordered lattice of magnetic impurities in a metallic host exhibits several characteristic features in photoemission spectroscopy.
First, below the material specific Kondo temperature T_{K}, the valence band spectrum shows an increase of spectral weight slightly above the Fermi level: the Kondo resonance. This resonance is of $f^{1-\delta}$ character ($\delta \lessapprox 0.2$) and is furthermore accompanied by its crystal-field and spin-orbit partner at $\Delta E_{\mathrm{CF}} \approx 30\,\mathrm{meV}$ and $\Delta E_{\mathrm{SOP}} \approx 280\,\mathrm{meV}$ respectively. At even higher binding energies one observes the ionisation peak with predominantly f^0 character, resulting from direct photoemission of an f electron.
Second, when the temperature is considerably lowered below the Kondo temperature $T^* \ll T_{\mathrm{K}}$ the isolated Kondo singlets might form a heavy fermion band leading to a renormalized band structure with strong f character in the vicinity of the Fermi level.
Third, the different f level occupations f^0, f^1 and f^2 in the valence band are reflected in the respective core level spectra by a charactersitic final state multiplet splitting.
These spectral features are characteristic for Kondo systems and can be observed by angle-resolved as well as X-ray photoelectron spectroscopy, which renders these methods powerful tools for the investigation of strong correlation in rare earth systems.

2.2 Spin-orbit coupling

Next to strong electronic correlation, spin-orbit coupling (SOC) plays an important role for the emergent phenomena in the material systems investigated in this work. SOC describes the interaction between the electron's spin and orbital momentum. In the framework of a non-relativistic approximation of the Dirac equation the Hamilton operator H_{SOC} incorporating the spin-orbit coupling reads as follows [62]:

$$H_{\mathrm{SOC}} = \frac{\hbar}{4m_e^2c^2}\boldsymbol{\sigma} \cdot (\nabla V \times \mathbf{p}) \tag{2.5}$$

with the Pauli matrix vector $\boldsymbol{\sigma}$ being the spin operator and $\mathbf{p}$ the momentum operator. $\hbar$ is the reduced Planck constant, m_e the effective electron mass and c the speed of light. ∇V ist the gradient of the electrostatic potential. It is highest close to the nucleus of the atom and increases with increasing atomic number Z. Therefore SOC is strongest in heavy elements for example Bi or Pb and in electronic levels close to the atomic core.

This becomes apparent for example in photoemission spectroscopy of core levels. These levels are spin-orbit split by means of a few electron volts up to several hundred electron volts. The two spin-orbit partners reflect the two possible configurations of the total momentum $j = l \pm s$ for $l \geq 1$ where the magnetic moments of spin and orbital momentum are either aligned parallel or antiparallel [63].

At surfaces of pristine metals where inversion symmetry is broken, spin-orbit coupling lifts the spin degeneracy of electronic states. These states become energetically separated as well as spin polarized for $k_{||} > 0$. This effect is known as the Rashba-Bychkov effect and has been described theoretically in 1984 by *E. I. Rashba* and *Y. A. Bychkov* [64].

It is observed on surfaces of pristine metals like Au(111) or Bi [65–68] but also on substitutional surface alloys like Bi/Ag(111), Bi/Cu(111), Pb/Ag(111) [69–74].

Another major effect of spin-orbit coupling is the occurrence of topologi-

cally non-trivial insulators (TIs). Here spin-orbit coupling inverts the order of selected bands in the bulk electronic structure of a material, causing an inverted band gap. At the transition to the vacuum or another trivial insulator, characterized by normal band order, this gap needs to be closed, leading to the formation of topological surface states (TSSs) [4, 75]. These bands of almost linear dispersion are protected by their origin in the bulk band structure of the TI which makes them very robust against surface defects [76].
The first experimental proof of this class of materials was found in HgTe/CdTe quantum wells in 2007 in Würzburg [77]. The first observation of TSSs in a three-dimensional material was made for a $Bi_{1-x}Sb_x$ alloy [4, 6], whereupon several other Bi-based compounds have been identified to be topologically non-trivial i.e. Bi_2Se_3 and Bi_2Te_3 [7, 8]. Bi hereby plays a crucial role for the emergence of topologically non trivial behaviour, as its huge spin-orbit splitting leads to the inverted band gap in the first place.
Since then the variety of topological phases has evolved immensely. Next to the first 2D and 3D topological insulators, there are magnetically doped topological insulators like V- or Cr-doped $(Bi,Sb)_2Te_3$ showing the quantum anomalous Hall effect [78] as well as $MnBi_2Te_4$ the first antiferromagnetic TI [79, 80].
Furthermore, there are topological crystalline insulators like SnTe or $Pb_{1-x}Sn_xSe$ where the topological nature of electronic states arises from crystal symmetries [81–83]. Recently the classification of topological materials has been extended to the class of semimetals. For example topologically protected band touching points emerge in Weyl semimetals like TaP or TaAs featuring Fermi-arc surface states [4, 84–87].
Finally the field of strongly correlated materials has not been left untouched by the emergence of topologically non-trivial materials. Both, topological surface states as well as Weyl nodes have been predicted to arise in strongly correlated systems forming topological Kondo insulators (TKIs) [1, 3] and Weyl Kondo semimetals (WKSMs) [88]. In the former the topological surface states are predicted to close the hybridization gap between conduction and heavy fermion band in a Kondo insulator.
The driving force for topologically non trivial states in Kondo insulators is

on the one hand the strong spin-orbit coupling of the lanthanide $4f$ levels, but has recently been shown to depend also on the spin-orbit coupling of the conduction band electrons [1, 89]. Here SOC constitutes the tuning parameter between phases of topological Kondo insulators, Dirac-Kondo semimetals and Weyl Kondo semimetals [88–90]. Transport measurements on the substitutional series $Ce_3Bi_4(Pt_{1-x}Pd_x)_3$ suggest a phase transition from TKI to WKSM by reducing the conduction electrons SOC when substituting heavy Pt atoms by considerably lighter Pd atoms [91]. Despite massive theoretical and experimental effort, however, direct observations of topologically protected surface states in Kondo insulators are still controversial [1, 92].
The focus of this work, though, will not be the investigation of TKI or WKSM candidates. In fact it will, in a very general way, investigate the influence of strong spin-orbit coupling on the electronic structure of correlated materials. This is achieved by adding Bi, a large Z material with a huge intrinsic spin-orbit coupling, to the surface alloy $CeAg_x$/Ag(111), in order to increase the SOC in $CeAg_x$. By that, one can on the one hand, build upon the profound knowledge available for the substitutional surface alloy $BiAg_2$/Ag(111) [69, 93] and on the other hand on basic principles applicable for Ce-based surface alloys.

3

Methodology

3.1 Photoelectron spectroscopy

Evaluating the electronic structure of strongly correlated material systems is the main objective in the present work. In solid state physics, photoelectron spectroscopy has gained considerable value as a powerful tool to determine various aspects of a material's electronic structure. The use of high photon energies in the X-ray regime for example, allows for the revelation of the chemical composition of a material and to some extend even the determination of specific binding partners [31]. By exciting the sample with light of lower photon energies in the ultraviolet (UV) range, one obtains insight into the valence band density of states or even the $\boldsymbol{k}$-resolved band structure.
The effect of electron emission upon excitation with light was first observed in 1887 by Heinrich Hertz [94] and explained in 1905 by Albert Einstein [95]. Accordingly, the binding energy E_{bin} of an electron in a solid is related to the photon energy $h\nu$ of the incoming light as follows [31]:

$$E_{bin} = h\nu - E'_{kin} - \Phi_S \tag{3.1}$$

Here E'_{kin} is the kinetic energy of the emitted electron after leaving the sample and Φ_S the work function of the sample. In the experimental setup, sample and electron analyser are set to the same electrical ground whereby their chemical potentials become equal. Thus it is not necessary to know the material specific work function of each sample, but only the constant work function of the analyser. The kinetic Energy E_{kin} detected in the photoemission experiment is therefore related to the binding energy of the electrons via equation 3.2

$$E_{bin} = h\nu - E_{kin} - \Phi_A \tag{3.2}$$

where Φ_A is the analyser work function.
The distance an excited photoelectron can travel without being scattered inelastically, is given by the inelastic mean free path λ. In the desired photon energy range of about $10-2000\,\mathrm{eV}$, it is only of a few Å [31]. Therefore the sample has to be free of surface contaminations and the photoemission experiment hast to be carried out under ultra high vacuum (UHV) conditions. But still, PES is a very surface sensitive technique.
In general, depending on the excitation energy, one distinguishes between two branches of photoemission. For ultraviolet photoelectron spectroscopy (UPS) photon energies in the vacuum ultraviolet regime up to $h\nu \lessapprox 100$ eV are used to determine the valence band density of states. In addition, angle-resolved photoelectron spectroscopy (ARPES) gives access to the $\boldsymbol{k}$-dependent band structure by simultaneously detecting the kinetic energy of the emitted electrons and their emission angle. Higher photon energies in the keV-range are used in X-ray photoelectron spectroscopy (XPS). This leads to the emission of electrons from core levels, giving access to the stoichiometry of the sample as well as the chemical environment of particular elements [31].

3.1.1 The photoemission process

The interaction of an electromagnetic field with matter is described by the interaction Hamiltonian H_{int}, as a transition from a one-electron initial state

i to a one-electron final state f. In the framework of second quantization, this is described as the destruction of the initial state by the annihilation operator a_i while simultaneously creating the final state with the creation operator $a_f^\dagger$. The electron – photon interaction is represented by the matrix element M_{fi}. Consequently, H_{int} results from a summation over all possible initial and final states as given by equation 3.3 [96].

$$H_{int} = \sum_{i,f} M_{fi} a_f^\dagger a_i \tag{3.3}$$

According to Fermi's golden rule, this leads to a transition probability $p(\hbar\Omega)$ of the photoemission experiment, between the ground state $|N, 0\rangle$ and all s possible excited final states $|N, s\rangle$ as shown in equation 3.4 [96]

$$p(\hbar\Omega) = \frac{2\pi}{\hbar} \sum_s |\langle N, s|H_{int}|N, 0\rangle|^2 \delta(E_s^N - E_0^N - \hbar\Omega). \tag{3.4}$$

The δ-function contains the energy conservation between the final state energy E_s^N, the initial state energy E_0^N and the excitation energy $\hbar\Omega$. For photoemission in the valence band the interaction Hamiltonian H_{int} reads

$$H_{int} = \sum_{\boldsymbol{k},\boldsymbol{\kappa}} M_{\boldsymbol{k},\boldsymbol{\kappa}} a_{\boldsymbol{\kappa}}^\dagger a_{\boldsymbol{k}} \tag{3.5}$$

with a Bloch-like initial state $a_{\boldsymbol{k}}$ of wave vector $\boldsymbol{k}$ and a free-electron final state $a_{\boldsymbol{\kappa}}$ with wave vector $\boldsymbol{\kappa}$. The final state $|N, s\rangle$ is decomposed into an antisymmetric product of the emitted electron $|\Phi_{\boldsymbol{\kappa}}\rangle$ and the remaining excited $(N-1)$-electron system $|(N-1), s\rangle$ with the antisymmetrization factor A as shown in equation 3.6 [96]

$$|N, s\rangle = A(|\Phi_{\boldsymbol{\kappa}}\rangle \otimes |(N-1), s\rangle) = a_{\boldsymbol{\kappa}}^\dagger |(N-1), s\rangle. \tag{3.6}$$

The excited electron is of the energy $\epsilon_{\boldsymbol{\kappa}}$ and carries a crystal momentum $\hbar\boldsymbol{\kappa}$, whereas the remaining excited states $|(N-1), s\rangle$ have the energy $E_\mathrm{s}^{(N-1)}$. According to this, the transition probability of detecting an excited electron

reads [96]

$$p(\epsilon_{\boldsymbol{\kappa}}, \boldsymbol{\kappa}) = \frac{2\pi}{\hbar} \sum_s |\langle N-1, s|a_{\boldsymbol{\kappa}} H_{int}|N, 0\rangle|^2 \delta(E_s^{(N-1)} + \epsilon_{\boldsymbol{\kappa}} - E_0^{(N)} - \hbar\Omega). \quad (3.7)$$

Using equation 3.5 and developing the matrix element $M_{\boldsymbol{k},\boldsymbol{\kappa}}$ this is transformed to

$$p(\epsilon_{\boldsymbol{\kappa}}, \boldsymbol{\kappa}) = \frac{2\pi}{\hbar} \sum_{s,\boldsymbol{k}} |M_{\boldsymbol{k},\boldsymbol{\kappa}}|^2 |\langle N-1, s|a_{\boldsymbol{k}}|N, 0\rangle|^2 \delta(\epsilon_s^{(N-1)} + \epsilon_{\boldsymbol{\kappa}} - \mu - \hbar\Omega) \delta(\boldsymbol{k}_{||} - \boldsymbol{\kappa}_{||} - \boldsymbol{G}_{||}) \quad (3.8)$$

where $\epsilon_s^{(N-1)} = E_s^{(N-1)}$ - $E_0^{(N-1)}$ is the excitation energy of the remaining $(N-1)$-electron system and $\mu = E_0^{(N)}$ - $E_0^{(N-1)}$ is the chemical potential. The second δ-function describes the conservation of the wave vector component $\boldsymbol{k}_{||}$, parallel to the surface, where $\boldsymbol{G}_{||}$ is the reciprocal lattice vector component parallel to the surface and $\boldsymbol{\kappa}_{||}$ the excited electron's momentum parallel to the surface.

The matrix element $|M_{\boldsymbol{k},\boldsymbol{\kappa}}|^2$ contains the perturbation operator H_{PE}, describing the interaction of the electron in the system with the electromagnetic field $\boldsymbol{A}$ of the incoming light. It is defined according to equation 3.9

$$H_{PE} = \frac{e}{m_e c} \boldsymbol{A} \cdot \boldsymbol{p} \quad (3.9)$$

where $\boldsymbol{p} = -i\hbar\nabla$ is the momentum operator of the unperturbed system. The one-particle matrix element $|M_{\boldsymbol{k},\boldsymbol{\kappa}}|^2$ in itself might cause strong variations in the transition probability $p(\epsilon_{\boldsymbol{\kappa}}, \boldsymbol{\kappa})$ depending on the orbital character of the excited state as well as the polarization and direction of incidence of the incoming light. This, however, is not subject to the present work and will not be discussed in more detail. Additional information regarding matrix element effects in photoemission can be found in [97].

The excitations in the remaining system due to the sudden removal of one electron, are described in equation 3.8 by the second matrix element as well as the first δ-function. This is summarized in a fundamental quantity of the

Hamiltonian system: the spectral function $\mathcal{A}^-(\boldsymbol{k}, \omega)$ with

$$\mathcal{A}^-(\boldsymbol{k}, \omega) = \sum_s |\langle N-1, s|a_{\boldsymbol{k}}|N, 0\rangle|^2 \delta(\omega + \epsilon_s^{(N-1)}) \tag{3.10}$$

where $\mathcal{A}(\boldsymbol{k}, \omega = 0)$ corresponds to the Fermi level. The spectral function can be derived from the imaginary part of the one-electron Green's function [98]

$$\mathcal{A}^-(\boldsymbol{k}, \omega) = \frac{1}{\pi} \mathfrak{Im} \mathcal{G}^-(\boldsymbol{k}, \omega). \tag{3.11}$$

Concluding, the intensity of a photoemission experiment is given by the spectral function $\mathcal{A}^-(\boldsymbol{k}, \omega)$ varied by the one-electron matrix element $M_{\boldsymbol{k},\boldsymbol{\kappa}}$.
In case of negligible electron – electron interaction the spectral function is reduced to a δ-function at the energy $\epsilon_{\mathrm{s_i}}^{(N-1)}$ of the Bloch state probed by the photoemission experiment. In fact, the spectral function does include all possible excited states of a system and therefore also describes the photoemission process in case of strong electron – electron interaction, where many of the excited states $|(N-1), s\rangle$ are non zero. As a result the line shape of the spectral function is significantly modified. The deviations from the simple Dirac-peak are best described by a complex quantity, the so called *self energy* $\Sigma(\boldsymbol{k}, \omega)$, with $\Sigma(\boldsymbol{k}, \omega) = \Sigma'(\boldsymbol{k}, \omega) + \mathrm{i}\Sigma''(\boldsymbol{k}, \omega)$ [98].
Describing all interactions in a strongly correlated material is a complex many body problem that has in general no analytical solution. Therefore one is compelled to rely on approximations. In the framework of Landau's Fermi-liquid theory the interaction of electrons is described using the quasiparticle picture [99, 100]. The quasiparticle includes the bare particle, for example an electron, dressed by an interaction cloud, representing its effect on the surrounding system. The self energy solely describes these interaction effects and is therefore given by the difference between the energy of the quasiparticle $\epsilon_{\boldsymbol{k}}^{\mathrm{QP}}$ and the energy of the bare particle without its interaction cloud $\epsilon_{\boldsymbol{k}}$:

$$\Sigma'(\boldsymbol{k}, \omega) = \epsilon_{\boldsymbol{k}}^{QP} - \epsilon_{\boldsymbol{k}}. \tag{3.12}$$

The concept of self energy can be applied to the formulation of the spectral function as shown in equation 3.13 [96]

$$\mathcal{A}(\boldsymbol{k},\omega) = \frac{1}{\pi}\frac{|\Sigma''(\boldsymbol{k},\omega)|}{[\omega - \epsilon_{\boldsymbol{k}} - \Sigma'(\boldsymbol{k},\omega)]^2 + [\Sigma''(\boldsymbol{k},\omega)]^2}. \tag{3.13}$$

Details of the underlying mathematics can be found in [9]. The effects of electron correlation on the spectral function are thus included in the term of the self energy.

Figure 3.1 illustrates the changes in the spectral function due to these interaction effects. Whereas the dashed line at $\epsilon_{\boldsymbol{k}}$ represents the δ-peak for the non-interacting system, the solid line represents the spectrum when electron – electron interactions cannot be neglected.

First, there appears a narrow structure close to the Fermi energy E_{F}. This is the quasiparticle peak. Its energetic position is shifted with respect to the δ-peak to lower binding energies E_{bin}. This reflects the change in energy due to the interaction and is included in the real part of the self energy [96].

Second, the quasiparticle peak is broadened with respect to the δ-peak of the non-interacting system. The broadening is defined by the lifetime of the quasiparticle and is included in the imaginary part of the self energy.

Third, a considerable proportion of spectral weight is transferred to higher binding energies. This is often referred to as the incoherent part of the spectral function. Due to the strong electron – electron interaction, the sudden removal of one electron leaves the remaining system in an excited state with excitation energy $\epsilon_s^{(N-1)}$. This is reflected in the weight of the incoherent part of the spectral function [55, 96]. The quasiparticle-peak and the incoherent part of the spectral function correspond to the Kondo resonance and the ionisation peak in figure 2.2 in section 2.1.2 respectively.

Since photoemission spectroscopy directly probes the spectral function, which again includes all possible excitations in the system, real and virtual alike, PES is a well suited method to gain insight into the complex many body phenomena emerging at low temperatures in the systems investigated in this work.

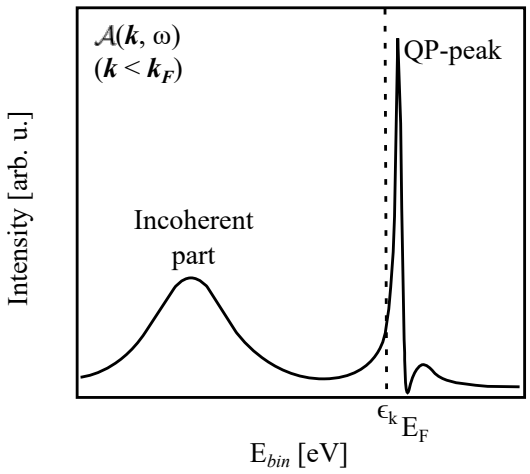

Figure 3.1: Illustration of the spectral function $\mathcal{A}(\boldsymbol{k}, \boldsymbol{\omega})$ for a Fermi-liquid for $\boldsymbol{k} < \boldsymbol{k}_F$. In case of strong electon – electron interaction (solid line), the quasiparticle-peak is shifted in energy as well as broadened with respect to the δ-peak at $\epsilon_{\boldsymbol{k}}$ of the non-interacting case (dashed line). Furthermore, spectral weight is transferred to the incoherent part of $\mathcal{A}(\boldsymbol{k}\ \omega)$ at higher binding energies, representing the excitations $\epsilon_s^{(N-1)}$ in the remaining electron system. Figure according to [55].

3.1.2 Angle-resolved photoelectron spectroscopy

Detecting the intensity distribution of the emitted photoelectrons depending on their kinetic energy E_{kin} as well as their emission angles ϕ and θ allows for the investigation of the dispersion relation $E_{bin}(\boldsymbol{k})$ of the respective state prior to the photoemission process. The relation of kinetic energy E_{kin} and binding energy E_{bin} has already been discussed in section 3.1. The momentum $\boldsymbol{k} = k_x \boldsymbol{e}_x + k_y \boldsymbol{e}_y + k_z \boldsymbol{e}_z$ relates to the polar and azimuthal angle θ and ϕ of the emitted electrons as follows:

$$\begin{aligned} k_x &= \sqrt{\frac{2m_e}{\hbar^2} E_{kin}}\ \sin\theta\ \cos\phi \\ k_y &= \sqrt{\frac{2m_e}{\hbar^2} E_{kin}}\ \sin\theta\ \sin\phi \end{aligned} \tag{3.14}$$

Thereby m_e is the free electron mass, $\hbar$ the reduced Planck constant and E_{kin} the kinetic energy of the emitted electrons. Note that these equations only hold true for low photon energies of $h\nu < 100$ eV where the momentum of the incoming photon can be neglected.
$\boldsymbol{k}_x$ and $\boldsymbol{k}_y$ with $\boldsymbol{k}_x = k_x \boldsymbol{e}_x$ and $\boldsymbol{k}_y = k_y \boldsymbol{e}_y$ are the components of the wave vector $\boldsymbol{k}$ parallel to the sample surface $\boldsymbol{k}_{||} = k_x \boldsymbol{e}_x + k_y e_y$. They are conserved upon transition to the vacuum. The wave vector component perpendicular to the surface $\boldsymbol{k}_{\perp} = k_z \boldsymbol{e}_z$, however, is affected by the surface potential at the transition between sample and vacuum, where emitted electrons are refracted and is therefore not conserved.
In the experiment the two emission angles θ and ϕ are related to the wave vector $\boldsymbol{k}$ of the emitted electron as illustrated in figure 3.2.

An ARPES measurement therefore consists of a data set with up to four dimensions: The photoelectron intensity I(E_{kin}, θ, ϕ) as a function of kinetic energy E_{kin} and the two emission angles θ and ϕ which converts to I(E_{bin}, $\boldsymbol{k}_x$, $\boldsymbol{k}_y$).
For the purpose of analysing and visualizing distinctive features in various ARPES-data sets it is suitable to reduce the dimensionality of the respective spectra, by keeping one parameter of either E_{bin}, $\boldsymbol{k}_x$ or $\boldsymbol{k}_y$ constant.

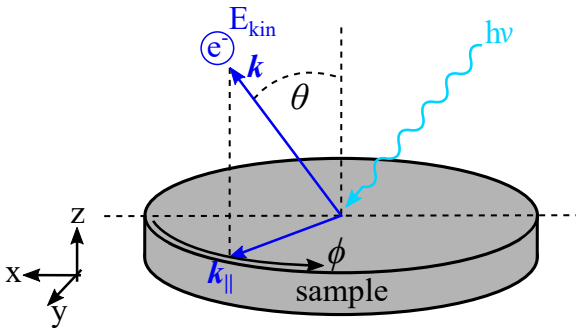

Figure 3.2: Schematic ARPES geometry. Illustration of the relation between detected emission angles θ and ϕ and the wave vector component $\boldsymbol{k}_{||}$ parallel to the sample surface. $h\nu$ is the energy of the incoming photon whereas e^- is the emitted photoelectron with kinetic energy E_{kin} and momentum $\boldsymbol{k}$.

For constant E_{bin}, $I(E_{bin} = \text{const.}, \boldsymbol{k}_x, \boldsymbol{k}_y)$ is referred to as *constant energy cut*. The dispersion relation $I(E_{bin}, \boldsymbol{k}_x, \boldsymbol{k}_y = \text{const.})$ in either $\boldsymbol{k}_y$ or $\boldsymbol{k}_x$ direction is shown, if either $\boldsymbol{k}_x$ or $\boldsymbol{k}_y$ are fixed.
Furthermore, the dispersion of a band can be tracked by one-dimensional cuts through the spectra at either a fixed wave vector to obtain an *energy distribution curve* (EDC) $I(E_{bin})$ or at a constant energy to visualize the *momentum distribution curve* (MDC) $I(\boldsymbol{k}_x \text{ or } \boldsymbol{k}_y)$. The maxima of the peaks in these spectra correspond to the band position at the respective energy and momentum.

3.1.3 X-ray photoelectron spectroscopy

In the X-ray regime with photon energies of $h\nu > 1\,\text{keV}$ the impulse of the incoming photon can not be neglected anymore which renders equations 3.14 invalid. Therefore, XPS is typically used to investigate strongly localized core levels with negliable dispersion rather than weakly bound, dispersive features.
The energy distribution of these core levels is unique for each element which lead to the first application for XPS as *electron spectroscopy for chemical*

analysis (ESCA) in the late 1950ies and early 1960ies [31].
The binding energy is determined from the kinetic energy of the emitted electrons according to equation 3.2. For orbital angular momenta of $l \geq 1$ the detected core levels are split into two spin-orbit partners $j = \mathrm{l} \pm s$ with a characteristic intensity ratio of $I_j = 2j + 1$.
Apart from the core level peaks a typical XPS-spectrum exhibits additional structures referred to as Auger lines [31]. Those lines arise when a core hole, produced by a photoemission process, is refilled by an electron of a weaker bound state. The released energy is then transferred to another electron which gets photoemitted. This process is therefore independent of the primary excitation energy, but determined by the energy difference between the involved orbitals. Thus the kinetic energy of an Auger line does not shift upon variation of the exciting photon energy [31, 96, 101].
Apart from the determination of the chemical composition of a given material, XPS allows to distinguish between surface and bulk material properties. The intensity of the photoemission signal is damped with increasing layer thickness according to equation 3.15 [31]

$$I = I_0 \, e^{\frac{d}{\lambda \cdot \cos(\alpha)}}. \tag{3.15}$$

Thereby I_0 is the undamped intensity d the layer thickness, λ the inelastic mean free path and α the angle between surface normal and detection axis. λ is determined by the specific element and material composition as well as the kinetic energy of the emitted electron [31]. According to equation 3.15 the information depth of a PES experiment is dependent on the sample orientation. At $\alpha = 0°$ (normal emission) the probing depth is equal to λ. At $\alpha = 60°$ off normal emission, the information depth is reduced to $\cos(60°) \cdot \lambda = 0.5 \cdot \lambda$, giving access to about half the layer thickness as compared to $\alpha = 0°$. XPS measurements at large emission angles are therefore more sensitive to the electronic structure at the sample surface. This mechanism is exploited in section 5, where emission angle dependent Ce $3d$ spectra are analyzed in order to gain insight into the bulk and surface dependent hybridization strength Δ and f level occupancy n_f.

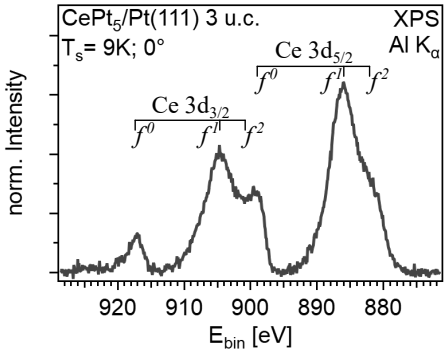

Figure 3.3: Ce 3*d* core level final state multiplet structure. The spectrum shows the Ce $3d_{3/2}$ and $3d_{5/2}$ core levels of $CePt_5$ on Pt(111) recorded with an excitation energy of $h\nu(\mathrm{Al\,K_\alpha}) = 1486.6\,\mathrm{eV}$ at a temperature of $T_s = 9\,\mathrm{K}$ under normal emission. Both spin-orbit partners split into f^0, f^1 and f^2 contributions, representing zero, single and double occupancy of the Ce $4f$ level in the initial state, respectively.

As already briefly discussed in subsection 2.1.2, the Ce $3d$ core levels exhibit a peculiar structure in strongly correlated systems. They split not only into the two spin-orbit components with $j = \frac{3}{2}$ and $j = \frac{5}{2}$, but each spin-orbit partner is again split into three peaks representing the different occupancies f^0, f^1 and f^2 of the Ce $4f$ level. The spectroscopic notations f^0, f^1 and f^2 thereby always refer to the photoemission final state, where an additional core hole is present. An exemplary spectrum of a Ce $3d$ core level of $CePt_5$/Pt(111) in figure 3.3 illustrates this peculiar final state multiplet structure. The f^1 component of both the Ce $3d_{3/2}$ and Ce $3d_{5/2}$ peak at $E_{bin}(f^1(\mathrm{Ce}\ 3d_{3/2})) \approx 905$ eV and $E_{bin}(f^1(\mathrm{Ce}\ 3d_{5/2})) \approx 886\,\mathrm{eV}$ constitute the main features in the spectrum. Furthermore the f^0 share of the Ce $3d_{3/2}$ peak at $E_{bin}(f^0(\mathrm{Ce}\ 3d_{3/2})) \approx 917$ eV is clearly distinguishable. The f^2 shares of both spin-orbit partners as well as the f^0 share of the Ce $3d_{5/2}$ peak at $E_{bin}(f^2(\mathrm{Ce}\ 3d_{3/2})) \approx E_{bin}(f^0(\mathrm{Ce}\ 3d_{5/2})) \approx 900\,\mathrm{eV}$ and $E_{bin}(f^2(\mathrm{Ce}\ 3d_{5/2})) \approx 882\,\mathrm{eV}$ respectively are only apparent as shoulders next to the f^1 features.

The origin of this structure lies in the nature of PES probing the final state of the system under investigation rather than the initial state. The XPS final

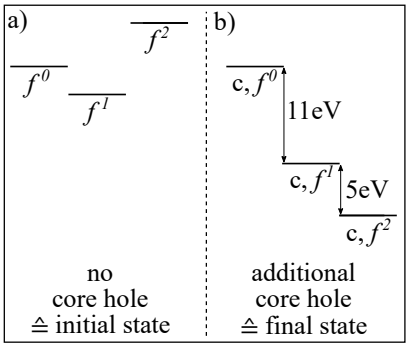

Figure 3.4: Influence of a Ce 3*d* core hole on the *f* level energy scheme. The energy scheme of the Ce $4f$ level in the initial state with no core hole present is shown in a), whereas the situation for the final state with an additional core hole in the Ce $3d$ shell is depicted in b). The attractive core hole potential leads to a reordering of the $4f$ energy level scheme, causing the complex Ce $3d$ core level spectrum as seen in figure 3.3. Figure according to [42, 96].

state contains an additional core hole, in this case in the Ce $3d$ orbital. This core hole acts as an additional positive charge. Due to their strong localization near the core, the Ce $4f$ electrons are affected by this additional positive charge. This causes a drastic reordering of the Ce $4f$ energy level scheme depending on the occupancy of the f level. This is schematically shown in figure 3.4 where the energy level scheme of the f^0, f^1 and f^2 components of the Ce $4f$ level is illustrated before (a) and after (b) photoemission from the Ce $3d$ core level. The energy differences between f^0, f^1 and f^2 are shown next to figure 3.4 for both cases respectively.

If one sets the energy of the f^0 level $\mathrm{E}(f^0) = 0\,\mathrm{eV}$, the initial state level scheme orders as follows [96]: The f^1 configuration has the lowest energy of $\mathrm{E}(f^1) = \epsilon_f \approx -1.5\,\mathrm{eV}$ and therefore forms the initial ground state. The energy of the f^2 configuration is given by $2\epsilon_f$ but is lifted to higher energies by the $f-f$ Coulomb repulsion $U_{ff} \approx 6\,\mathrm{eV}$. Therefore the f^1 configuration is the ground state whereas f^0 and f^2 are the first and second excited states as can be seen in figure 3.4 a).

This order changes when a core hole is produced in the Ce $3d$ level. The

Coulomb potential U_{fc} is of the order of 10 eV and acts on each f electron as an attractive force. Therefore the new level scheme as shown in figure 3.4 b) features the c, f^2 configuration at the lowest binding energy, the c, f^1 configuration at about 5 – 6 eV higher binding energies, whereas the energy of the c, f^0 configuration remains unchanged. In other words, the core hole is screened more effectively by the localised f electrons of the c, f^2 and c, f^1 configuration in contrast to the delocalised electrons of the c, f^0 configuration [96]. Note that the c in the configuration notation c, f^n emphasizes the presence of the core hole and is referring to the final state.
In summary the creation of a core hole in the Ce $3d$ state has two effects. It reorders the energy level scheme of the different $4f$ occupancies and increases the energetic splitting between the individual configurations, making them distinguishable in XPS. Therefore XPS serves as a high energy probe for the low energy excitations in the valence band.
A careful evaluation of the respective spectral weights $\mathrm{I}(f^0)$, $\mathrm{I}(f^1)$ and $\mathrm{I}(f^2)$ of the f^0, f^1 and f^2 peaks in the Ce $3d$ XPS spectra allows to determine the effective occupancy n_f of the f level as well as the $c-f$ hybridization Δ.
In case of $\Delta = 0$ eV, $\mathrm{I}(f^0)$ directly corresponds to c_0 which again relates to n_f as $|c_0|^2 = 1 - n_f$. However, due to a finite admixture of the f^2 final state the hybridization Δ needs to be taken into account. Figure 3.5 a) shows the relation between the relative weight of the f^0 peak

$$w_{rel}(f^0) \;=\; \frac{\mathrm{I}(f^0)}{\mathrm{I}(f^0) + \mathrm{I}(f^1) + \mathrm{I}(f^2)} \tag{3.16}$$

and its proportion to the ground state $|c_0|^2$ for three different values of Δ. Especially for small $w_{rel}(f^0)$, the discrepancy between $w_{rel}(f^0)$ and $|c_0|^2$ can be up to 50% for values of Δ between 60 – 120 meV [49, 102].

The magnitude of Δ is mainly related to the relative weight of the f^2 peak

$$w_{rel}(f^2) \;=\; \frac{\mathrm{I}(f^2)}{\mathrm{I}(f^1) + \mathrm{I}(f^2)} \tag{3.17}$$

[102]. Larger Δ on the one hand increase the f^2 proportion in the initial state and on the other hand the hybridization between f^2 and f^1 final states.

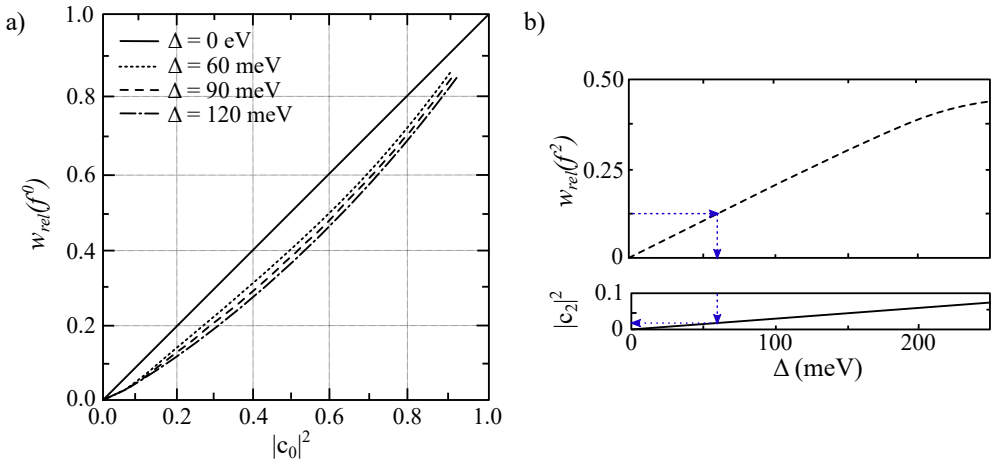

Figure 3.5: Correspondence of the relative spectral weights $w_{rel}(f^0)$ and $w_{rel}(f^2)$ to the ground state proportions c_0 and c_2. a) shows the relation between the relative intensity of the f^0 peak $w_{rel}(f^0) = \mathrm{I}(f^0)/[\mathrm{I}(f^0)+\mathrm{I}(f^1)+\mathrm{I}(f^2)]$ and its ground state proportion $|c_0|^2$ for $c-f$ hybridizations of $\Delta = 0$ meV (solid line), $\Delta = 60$ meV (dotted line), $\Delta = 90$ meV (dashed line) and $\Delta = 120$ meV (dashed-dotted line). b) illustrates the relation between the relative intensity of the f^2 peak $w_{rel}(f^2) = \mathrm{I}(f^2)/[\mathrm{I}(f^1)+\mathrm{I}(f^2)]$ and the $c-f$ hybridization Δ as well as the f^2 ground state proportion c_2. Figure according to [102].

The f^1 final state then again strongly overlaps with the f^1 initial state, which eventually enhances also the f^2 spectral weight [102]. The relation between the intensity ratio of the f^2 peak $w_{rel}(f^2)$ and the hybridization Δ according to [102] is shown in figure 3.5 b).
However the determination of I(f^0), I(f^1) and I(f^2) by means of Ce 3d XPS spectra is rather difficult. First several of the different f contributions overlap as discussed in relation to figure 3.3. Second the determination of the inelastic background is crucial, in order to determine the various f^n weights correctly. A detailed explanation of the background treatment and peak intensity determination will be given in subsection 3.4.

3.1.4 Gunnarsson-Schönhammer formalism for calculating core level spectra

Another approach to determine material properties like n_f or Δ, is to reproduce the measured Ce 3d XPS spectra using the Gunnarsson-Schönhammer (GS) formalism for core level spectroscopy [49]. It is based on the SIAM, where the key aspects taken into account are the conduction as well as impurity (f) states, the Coulomb repulsion U_{ff} between two f electrons on the same impurity site, the $c-f$ hybridisation V and the Coulomb potential U_{fc} resulting from core level photoemission [14, 49].
In order to find an analytical solution for the SIAM at $T = 0\,K$ and for finite U_{ff}, *Gunnarsson* and *Schönhammer* treated the degeneracy N_f of the f level as infinite $N_f \to \infty$ and specifically showed that this already holds true for $N_f \gtrapprox 6$ [42, 49, 53, 102]. This results in a small number of basis states classified by the order of $1/N_f$. Those basis states are shown in figure 3.6. The three states *0*, *a* and *b* in the upper row of figure 3.6 compose the first order of $(1/N_f)^0$. This includes the ground state $|0\rangle$, where all conduction band (CB) states below the Fermi level ϵ_F as well as the core level ϵ_c are occupied, whereas the f level ϵ_f is empty. For states $|\epsilon\rangle$ (a), one CB electron transfers to the f level, whereas for states $|\epsilon, \epsilon'\rangle$ (b) two CB electrons fill the f level, resulting in double occupancy [42]. States (b) are explicitly

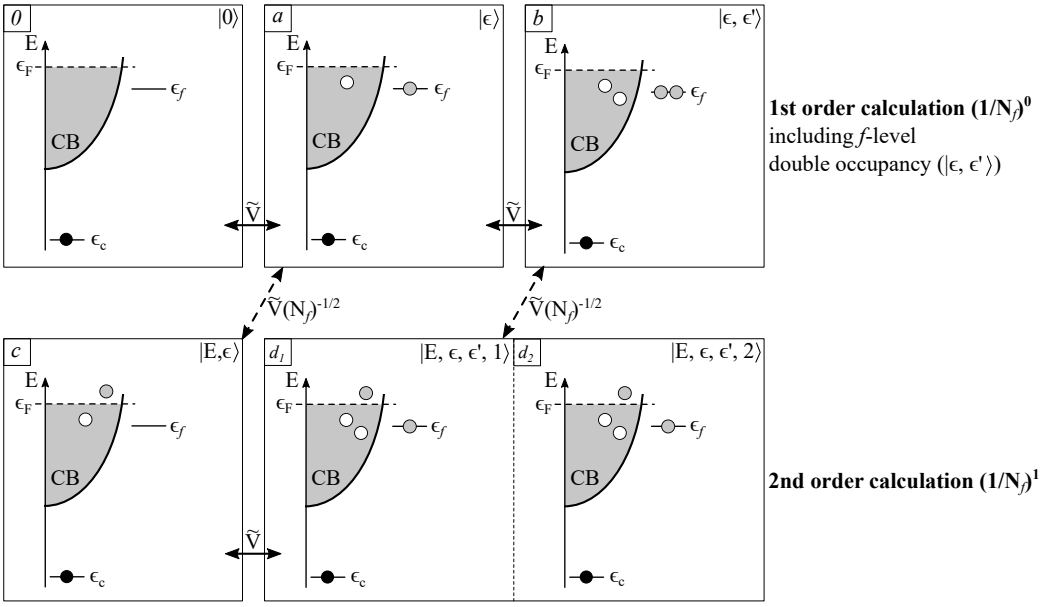

Figure 3.6: Gunnarsson-Schönhammer basis states. Schematical representation of the GS-model ground states for first and second order of $1/N_f$. The grey area depicts the filled conduction band. Empty circles represent the absence of an electron, whereas filled circles symbolize electrons. ϵ_F is the energy of the Fermi level, ϵ_f and ϵ_c represent the impurity f level and the core level respectively. States in the same row couple with $\tilde{V}$, states in different rows with $\tilde{V}/\sqrt{N_f}$. Figure adapted from [42, 103].

of importance when describing spectroscopies where a core hole is created, since f^2-like states are strongly influenced by the attractive potential U_{fc} of the core hole [49].
The second row in figure 3.6 shows the basis states added for calculations of the second order of $(1/N_f)^1$. These are states of the form $|E, \epsilon\rangle$ (c) where one electron has been promoted to E $> \epsilon_F$ and $|E, \epsilon, \epsilon'; 1\rangle$ and $|E, \epsilon, \epsilon'; 2\rangle$ (d_1 and d_2) with two holes in the CB, one electron above ϵ_F and one electron in the f level. The distinction between states d_1 and d_2 refers to CB holes of the same ($|E, \epsilon, \epsilon'; 1\rangle$) or different quantum numbers ($|E, \epsilon, \epsilon'; 2\rangle$) [42].
Figure 3.6 furthermore shows, that states in the same row are coupled by the strength $\tilde{V} = \sqrt{N_f}$V whereas states in different rows couple by $\tilde{V}/\sqrt{N_f}$.
Following the scheme presented in figure 3.6 one can imagine an infinite number of basis states. *Gunnarsson* and *Schönhammer*, however, showed that calculations including basis states up to second order in $1/N_f$ already result in good agreement with experimental spectra [49].
A typical XPS spectrum calculated with the GS formalism is shown in figure 3.7 a). The essential input parameters for the simulation are:

$$\begin{aligned}
\epsilon_f &:= \text{binding energy of the impurity level} \\
U_{fc} &:= \text{core hole Coulomb potential} \\
U_{ff} &:= f\text{-}f \text{ Coulomb repulsion} \\
V &:= \text{hybridization matrix element} \\
B^-/B^+ &:= \text{lower and upper CB limit} \\
N_f &:= f \text{ level degeneracy} \\
\Delta_{SO} &:= \text{Ce } 3d \text{ spin-orbit splitting} \\
Lw/Gw &:= \text{Lorentzian and Gaussian broadening}
\end{aligned}$$

In figure 3.7 a) the Lorentzian and Gaussian widths are chosen deliberatelly small as $Lw = Gw = 0.1$ eV, to disentangle the differnt f^n contributions to the spectrum. The input parameters are $\epsilon_f = -1.3$ eV, $U_{fc} = 12$ eV, $U_{ff} = 9.5$ eV, $V = 245$ meV, $B^-/B^+ = 4$ eV, $N_f = 14$ and $\Delta_{SO} = 18.7$ eV. The light blue line

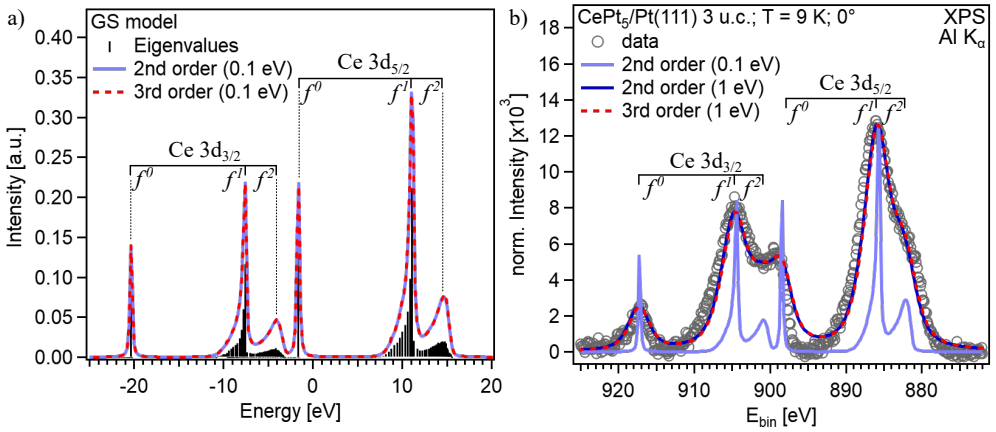

Figure 3.7: GS-model calculations for Ce 3*d* core level spectra. a) shows GS-model calculations of Ce 3*d* spectra for second (light blue line) and third order (dashed red line) in $1/N_f$. Black bars represent the respective energy eigenvalues of the different f^n contributions, marked with f^0, f^1 and f^2 for both spin-orbit channels respectively. In a) $Lw = Gw = 0.1\,\text{eV}$ has been chosen to reduce the overlap of different f^n contributions. The comparison with experimental data is shown in b) with a broadening of $Lw = Gw = 1.0\,\text{eV}$.

represents the second order calculation whereas the dashed red line shows the third order calculation using the same parameters.

The different f^n final state contributions are clearly resolved for both Ce 3*d* spin-orbit partners. Furthermore there is no distinguishable difference between the second and third order calculation.

The black bars in figure 3.7 a) represent the eigenstates of the different f^n contributions. Whereas the f^0 final state is composed of exactly one eigenstate the f^1 and f^2 lines show a multiplet structure. This results in a stronger broadening of the f^1 and f^2 lines with respect to the f^0 line. The quantized eigenstates result from the computational implementation of the GS-formalism using a quantized conduction band.

The energy and intensity axes in figure 3.7 a) are chosen arbitrarily and have to be scaled according to the experimental data to allow for a comparison of GS-model fits with measured Ce 3*d* spectra. This is shown exemplarily in

figure 3.7 b). Grey circles represent the XPS spectrum of the Ce 3*d* core levels of 3 u.c. $CePt_5$/Pt(111). The data are background corrected as described in subsection 3.4. The light blue line represents the GS-spectrum as shown in figure 3.7 a), shifted and scaled to the respective energy range and normalized to the f^1 peak intensities of the experimental data. Furthermore figure 3.7 b) shows the GS-spectra of second (dark blue line) and third order (dashed red line) with increased broadening of $Lw = Gw = 1\,\text{eV}$. The broadened spectra have been normalized to the f^1 type peak maxima as well. Again there is no significant difference between the calculations of second and third order, which is in good agreement with literature [42, 49, 102, 103].
Figure 3.7 b) illustrates that the correct set of input parameters allows for an accurate modeling of experimental spectra with the GS-formalism. The respective occupancies occ^0, occ^1 and occ^2 of the different f^n contributions are calculated as well in the GS-formalism, leading to a definition of n_f^{GS} as

$$n_f^{\text{GS}} \;=\; occ^1 \;+\; 2occ^2 \tag{3.18}$$

accounting for the number of f electrons in the respective f^n configurations [49]. The determination of Δ is performed according to [42, 49, 103]. Here Δ^{GS} is given by the maximum of $\pi|V(\epsilon)|^2$ with

$$\Delta^{GS} = \pi|V(\epsilon)|^2_{max} = \pi\text{max}[\frac{2V^2\sqrt{B^2-\epsilon^2}}{B^2}] = \frac{2V^2}{B} \tag{3.19}$$

with $V(\epsilon)$ being the energy dependent hybridization matrix element. In section 5 the Ce 3*d* spectra of several layer thicknesses of $CePt_5$/Pt(111) will be analysed using both methods, as described above. On the one hand, in subsection 5.2, n_f and Δ are determined on the basis of the relative spectral weights $w_{rel}(f^0)$ and $w_{rel}(f^2)$ of the f^0 and f^2 contributions to the spectrum. On the other hand, in subsection 5.4 all spectra are modeled with the GS-formalism, presenting a complementary approach to obtain n_f and Δ.

3.2 Low-energy electron diffraction

The main objective of the present work is to determine the influence of varying layer thicknesses and binding partners on the manifestation of electronic correlation in Ce-based surface alloys. Therefore, different surface alloy thicknesses have to be clearly distinguished from one another. Earlier works on $CePt_5$/Pt(111) showed, that different initial Ce coverages result in a variety of well ordered surface reconstructions that can be resolved by low-energy electron diffraction (LEED) [27, 30, 104, 105]. Hence LEED is also used in this work to identify various $CePt_5$ and $CeAg_x$ surface alloy thicknesses as well as to determine possible structures upon Bi deposition.

A typical LEED-setup is schematically shown in figure 3.8 b). Electrons of a fixed energy E_0 are emitted from an electron gun, hit the sample and are elastically scattered by the Coulomb potential of the electrons at the sample surface. In case of an ordered lattice the diffracted electrons interfere constructively and destructively, forming a characteristic diffraction pattern depending on the sample surface geometry. The backscattered electrons are detected by a fluorescent screen. An image of these diffraction spots parallel to the sample surface corresponds to the two-dimensional reciprocal lattice and is exemplarily shown for the Ag(111) surface with an incident electron-beam energy of $E_0 = 50\,\mathrm{eV}$ in figure 3.8 a). Note that the colours have been artificially changed to a black and white scale.

According to *de Broglie* a wave length λ_{dB} is assigned to the electrons as [108]:

$$\lambda_{dB} = \frac{h}{p} = \frac{h}{\sqrt{E_0\, 2m_e}} \sim \sqrt{\frac{1.5\ \mathrm{eV}}{E_0\ \mathrm{in\ eV}}}\ \mathrm{in\ nm}. \tag{3.20}$$

For typical LEED electron energies of $E_0 = 10 - 200\,\mathrm{eV}$, λ_{dB} is of the order of a few angstroms (Å), which corresponds to length scales of intra atomic distances in solids. In the low energy regime, the scattering cross section of electrons is very high and they can only penetrate the very first atomic layers at the sample surface [109]. LEED, therefore, is a very surface sensitive technique that can only probe the lattice structure at the sample surface.

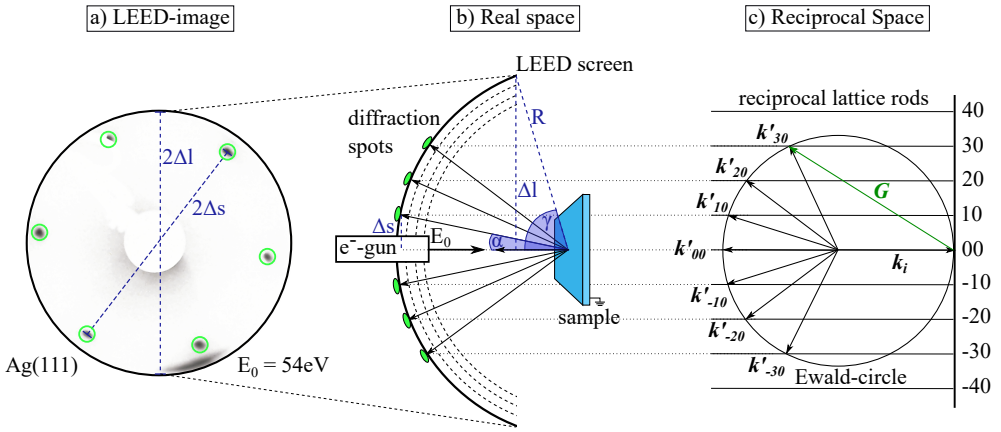

Figure 3.8: Essential aspects of the LEED experiment. b) schematically shows a typical LEED-setup in real space, featuring the electron gun (e^--gun), the grounded sample, the fluorescent LEED-screen as well as some schematical diffraction spots (green ellipses). a) shows an exemplary image of a LEED diffraction pattern for Ag(111) recorded at $E_0 = 50\,\text{eV}$. The green circles frame the diffraction spots. Note that the colours have been artificially changed to a black and white scale. Furthermore the screen radius Δl, the diffraction spot distance Δs, the opening angle of the screen γ as well as the diffraction spot angle α are marked. c) shows the Ewald-construction in the two-dimensional reciprocal space. Diffraction spots appear where the Ewald-circle intersects the rods of the two-dimensional reciprocal lattice and the Laue-equation is fulfilled. Those spots are marked with $\boldsymbol{k'}_{-30}$, ..., $\boldsymbol{k'}_{30}$. Figure adapted on the basis of [35, 106, 107]

The condition for constructive interference is summarized in the Laue-equation [107]. Spots of constructive interference appear, when the difference between incoming wave vector $\boldsymbol{k_i}$ and diffracted wave vector $\boldsymbol{k'}$ matches the reciprocal lattice vector $\boldsymbol{G}$ with $\boldsymbol{k'} - \boldsymbol{k_i} = \boldsymbol{G}$ [35, 107, 110]. This is visualised by the Ewald-construction as shown in figure 3.8 c) [110, 111]. Since the electrons get diffracted only at the sample surface the reciprocal lattice reduces to infinite rods perpendicular to the surface. The incoming wave vector $\boldsymbol{k_i}$ with magnitude $|\boldsymbol{k_i}| = \frac{2\pi}{\lambda_{dB}}$ has its origin at an arbitrary spot in the lattice. The Ewald-circle is drawn around the base of $\boldsymbol{k_i}$ with radius $|\boldsymbol{k_i}|$. The lattice is constructed in a way, that its origin (00) matches the intersection of $\boldsymbol{k_i}$ and the Ewald-circle.
In figure 3.8 c) the Ewald-construction is shown for a two-dimensional surface lattice with a fixed electron energy E_0 and for normal incidence where $\boldsymbol{k_i}$ is perpendicular to the sample surface. This is also the case in the actual experiment as can be seen in figure 3.8 b) but is in general no necessary condition.
Interference spots are observed at each intercept of the Ewald-circle with the rods of the reciprocal lattice, where the Laue-equation is fulfilled. These spots are labeled with $\boldsymbol{k'}_{-30}$, ..., $\boldsymbol{k'}_{30}$ in figure 3.8 c). By increasing the incident beam energy E_0 the Ewald-circle increases and diffraction spots of higher order appear on the screen.
In case of elastic scattering the magnitude of incoming and scattered wave vector is the same $|\boldsymbol{k_i}| = |\boldsymbol{k'}|$. This leads to $|\boldsymbol{G}| = 2|\boldsymbol{k_i}|\sin(\alpha)$, which transforms to the Bragg-equation in 3.21 [107]

$$n\lambda_{dB} = 2d_{hkl}\sin(\alpha), \tag{3.21}$$

using $|\boldsymbol{G}| = n\frac{2\pi}{d_{hkl}}$ and $|\boldsymbol{k_i}| = \frac{2\pi}{\lambda_{dB}}$. Here α is the angle of a diffraction spot relative to the sample normal as shown in figure 3.8 b) and d_{hkl} is the distance between two lattice planes in the crystal. For calculating d_{hkl} and subsequently the lattice constant a as well as the nearest neighbour distance a_{NN}, α is determined by the LEED – screen radius Δl, the opening angle of the screen γ and the distance from a given diffraction spot to the diffraction

pattern center Δs using relation 3.22

$$\frac{\Delta s}{\sin(\alpha)} = \frac{\Delta l}{\sin(\gamma)}. \tag{3.22}$$

This is visualized in figure 3.8 a) and b) where the respective quantities are illustrated. The lattice plane distance d_{hkl} is calculated as follows:

$$d_{hkl} = \frac{n\lambda_{dB}\Delta l}{\Delta s \sin(\gamma)}. \tag{3.23}$$

The lattice plane distance d_{hkl} then again relates to the lattice constant a as 3.24

$$d_{hkl} = \frac{a}{\sqrt{h^2 + k^2 + l^2}} \tag{3.24}$$

where h, k and l are the Miller indices of the sample surface plane. In case of an fcc-lattice in (111)-direction, this amounts to $d_{hkl} = \frac{a}{\sqrt{3}}$ with $h = k = l = 1$. Using equations 3.23 and 3.24 the lattice constant a of Ag in figure 3.8 a) is estimated as $a(\mathrm{Ag}) = 4.14\,\text{Å}$. In literature $a_{\mathrm{lit}}(\mathrm{Ag})$ is given as $a_{\mathrm{lit}} = 4.08$ Å [112, 113]. Therefore the error of a lattice constant determined with LEED in the present work is estimated to 1.7 %.

3.3 Experimental setup

All of the measurements shown in this work have been performed in one of the UHV photoemission-setups at the chair of experimental physics VII in Würzburg. The epitaxial growth of Ce-based surface alloys on metal substrates requires great control over a wide range of preparation parameters such as the Ce-deposition rate as well as substrate and annealing temperatures. This gets even more crucial, when a third element is included in the preparation process, as has been done with Bi on $CeAg_x$ on Ag(111), as discussed in section 6. Furthermore, ARPES and XPS measurements on Kondo systems like $CePt_5$ or $CeAg_x$ require very low temperautres in the range of

$T_s \leq 10\,\mathrm{K}$, since the spectral peculiarities of the Kondo effect are strongly temperature dependent and the Kondo ground state is accessible only well below the systems T_K.
Therefore, the existing setup of three adjoining UHV chambers has been extended by another preparation chamber meeting the aforementioned requirements and the photoemission experiment has been further optimized for low temperatures. Although some of the presented measurements have been performed using the former setup, more or less every preparation has also been repeated in the new setup. Therefore, only the new layout will be introduced in detail in the following.
An overview of the layout changes is schematically shown in figure 3.9. The layout of the existing setup is shown in a) whereas b) illustrates the changes and additions made throughout the course of this work. In summary the changes that have been made are the following:

- A new preparation chamber has been attached at the back left side of the existing one.
- The new preparation chamber has been equipped with a four-axes manipulator and a new sample heating stage.
- The sample loading chamber (*load lock*) has been remodeled and moved to the front right side of the existing preparation chamber.
- The analysis chamber cryostat has been equipped with a new sample stage and cooling shield.
- The sample holder and transfer system has been changed from a home built one to a flag style sample holder and transfer system.

In the new setup, the samples are mounted *ex-situ* on a flag style sample holder and are inserted into the vacuum via the *load lock* at the front of the existing preparation chamber. The load lock is separated from the former preparation chamber by a manually operated valve and reaches a base pressure in the range of $10^{-8}\,\mathrm{mbar}$ within an hour after venting.

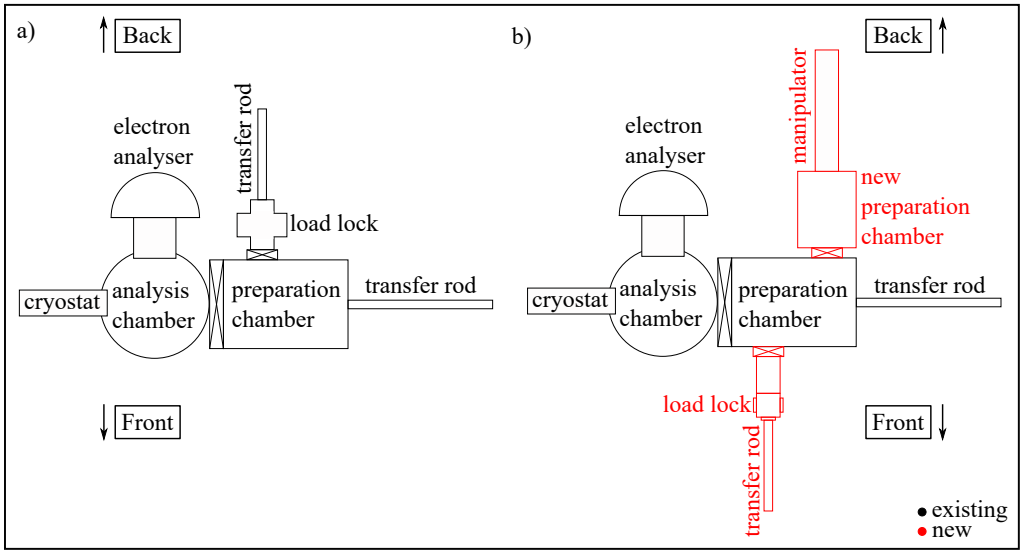

Figure 3.9: Overview of the UHV setup changes. a) and b) show the experimental setup before and after remodeling. A new preparation chamber has been attached at the back left side of the existing preparation chamber. It is equipped with a 4-axes manipulator for sample preparation. The sample loading chamber (*load lock*) has been moved to the front of the existing preparation chamber. New parts and setup changes are highlighted in red in the new setup in b).

The former preparation chamber now mainly serves two purposes. On the left hand side it is equipped with a garage for sample storage whereas on the right hand side it still features several evaporators as well as a SPECTRALEED manufactured by OMICRON for the LEED experiment. In the former preparation chamber a base pressure of $2 \cdot 10^{-10}$ mbar is reached.
The new preparation chamber is attached to the back right side of the existing preparation chamber as can be seen in figure 3.9 b). A detailed technical drawing of the new chamber is shown in appendix A.1 in figures A.1 and A.2. It is separated from the former preparation chamber by a valve and typically reaches base pressures of $3 \cdot 10^{-10}$ mbar. It has been aligned with the right part of the former preparation chamber to give access to a maximum number of possible effusion cells with the newly installed manipulator.
The new preparation chamber features a sputter-gun for cleaning the sample surface by Ar^+-ion bombardment. Furthermore, it is equipped with a 4-axes manipulator with motion in x-, y- and z-direction as well as rotation around the longitudinal axis. The sample stage mounted on the manipulator is equipped with an electron-beam heating stage, incorporating a thoriated tungsten filament. For heating, the sample is usually grounded whereas the filament is set to negative voltages in the order of 300 V. A current of $3-4$ A is applied to the filament enabling emission currents up to 120 mA.
The sample temperature can be measured by a type-K thermocouple attached to the back side of the heating stage, contacting the front end of the sample holder, and by a pyrometer attached *ex-situ* to a window flange in the field of view of the sample.
Due to its position on the manipulator the new heating stage is mobile throughout the entirety of the new preparation chamber as well as the right part of the former setup. This provides access to a variety of effusion cells, including several possibilities of coevaporating more then one material onto the substrate at the same time, as well as simultaneously heating the substrate at any desired position along the stroke of the manipulator. The new preparation chamber therefore allows for the exploration of a wider range of preparation parameters and better control compared to the former setup. A detailed description of the heating stage is given in appendix A.1.

The photoemission measurements are carried out in the analysis chamber. It is accessed via a transfer rod through the former preparation chamber and is again separated by a valve. The base pressure in the analysis chamber typically reaches $2 \cdot 10^{-10}$ mbar.
For core level spectroscopy the chamber is equipped with a monochromatized X-ray source fabricated by Spellman high voltage electronics corporation. It features an Al-anode with an excitation energy of $h\nu(\mathrm{Al\,K}_\alpha) = 1486.6\,\mathrm{eV}$.
For exciting valence electrons a He-discharge lamp of the type *Intense VUV Photon Source* by the company MBScientific AB is available. The He-lamp is equipped with a monochromatizer to tune the excitation energies to $h\nu = 21.22\,\mathrm{eV}$ (He I_α), $h\nu = 23.09\,\mathrm{eV}$ (He I_β), $h\nu = 40.81\,\mathrm{eV}$ (He II_α) or $h\nu = 48.37\,\mathrm{eV}$ (He II_β) respectively [114]. During the operation of the He–discharge lamp the pressure in the analysis chamber rises to $8 \cdot 10^{-10}$ mbar due to He gas leaking from the plasma chamber into the anaylsis chamber.
The emitted photoelectrons are detected by a hemispherical analyser *Scienta R4000* manufactured by GAMMADATA Instrument AB. The entrance slit of the analyser is aligned parallel to the longitudinal axis of the cryostat. Varying the entrance slit width influences energy and angular resolution as well as the transmission function of the spectrometer. After passing the analyser the photoelectrons are multiplied by a microchannel plate (MCP) and detected by a phosphorous screen. This is again recorded by a *Basler Scout 71GM* CCD camera whose image is visible on the measurement computer.
The analyser is operated in either a transmission or an angular mode. The transmission mode is optimized for maximum transmission of photoelectrons but does not resolve their angular distribution. Therefore it is suitable for the investigation of non-dispersive features as for example core levels. The angular mode resolves the emission angle along the entrance slit and therefore allows for the investigation of dispersive features. The maximal acceptance angle hereby is $\pm\,15°$. It can be reduced to $\pm\,7°$ for better angular resolution. The pass energy of the analyser spans from $E_p = 1 - 200\,\mathrm{eV}$. It determines the minimum energy the photoelectrons need, to be able to pass inbetween the two hemispheres of the analyser. Higher pass energies allow for the simultaneous detection of a wider energy range, but reduce the energy resolution.

Therefore higher pass energies are usually applied in XPS measurements whereas the lower pass energy range is used for ARPES. In general one has to find a suitable compromise between measurement time and desired energy resolution. In the angular mode slits of 0.3 mm and 0.5 mm widths have been combined with $E_p = 5$ eV and $E_p = 10$ eV leading to energy resolutions of ΔE(0.3;5) = 5.18 meV, ΔE(0.3;10) = 7.58 meV, ΔE(0.5;5) = 6.97 meV and ΔE(0.5;10) = 7.97 meV respectively [115]. In the transmission mode only the largest settings for slit and pass energy are used, which is 1.5 mm and $E_p = 200$ eV. This results in an energy resolution of ΔE(1.5;200) = 750 meV [116].
During the photoemission experiment the sample is positioned on a He-flow cryostat incorporated in a 4-axes manipulator. The manipulator allows for motion of the sample in all three directions of space as well as rotation around the longitudinal axis of the cryostat. By gradually rotating the sample around this axis a detection of the photocurrent depending on both emission angles ϕ and θ is possible.
The open cycle cryogenic system utilizes liquid He from a He-dewar. By pumping the He-exhaust and carefully aligning the He-transfer line inside the cryostat the cold-head temperature reaches below 4.2 K. This corresponds to sample temperatures of $T_s \approx 7$ K during the photoemission experiment. The design of the sample stage as well as the cooling shield around the sample stage is essential for reaching these low temperatures and has been optimized during the course of this work. Further details regarding the cryostat sample stage and cooling shield can be found in appendix A.1, figure A.4.

3.4 Data processing

ARPES

The imaging properties of the spectrometer cause a curvature of the Fermi edge in the measured spectra, when using a straight analyser entrance slit.

This curvature is corrected by using a reference spectrum of a polycrystalline sample without any dispersive features. During this work the reference spectra have been taken on a scraped Ta-screw or -foil located next to the sample. The curvature of the Fermi edge is estimated by fitting a *Fermi Dirac distribution* (FDD) to every polar angle of the reference spectrum and determining the position of the Fermi edge at each angle. Plotting the Fermi position against the the polar angle results in a curve following a sixth degree polynomial. This polynomial thereupon acts as a correction function for the actual spectrum measured with the same experimental settings. Therefore one needs a reference measurement for each set of parameters.
Furthermore the energy axis of the spectra are converted into $E - E_{\mathrm{F}}$ resulting in a negative binding energy axis. Polar and azimutal angles are converted into k_x and k_y according to equations 3.14.

The ARPES spectra close to E_{F} reveal the occupied part of the Kondo resonance. The FWHM of the Kondo resonance heavily depends on the systems Kondo temperature T_{K} and the sample temperature T_s. If T_s is well determined, it is possible to estimate T_{K}, by applying a Lorentzian fit to the occupied part of the Kondo resonance, as expressed in equation 2.4 [56]. However, the quality of this fit is strongly influenced by the treatment of the inelastic background as well as the precise position of the Fermi level. The Fermi level position is determined by a reference measurement on a sputtered Ta-screw or -foil next to the sample. This reference measurement is also used for determining T_s according to subsection 3.4. The inelastic background is determined as illustrated in figure 3.10, by means of an EDC at the $\overline{\Gamma}$-point of 4 u.c. $CePt_5$/Pt(111), recorded with hν(He II$_\alpha$) at $T_s = 10\,\mathrm{K}$, shown in dark blue. The spectrum is normalized to one at $E - E_F = -150\,\mathrm{meV}$, to allow for a comparison between different measurements, as described in section 5. The inelastic background is composed of a Fermi Dirac distribution (FDD), superimposed by a polynomial of 4th order to account for the increasing slope towards lower $E - E_F$, as shown in black. Additionally the first band maximum a is modelled by a Gaussian, set at $E - E_F = -0.45\,\mathrm{eV}$, shown in light blue. The resulting total fit to the background is shown in

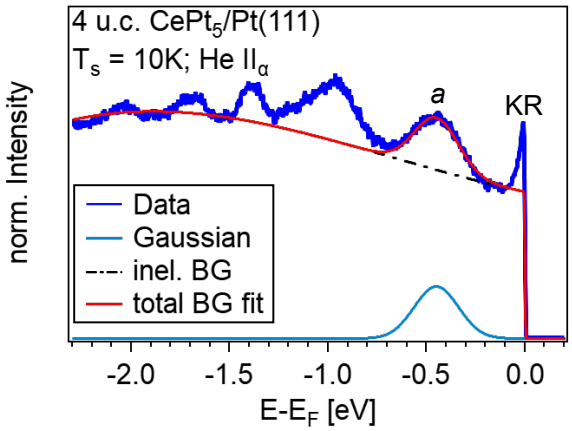

Figure 3.10: Inelastic background at the Kondo resonance. The background at low $|E - E_F|$ is estiamted by a Fermi Dirac distribution superimposed by a polynomial of 4th order, as shown by the dashed-dotted black line. At $E - E_F = -0.45\,\mathrm{eV}$, a Gaussian is added to the background to model the first band maximum a, as depicted in light blue. The resulting total fit is shown in red.

red. The background is manually customized to each spectrum and held constant throughout the fit of the Kondo resonance, leaving the shape of the Lorentzian as the only free parameter. To reduce the number of free parameters in the Lorentzian, its position, which is determined by the Kondo energy $\delta_\mathrm{K} = \mathrm{k}_B \mathrm{T}_\mathrm{K}$ and its FWHM, given by equation 2.4, are coupled, leaving T_K as well as the height of the Lorentzian as the only fit parameters. The offset in intensity is given by the normalization of the experimental data to one. In summary, the total fit to the spectrum is given by a background, consisting of a FDD superimposed with a 4th order polynomial, multiplied with the Lorentzian function for the Kondo resonance, plus a Gaussian centered at $E - E_F = -0.45\,\mathrm{eV}$.

How crucial it is to correctly determine the energetic position of the Fermi level, when fitting the Kondo resonance, is illustrated in figure 3.11. a) shows, in grey, the Kondo resonance of 4 u.c. $CePt_5/Pt(111)$ at $T_s = 10\,\mathrm{K}$. The Fermi Dirac distribution is shown in black for three different positions of $E_F = 1\,\mathrm{meV}$, $E_F = 0\,\mathrm{meV}$ and $E_F = -1\,\mathrm{meV}$. With the bare eye one can

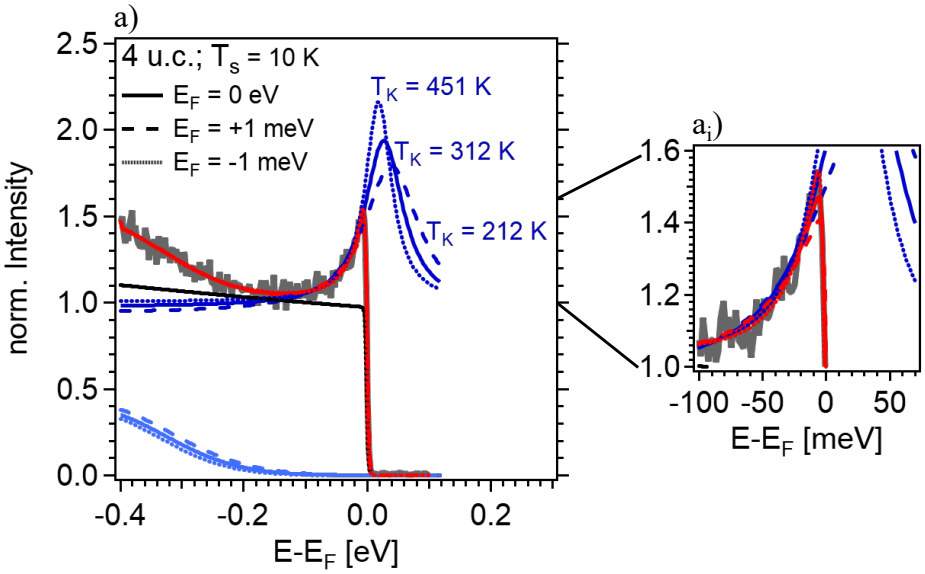

Figure 3.11: Influence of the Fermi level position E_F on the Kondo resonance fit. a) shows three different fits to the Kondo resonance of 4 u.c. $CePt_5$/Pt(111), that differ due to varying Fermi level positions of $E_F = 1$ meV, $E_F = 0$ meV and $E_F = -1$ meV. The experimental data is shown in grey, the three different Fermi Dirac distributions in black. The resulting total fit to the Kondo resonance, depicted in red, barely differs for different E_F. Minor differences become apparent in a_i. However, the Lorentzian fit to the Kondo resonance in dark blue, differs largely for the three different E_F, leading to a huge span in the determined T_K.

barely distinguish between the three resulting total fits in red as one can also not distinguish between the different Fermi level positions in black, as shown in a). Small differences in the total fit only become apparent in the magnification of the Kondo resonance in figure 3.11 a_i). The Lorentzian fit to the Kondo resonance, however, differs largely between the three E_F, leading to a span of Kondo temperatures ranging from $T_K = 212$ K for $E_F = 1$ meV to $T_K = 451$ K for $E_F = -1$ meV. This is taken into account in subsection 5.5 when T_K is estimated for different layer thicknesses of $CePt_5$/Pt(111), leading to large errors in the determined T_K.

XPS

The XPS spectra are integrated over the whole transmission axis and converted into binding energy using equation 3.2, resulting in a one dimensional plot I(E_{bin}). The visible peaks of maximum intensity are assigned to their respective elements according to literature [117] and labeled as described in section 3.1.3.

For the investigation of the influence of strong correlation especially the detailed spectra of the Ce 3d core levels are of importance. In order to correctly estimate the different f^n contributions to the spectrum a careful correction of the inelastic background has to be applied to the spectra. The consecutive steps of the background treatment for Ce 3d spectra are shown in figure 3.12.

First a linear background is estimated in the low binding energy range of $E_{bin} < 876\,\text{eV}$ and subtracted from the spectrum. This is shown in figure 3.12 a). The raw data is shown in grey, the linear background in light blue and the resulting spectrum in black. The linear rise in the low binding energy range is caused by the Ce MNN Auger line, that is very close to the Ce 3d core levels, as can be seen in the overview spectrum in figure 5.1 a).

In a second step a Shirley-type background [118] is estimated for each group of peaks as shown in figure 3.12 b). Using a Shirley background one estimates the proportion of inelastically scattered electrons to the spectrum by integrating over the spectral weight of all the elastically scattered electrons at higher kinetic energies. Therefore the background rises proportionally with the peak intensity as can bee seen in figure 3.12 b). The spectrum resulting form the linear correction is shown in black. The red crosses mark the areas of the respective Shirley backgrounds, shown in light blue and the corrected spectrum is shown in dark blue. To estimate the f^0 and f^2 spectral weights the Ce $3d_{3/2}$ f^0 peak as well as the Ce $3d_{5/2}$ f^1/f^2 peak structure is taken into account. The weight is determined by fitting a standard *Voigt* line shape to the individual spectra as shown in figure 3.12 c). Due to the spin-orbit multiplicity the weight of the Ce $3d_{5/2}$ peaks is scaled by 3/5 when compared to the Ce $3d_{3/2}$ f^0 peak. The resulting intensities are used according to equations 3.17 and 3.16 to determine Δ and $|c_0|^2$.

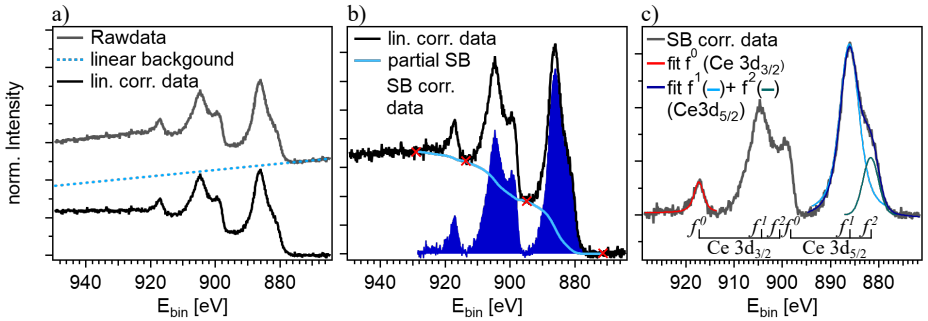

Figure 3.12: Background treatment of Ce 3*d* core level spectra. First a linear background (dashed blue line) ist estimated at lower E_{bin} as shown in a). Second a Shirley background divided into three parts (light blue line) is subtracted from the linear corrected spectrum (black) as shown in b). To determine I(f^0), I(f^1) and I(f^2) *Voigt* line shapes are fitted to Ce $3d_{3/2}$ f^0 peak (dark blue line) and Ce $3d_{5/2}$ f^1/f^2 peak (light blue line) as illustrated in c).

Determination of the sample temperature

The Kondo effect is strongly temperature dependent. Therefore many measurements in this thesis had to be carried out at low temperatures. To determine the sample temperature T_s, a reference measurement on a metallic sample without any dispersive features at the Fermi edge is made. This was done on a Ta-screw or -foil on the sample holder, next to the sample. Due to the close proximity of the Ta piece to the sample one assumes their temperatures to be equal.

The ideal Fermi edge at $T = 0\,\mathrm{K}$ is a step function. In the experiment it is broadened by two factors: the experimental resolution and the sample temperature. Therefore, one assumes the fit of the Fermi edge to be a convolution of a step function, a Gaussian g_{res} broadened by experimental resolution and a Gaussian g_{T_s} broadened by temperature. The Gaussians are cumulated in an effective Gaussian g_{eff}. The respective FWHM Γ relate as follows:

$$\Gamma_{eff}^2 = \Gamma_{T_s}^2 + \Gamma_{res}^2 \tag{3.25}$$

with $\Gamma_{eff} = 3.526 k_B T_{eff}$ and $\Gamma_{T_s} = 3.526 k_B T_s$. Γ_{res} is the experimental

resolution as listed in section 3.3. Therefore the sample temperature T_s is determined as

$$T_s = \frac{\sqrt{(3.526 k_B T_{eff})^2 - \Gamma_{res}^2}}{3.526 k_B} \tag{3.26}$$

A more detailed description of this method for determining the sample temperature can be found in [119].

3.5 Sample preparation

Thin films of $CePt_5$ on Pt(111) and $CeAg_x$ on Ag(111) were prepared using elemental Ce by MaTecK GmbH with a purity of 99.9 %. It is stored in oil to slow down oxidation. Nevertheless before inserting Ce into the evaporator a visible layer of black Ce-oxide has to be removed by manually grinding the Ce chunk with a diamond file. As soon as all the black Ce-oxide is removed and only shiny metallic Ce is visible the material is inserted into the evaporator and pumped to high vacuum conditions. Otherwise a new layer of Ce-oxide is visibly formed within minutes.
The evaporator is a standard *EFM3/4* electron beam evaporator manufactured by Scienta Omicron. The evaporant is stored in a Mo-crucible. A W-filament is placed directly above the crucible for heating the evaporant by electron beam bombardment. A water cooled Cu-shield surrounds the crucible and a manually operated shutter is positioned at the exit of the evaporator to precisely control the evaporation time.
After the UHV-setup is baked and UHV conditions are reached, the Ce inside the crucible has to be cleaned further to ensure stable evaporation conditions. Therefore Ce is heated repeatedly to temperatures slightly above the melting point of pure Ce of $T_{m,Ce} = 789\,^{\circ}\mathrm{C}$. This ensures that all the remaining Ce-oxide, which has a much higher melting point of $T_{m,CeO} > 2000\,^{\circ}\mathrm{C}$, diffuses to the surface of the Ce-chunk. During each evaporation process, this layer of Ce-oxide breaks apart allowing pure Ce from the inside of the block to be evaporated. The progression of the cleaning process is monitored by the

flux-meter that is integrated in the evaporator. The flux-meter measures an ion current right at the exit of the evaporator. This current is proportional to the amount of evaporated Ce [120]. At the beginning of the cleaning process the ion flux is heavily fluctuating. This is caused by the inhomogeneity of the Ce block inside the evaporator. The more homogeneous the evaporant gets, meaning the more the Ce-oxide moves to the surface leaving clean Ce on the inside, the more stable the ion flux. The cleaning process is assumed to be complete, when a stable flux in the low μA-range is reached.
At the beginning of each preparation the substrate is cleaned by Ar^+-ion sputtering at a beam energy between $1-1.5\,\mathrm{kV}$ and an Ar partial pressure of $5.0 \cdot 10^{-5}\,\mathrm{mbar}$.
Subsequently the substrate is annealed by an electron beam emitted from a thoriated W-filament in order to heal surface defects that occur during sputtering. The Pt substrate is heated to a temperature of $T_{Pt} = 900\,^\circ\mathrm{C}$, whereas the Ag substrate is heated to $T_{Ag} = 600\,^\circ\mathrm{C}$. The temperature is monitored via a pyrometer mounted *ex-situ* on a window port in the field of view of the sample surface.
Afterwards the substrate quality is examined by LEED. The diffraction images of the clean Pt(111) and Ag(111) substrates are shown in figure 3.13 a) and b). The LEED image of a clean substrate features a low background intensity while the diffraction spots appear sharp and bright. This is typically reached after two to three preparation cycles.When the substrate LEED image confirms a clean surface, the thin film preparation is started.

For that the Ce evaporator is set to a voltage of 1 kV and the filament current is increased until an emission current is detected. Emission usually starts at a filament current of $I_{fil} = 0.8-1\,\mathrm{A}$. The current is increased until an ion flux in the low μA range is reached. For preparing Ce thin films on Pt and Ag a flux of $I_{flux} = 2.5\,\mu\mathrm{A}$ is used in this work. The evaporator is preheated to the desired flux for five minutes before sample preparation, to ensure stable evaporation conditions.
The film thickness is controlled by the evaporation time t_e. t_e spans between one and ten minutes depending on the desired film thickness.
After Ce is deposited, the sample is annealed immediately to prevent oxi-

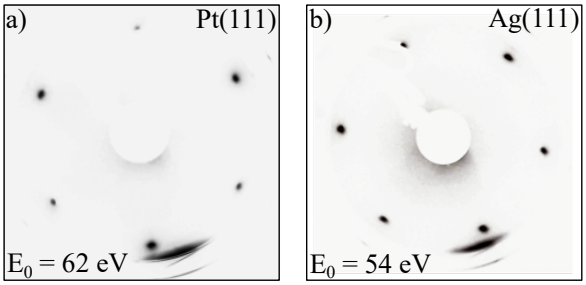

Figure 3.13: Pt(111) and Ag(111) substrate diffraction patterns. a) and b) show the diffraction patterns of clean Pt(111) and Ag(111) at energies of $E_0 = 62\,\text{eV}$ and $E_0 = 58\,\text{eV}$ respectively. Both images exhibit a low background intensity while presenting sharp and bright diffraction spots in the characteristic hexagonal order. Note that the colour code has been artificially changed to a black and white scale.

dation of the Ce layer. For $CePt_5$ the sample is heated to $T_{CePt_5} = 700\,°\text{C}$, whereas $CeAg_x$ is only heated to $T_{CeAg_x} = 600\,°\text{C}$. In case of $CePt_5$/Pt(111) it is known, that annealing the sample produces a terminating Pt layer at the surface. This prevents the $CePt_5$ thin film from oxidation, enabling measurement times of several hours in the first place [121, 122].
For adding Bi to the thin film a standard Knudsen cell evaporator fabricated by Dr.Eberl is available. Bi is evaporated at temperatures of $T_{Bi} = 500\,°\text{C}$. The evaporation time is controlled by opening and closing the shutter in front of the evaporator.
The amount of evaporated Bi is calibrated on the basis of the known surface alloy $BiAg_2$/Ag(111) [69]. A third of a monolayer Bi on Ag(111) very reliably forms a $(\sqrt{3}\,\text{x}\,\sqrt{3})R30°$ reconstruction [69]. This is reached after an evaporation time of $t_e = 4\,\text{min}\,10\,\text{s}$. For the sake of clarity the detailed steps carried out for the preparation of the Bi:$CeAg_x$/Ag(111) surface alloy will be discussed in the respective part in section 6.

4

Heavy fermion material systems

Cerium is the second element in the lanthanide series. It was discovered in 1803 by *Jöns Jakob Berzelius* and *Wilhelm von Hisinger* and independently by *Martin Heinrich Klaproth*. Pure Ce, however was chemically isolated for the first time only in 1843 by *Carl Gustav Mosander* [123, 124]. It has the electronic configuration [Xe]$4f^1 5d^1 6s^2$, whereby the single f electron is responsible for most of the intriguing phenomena the element Ce presents.
The single f electron causes a rather low ionisation energy leading to a high reactivity of pure Ce. It easily binds oxygen forming various cerium oxides, which is why it is used for example in catalyst technology [125]. As ferrocerium it is highly pyrophoric and produces hot sparks with temperatures up to 3000°C when exposed to oxygen. This property is used for example in conventional lighters but also in emergency combustion devices in survival kits [125].
For the effects studied in this work mainly the single, unpaired spin associated with the $4f$ electron is of importance. It constitutes a magnetic moment leading to the intriguing low temperature phenomena like the Kondo effect and heavy fermion behaviour already discussed in section 2. Providing exactly one f electron, Ce often serves as a model system for the investigation of these effects and has been widely discussed in theory and experiment [32, 33, 49].

The low temperature behaviour of Ce-based compounds is thereby strongly dependent on the chemical environment of the Ce ion. In metallic Ce, for example, an isostructural $\gamma \rightarrow \alpha$ transition with a volume collapse of approximately 15 % is observed when the temperature is lowered. Thereby the γ-phase is stable at high temperatures or low pressures, whereas the α-phase emerges at low temperatures or high pressures. This so called *Kondo volume collapse* is related to the partial promotion of the $4f$ electron to the $5d\,6s$ conduction states in the α-phase as described by the SIAM [14, 126].
In $La_{1-x}Ce_xCu_6$ one observes the evolution from the single impurity regime to coherent heavy fermion behaviour by gradually varying the concentration x of La atoms [127]. Furthermore by replacing Cu atoms with Au in $CeCu_{6-x}Au_x$, at a critical concentration x_c of Au atoms between $0.1 < x_c < 0.2$, one approaches a quantum phase transition from a paramagnetic ground state in $CeCu_6$ to a long range antiferromagneticaly ordered state [61, 128].
These two examples show that the local environment of the Ce ion in a compound strongly influences the manifestations of Kondo physics at low temperatures. The following parts give an overview over the known structural and electronical properties of $CePt_5$ and $CeAg_x$.

4.1 $CePt_5$ on Pt(111)

There are various bulk compounds of Ce and Pt. The bulk material $CePt_2$ for example orders antiferromagneticaly at low temperatures as has been investigated by magnetic suszeptibility and specific heat measurements [129]. Bulk $CePt_5$ has been reported to order antiferromagneticaly as well at low temperatures and no signs for heavy fermion behaviour have been reported [130,131]. Specific heat and suszeptibility measurements on the substitutional compound $CePt_{5-x}M_x$ (M = Al, Ga) however show an initial reduction of magnetic interactions and indicate a weak Kondo coupling below $T = 1\,\mathrm{K}$. An overview over several bulk binary Ce – Pt compounds can be found in [132].

The characteristics of binary Ce – Pt, however, change quite dramatically when considering thin films grown on single crystalline substrates. An overview over a series of Ce – Pt surface alloys is given in [133]. The stoichiometry ranges from Ce rich alloys like Ce_7Pt_3 to Pt rich phases like $CePt_5$.
In [26] a surface alloy of a stoichiometry between $CePt_{2.23}$ and $CePt_3$ has been investigated by LEED and XPS. The surface alloy forms a compressed (2 x 2) reconstruction with respect to the Pt(111) substrate. The XPS data show the characteristic multiplet splitting of the Ce $3d$ core levels reflecting the f occupancy in the valence band. This is a clear sign for $c-f$ hybridization in Ce – Pt surface alloys [26]. This work furthermore suggests a Pt termination of the alloyed surface by means of CO and O_2 adsorption studies that amounted to very low sticking coefficients, explaining the inertness of binary Ce – Pt surface alloys.

4.1.1 Crystal structure of $CePt_5$/Pt(111)

Among the different Ce – Pt surface alloys reported in [133] $CePt_5$ is the Pt richest. The bulk phase of $CePt_5$ is of the *Laves type*, meaning that it is composed of a layered structure of alternating Pt-Kagome and $CePt_2$-layers. The crystal structure of $CePt_5$ is shown in figure 4.1. It crystallizes in the hexagonal $CaCu_5$ structure with $P6/mmm$ (D_{6h}) space group symmetry. The alternating Pt-Kagome and $CePt_2$-layers are shown in figure 4.1 a). The top view along the (001) direction in b) illustrates that the Ce ions (blue) occupy the hexagonal gaps in the Pt-Kagome layer (dark grey) whereas the Pt ions of the $CePt_2$-layer (light grey) sit in the triangular gaps. Figure 4.1 c) shows the primitive unit cell of bulk $CePt_5$ with the lattice parameters $a_1 = 5.367$ Å and $a_3 = 4.391$ Å as determined in [132].

Thin films of $CePt_5$ grown on pristine Pt(111) have been reported to form various surface reconstructions depending on the initial Ce coverage and therefore the $CePt_5$ film thickness [27, 30, 133]. The different phases have been investigated using a combination of scanning tunneling microscopy

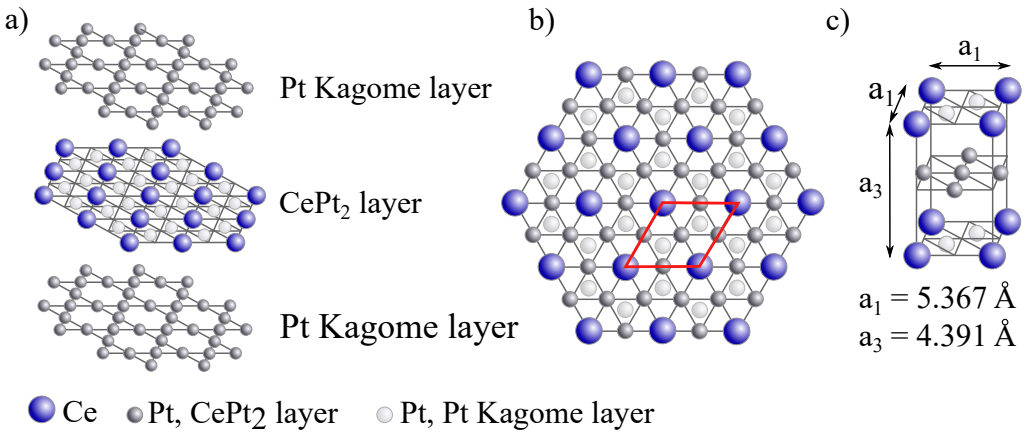

Figure 4.1: Lattice structure of bulk $CePt_5$. $CePt_5$ crystallizes in the hexagonal $CaCu_5$-type crystal structure. It belongs to the laves phase, featuring alternating Pt-Kagome and $CePt_2$-layers as depicted in a). The top view perpendicular to the (001) direction is shown in b) with the surface unit cell marked in red, whereas c) illustrates the primitive hexagonal unit cell with lattice parameters according to [132]. Figure adapted from [30].

(STM) and low energy electron diffraction (LEED), combining the respective information gained in real and reciprocal space [27]. The $CePt_5$ film thickness nomenclature in this work follows the one reported in [27], where it is given in multiples of $CePt_5$ unit cells (u.c.). Hereby one unit cell amounts to approximatelly 0.5 monolayers of initial Ce coverage [27].

All of the reported reconstructions have been reproduced in the present work and are shown in figure 4.2 b) - i) in order of increasing layer thickness. In short, at low coverages in the range of $1-2$ u.c. the $CePt_5$ surface alloy forms a $(2\,x\,2)$ reconstruction with respect to the Pt substrate. At intermediate film thicknesses of $3-4$ u.c. the $(2\,x\,2)$ reconstruction is rotated by $30°$ with respect to the Pt substrate. Additional satellite spots emerge around the main $(2\,x\,2)R30°$ spots at a film thickness of 3 u.c. and vanish again at 4 u.c..

At higher coverages additional reflexes, aligned along the Pt(111) substrate, emerge next to the rotated $(2\,x\,2)R30°$ reconstruction, grow stronger, until at film thicknesses > 10 u.c. only the non rotated $(2\,x\,2)$ spots remain. In the

following the different phases will be discussed in more detail.

The pristine Pt(111) substrate is shown in figure 4.2 a) for an electron beam energy of $E_0 = 62\,\text{eV}$. The spots are ordered hexagonally reflecting the hexagonal symmetry of the (111)-direction of an *fcc* lattice. Every second spot appears brighter than its neighbour, highlighted by red circles in figure 4.2 a). This is due to the threefold rotational symmetry, characteristic for the *fcc* (111) orientation. The nearest neighbour distance of Pt(111) has been estimated to $a_{\text{NN}}[\text{Pt(111)}] = (2.813 \pm 0.048)\,\text{Å}$ which amounts to a lattice parameter of $a[\text{Pt(111)}] = (3.978 \pm 0.068)\,\text{Å}$. This is in good agreement with literature, with $a_{\text{lit}}[\text{Pt(111)}] = 3.92\,\text{Å}$ [134].

At very low Ce coverages, a $CePt_5$ alloy of 1 u.c. thickness is formed, exhibiting a diffraction pattern as shown in figure 4.2 b). Its reconstruction features weak diffraction spots with a $(2\,\text{x}\,2)$ periodicity with respect to the Pt(111) substrate. An accurate determination of the nearest neighbour distance yields $a_{\text{NN}}[1\,\text{u.c.}] = (5.583 \pm 0.095)\,\text{Å}$. The reconstruction determined within the accuracy of the nearest neighbour distance is therefor a slightly compressed $(2\,\text{x}\,2)$. By taking a close look at the spots of the second order one also clearly sees a threefold variation in the reflex intensity, highlighted with red circles in figure 4.2 b). This is due to the Pt(111) substrate that is still visible below the $CePt_5$ film of 1 u.c. thickness.

By doubling the Ce evaporation time a $CePt_5$ alloy of 2 u.c. layer thickness is formed. It shows a similar diffraction pattern as the 1 u.c. phase, though featuring more intense $(2\,\text{x}\,2)$ reflexes. The nearest neighbour distance is determined to $a_{\text{NN}}[2\,\text{u.c.}] = (5.473 \pm 0.093)\,\text{Å}$. This results in a $(1.95\,\text{x}\,1.95)$ reconstruction with respect to the pristine Pt substrate, which is slightly more compressed than the diffraction pattern resulting from a film thickness of 1 u.c.. Furthermore, the threefold symmetry of the Pt substrate is still slightly visible amongst the diffraction spots of second order (red circles).

At the transition to a layer thickness of 3 u.c. a drastic change in the diffraction pattern is observed. The main diffraction spots, highlighted by red circles, are rotated by 30° with respect to the Pt substrate. Furthermore, the main spots are surrounded by six satellite spots, marked in blue, with an orientation along the Pt(111) substrate. The main reflexes amount to

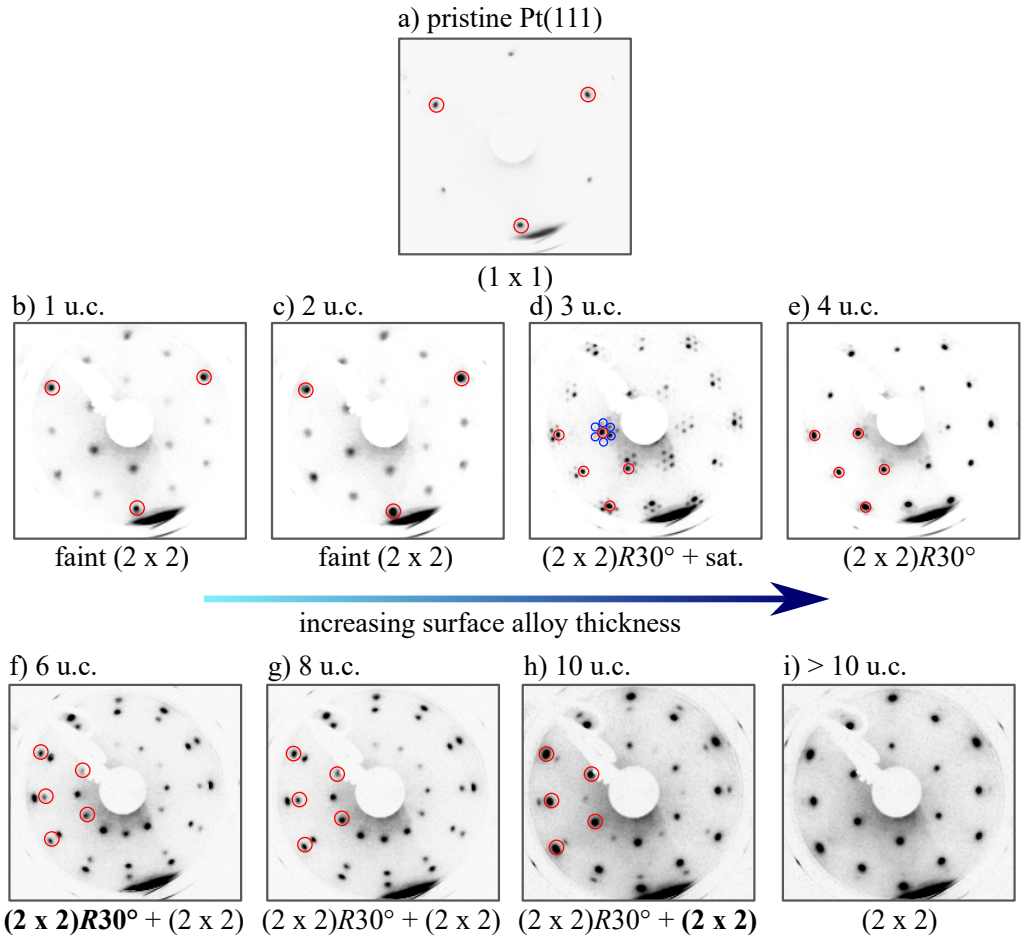

Figure 4.2: Surface reconstructions of $CePt_5$/Pt(111). All diffraction patterns are recorded using $E_0 = 62\,eV$. a) shows the hexagonal $(1\,x\,1)$ reconstruction of the pristine Pt substrate. b) 1 u.c.: faint, slightly compressed $(2\,x\,2)$ reconstruction superimpose the $(1\,x\,1)$ substrate spots. c) 2 u.c.: stronger, compressed $(2\,x\,2)$ reconstruction. d) 3 u.c.: $(2\,x\,2)R30°$ reconstruction and unrotated satellite spots of $\approx(10\,x\,10)$ periodicity. e) 4 u.c.: compressed $(2\,x\,2)R30°$ reconstruction. f)–h): $\sim$7 u.c.–10 u.c.: $(2\,x\,2)R30°$ spots diminish in favor of non rotated $(2\,x\,2)$ spots. i) >10 u.c.: unrotated $(2\,x\,2)$ reconstruction.

a nearest neighbour distance of $a_{\mathrm{NN}}[3\,\mathrm{u.c.}] = (5.89 \pm 0.10)$ Å. This results in a $(2\,\mathrm{x}\,2)R30°$ reconstruction for the main spots. Furthermore, the threefold symmetric intensity variation of the reflexes caused by the Pt substrate is no longer visible and the diffraction pattern is truly sixfold symmetric. The satellite superstructure has a nearest neighbour distance of $a_{\mathrm{NN}}[3\,\mathrm{u.c.}, \mathrm{sat.}] = (28.84 \pm 0.49)$ Å. This approximately amounts to a $(10\,\mathrm{x}\,10)$ reconstruction with respect to the Pt substrate. The superstructure results from varying Ce adsorption sites on the Pt substrate. Ce atoms are alternatingly situated on gaps between the Pt atoms or on top of Pt atoms. This results in a periodic, long range surface corrugation of about 80 pm height [27]. The huge periodicity in real space translates to a small diffraction pattern in reciprocal space, resulting in the satellite spots in the LEED pattern as shown in figure 4.2 d). This moiré pattern arises, with an even larger periodicity, already at thinner $CePt_5$ films of 1 and 2 u.c. causing the blurring of the diffraction spots visible in figures 4.2 b) and c) [27].

At a film thickness of 4 u.c., shown in figure 4.2 e), the satellite spots vanish, whereas the main spots, marked in red, remain and are still rotated by 30° with respect to the Pt substrate. The nearest neighbour distance is determined to $a_{\mathrm{NN}}[4\,\mathrm{u.c.}] = (5.406 \pm 0.092)$ Å resulting in a compressed $(2\,\mathrm{x}\,2)R30°$ reconstruction.

For higher Ce coverages additional spots with an orientation along the Pt(111) substrate accompany the $(2\,\mathrm{x}\,2)R30°$ structure as highlighted by red circles in figures 4.2 f) – h). This sets in at film thicknesses of 5 u.c. (not shown) and increases in intensity between 7 – 10 u.c.. At film thicknesses >10 u.c. the rotated $(2\,\mathrm{x}\,2)R30°$ reconstruction is completely vanished and the diffraction spots, that are aligned with the Pt(111) substrate, remain. Evaluating this diffraction pattern results in a nearest neighbour distance of $a_{\mathrm{NN}}[> 10\,\mathrm{u.c.}] = (5.394 \pm 0.092)$ Å which is in good agreement with the bulk $CePt_5$ lattice constant of $a_{\mathrm{lit}}(\mathrm{bulk}) = 5.367(5)$ Å [132].

Since the formation of Kondo singlets and heavy fermions is largely determined by the local environment of the Ce ion, the different surface reconstructions corresponding to different $CePt_5$ film thicknesses are likely to have an impact on the latter. This will be discussed in more detail in section 5.

4.1.2 Electronic structure of $CePt_5$/Pt(111)

Previous photoemission studies on $CePt_5$/Pt(111) focused on the investigation of a surface alloy with nominally 4 u.c. layer thickness, that is characterized by the $(2\,x\,2)R30°$ diffraction pattern in LEED as shown in figure 4.2 e). This reconstruction shows a distinct Kondo resonance at the Fermi edge at temperatures below $T_s \approx 200\,\mathrm{K}$. Furthermore at temperatures below $T_s \approx 13\,\mathrm{K}$ the emergence of a coherent f band is observed that hybridizes with the conduction band leading to a hybridization gap $\Delta \approx 2-5\,\mathrm{meV}$ [60, 61]. Later X-ray absorption (XAS) and X-ray magnetic circular dichroism (XMCD) studies address the different surface reconstructions emerging from varying $CePt_5$ surface alloy film thicknesses [30, 135]. These works observe a dependence of the f^0 spectral weight on the layer thickness and therefore estimate a change of the Ce valence as the $CePt_5$ film grows in thickness. A summary of the results is shown in figure 4.3 a). The left hand axis shows the relative f^0 weight $w_{rel}(f^0)$ to the XA spectra whereas the right hand axis corresponds to the respective Ce valence v. Both are shown in dependence of the surface alloy film thickness in unit cells. One clearly observes a maximum of $w_{rel}(f^0)$ and therefore a maximum in the Ce valence around $2-3$ u.c. film thickness. However, when comparing XPS and XAS results for the determination of n_f or v the different final state nature of both methods has to be taken into account [49]. Considering $U_{ff} \to \infty$, prohibiting double occupancy of the f level, the XPS ground state is given by equation 4.1

$$|\Phi_0\rangle = c_0|f^0\rangle + c_1|f^1\rangle. \tag{4.1}$$

The f^0 peak in the XPS spectrum corresponds to a final state of the structure 4.2

$$|\tilde{f}^0\rangle = \tilde{c}_0|f^0\rangle + \tilde{c}_1|f^1\rangle. \tag{4.2}$$

Therefore the total weight p_0 of the f^0 peak in the spectrum is given as a superposition of its initial state weights c_0 and c_1 and final state weights $\tilde{c}_0$

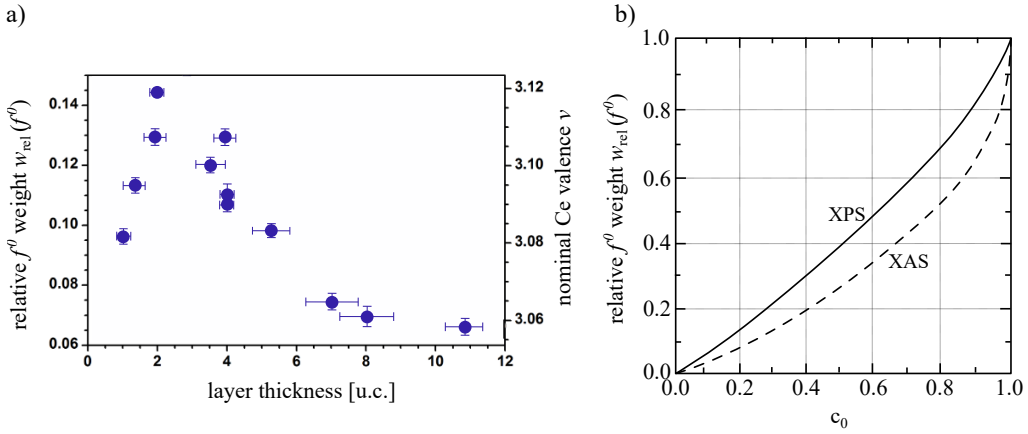

Figure 4.3: Layer thickness dependent Ce valence as determined by XAS. a) shows the relative f^0 weight $w_{rel}(f^0)$ (left axis) and nominal Ce valence v (right axis) in dependence of the $CePt_5$ surface alloy film thickness. A maximum of the f^0 weight and the respective Ce valence is observed around 2 – 3 u.c. layer thickness. Graphic adapted from [30, 135]. b) illustrates the difference between the determination of the f^0 ground state proportion c_0 by the intensity ratios $w_{rel}(f^0)$=$w^{0\to1}/w^{1\to2}$ for XAS and $I(f^0)/[I(f^0)+I(f^1)+I(f^2)]$ for XPS. Graphic adapted from [49].

and $\tilde{c}_1$ as expressed in equation 4.3

$$p_0 = |c_0\tilde{c}_0 + c_1\tilde{c}_1|^2. \tag{4.3}$$

Due to the huge energy separation between the final state c, f^0 and c, f^1 peak of $\approx 11\,\text{eV}$ there is only a small admixture of $\tilde{c}_1$ and $\tilde{c}_0$ is close to one. Hence, the weight of the c, f^0 peak in the spectrum is a proper measure of c_0 in the initial state [49].
In XAS, however, the excited electron remains in the system and the final state configuration c, f^0 and c, f^1 in XPS has to be replaced by c, f^1 and c, f^2 for XAS. The energy separation between the c, f^1 and c, f^2 final state, however, is only of the order of $\approx 5\,\text{eV}$. Therefore, the c, f^2 final state admixes stronger in XAS and the deviation between the relative c, f^0 weight in the spectrum and c_0 are larger [49]. This is schematically shown in figure 4.3 b), where the course of the deviation between the relative f^0 weight in the spectrum and the initial state c_0 coefficient is shown for XPS (solid line) and XAS (dashed line) [49]. At low f^0 spectral weights the difference in c_0 between XPS and XAS is up to 50 %. These differences depending on the experimental method have to be taken into account when comparing results for n_f or v acquired by either XPS or XAS. An estimation of the resulting Kondo temperatures T_K in [30, 135] results in $T_\text{K} \approx 125\,\text{K}$ for a $CePt_5$ film thickness of 1 u.c. and $T_\text{K} \approx 200\,\text{K}$ for 4 u.c..

4.2 $CeAg_x$ on Ag(111)

The second system investigated in this work is a surface alloy consisting of Ce and Ag. It is grown *in situ* as described in subsection 3.5 by evaporating Ce on a single crystalline Ag(111) substrate and subsequent annealing. The stoichiometry of the resulting $CeAg_x$/Ag(111) surface alloy is not known, however it forms a regular hexagonal crystalline lattice as analysed by LEED in section 6.1.

The bulk intermetallic exhibits various stoichiometries as for example CeAg, $CeAg_2$, $CeAg_3$ or Ce_3Ag as well as a variety of different lattice structures [136–142]. CeAg for example exhibits a cubic structure with a lattice constant of $a = 3.733\,\text{Å}$, but undergoes a transition to a tetragonal symmetry at $T_s = 16\,\text{K}$ [136, 137]. At $T_s \approx 5.6\,\text{K}$ a ferromagnetic order with a saturation magnetic moment of $0.7 - 1.25\mu_\text{B}$ is established [136, 137, 143]. At even lower temperatures, however, this magnetic order seems to be disturbed as indicated by anormalities in the electrical resistivity and the Curie temperature under pressure [137, 143]. Amongst an additional high pressure phase transition or enhanced scattering at domain boundaries, also an enhanced Kondo screening at low temperatures and high pressures is discussed as a possible reason for the behaviour of the low temperature resistivity [143].

Weibel et al. performed PES and BIS (*Bremsstrahlung Isochromat Spectroscopy*, also known as IPES (*Inverse Photoelectron Spectroscopy*)) measurements on cubic CeAg at temperatures of $T_s = 20\,\text{K}$. The spectra clearly show an f^0-like ionization peak at $E - E_\text{F} = -2.5\,\text{eV}$, the spin-orbit partner of the Kondo resonance at $E - E_\text{F} = -0.28\,\text{eV}$, as well as the f^2-like final state in the BIS spectrum at $E - E_\text{F} = 5\,\text{eV}$ [136]. This is shown in figure 4.4 a). The actual Kondo resonance at or slightly above the Fermi level, however, is developed only very weakly. Whereas band structure calculations estimate an f level occupancy of $n_f = 0.94$, *Weibel et al.'s* photoemission experiments result in a considerably higher n_f of $n_f = 0.995$, resulting in a Kondo temperature of $T_\text{K} = 3\,\text{K}$ for bulk CeAg [136, 137]. This again is in good agreement with the pronounced ionization peak and the weak Kondo resonance as observed in the spectra in figure 4.4 a).

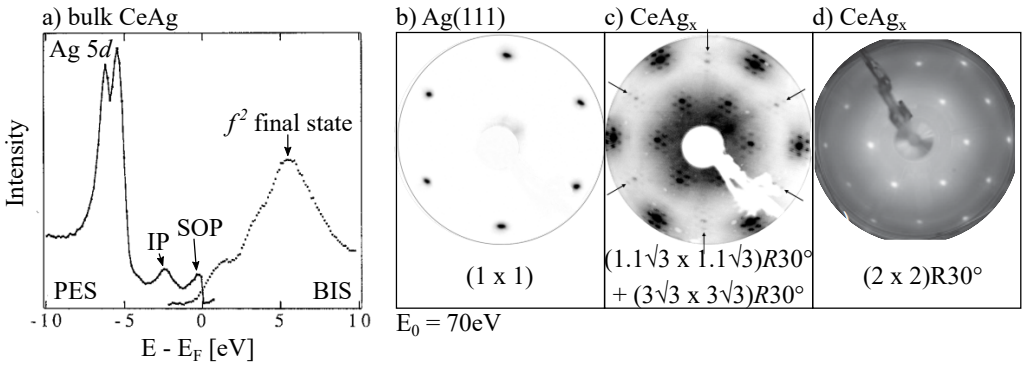

Figure 4.4: Electronic structure of bulk CeAg and surface reconstruction of CeAg$_x$/Ag(111). a) shows combined PES and BIS spectra of bulk CeAg with prominent features corresponding to the Ag $5d$ band at $E - E_\mathrm{F} = -6\,\mathrm{eV}$, the ionization peak at $E - E_\mathrm{F} = -2.5\,\mathrm{eV}$, the spin-orbit partner of the Kondo resonance at $E - E_\mathrm{F} = -0.28\,\mathrm{eV}$ and the f^2 final state at $E - E_\mathrm{F} = 5\,\mathrm{eV}$. Graphic adapted from [136]. b) – d) show the $(1\,\mathrm{x}\,1)$ reconstruction of Ag(111), the $(1.1\sqrt{3}\,\mathrm{x}\,1.1\sqrt{3})R30° + (3\sqrt{3}\,\mathrm{x}\,3\sqrt{3})R30°$ reconstruction of CeAg$_x$/Ag(111) as reported in [144] and the $(2\,\mathrm{x}\,2)R30°$ reconstruction for CeAg$_x$/Ag(111) as shown in [28].

The bulk intermetallic CeAg, therefore, suggests that Kondo behaviour is at least possible in binary Ce – Ag compounds, however, only weak and at very low temperatures. For thin films of CeAg$_x$/Ag(111) the general understanding is similar [28, 144]. *Praetorius et al.* report a CeAg$_x$/Ag(111) surface alloy forming a hexagonal $(1.1\sqrt{3}\,\mathrm{x}\,1.1\sqrt{3})R30°$ structure with respect to the Ag(111) substrate with additional satellite reflexes, forming a $(3\sqrt{3}\,\mathrm{x}\,3\sqrt{3})R30°$ reconstruction with respect to the CeAg$_x$ main structure [144] as shown in figure 4.4 c). This thin film is subsequently investigated with XAS and XMCD exhibiting a vanishing f^0-share to the XA spectra. The suszeptibility extracted from XMCD measurements, however, points towards a reduction of the magnetic moment with decreasing temperature. The Kondo temperature necessary for enabling this reduction of the magnetic moment through Kondo screening of the Ce ion is $T_\mathrm{K} \geq 20\,\mathrm{K}$. This, however, is contradictory to the reported XAS data as well as the band

structure measurements performed in [28].

Schwab et al. performed on- and off-resonance ARPES measurements on a $(2\,\mathrm{x}\,2)R30°$ reconstruction of $CeAg_x$/Ag(111) as shown in figure 4.4 d). The ionization peak as well as the spin-orbit partner of the Kondo resonance are clearly visible at $E - E_\mathrm{F}(\mathrm{IP}) = -2.2\,\mathrm{eV}$ and $E - E_\mathrm{F}(\mathrm{SOP}) = -0.27\,\mathrm{eV}$, whereas the Kondo resonance itself is not observed [28]. *Schwab et al.* therefore assign a "vanishing" Kondo temperature to $CeAg_x$/Ag(111) [28].

Section 6 of this work investigates the influence of different surface alloy film thicknesses as well as of Bi addition on the manifestation of electronic correlation in $CeAg_x$/Ag(111) with photoemission spectroscopy. Section 6 therefore first presents the lattice structure of two $CeAg_x$ surface alloys of different layer thicknesses as well as the lattice structure resulting from Bi deposition. Subsequently the electronic structure is investigated by ARPES and XPS.

5

Tunability of the electronic structure in $CePt_5$/Pt(111)

The lattice structure of the surface alloy $CePt_5$/Pt(111) considerably varies with increasing layer thickness. This is shown in subsection 4.1 as well as previous works [27,30,105,122]. The following part focuses on whether these thickness-dependent changes in the lattice structure also affect the electronic structure of $CePt_5$/Pt(111) and in particular the manifestation of strong correlation. Previous XAS and XMCD measurements suggest a dependence of the effective occupancy n_f of the Ce $4f$ level on the film thickness of the surface alloy [30,135]. However, due to the small energy scales of Kondo physics and heavy fermion behaviour, the experimental investigation of these phenomena is highly demanding.

A new setup for epitaxially growing Ce-based thin films was implemented during this work and guarantees reproducability of pristine and highly ordered surface alloys of $CePt_5$/Pt(111) and $CeAg_x$/Ag(111) of various layer thicknesses (see subsection 3.3).

Furthermore, the PES setup was optimized for low temperatures to enable measurements below the Kondo temperature T_K or even the coherence temperature T^* of a system. In case of Ce compounds this typically requires

temperatures below $T < 15\,\mathrm{K}$ during measurement. The experimental setup established during the course of this work, as described in section 3.3, meets all of these requirements.

This section is dedicated to establishing XPS as a powerful method for investigating Kondo physics in Ce-based compounds. In particular n_f and Δ are estimated on the basis of the multiplet structure in Ce $3d$ core level spectra. One expects the local environment of the Ce atom to influence the $c-f$ hybridization Δ and therefore n_f [33]. The local environment of the Ce atom changes in particular at the interface to the Pt(111) substrate, at the sample surface and in dependence of the surface alloy lattice structure and therefore the $CePt_5$ layer thickness. Those three parameters are addressed in subsection 5.2 by angle-dependent and therefore bulk- and surface-sensitive XPS studies of Ce $3d$ core levels of varying layer thicknesses.

Furthermore, n_f is expected to increase when raising the sample temperature T_s from well below T_K to above. This enables to access the system's Kondo temperature by XPS, as the temperature of maximum n_f-change, with $T_\mathrm{K} = \mathrm{T}(\frac{\delta n_f}{\delta T})_\mathrm{max}$. In subsection 5.3 this is used to assign a Kondo temperature to a selection of different layer thicknesses of $CePt_5$ on the basis of Ce $3d$ XPS spectra.

The analysis of a multitude of different Ce $3d$ core level spectra reveals that the low temperature, ground state n_f as well as the Kondo temperature T_K are dependent on the $CePt_5$ surface alloy layer thickness. Additionally it is shown, that surface and bulk of the thin film exhibit different n_f. These findings are subsequently confirmed by modelling the various Ce $3d$ core level spectra in the framework of the Gunnarsson-Schönhammer theory in subsection 5.4 and finally by ARPES measurements of the Kondo resonance in the valence band of $CePt_5$/Pt(111) of selected layer thicknesses in subsection 5.5.

5.1 Bulk and surface electronic structure

The exceptional structure of the Ce 3*d* core levels in $CePt_5$ on Pt(111) provides valuable access to the low energy excitations in the valence states, as discussed in subsections 2.1.2 and 3.1.3. Therefore the following part treats the evaluation of layer thickness- and temperature-dependent Ce 3*d* core level spectra acquired with XPS. All measurements have been recorded using an excitation energy of $h\nu(\mathrm{Al\ K}_\alpha) = 1486.6\,\mathrm{eV}$ with an experimental resolution of approximately $\Delta E = 750\,\mathrm{meV}$.

Figure 5.1 a) shows an overview spectrum of 4 u.c. $CePt_5$/Pt(111) at room temperature (RT) and normal emission (0°). The spectrum is not background corrected.

All peaks in the spectrum can be assigned to the expected core levels of Ce or Pt in the presented energy range [117]. Within the accuracy of the measurement there are no signs for surface contamination with residual gas. Nevertheless, the measurement times for one preparation of $CePt_5$/Pt(111) have been kept below ten hours since Ce compounds tend to oxydize rapidly. The spin-orbit split Ce 3*d* core levels are visible in the energy range between $E_{bin} = 870 - 940\,\mathrm{eV}$. The multiplet structure with f^0, f^1 and f^2 proportions is already distinguishable in the overview spectrum despite the rather coarse energy step of $\Delta E_{\mathrm{step}} = 1\,\mathrm{eV}$. However, to estimate n_f for different layer thicknesses, temperatures and emission angles, more detailed spectra of the respective Ce 3*d* core levels are recorded.

Figure 5.1 b) shows the Ce 3*d* spectra for increasing layer thicknesses in darkening shades of blue and grey both for normal emission (0°, solid lines) and 60° off normal emission (60°, dashed lines). All spectra are recorded with an energy step of $E_{\mathrm{step}} = 100\,\mathrm{meV}$ at a sample temperature of $T_s \approx 9\,\mathrm{K}$. Higher layer thicknesses are artificially shifted to higher intensities for better distinguishability. All spectra are normalized to the number of sweeps and Shirley background corrected as described in subsection 3.4. Furthermore, the spectra recorded at 60° off normal emission have always been recorded immediately after the normal emission data on the same preparation, reduc-

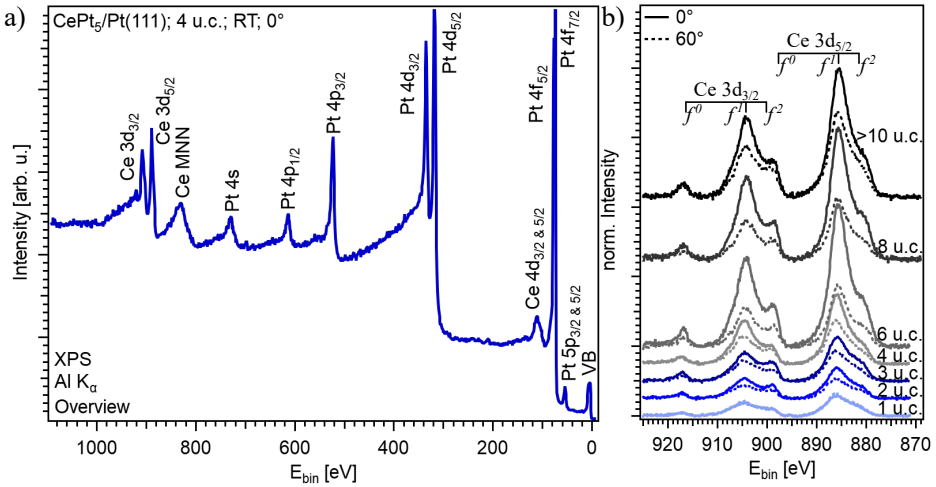

Figure 5.1: XPS overview and Ce 3*d* spectra of CePt$_5$/Pt(111). a) shows an overview spectrum of a CePt$_5$ surface alloy of 4 u.c. layer thickness at room temperature (RT) and normal emission (0°). b) depicts the detailed Ce 3*d* spectra at $T_s = 9$ K of increasing layer thicknesses indicated by darkening shades of blue and grey for normal emission (solid lines) and 60° off normal emission (dashed lines). The final state multiplet is indicated for each spin orbit channel by f^0, f^1 and f^2 respectively. All spectra have been recorded with an excitation energy of $h\nu(\text{Al K}_\alpha) = 1486.6$ eV and a resolution of $\Delta E = 750$ meV.

ing possible errors due to varying sample quality.

First of all, the characteristic final state multiplet structure with f^0, f^1 and f^2 proportions is clearly visible for all recorded layer thicknesses and both emission angles. For most layer thicknesses the total Ce 3*d* intensity at an emission angle of 60° is lower than at normal emission. An exception is observed at a layer thickness of 1 u.c., where the Ce 3*d* spectra for both emission angles have similar intensity. Furthermore, throughout the growing layer thicknesses the total intensity of the Ce 3*d* core levels continuously increases up to a layer thickness of 6 u.c.. For 6 – >10 u.c. the intensity saturates.

The growing total Ce 3*d* intensity, is understood in terms of the XPS information depth. The photoelectrons detected in XPS originate from the

first few Å beneath the sample surface. The intensity of the topmost layer is thereby undamped whereas the intensity of deeper layers gets damped exponentially, depending on their distance to the sample surface (see subsection 3.1.3) [31]. Therefore in the thin layer thickness regime, increasing the $CePt_5$ layer thickness, strongly contributes to the overall Ce $3d$ signal. At larger layer thicknesses, due to the exponential damping, the subjacent layers contribute less and less to the total Ce $3d$ signal, causing its intensity to saturate.
The decrease of intensity between normal emission and 60° is visible throughout all layer thicknesses >2 u.c.. The information depth at an emission angle of 60° is only 50 % of its value at normal emission, leading to an even larger contribution of the surface region to the spectrum. Hence, the reduction of Ce $3d$ intensity at 60° suggests a depletion of Ce at the sample surface. This is in good agreement with the findings in [26, 122] where a Pt termination of the $CePt_5$ surface is reported.
The influence of these structural changes on Δ and n_f between $CePt_5$ surface and bulk as well as throughout the increasing layer thicknesses is investigated in detail in the following part.

5.2 Manifestation of strong correlation in Ce $3d$ core level spectra

In order to determine variations in the relative f^n proportions throughout the increasing layer thicknesses, figure 5.2 shows the Ce $3d$ core level spectra of the previous subsection arranged more suitably. Layer thicknesses of 1 – 3 u.c. are compared in figure 5.2 a), 3 and 4 u.c. in b) and 4 – >10 u.c. in c). The upper part of each figure shows the Ce $3d$ spectra recorded at normal emission (0°), whereas the lower part depicts the spectra recorded at 60° off normal emission (60°). All spectra in figure 5.2 a), b) and c) are normalized to the intensity of the f^1 peak of the Ce $3d_{3/2}$ spin-orbit partner

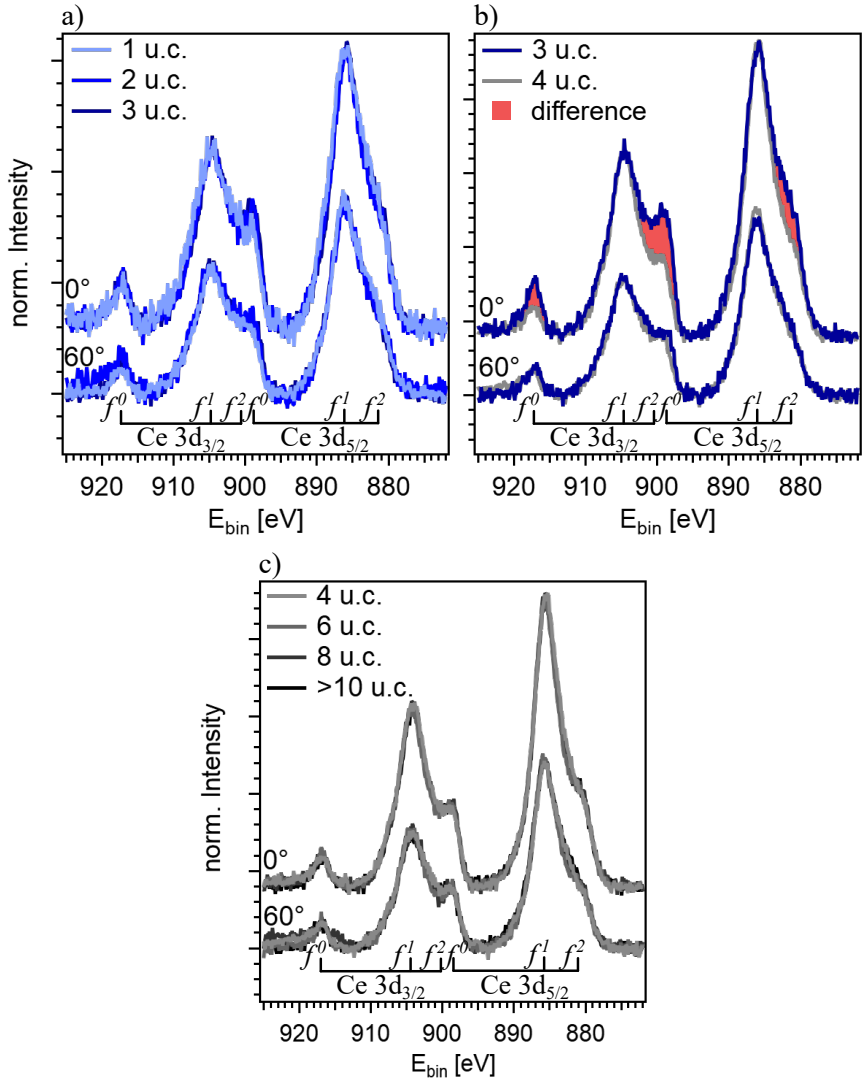

Figure 5.2: Ce 3*d* core level spectra of CePt$_5$/Pt(111) for varying layer thicknesses. a) shows layer thicknesses of 1 – 3 u.c., b) 3 and 4 u.c. and c) 4 – >10 u.c.. The upper spectra are acquired at normal emission (0°), whereas the lower spectra are taken at 60° off normal emission (60°). Increasing layer thicknesses are visualized by darkening shades of blue and grey. The spectra are normalized to the intensity of the Ce $3d_{3/2}$ f^1 peak of the largest layer thickness respectively. The f^0, f^1 and f^2 shares of the Ce 3*d* spin-orbit partners are visible for all layer thicknesses. The f^0 and f^2 proportions vary most between 3 and 4 u.c. layer thickness in b), highlighted by the red area.

of the highest layer thickness shown in the respective figure. This is 3 u.c. in a), 4 u.c. in b) and >10 u.c. in c).
A layer thickness dependent variation of the relative f^0 weight $w_{rel}(f^0)$ and therefore a change of n_f is most recognizable in figure 5.2 b), where layer thicknesses of 3 u.c. (blue line) and 4 u.c. (grey line) are compared. 3 u.c. layer thickness, at normal emission, clearly shows a higher f^0 share in the Ce $3d_{3/2}$ spin-orbit partner at $E_{bin} \approx 917$ eV as compared to the respective feature at 4 u.c.. Furthermore the f^2 shoulder on the low binding energy side of the Ce $3d_{5/2}$ spin-orbit partner at $E_{bin} \approx 880$ eV is increased and slightly shifted to higher binding energies for 3 u.c.. This also affects the f^2/f^0 peak on the low binding energy side of the Ce $3d_{3/2}$ f^1 peak at $E_{bin} \approx 900$ eV, which is again larger for 3 u.c. layer thickness as compared to 4 u.c.. The differences in the spectra are emphasized by red areas in figure 5.2 b).
The magnitude of the f^0, f^1 and f^2 shares change, when going from normal emission to an emission angle of 60°, shown in the bottom part of figure 5.2 b). The f^0 share of the Ce $3d_{3/2}$ spin-orbit partner of both layer thicknesses now has similar weight. The f^2 shoulder at the Ce $3d_{5/2}$ peak, however, is still slightly higher for 3 u.c. layer thickness, leading to a slightly higher f^2/f^0 weight at the low binding energy side of the Ce $3d_{3/2}$ f^1 peak. In summary the spectra in figure 5.2 b) suggests a substantial change of n_f between 3 and 4 u.c. layer thickness at normal emission, that is diminished at 60°.
In figure 5.2 a) thinner $CePt_5$ films of 1 and 2 u.c. are compared to the film thickness of 3 u.c. The normal emission data in the top part show similar f^0, f^1 and f^2 shares for all three layer thicknesses. Only the 1 u.c. phase shows a slight decline in the intensity of the f^2/f^0 structure at the low binding energy side of the Ce $3d_{3/2}$ f^1 peak. In the bottom part of figure 5.2 a) the Ce $3d$ spectra of the thin film thicknesses are shown for 60° off normal emission. Here the f^0 share at $E_{bin} \approx 917$ eV has similar intensity for 2 and 3 u.c. whereas it is slightly reduced for a layer thickness of 1 u.c.. The f^2 share of the Ce $3d_{5/2}$ peak at $E_{bin} \approx 880$ eV, however, is slightly higher for 1 u.c. leading to a comparable intensity of the f^2/f^0 structure at $E_{bin} \approx 900$ eV between 1 u.c. and 2 and 3 u.c.. Therefore, n_f is expected to be similar for 2 and 3 u.c. $CePt_5$/Pt(111) at both emission angles, whereas 1 u.c. layer thickness might

exhibit larger Δ but smaller n_f due to the different weights in the f^2 and f^0 peaks in figure 5.2 a).
Furthermore, the spectra in the low layer thickness regime of 1 – 3 u.c. exhibit a lower signal to noise ratio than the larger layer thicknesses of 4 – >10 u.c. These are shown in figure 5.2 c) in darkening shades of grey for normal emission (0°, top part) and 60° off normal emission (60°, bottom part). For both emission angles, all spectra show similar intensities for each f^0, f^1 and f^2 final state. This suggests similar n_f and Δ for the higher layer thickness regime of $CePt_5$ on Pt(111). Qualitatively, the biggest change in n_f is therefore observed between 3 and 4 u.c. layer thickness.

The manifestation of Kondo physics in the valence band of any material is heavily temperature dependent. Figure 5.3 illustrates whether the temperature dependence of the valence band features is also reflected in the f^n proportions of the Ce 3*d* multiplet. Therefore the Ce 3*d* core level spectra of all investigated layer thicknesses of $CePt_5$/Pt(111) and both emission angles are also recorded at $T_s = 290\,\mathrm{K}$. A comparison of the spectra with $T_s = 9\,\mathrm{K}$ and $T_s = 290\,\mathrm{K}$ is shown in figure 5.3 a) – g). Again the spectra recorded at normal emission are always shown in the top part of each graph, whereas the data for 60° off normal emission are shown in the bottom part. Spectra acquired at $T_s = 290\,\mathrm{K}$ are shown in red, whereas spectra recorded at $T_s = 9\,\mathrm{K}$ are shown in blue.
The thin layer thickness regime of 1 – 3 u.c. in figures 5.3 a) – c) exhibits a lower signal to noise ratio than the larger layer thicknesses of 4 – >10 u.c. in d) – g), as already observed in figure 5.2 a). Furthermore, layer thicknesses of 1 – 3 u.c. show a difference in the f^0 and f^2/f^0 contribution at $E_{bin} \approx 917\,\mathrm{eV}$ and $E_{bin} \approx 900\,\mathrm{eV}$ between $T_s = 9\,\mathrm{K}$ and $T_s = 290\,\mathrm{K}$. For both emission angles the f^0 and f^2/f^0 contributions decrease when raising the temperature from $T_s = 9\,\mathrm{K}$ to $T_s = 290\,\mathrm{K}$.
For larger film thicknesses of 4 – >10 u.c. in figure 5.3 d) – g), the temperature dependent changes in the f^n weights are reduced, but still the data recorded at $T_s = 9\,\mathrm{K}$ show slightly higher f^0 and f^2/f^0 proportions as compared to the spectra recorded at $T_s = 290\,\mathrm{K}$.

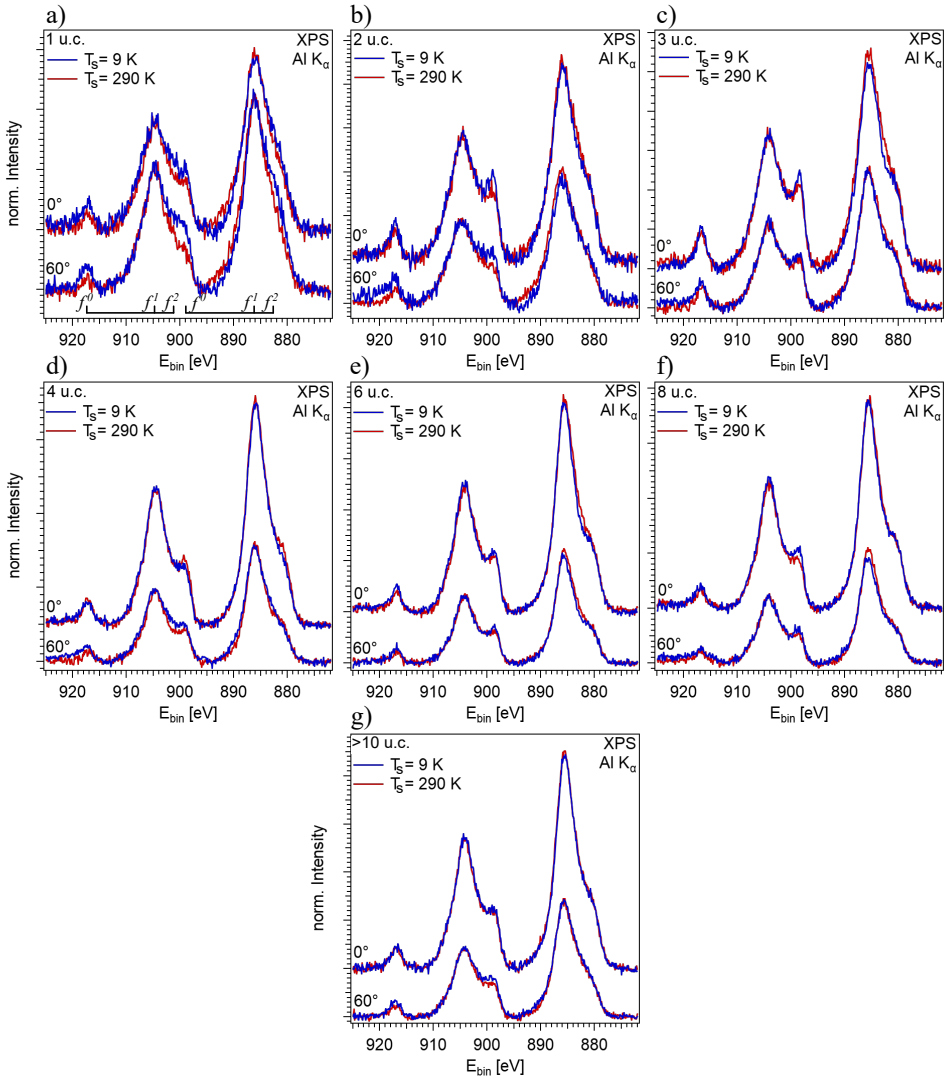

Figure 5.3: Ce 3*d* core level spectra for $T_s = 9\,\mathrm{K}$ and $T_s = 290\,\mathrm{K}$. a) – g) show the Ce 3*d* core levels for layer thicknesses of 1 – >10 u.c. for normal emission (0°, top part) and 60° off normal emission (60°, bottom part) depending on the sample temperature. Spectra for $T_s = 9\,\mathrm{K}$ are depicted in blue, whereas spectra obtained at $T_s = 290\,\mathrm{K}$ are shown in red. All spectra are normalized to the intensity of the respective Ce $3d_{3/2}$ f^1 peak. Measurements were performed with $h\nu$(Al Kα) = 1486.6 eV and $\Delta E = 750\,\mathrm{meV}$.

Despite these small changes, all layer thicknesses show the characteristic f^0, f^1 and f^2 final state multiplet also at $T_s = 290\,\mathrm{K}$. The variations in the f^0 and f^2/f^0 weights suggest an increase of n_f for the thin layer thickness regime of 1 – 3 u.c. when increasing the temperature from $T_s = 9\,\mathrm{K}$ to $T_s = 290\,\mathrm{K}$, whereas for larger layer thicknesses no significant change in n_f is expected. Though qualitatively illustrating the layer thickness, emission angle and temperature dependent changes in the respective f^n weights, this comparative analysis cannot give specific values for Δ and n_f. Therefore the relative weights of the f^2 and f^0 peaks to the spectrum have been estimated for all recorded Ce 3*d* core levels and used according to subsection 3.4 and equations 3.17 and 3.16 to determine Δ and subsequently n_f.

The layer thickness dependent hybridization strength Δ resulting from equation 3.17 is shown in figure 5.4 a). Dots represent normal emission, whereas circles show Δ for 60° off normal emission. Δ estimated for $T_s = 9\,\mathrm{K}$ are shown in blue, the ones obtained for $T_s = 290\,\mathrm{K}$ in red. The errors are estimated by the error margin of the Voigt fit and the accompanying variations in the f^1 and f^2 peak areas. The solid and dashed lines as well as the shaded areas serve as guides to the eye for the respective set of parameters.

For $T_s = 9\,\mathrm{K}$ and normal emission, Δ is more or less constant at a value of $\bar{\Delta}^{0°}_{9\mathrm{K}} = (88.1 \pm 1.8)\,\mathrm{meV}$ over the whole layer thicknesses regime, emphasized by the solid blue line as a guide to the eye. At 60° and $T_s = 9\,\mathrm{K}$ Δ is larger for all layer thicknesses as compared to 0°. Δ estimated at 1 u.c. and 60° is exceptionally large with $\Delta^{60°}_{9\mathrm{K}}(1\,\mathrm{u.c.}) = (145.1 \pm 7.3)\,\mathrm{meV}$, whereas the average for 2 – >10 u.c. is $\bar{\Delta}^{60°}_{9\mathrm{K}}(2 - >10\,\mathrm{u.c.}) = (104.7 \pm 2.1)\,\mathrm{meV}$. The general trend of Δ for $T_s = 9\,\mathrm{K}$ and 60° is emphasized by the dashed blue line.

For $T_s = 290\,\mathrm{K}$, Δ shows a stronger variation with increasing layer thickness but a weaker dependence on the emission angle. For both emission angles Δ increases from $\approx 40\,\mathrm{meV}$ to $\approx 80\,\mathrm{meV}$ for 1 – 3 u.c. and saturates for 4 – >10 u.c. The average values amount to $\bar{\Delta}^{0°}_{290\mathrm{K}}(1 - 3\,\mathrm{u.c.}) = (63.7 \pm 1.3)\,\mathrm{meV}$ and $\bar{\Delta}^{60°}_{290\mathrm{K}}(1 - 3\,\mathrm{u.c.}) = (60.2 \pm 1.2)\,\mathrm{meV}$, whereas 4 – >10 u.c. layer thickness show larger mean Δ with $\bar{\Delta}^{0°}_{290\mathrm{K}}(4 - >10\,\mathrm{u.c.}) = (94.0 \pm 1.9)\,\mathrm{meV}$ and $\bar{\Delta}^{60°}_{290\mathrm{K}}(4 - >10\,\mathrm{u.c.}) = (100.1 \pm 2.0)\,\mathrm{meV}$.

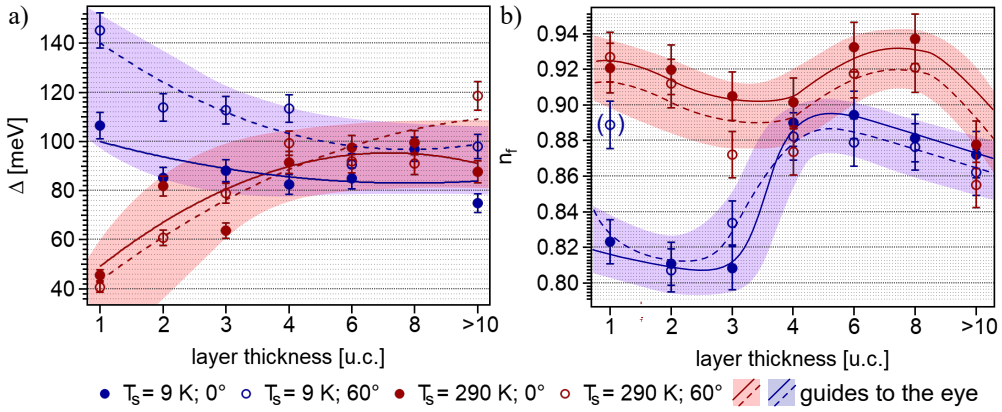

Figure 5.4: $c-f$ hybridization Δ and effective occupancy n_f for $CePt_5$/Pt(111). a) shows the layer thickness and temperature dependent hybridization strength Δ, whereas b) depicts the resulting n_f. Blue and red symbols correspond to $T_s = 9\,\mathrm{K}$ and $T_s = 290\,\mathrm{K}$ respectively. The values estimated for normal emission (0°) are depicted as dots, whereas 60° off normal emission is represented by circles. Solid and dashed blue and red lines as well as the shaded blue and red areas serve as guides to the eye for the respective set of parameters.

Again, solid and dashed red lines in figure 5.4 a) resemble the general evolution of $\Delta_{290\mathrm{K}}$ throughout the increasing layer thicknesses for 0° and 60° respectively. Figure 5.4 a) also shows, that Δ for layer thicknesses > 4 u.c. is similar at $T_s = 9\,\mathrm{K}$ and $T_s = 290\,\mathrm{K}$. This is illustrated especially by the shaded areas, that overlap in this region.

In order to take into account the influence of finite Δ when determining n_f, the mean $\bar{\Delta}$ estimated above are categorized into three groups of low ($\Delta = 60\,\mathrm{meV}$), intermediate ($\Delta = 90\,\mathrm{meV}$) and high ($\Delta = 120\,\mathrm{meV}$) Δ, according to figure 3.5 a). The mean $\bar{\Delta}$ and the corresponding assumed Δ for calculating n_f are summarized in table 5.1 for all temperatures, emission angles and layer thicknesses.

Subsequently n_f is calculated as $n_f = 1 - |c_0|^2$, using the corrected c_0, according to subsection 3.1.3. The resulting layer thickness dependent effective occupancy n_f is shown in figure 5.4 b). Dots and circles represent 0° and 60°, whereas blue and red again stands for $T_s = 9\,\mathrm{K}$ and $T_s = 290\,\mathrm{K}$, respectively.

			$\bar{\Delta}$	Δ acc. fig. 3.5
9 K	0°	1 –>10 u.c.	88.1 ± 1.8	90 meV
9 K	60°	1 u.c.	145.1 ± 2.9	120 meV
9 K	60°	2 –>10 u.c.	104.7 ± 2.1	90 meV
290 K	0°	1 – 3 u.c.	63.7 ± 1.3	60 meV
290 K	0°	4 –>10 u.c.	94.0 ± 1.9	90 meV
290 K	60°	1 – 3 u.c.	60.2 ± 1.2	60 meV
290 K	60°	4 –>10 u.c.	100.2 ± 2.0	90 meV

Table 5.1: Summary of the mean hybridization strengths $\bar{\Delta}$. For all layer thicknesses, temperatures and emission angles the determined values of $\bar{\Delta}$ are divided into groups of low ($\Delta = 60$ meV), intermediate ($\Delta = 90$ meV) and high ($\Delta = 120$ meV) Δ, according to figure 3.5.

Over the whole range n_f determined for $T_s = 9$ K and 0° shows a discernible layer thickness dependence. For 1 – 3 u.c. n_f, on average, assumes rather low values of $\bar{n_f}(1-3\,\text{u.c.}) = (0.814 \pm 0.016)$, whereas it is considerably larger for 4 –>10 u.c. with $\bar{n_f}(4->10\,\text{u.c.}) = (0.884 \pm 0.018)$, leading to a step-like increase of n_f between 3 and 4 u.c. layer thickness.
The n_f determined for $T_s = 9$ K and 60° follow this trend. However, they are slightly higher for 1 – 3 u.c. as compared to 0°, and lower for 4 –> 10 u.c.. Yet, the step-like increase of n_f between 3 and 4 u.c. is also observed at 60° off normal emission. This evolution of n_f with increasing layer thicknesss is emphasised by the solid and dashed blue lines for 0° and 60° emission angles as well as the shaded blue area.
The biggest change in n_f occurs between 3 and 4 u.c. which is in good agreement with the Ce 3d spectra in figure 5.2 b). The change in n_f amounts to $\delta n_f^{34} = 0.0817$, which is an increase of $\approx 10\,\%$ with regard to $n_f(3\,\text{u.c.})$.
At $T_s = 290$ K the step-like increase of n_f between 3 and 4 u.c. vanishes. n_f assumes constant values for both normal emission and 60° off normal emission that are larger compared to $T_s = 9$ K. The average value for layer thicknesses of 1 –>10 u.c. at $T_s = 290$ K and 0° is $\bar{n_f}(290\,\text{K}, 0°) = (0.913 \pm 0.018)$, whereas for 60° it is $\bar{n_f}(290\,\text{K}, 60°) = (0.897 \pm 0.018)$. The general evolution of n_f for

			$\bar{n_f}$	$\bar{v}$
9 K	0°	1 – 3 u.c.	0.814 ± 0.016	3.186 ± 0.064
9 K	0°	4 – >10 u.c.	0.884 ± 0.018	3.116 ± 0.062
9 K	60°	1 u.c.	0.889 ± 0.018	3.111 ± 0.062
9 K	60°	2, 3 u.c.	0.820 ± 0.016	3.180 ± 0.064
9 K	60°	4 – >10 u.c.	0.875 ± 0.018	3.125 ± 0.063
290 K	0°	1 – >10 u.c.	0.913 ± 0.018	3.087 ± 0.062
290 K	60°	1 – >10 u.c.	0.897 ± 0.018	3.103 ± 0.062

Table 5.2: Mean effective occupancy $\bar{n_f}$ and Ce valence $\bar{v}$. All determined n_f of figure 5.4 b) as well as $\bar{v}$, divided into suitable subgroups depending on layer thickness, temperature and emission angle.

$T_s = 290$ K is emphasised by solid and dashed red lines for 0° and 60° respectively in figure 5.4 b) as well as by the shaded red area.

A summary of the mean values of n_f and the resulting mean Ce valence $\bar{v} = 4 - \bar{n_f}$ calculated in suitable ranges depending on temperature, emission angle and layer thickness as described above, is given in table 5.2.
The extensive analysis of n_f throughout the whole parameter range reveals three main aspects that determine its value. First, one observes a sudden increase of n_f between 3 and 4 u.c. layer thickness. Second the n_f determined for an emission angle of 60° are mostly smaller than their respective 0° values for 4 – >10 u.c., but larger for lower layer thicknesses of 1 – 3 u.c.. Third, the thin and thick layer thickness regimes show different temperature dependencies of n_f.
The sudden increase of n_f between 3 and 4 u.c. layer thickness at $T_s = 9$ K for both emission angles is supported by the bare background corrected Ce $3d$ spectra in figure 5.2 as well. There, a clear change in the f^0 and f^2/f^0 weight is observed between 3 and 4 u.c. in b), whereas the spectra for 1 and 2 u.c. in a) show similar f^n weights as the spectrum for 3 u.c. and 6 – >10 u.c. in c) are very similar to 4 u.c..
The difference in n_f between thinner and thicker $CePt_5$ surface alloys has also been reported in [26, 30, 135]. *Tang et al.* report a crossover from a

more "α-like" phase, which is close to the mixed-valent regime with $n_f \approx 0.75$ ($v \approx 3.25$) to a more "γ-like" phase with higher $n_f \approx 0.95$ ($v \approx 3.05$) between low Ce coverages of ≈ 1.5 monolayers and higher coverages of > 2.1 monolayers [26]. The diffraction patterns of the respective thin films in [26] exhibit a $(1.96\,\mathrm{x}\,1.96)R30°$ reconstruction with satellites for thinner and $(1.96\,\mathrm{x}\,1.96)$ for thicker films. This is in agreement with the diffraction patterns of 3 and > 10 u.c. in this work, however, a stoichiometry of $CePt_3$ to $CePt_{2.23}$ for lower to higher initial Ce coverages is given in [26]. *Tang et al.* estimate a Ce valence of $v = 3.12$ for the low and $v = 3.07$ for the high layer thickness regime. However, the determination of v is solely based on the f^0 contribution to the total weight of $[\mathrm{I}(f^0) + \mathrm{I}(f^1) + \mathrm{I}(f^2)]$ [26]. The influence of Δ is not taken into account in [26], leading to an over-/ underestimation of n_f/v [102].
Praetorius et al. build upon this first investigation carrying out XAS and XMCD measurements on various layer thicknesses of $CePt_5$ on Pt(111) [30, 135]. The resulting Ce valences v are shown in figure 4.3 a). They observe a maximum of the Ce valence of $v \approx 3.12$ at $2-3$ u.c. layer thickness followed by a continuous decline for $4-12$ u.c. to $v \approx 3.06$. Also in this work the influence of a finite hybridization Δ is not taken into account.
The enhancement of v in the lower layer thickness regime is attributed to enhanced tensile strain at the interface between the Pt(111) substrate and the $CePt_5$ alloy [30, 122, 135]. This tensile strain reduces the in plane as well as out of plane lattice constants a_1 and a_3 (see figure 4.1 c)) of the $CePt_5$ unit cell. At layer thicknesses > 4 u.c. a relaxation towards the bulk values given in figure 4.1 c) sets in. A reduction of the unit cell volume leads to an enhanced overlap of the Ce $4f$ orbitals with the conduction band, encouraging the delocalization of the f electron, causing smaller n_f. The relaxation of a_1 and a_3 towards the bulk values sets in at 4 u.c., reducing the $c-f$ overlap and consequently increasing n_f [122, 135].
A larger f electron delocalization in connection with a reduction of the unit cell volume is a well known phenomenon in Kondo or heavy fermion materials. Most known is probably the Kondo volume collapse between γ- and α-Ce, where the onset of $c-f$ hybridization at low temperatures leads to a volume collapse of $\approx 15\,\%$ between the strongly hybridized α- and the almost

unhybridized γ-phase of Ce [33,126]. This mechanism is exploited further by inducing γ- to α-like transitions in many Ce-based compounds like $CeAu_2Si_2$, $CeCu_2Ge_2$, $CePd_2Si_2$, $CeRh_2Si_2$ and $CeCu_2Si_2$, where a reduction of the unit cell volume is induced by external pressure [145–148]. In the surface alloy $CePt_5$/Pt(111) this external pressure is exercised by the Pt substrate causing a reduced unit cell size at lower layer thicknesses. This leads to the increased Ce valence v in $CePt_5$ for $1-3$ u.c..

What is striking is that the n_f (v) determined in this work are considerably lower (higher) over the whole layer thickness regime as in [26,30,135]. This is due to the influence of the hybridization Δ, based on the f^2 weight to the spectrum, which is neglected in [26,30,135]. As depicted in figure 3.5 a) a neglect of Δ underestimates the relative f^0 weight up to 50 %. In this work the mean Δ for $T_s = 9$ K and normal emission is estimated to $\Delta = 90$ meV. According to figure 3.5 a) this leads to an error of ≈ 45 % in $w_{rel}(f^0)$. If one includes this Δ-based error in the values for $w_{rel}(f^0)$ determined in [135], these are increased to $w_{rel}(f^0) = 0.203$ for a layer thickness of ≈ 3 u.c. and $w_{rel}(f^0) = 0.102$ for layer thicknesses of $\approx 8-12$ u.c.. According to equation (6) in [135] this leads to $n_f = 0.831$ and $v = 3.169$ for ≈ 3 u.c. and $n_f = 0.907$ and $v = 3.093$ for $8-12$ u.c.. These adjusted values are in good agreement with n_f and v determined in this work for the thin and thick layer thickness regimes after all.

The second trend observed in figure 5.4 b) is that n_f at an emission angle of 60° is lower as compared to normal emission for $4->10$ u.c., but larger for $1-3$ u.c.. The dependency of n_f on the emission angle is also discernible in the bare background corrected Ce $3d$ spectra. Therefore all recorded Ce $3d$ spectra are compared regarding the emission angle in appendix A.2. There, they are normalized to the f^1 line of the Ce $3d_{3/2}$ peak of the respective 0°-spectrum. The resulting graphs are shown in figures A.5 and A.6 for $T_s = 9$ K and $T_s = 290$ K respectively.

As discussed in subsection 3.1.3 measurements performed at an emission angle of 60° have half the probing depth as the respective normal emission measurement. Therefore, they are a lot more sensitive to the electronic structure at the sample surface. The smaller values of n_f at an emission angle of

60° therefore suggest a larger delocalization of the f electron at the sample surface.

In general the sample surface constitutes a different chemical environment for the Ce atoms as compared to the bulk of the $CePt_5$ alloy. This is on the one hand simply due to the crossover from the crystalline film to the vacuum, but on the other hand, and more interestingly in case of $CePt_5$, due to the Pt termination of the sample surface. The Pt termination is established by a Pt Kagome layer with additional Pt atoms in the Kagome holes [122]. This provides the Ce atoms of the topmost layer with an increased number of coordination partners, promoting a larger hybridization between f and conduction band electrons [33]. Therefore the f level is more easily depopulated resulting in lower n_f. At lower layer thicknesses of 1 – 3 u.c., however, n_f is larger at an emission angle of 60°, indicating less f electron delocalization at the surface of the thinner $CePt_5$ films. Especially large is $n_f(1\,\text{u.c.}, 60°) = (0.889 \pm 0.018)$. Considering the diffraction patterns in subsection 4.1.1, the striking difference between thinner and thicker layers of $CePt_5$ is the existence of a moiré-type surface corrugation for 2 and 3 u.c.. Potentially this moiré structure, that is a result of the strain executed by the Pt substrate, prevents a full Pt termination of the surface, an thus reduces the f electron delocalization.

Third, the thin and thick layer thickness regimes of $CePt_5$ show a different evolution of n_f with increasing temperature. At $T_s = 290\,\text{K}$ the step-like change in n_f between 3 and 4 u.c. has completely vanished, leading to constant values over the whole layer thickness regime within the range of the error. In other words, for 1 – 3 u.c. a temperature dependent change in n_f is observed when going from $T_s = 9\,\text{K}$ to $T_s = 290\,\text{K}$, whereas for layer thicknesses > 4 u.c. n_f stays constant over the whole temperature range within the range of the error. This is supported by the background corrected Ce $3d$ spectra in figure 5.3. The spectra for 1 – 3 u.c. in a) – c) show clear differences between $T_s = 9\,\text{K}$ and $T_s = 290\,\text{K}$ with lower f^0 and f^2 contributions at $T_s = 290\,\text{K}$, whereas the spectra for 4 – >10 u.c. show no strong temperature dependence. A temperature dependent change of n_f is expected when increasing the sample temperature from well below the systems Kondo tem-

perature to well above [26, 48]. This suggests a T_K between 9 – 290 K for 1 – 3 u.c., whereas it is in the range of 290 K for > 4 u.c.. Therefore in the following subsection the temperature dependent evolution of n_f is analysed in more detail for layer thicknesses of 2 – 4 u.c..

5.3 Layer thickness dependent Kondo temperature

The effective occupancy n_f of the f level and particularly its change with temperature allows for an estimation of T_K on the basis of core level spectra. In general n_f increases when raising the temperature from (well) below to above T_K, and T_K is determined as the point of maximum $\delta n_f/\delta T$-change [26, 48, 135]. Therefore, the Ce 3d core level spectra have been recorded again for an intermediate temperature of $T_s = 150$ K for 2 – 4 u.c.. The resulting spectra are shown in black in figure 5.5 a) – c) together with the respective spectra at $T_s = 9$ K (blue) and $T_s = 290$ K (red). The upper spectra are recorded at normal emission (0°), whereas the lower spectra correspond to 60° off normal.

At a layer thickness of 2 u.c. in a) the spectrum taken at $T_s = 150$ K and normal emission shows similar f^0 and f^2/f^0 weights at $E_{bin} = 917$ eV and $E_{bin} = 900$ eV as the data taken at $T_s = 9$ K. At 60°, however, the f^0 and f^2/f^0 shares in the spectrum are smaller for $T_s = 150$ K as compared to $T_s = 9$ K but still larger than the ones observed for $T_s = 290$ K. For 3 u.c. and 0° in b) the f^0 and f^2/f^0 weights decrease continuously between $T_s = 9$ K – 290 K. At 60° the f^0 share shows no difference between the three temperatures, whereas the f^2/f^0 peak is significantly diminished. This is most likely dominated by the decrease of the f^2 share as visible at $E_{bin} = 880$ eV. At 4 u.c. layer thickness in c) the spectra recorded at $T_s = 150$ K show less f^0 and f^2/f^0 weight than the respective spectra at $T_s = 9$ K at both emission angles but seemingly also less than the spectra recorded at $T_s = 290$ K. This is rather contraintuitive at first and will be discussed later.

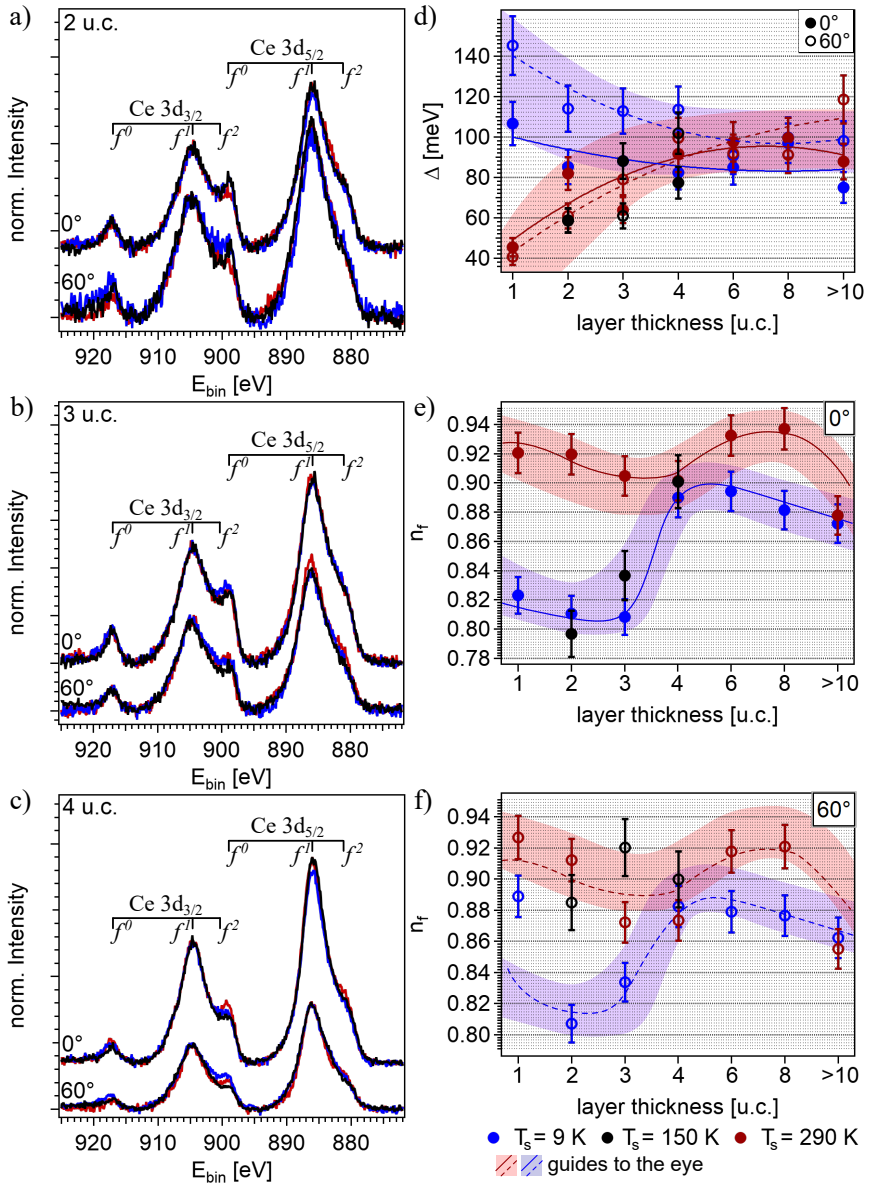

Figure 5.5: Estimation of T_K on the basis of $\delta n_f/\delta T$. a)–c) show the respective spectra at $T_s = 9\,\mathrm{K}$ (blue), $T_s = 150\,\mathrm{K}$ (black) and $T_s = 290\,\mathrm{K}$ (red) for normal emission (0°, top) and 60° off normal emission (60°, bottom) for 2, 3 and 4 u.c. $CePt_5$/Pt(111). d) shows the hybridization Δ for all temperatures and emission angles, whereas e) and f) show the resulting n_f for 0° and 60°. The shaded red and blue areas as well as the solid and dashed, red and blue lines in d–f) emphasize the trend of Δ and n_f for $T_s = 290\,\mathrm{K}$ and $T_s = 9\,\mathrm{K}$ and 0° and 60° respectively.

Figure 5.5 d) – f) show, in black, the resulting Δ and n_f for $T_s = 150\,\mathrm{K}$ calculated according to section 3.4, compared with the respective values for $T_s = 9\,\mathrm{K}$ in blue and $T_s = 290\,\mathrm{K}$ in red. The hybridization for $T_s = 150\,\mathrm{K}$ follows the course of $\Delta_{290\,\mathrm{K}}$ in the relevant layer thickness regime. This is emphasized by the overlap of the black data points with the shaded red area, which illustrates the general trend of Δ for $T_s = 290\,\mathrm{K}$ according to figure 5.4 a).
Particularly interesting are the results obtained for n_f at 0° and 60° emission angle, shown in e) and f). For 2 and 3 u.c. $n_f(150\,\mathrm{K})$ is on the order of $n_f(9\,\mathrm{K})$ as emphasized by its overlap with the shaded blue area, whereas $n_f(290\,\mathrm{K})$ is considerably larger as is shown in red. At a layer thickness of 4 u.c. however, the n_f estimated for all three temperatures overlap within the range of the error, showing no clear temperature dependence. Figure 5.5 f) shows the n_f estimated for 60°. Whereas n_f for 4 u.c. again overlaps for all three temperatures within the range of the error, at 2 and 3 u.c. $n_f(150\,\mathrm{K})$ is in the range of $n_f(290\,\mathrm{K})$ and therefore significantly larger than $n_f(9\,\mathrm{K})$.

The increase of n_f between $T_s = 150 - 290\,\mathrm{K}$ for 2 and 3 u.c. layer thickness and normal emission indicates, that $T_\mathrm{K}^{0°}(2, 3\,\mathrm{u.c.})$ is on the order of $150\,\mathrm{K} < T_\mathrm{K}^{0°}(2, 3\,\mathrm{u.c.}) < 290\,\mathrm{K}$. At 60°, the data suggest $T_\mathrm{K}^{60°}(2, 3\,\mathrm{u.c.}) < 150\,\mathrm{K}$, since the major change in n_f already happens between $T_s = 9\,\mathrm{K}$ and $T_s = 150\,\mathrm{K}$. For a layer thickness of 4 u.c. and both emission angles an estimation of $T_\mathrm{K}(4\,\mathrm{u.c.})$ on the basis of the Ce $3d$ spectra is difficult, since the changes in n_f for the three recorded temperatures are small. This could be caused either by $T_\mathrm{K}(4\,\mathrm{u.c.}) < 9\,\mathrm{K}$ or $T_\mathrm{K}(4\,\mathrm{u.c.}) > 290\,\mathrm{K}$, setting the estimated n_f in the saturation regime above or below T_K. $T_\mathrm{K}(4\,\mathrm{u.c.}) < 9\,\mathrm{K}$ can be discarded in light of the valence band photoemission spectra shown in subsection 5.5, where a Kondo resonance is clearly visible up to $T_s = 64\,\mathrm{K}$. Therefore, $T_\mathrm{K}(4\,\mathrm{u.c.})$ is more likely to be in the range of 290 K, however a more detailed investigation of the temperature dependent n_f at additional T_s is necessary to conclusively settle this question.
Of course the estimation of $150\,\mathrm{K} < T_\mathrm{K}^{0°}(2, 3\,\mathrm{u.c.}) < 290\,\mathrm{K}$ is rather coarse. However, *Praetorius et al.* determine T_K for a layer thickness of 1 u.c.

as $T_K(1\,\text{u.c.}) = 125\,\text{K}$ and for 4 u.c. as $T_K(4\,\text{u.c.}) = 200\,\text{K}$, supporting the impression of the presented analysis, that T_K is smaller in the thin layer thickness regime as compared to layer thicknesses >4 u.c. [135]. Whether $T_K(4\,\text{u.c.}) = 200\,\text{K}$ can neither be supported nor denied on the basis of the available data in this work, as discussed above. However, a T_K in the range of 200 K is also supported by other works, where a Kondo resonance as well as its spin-orbit partner are observed up to $T_s = 120\,\text{K}$. [149].
The low weight of the f^2/f^0 peak at $E_{bin} = 900\,\text{eV}$ for 4 u.c. and $T_s = 150\,\text{K}$ can be attributed to the low weight of the f^2 shoulder at $E_{bin} = 880\,\text{eV}$, as is also reflected in the small Δ as shown in figure 5.5 d). The f^0 weigth itself at $E_{bin} = 917\,\text{eV}$ is comparable between all three temperatures.

The previous parts of section 5 explain in great detail how a careful analysis of Ce 3*d* core level spectra allows for an estimation of the effective occupancy n_f of the f level as well as the hybridization strength Δ. While some of the reported results, like for example the step-like increase of n_f between 3 and 4 u.c. are very much visible already in the raw experimental data, some other changes only become apparent by the quantitative analysis of the final state weights, like for example the differences between surface and bulk n_f in the 60° and 0° spectra. However, all of the presented analysis so far, relies exclusively on the experimental spectra and can be performed without any further knowledge of the system under investigation. In the following subsection a different approach is taken to extract n_f and Δ from the Ce 3*d* core level spectra. That is simulating the spectra in the framework of the Gunnarsson-Schönhammer model as described in subsection 3.1.4 [49].

5.4 Gunnarsson-Schönhammer model fits to Ce 3*d* core level spectra

On the basis of the Gunnarsson-Schönhammer (GS) formalism for core level spectroscopy it is possible to evaluate Δ and n_f by reproducing the measured Ce 3*d* core level spectra with model fits. The main assumptions

and input parameters of the GS-model have been introduced in subsection 3.1.4. The following part describes how the order of magnitude of these input parameters is first determined on the basis of the measured spectra, whereas the subsequent parts show the GS-model fits to all Ce $3d$ core level spectra, depending on layer thickness, emission angle and temperature.

5.4.1 Gunnarsson-Schönhammer model – input parameters

Before analysing the layer thickness dependent changes in the Ce $3d$ core level spectra in subsection 5.4.2, the general order of magnitude for each input parameter to the GS-model has to be identified.
The creation of a core hole by XPS leads to an amplification of the energetic separation of the different f^n final states, as discussed in subsection 3.1.3. If the energy of the f^0 contribution is set to zero the splitting between f^0 and f^1 (δ_{f^0/f^1}) and f^0 and f^2 (δ_{f^0/f^2}) is given by

$$\delta_{f^0/f^1} = \epsilon_f - U_{fc} \tag{5.1}$$

$$\delta_{f^0/f^2} = 2(\epsilon_f - U_{fc}) + U_{ff} \tag{5.2}$$

Therefore, at a given ϵ_f, the energy differences between the f^0 and f^1 lines as well as the f^0 and f^2 lines determine U_{fc} and U_{ff}.
The binding energy ϵ_f of the f level is estimated on the basis of the ionization peak in the valence band spectrum. Figure 5.6 shows the band structure of a $CePt_5$ surface alloy of 4 u.c. layer thickness along the $\overline{\Gamma M}$-direction. The ionisation peak is characterized by a broad structure without dispersion, that is usually situated between $-1\,\mathrm{eV} > E - E_F > -2$ eV [33, 54]. The ARPES data in figure 5.6 a) exhibit a complex highly dispersive bandstructure. At $E - E_F = -1\,\mathrm{eV}$ however, the intensity of the dispersive bands suddenly drops and is followed by a broad structure of increased intensity between $-1.1\,\mathrm{eV} > E - E_F > -1.5\,\mathrm{eV}$, highlighted by the brackets in figure 5.6. This

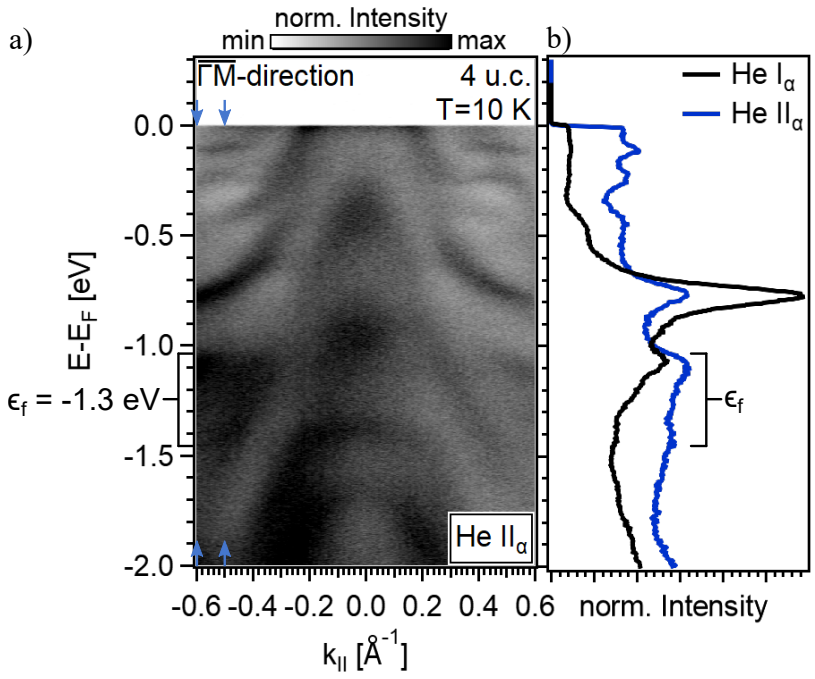

Figure 5.6: Determination of ϵ_f on the basis of the $CePt_5$ bandstructure recorded with He II$_\alpha$. The bandstructure recorded with He II$_\alpha$ exhibits an increased intensity between $-1.1\,\mathrm{eV} > E - E_\mathrm{F} > -1.5\,\mathrm{eV}$ (highlighted by the brackets) that is less pronounced with He I$_\alpha$. This is supported by the EDCs on the right, integrated between $-0.6\ \text{Å}^{-1} \leq \boldsymbol{k}_{||} \leq -0.5\ \text{Å}^{-1}$ for He II$_\alpha$ in blue and He I$_\alpha$ in black. ϵ_f is set to this intensity at $\epsilon_f = -1.3$ eV.

structure is emphasized in spectra recorded with an excitation energy of He II_α in contrast to He I_α, as shown in the EDCs next to the bandstructure in figure 5.6 b). The EDCs are integrated between $-0.6\,\text{Å}^{-1} \leq \boldsymbol{k}_{||} \leq -0.5\,\text{Å}^{-1}$ as indicated by the blue arrows in the bandstructure in a). The black line corresponds to an EDC determined by means of a similar spectrum recorded with He I_α (see also figure 5.13 a) and b)), whereas the blue line corresponds to the EDC extracted from figure 5.6 a). In the energy range between $-1.1\,\text{eV} > E - E_F > -1.5\,\text{eV}$ the He II_α – EDC shows an enhanced intensity as compared to the He I_α – EDC. Structures with high f character are emphasized by excitation with He II_α due to the enhanced cross section of the f orbital [150]. Therefore it is likely that this structure corresponds to the ionization peak described in subsection 2.1.2. Since it is not possible to clearly identify a maximum of this intensity a mean value of $E - E_F = -1.3\,\text{eV} = \epsilon_f$ is chosen for the GS-model fits.

With a fixed ϵ_f equation 5.1 is used for determining U_{fc}. δ_{f^0/f^1} is mainly driven by U_{fc} which is shown in figure 5.7 a), where several Ce $3d$ core level spectra calculated using the GS-formalism are shown. At a given $\epsilon_f = -1.3\,\text{eV}$, $U_{ff} = 5\,\text{eV}$ and $V = 245\,\text{meV}$, U_{fc} is varied from 10 – 15 eV, indicated by darkening shades of blue. Note that figure 5.7 shows only one spin-orbit channel of the Ce $3d$ core levels. One clearly observes an increase of δ_{f^0/f^1} with increasing U_{fc}. No other parameter that is varied in figure 5.7, which is U_{ff} in b), ϵ_f in c) and V in d), changes the energy difference between the f^0 and f^1 peak to that extend. Therefore at a given ϵ_f, δ_{f^0/f^1} is a measure for U_{fc}.

In figure 5.7 b) U_{ff} is varied from 1 eV – 9 eV while the other parameters are kept constant at $\epsilon_f = -1.3\,\text{eV}$, $U_{fc} = 12\,\text{eV}$ and $V = 245\,\text{meV}$. With increasing U_{ff}, indicated by darkening shades of red, the f^2 peak looses intensity and shifts towards the f^1 and f^0 peak. If U_{fc} is already reasonably well estimated according to figure 5.7 a), δ_{f^0/f^2} determines U_{ff}.

Figure 5.7 c) and d) illustrate the influence of ϵ_f and V. Both parameters have only minor influence on the energetic positions of the respective f^n contributions. However, they strongly influence the respective f^0 weight. The smaller $|\epsilon_f|$ or the larger V, the bigger is the f^0 contribution to the spectrum.

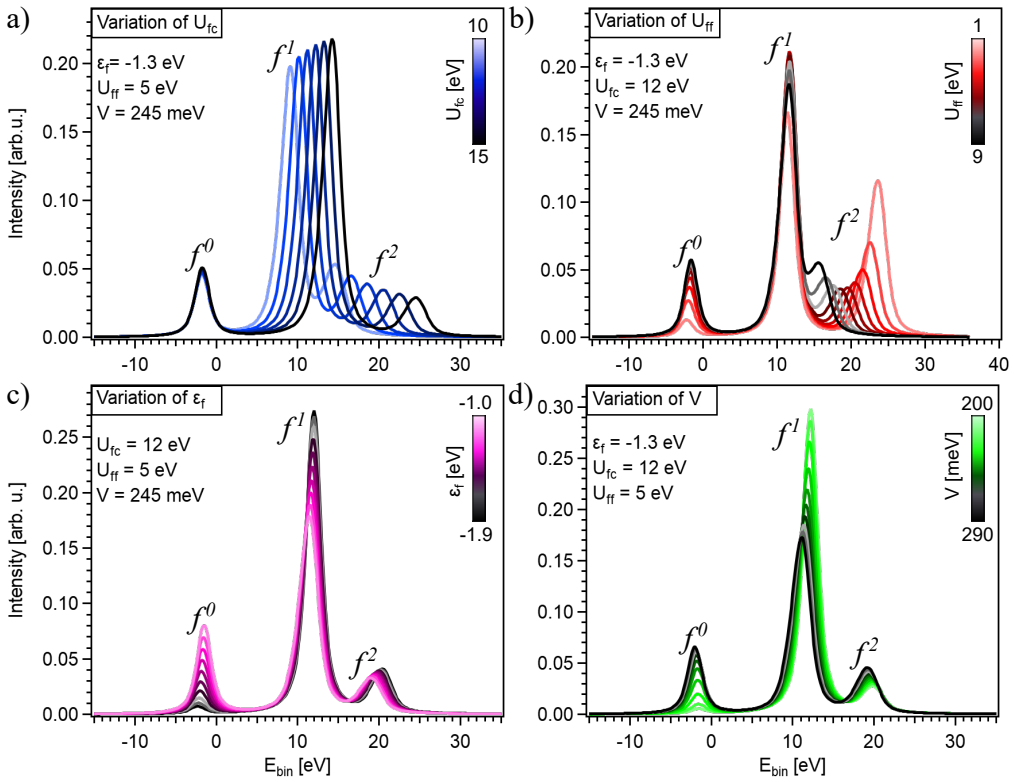

Figure 5.7: Influence of selected Gunnarsson-Schönhammer input parameters. a), b), c) and d) illustrate the influence of U_{fc}, U_{ff}, ϵ_f and V on the line shape of one spin-orbit channel of the Ce 3d core level. If not varied, as indicated in the respective figure, the default settings are $U_{fc} = 12\,\text{eV}$, $U_{ff} = 5\,\text{eV}$, $\text{E}(\epsilon_f) = \text{-}1.3\,\text{eV}$ and $V = 245\,\text{meV}$.

Therefore, a variation in the f^0 weight can in principle be modelled both by adjusting ϵ_f and V. However, a variation of ϵ_f is not resolvable in the measured valence band spectra as described in relation to figure 5.6. Therefore only V will be varied in the following sections to account for changes in $w_{rel}(f^0)$. Figure 5.8 shows a Ce 3d core level spectrum of a layer thickness of 3 u.c. $CePt_5$ on Pt(111). The spin-orbit splitting between Ce $3d_{3/2}$ and Ce $3d_{5/2}$ is determined by the energy difference between the respective f^1 shares as $\Delta_{SO} = 18.7\,\text{eV}$. The energetic positions of the Ce $3d_{3/2}$ f^0 peak as well as the Ce $3d_{5/2}$ f^1 and f^2 peaks are determined by Voigt fits as indicated in figure 5.8 in red and blue. Accordingly, the splittings δ_{f^0/f^1} and δ_{f^0/f^2} are

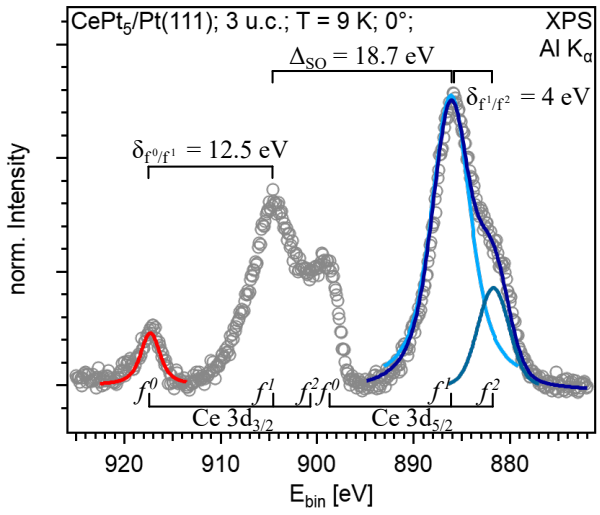

Figure 5.8: Exemplary estimation of Δ_{SO}, U_{fc} and U_{ff}. On the basis of δ_{f^0/f^1} and δ_{f^0/f^2}, U_{fc} and U_{ff} are determined for a Ce $3d$ spectrum of 3 u.c. $CePt_5$ on Pt(111). The spin-orbit coupling is given as the distance between the two f^1 components of the Ce $3d_{3/2}$ and Ce $3d_{5/2}$ peaks to $\Delta_{SO} = 18.7\,eV$. The exact positions of the f^0, f^1 and f^2 shares are determined by red and blue Voigt fits respectively.

estimated as

$$\delta_{f^0/f^1} = 12.5\,\text{eV}$$
$$\delta_{f^0/f^2} = 12.5\,\text{eV} + 4\,\text{eV} = 16.5\,\text{eV}.$$

Using equation 5.1 and 5.2, with $\epsilon_f = -1.3\,\text{eV}$ one obtains

$$U_{fc} = 11.2\,\text{eV}$$
$$U_{ff} = 8.5\,\text{eV}.$$

These values are a first estimation of U_{fc} and U_{ff} and are refined to obtain the best fits to the Ce 3d spectra in subsection 5.4.2. The final values of $U_{fc}^{\text{final}} = 12\,\text{eV}$ and $U_{ff}^{\text{final}}(1-3\,\text{u.c.}) = 9.5\,\text{eV}$ and $U_{ff}^{\text{final}}(4-10\,\text{u.c.}) = 8.5\,\text{eV}$ as determined in subsection 5.4.2, however, are reasonably close to these starting values. Therefore, this method of estimating U_{fc} and U_{ff} is a valid starting point if attempting a GS-model without other previous knowledge.

5.4.2 Gunnarsson-Schönhammer model – fits

Figure 5.9 shows the Ce 3d core levels for all investigated layer thicknesses at normal emission and $T_s = 9\,\text{K}$ (grey data points) as well as the respective fits based on the GS-model (solid blue lines). In order to account for the changes in the spectra observed for increasing layer thicknesses, two input parameters of the GS-model are modified. These are the $f-f$ Coulomb repulsion U_{ff} and the hybridization matrix element V. The other parameters entering the GS-model are kept constant. These are $\epsilon_f = -1.3\,\text{eV}$, $U_{fc} = 12$ eV, $B^+/B^- = 3\,\text{eV}$, $\Delta_{SO} = 18.7\,\text{eV}$ and $N_f = 14$. A Lorentzian and Gaussian width (Lw and Gw) of $Lw = Gw = 1\,\text{eV}$ is assumed to account for the broadening of the spectra. The values for Lw and Gw have been chosen following literature [49, 151] as well as by matching the width of the respective f^1 peaks of both Ce 3d spin-orbit partners. There is no inelastic backgound added to the GS-models since the experimental data is already background corrected. In general the input parameters of the GS-model are

varied as little as possible throughout the whole layer thicknesses regime, to conclusively identify the decisive factors that describe the spectral changes throughout the increasing layer thicknesses.

First of all figure 5.9 shows, that it is possible to determine an appropriate GS-model fit for each layer thickness. For 1 – 3 u.c. in figure 5.9 a) – c) the best fit was obtained for $U_{ff} = 9.5\,\text{eV}$ and $V = 245\,\text{meV}$ except for a layer thickness of 1 u.c. shown in a). Here the Ce $3d_{3/2}$ f^0 peak is slightly lower than the GS-model fit with $V = 245\,\text{meV}$ shown in blue. This is supported by the f^2/f^0 peak at $E_{bin} = 900\,\text{eV}$. Therefore the GS-model fit is adapted by reducing V to $V = 235\,\text{meV}$ as indicated by the red GS-model fit.

In agreement with the measurements shown in subsection 5.2, these parameters change at a layer thickness of 4 u.c. In the larger $CePt_5$ layer thickness regime U_{ff} as well as V are lower with $U_{ff} = 8.5\,\text{eV}$ and $V = 225\,\text{meV}$, except at a layer thickness of 6 u.c. shown in figure 5.9 e). The GS-model fit using $V = 225\,\text{meV}$ underestimates the Ce $3d_{3/2}$ f^0 weight at $E_{bin} = 917\,\text{eV}$. A better fit was obtained for $V = 230\,\text{meV}$ as shown in red.

Figure 5.10 shows the Ce $3d$ spectra for the different layer thicknesses acquired at 60° off normal emission and $T_s = 9\,\text{K}$ as well as the GS-model fits in blue and red. For layer thicknesses of 1 and 2 u.c. the GS-model fits of the respective normal emission data are in good agreement with the 60° data and are therefore not changed as depicted in figure 5.10 a) and b). For 3 and 4 u.c., however, the experimental data deviate from their respective 0°-GS-model fits in blue. At 3 u.c., shown in figure 5.10 c), the f^0 weight is overestimated by the 0°-GS-model fit. This becomes apparent in the f^0 weight at $E_{bin} = 917\,\text{eV}$ and the f^2/f^0 weight at $E_{bin} = 900\,\text{eV}$. Therefore V is reduced to $V = 240\,\text{meV}$ to fit the 60° data. The opposite is true at 4 u.c. layer thickness in d). The experimental data exhibit a larger f^0 contribution at $E_{bin} = 917$ eV and $E_{bin} = 900\,\text{eV}$ as the 0° GS-model fit in blue accounts for. Therefore in the red GS-model fit, shown in figure 5.10 d), V is increased to $V = 235\,\text{meV}$.

For 6 – >10 u.c. the hybridization matrix element $V = 235\,\text{meV}$ is suitable as well for reproducing the f^0 components of the spectra. Therefore V is consequently larger at 60° as compared to 0°. This is indicated by the red

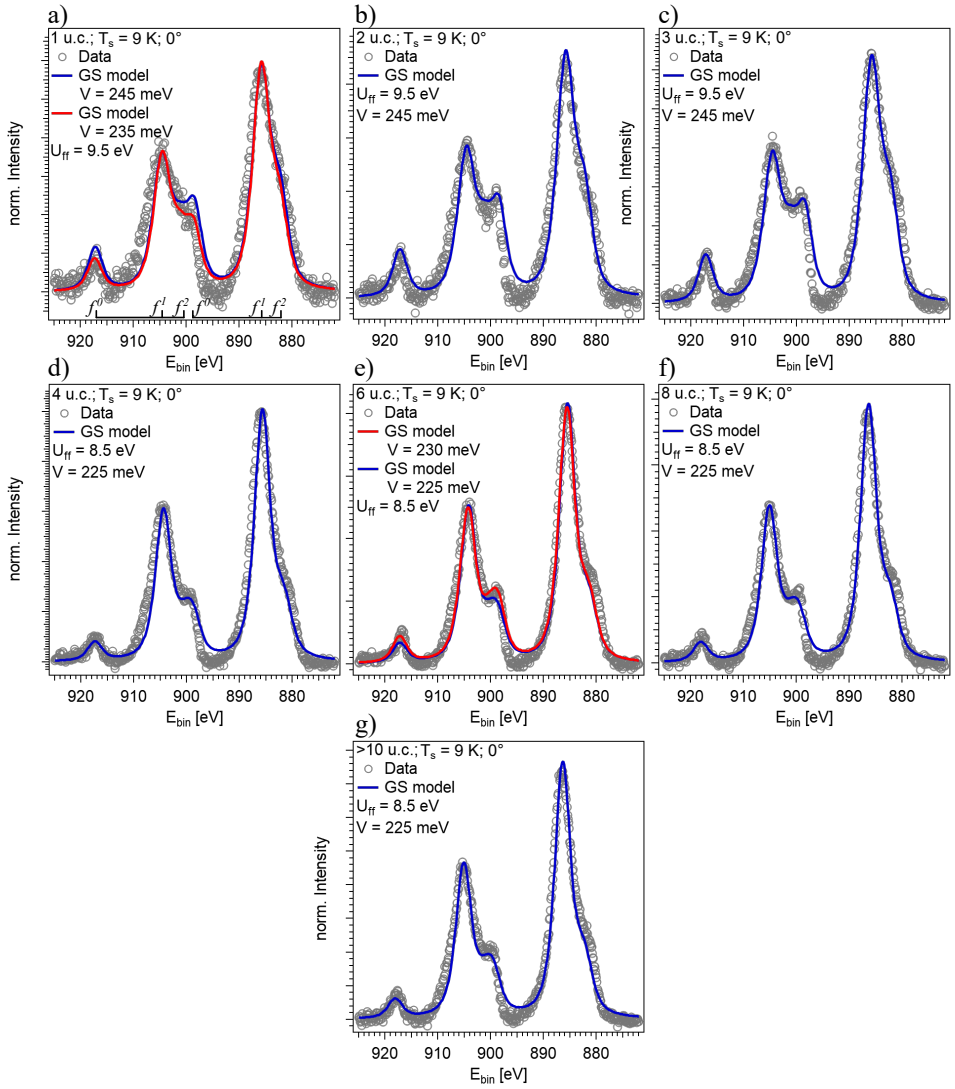

Figure 5.9: GS-model fits to the Ce 3*d* spectra at $T_s = 9\,\mathrm{K}$ and normal emission. a) – g) show the Ce 3*d* core level spectra for increasing layer thicknesses at normal emission (grey data points) and the respective best GS-model fits (blue and red lines). U_{ff} and V are varied to account for the changes in the experimental spectra. The other input parameters are kept constant at $\epsilon_f = -1.3\,\mathrm{eV}$, $U_{fc} = 12\,\mathrm{eV}$, $B^-/B^+ = 3\,\mathrm{eV}$, $\Delta_{SO} = 18.7\,\mathrm{eV}$ and $N_f = 14$. The GS-model fits are broadened by $Lw = Gw = 1\,\mathrm{eV}$.

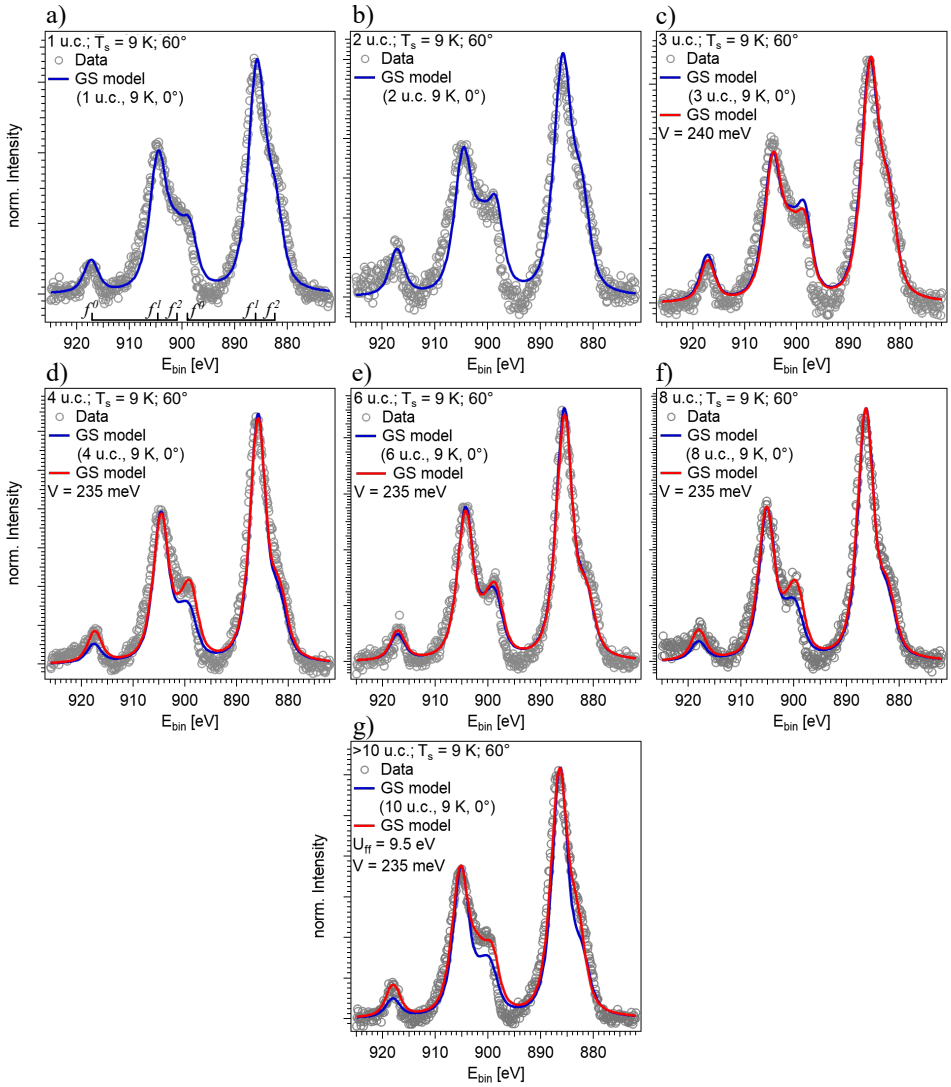

Figure 5.10: GS-model fits to the Ce 3*d* spectra at $T_s = 9$ K and 60° off normal emission. a) – g) show the Ce 3*d* core levels for increasing layer thicknesses at 60° off normal emission (grey data points) and the respective GS-model fits (blue and red lines). Blue GS-model fits represent the respective fits at normal emission, whereas red GS-model fits indicate a change of U_{ff} or Δ between 0° and 60°. The other parameters are not varied: $\epsilon_f = -1.3$ eV, $U_{fc} = 12$ eV, $B^-/B^+ = 3$ eV, $\Delta_{SO} = 18.7$ eV and $N_f = 14$. The GS-model fits are broadened by $Lw = Gw = 1$ eV.

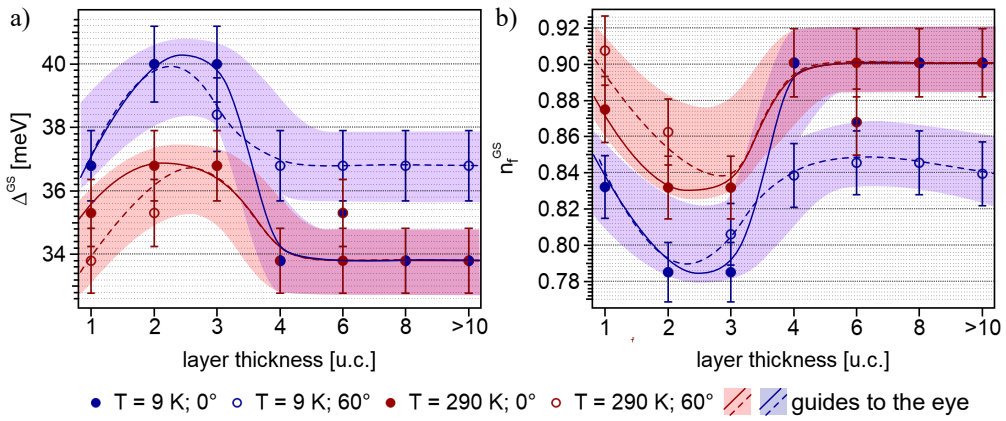

Figure 5.11: Hybridization Δ^{GS} and n_f^{GS} based on the GS-model fits. a) shows Δ^{GS} determined from the hybridization matrix element V according to equation 3.19, whereas b) shows n_f^{GS} estimated according to equation 3.18. Dots represent values for normal emission, circles for 60° off normal emission. Blue and red correspond to T = 9 K and T = 290 K respectively. Blue and red, solid and dashed lines as well as blue and red shaded areas serve as guides to the eye for the general trend of values estimated at T = 9 K and T = 290 K and 0° and 60° respectively.

lines in figure 5.10 e) – g). At >10 u.c. however, also the Coulomb repulsion U_{ff} is increased again to $U_{ff}(>10\,\text{u.c.}) = 9.5\,\text{eV}$ to obtain a suitable fit to the f^2 proportions in the spectrum. The larger V for the 60° data for layer thicknesses of 4 – >10 u.c. is in good agreement with the trends observed for n_f in figure 5.4 b).

The Ce 3d core levels of the different layer thicknesses recorded at $T_s = 290\,\text{K}$ are equally modeled with the GS-formalism, although the GS-model is in fact only developed for T = 0 K [49]. However, the analysis presented in the previous subsections shows that n_f is still considerably lower than one for all layer thicknesses at $T_s = 290\,\text{K}$. The respective spectra are shown and briefly discussed in appendix A.3 in figures A.7 and A.8 for normal emission and 60° off normal emission respectively.

For better comparability with the values for Δ and n_f, estimated on the basis of $w_{rel}(f^2)$ and $w_{rel}(f^0)$ in subsection 5.2, those quantities are determined again on the basis of the GS-model fits. The hybridization matrix element V of the GS-model is converted into Δ according to equation 3.19. The resulting Δ^{GS} for all layer thicknesses, emission angles and temperatures are shown in figure 5.11 a). Blue markers represent the results for $T_s = 9\,\mathrm{K}$, whereas red markers show Δ^{GS} for $T_s = 290\,\mathrm{K}$. Dots correspond to normal emission, whereas circles stand for 60° off normal emission. The error bars are estimated on the basis of a variation of V that still leads to a GS-model fit that is in good agreement with the experimental data. Hence ΔV is estimated to $\Delta V = \pm 4\,\mathrm{meV}$ resulting in an error margin for Δ^{GS} of $\pm 3\,\%$.
The determined values range from $33.8\,\mathrm{meV} \leq \Delta^{\mathrm{GS}} \leq 40\,\mathrm{meV}$. The overall trend for Δ^{GS} for both temperatures and emission angles is the same. Δ^{GS} starts out at an intermediate value at 1 u.c., increases towards 2 – 3 u.c., drops down at 4 u.c. and saturates for 4 – >10 u.c. at a constant value at or below the one obtained for 1 u.c. layer thickness. This general trend is emphasized by the blue and red solid and dashed lines as well as the blue and red shaded areas. Hereby dashed lines correspond to 60° off normal emission, whereas solid lines follow the values of normal emission. Moreover in the thin layer thickness regime of 1 – 3 u.c. the estimated Δ^{GS} are larger for $T_s = 9\,\mathrm{K}$ than $T_s = 290\,\mathrm{K}$. For layer thicknesses of 4 – >10 u.c. the Δ^{GS} for $T_s = 9\,\mathrm{K}$ and 0° as well as for both emission angles at $T_s = 290\,\mathrm{K}$ saturate at a constant value of $\Delta^{\mathrm{GS}} = 33.8\,\mathrm{meV}$. The estimated Δ^{GS} at $T_s = 9\,\mathrm{K}$ and 60° saturate as well, but at a higher value of $\Delta^{\mathrm{GS}} = 35.3\,\mathrm{meV}$. This is highlighted by the dashed blue line and another branch of the shaded blue area. For a layer thickness of 6 u.c. a slightly larger Δ^{GS} than 33.8 meV had to be chosen to correctly model the data acquired at $T_s = 9\,\mathrm{K}$ and 0° as well as $T_s = 290\,\mathrm{K}$ and 60°.
On the basis of the input parameters as defined in subsection 3.1.4 the GS-formalism allows for an estimation of the relative occupation (occ) of each f^n contribution. According to equation 3.18 this relates to the total occupation n_f^{GS} of the f level as $n_f^{\mathrm{GS}} = \mathrm{occ}^1 + 2\mathrm{occ}^2$. The layer thickness dependent results for n_f^{GS} are shown in figure 5.11 b) for both temperatures and emission angels. Blue and red again stand for $T_s = 9\,\mathrm{K}$ and $T_s = 290\,\mathrm{K}$, whereas dots

mark normal emission and circles 60° off normal emission. The course of n_f^{GS} precisely reflects the course of Δ^{GS} as described in relation to figure 5.11 a), however inverted, since larger Δ^{GS} result in smaller n_f^{GS}. The step-like increase of n_f^{GS} between 3 and 4 u.c. layer thickness amounts to a change of $\Delta(n_f^{GS}(34\,\text{u.c.})) = 0.1157$ which corresponds to a 14.7 % increase with respect to $n_f^{GS}(3\,\text{u.c.})$.
A difference between the course of Δ^{GS} and n_f^{GS} is observed at $T_s = 9\,\text{K}$ and 60° for the larger layer thickness regime of 4 – >10 u.c.. Though n_f^{GS} also saturates for the larger layer thicknesses, it is not completely constant as is Δ^{GS} in figure 5.11 a).

The similarity between the courses of Δ^{GS} and n_f^{GS} is striking at first, when compared to Δ and n_f estimated purely on the basis of the relative f^2 and f^0 weights in subsection 5.2. There, no obvious connection between the two courses is observed. For that reason a closer look is taken at U_{ff} and V, the parameters that predominantly influence the f^2 and f^0 weights in the GS-model fits.
Figure 5.12 a) – c) clarifies the interplay between U_{ff} and V, on the basis of the changes in the Ce 3d core level spectra between 3 and 4 u.c. layer thickness. The grey data points in figure 5.12 a) – c) show the Ce 3d spectrum of a $CePt_5$ alloy with 4 u.c. layer thickness taken at $T_s = 9\,\text{K}$ and 0°. The black line constitutes the GS-model fit to a Ce 3d spectrum taken on a layer thickness of 3 u.c. under similar experimental conditions. Figures 5.12 a) – c) successively illustrate the influence of varying solely V, U_{ff} and eventually both parameters, in order to adjust the GS-model fit to the experimental data of 4 u.c. layer thickness.
In a), first only V is decreased from $V(3\,\text{u.c.}) = 245\,\text{meV}$ to $V(4\,\text{u.c.}) = 225\,\text{meV}$, illustrated by the red line. That ensures a correct estimation of the f^0 contribution at $E_{bin} = 917\,\text{eV}$. However, the f^2 contribution at $E_{bin} = 880\,\text{eV}$ is overestimated and shifted to higher E_{bin} in the red GS – model fit. In b) V is kept constant at $V(3\,\text{u.c.}) = 245\,\text{meV}$, but U_{ff} is decreased from $U_{ff}(3\,\text{u.c.}) = 9.5\,\text{eV}$ to $U_{ff}(4\,\text{u.c.}) = 8.5\,\text{eV}$ as illustrated by the purple line. By doing so the f^2 contribution at $E_{bin} = 880\,\text{eV}$ fits nicely, however the f^0

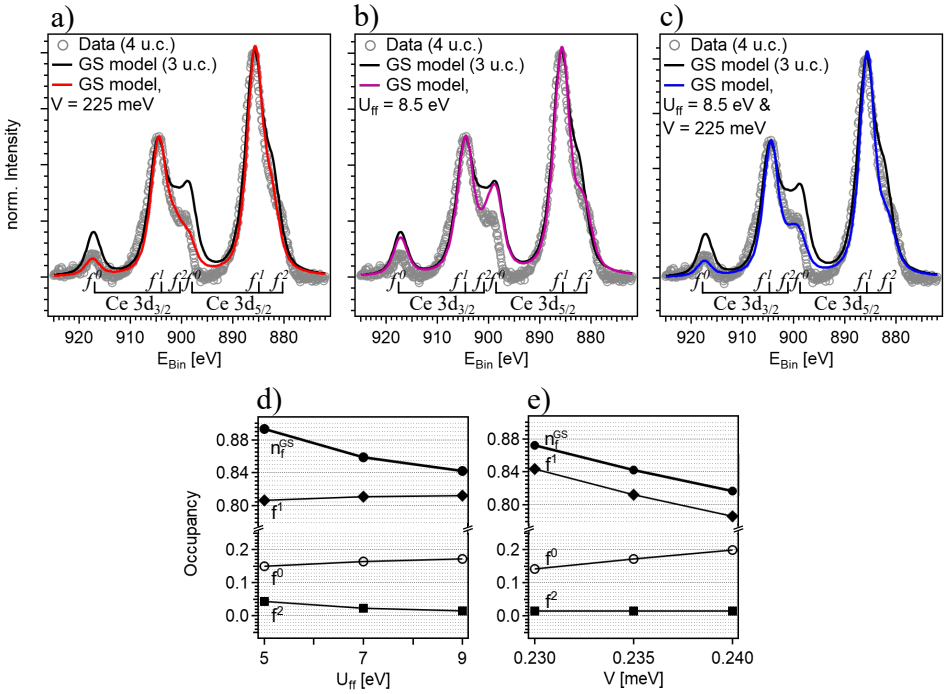

Figure 5.12: Detailed influence of U_{ff} and V on the GS-model fits and n_f. The grey data points correspond to the Ce $3d$ spectrum of 4 u.c. layer thickness (0°; $T_s = 9$ K), the black line shows the GS-model fit to a spectrum of 3 u.c. layer thicknesses. In a) – c) V(red line), U_{ff}(pink line) and finally both parameters (blue line) are varied to account for the changes between the spectrum of 4 u.c. layer thickness and the GS-model of 3 u.c.. d) and e) illustrate the influence of V and U_{ff} on n_f^{GS}. The remaining input parameters to the GS-model are $\epsilon_f = -1.3$ eV, $U_{fc} = 12$ eV, $B^+/B^- = 3$ eV, $N_f = 14$, $\Delta_{\mathrm{SO}} = 18.7$ eV and $Lw/Gw = 1$ eV.

contributions at $E_{bin} = 917\,\text{eV}$ and $E_{bin} = 900$ eV are largely overestimated. Eventually only the variation of both, V and U_{ff}, in c) (blue line), results in a proper fit to the f^0 as well as the f^2 contributions in the spectrum.
Figures 5.12 d) and e) illustrate how changes in U_{ff} and V reflect on the occupancy n_f^{GS} of the f level calculated according to equation 3.18. In d) U_{ff} is exemplarily varied from 5 eV – 9 eV at constant $V = 245\,\text{meV}$, whereas in e) V is varied from 230 meV to 240 meV at a constant $U_{ff} = 9\,\text{eV}$. The other parameters are kept constant as described in the caption of figure 5.12. Increasing U_{ff} from 5 to 9 eV in d) leads to a decrease of n_f^{GS} (dots). This is caused predominantly by the reduction of the f^2 occupancy (squares). The f^1 and f^0 occupancy (diamonds and circles) vary only little. Equally the increase of V in e) leads to a reduction of n_f^{GS}, however, here the reduction of n_f^{GS} is governed by an increase of f^0 on the expense of f^1. The f^2 occupancy is barely affected.
Therefore, the delicate variations of the f^2 weight in the Ce $3d$ spectra at $E_{bin} = 880\,\text{eV}$ are reflected by U_{ff} rather than V or Δ^{GS}. Hence Δ as determined in figure 5.4 a) on the basis of $w_{rel}(f^2)$ rather corresponds to U_{ff} as opposed to V in the parameter set of the GS-model. However, the huge overlap of the f^1 and f^2 components in the Ce $3d_{5/2}$ peak complicates a more precise determination, or a meaningful small scale variation of U_{ff}. In a different approach Δ^{GS} is estimated based on the relative spectral weight of the Ce $3\text{d}_{5/2}$ f^2 peak in the GS-model fits, according to the procedure described in subsection 3.1.3 and applied in subsection 5.2 to the experimental spectra. The resulting values for Δ^{GS} are shown in appendix A.4 in figure A.9. The course of Δ^{GS} still reflects the trend of n_f^{GS}, however, the absolute values are now in better agreement with Δ as given in figure 5.4 a). That is higher Δ^{GS} in the range of $\approx 107\,\text{meV}$ in the low layer thickness regime and lower Δ^{GS} of $\approx 83\,\text{meV}$ for layer thicknesses > 4 u.c..
The hybridization matrix element V, that translates to Δ^{GS}, therefore tracks the variation of n_f throughout the different layer thicknesses, explaining the similarities in the courses of Δ^{GS} and n_f^{GS} in figure 5.11. Comparing figures 5.4 b) and 5.11 b) shows, that n_f^{GS} roughly follows the same overall trend as n_f. That is smaller n_f at lower layer thicknesses of 1 – 3 u.c., an increase of

n_f between 3 and 4 u.c., followed by a saturation of n_f between 4 – >10 u.c.. The absolute values for n_f^{GS} deviate to some extend from n_f as determined in figure 5.4 b). Especially in the low layer thickness regime the GS-model fits result in even lower n_f^{GS} of $n_f^{\mathrm{GS}} = (0.785 \pm 0.016)$ for 2 and 3 u.c.. However, the error margins of both n_f^{GS} and n_f overlap, so that they coincide within the limits of accuracy.

The previous subsection shows how Ce $3d$ core level spectra are calculated within the Gunnarsson-Schönhammer formalism. It is explained how the various input parameters are determined on the basis of the experimental data and how small variations of the $f-f$ Coulomb repulsion U_{ff} and the hybridization matrix element V are necessary to account for the layer thickness, emission angle and temperature dependent changes in the spectra. The layer thickness dependence observed for the effective occupancy n_f^{GS}, as determined by the GS-model overall is in good agreement with the tendencies observed for n_f, estimated from the respective f^n spectral weights. That is lower n_f at 1 – 3 u.c. layer thickness with an increase at 4 u.c. and a subsequent saturation. For 1 – 3 u.c. the increase of n_f at higher temperatures is reproduced as well with the GS-model fits, however the weaker temperature dependence for 4 – >10 u.c. is not distinguishable. Also the variations caused by the change of emission angle are not traceable to full extend by the GS-model fits.
It is shown that the hybridization matrix element V is in principle suitable for modelling these small scale variations of the f^0 and f^2/f^0 weights. For example a reduction of V by 5 meV in figure 5.10 c) results in a distinctly better fit to the experimental data. Therefore, on the one hand it is possible to track small variations in the spectra with the GS-model fits, on the other hand the absolute values of V are to be considered carefully. In figure 5.11 a) the matrix element V is converted into Δ^{GS} according to equation 3.19. However this conversion is not unique. First, it is dependent on B, the maximum of the conduction band, which turns out to be a rather arbitrary parameter in the GS-model fit, as long as it is sufficiently large for the given ϵ_f. Increasing B further has no influence on the spectrum, yet

massively determines the transformation of V into Δ^{GS}. Second, the transformation of V to Δ^{GS}, as given in equation 3.19 is not unique [42, 61]. In other works, Δ^{GS} is given by an average value of $\Delta^{\mathrm{GS}}_{\mathrm{av}} = \pi V^2$, which results in significantly larger values [42, 61]. For example at a layer thickness of 3 u.c. $CePt_5$/Pt(111) $\Delta^{\mathrm{GS}}_{\mathrm{av}} = 189\,\mathrm{meV}$ instead of $\Delta^{\mathrm{GS}} = 40\,\mathrm{meV}$, as given by equation 3.19. This uncertainty in transforming V to Δ complicates a direct comparison between Δ as determined from the experimental data and Δ^{GS}. Additionally V and therefore Δ^{GS} mainly influences the f^0 weight to the spectrum (see figure 5.7 d)), whereas Δ is determined by the f^2 contribution to the Ce $3d_{5/2}$ peak. Therefore Δ^{GS} rather resembles a depletion of the f^1 occupancy and therefore n_f, by the combined effects of f^0 and f^2 as opposed to the hybridization Δ, that is solely estimated on the basis of the f^2 spectral weight.
In summary the GS-model fits give detailed insight into the decisive parameters that determine the manifestation of strong correlation in Ce-based compounds. However absolute values should be treated carefully and any observed variations should always be scrutinized and critically compared to the variations observable in the raw experimental data.

After an extensive treatment of the manifestation of strong correlation in Ce $3d$ core levels, the following subsection presents to what extend these findings can be confirmed by the low energy excitations in the valence band spectra.

5.5 Valence band structure of $CePt_5$/Pt(111)

The characteristic final state multiplet in the Ce $3d$ core level spectra, as discussed in the previous subsections, serves as a high energy probe for Kondo physics in the valence band, that happens on an energy scale orders of magnitude smaller. Below the characteristic Kondo temperature T_{K}, the distinguishing features of the Kondo effect in the valence band are the Kondo

resonance at or slightly above the Fermi edge and its crystal-field and spin-orbit partner. Additionally one expects an f^0 like ionization peak around the binding energy of the f level. Furthermore, as discussed in subsection 2.1.3, below a characteristic coherence temperature T^*, a regular lattice of Kondo singlets might lead to the formation of a flat, heavy fermion band at E_F, that might hybridize with the intersecting conduction bands. This leads to an energy gap opening at E_F of the order of a view meV [9].
The following subsection presents the valence band spectra of selected layer thicknesses of $CePt_5$/Pt(111), with emphasis on the layer thickness and temperature dependent evolution of the Kondo resonance at E_F. According to subsection 2.1.2 and equation 2.4, T_K is determined by the FWHM of the Kondo resonance at a given sample temperature T_s. With that, T_K is estimated for a set of layer thickness on the basis of valence band data and compared to T_K as obtained from Ce $3d$ core level spectra.
The band structure of thin films of $CePt_5$/Pt(111) has already been discussed in detail elsewhere and will not be subject of the following analysis [61, 105]. However, figure 5.13 in general illustrates how ARPES is suitable for investigating the spectral features of the Kondo effect in the valence band. Figure 5.13 a) and b) show the bandstructure of a $CePt_5$/Pt(111) surface alloy of 4 u.c. layer thickness along the $\overline{\Gamma\mathrm{M}}$-direction, acquired with two different excitation energies of $h\nu = 21.22\,\mathrm{eV}$ (He I_α) in a) $h\nu = 40.81\,\mathrm{eV}$ (He II_α) in b). At $h\nu = 40.81\,\mathrm{eV}$ the photoionization cross section of states with predominantly f character is more than three times higher as compared to an excitation with $h\nu = 21.22\,\mathrm{eV}$ [150]. Therefore, the Ce $4f$ states are emphasized in figure 5.13 b) as compared to a). Both spectra are normalized in intensity at $E - E_\mathrm{F} = -2.3\,\mathrm{eV}$ and $\boldsymbol{k}_{||} = 0\,\mathrm{\AA}^{-1}$. At first glance some major differences between figure 5.13 a) and b) are apparent. The five main intensities at $\boldsymbol{k}_{||} = 0\,\mathrm{\AA}^{-1}$ labeled with letters $a-e$ are all less intense in b) as compared to a). This is confirmed by figure 5.13 c) where two EDCs at $|\boldsymbol{k}_{||}| < 0.05\,\mathrm{\AA}^{-1}$ of figures a) and b) are compared. The characteristic bands are labeled with letters $a-e$ as well. For both excitation energies the band maxima lie at the same energy but are less intense for He II_α, shown in blue, as compared to He I_α, depicted in black.

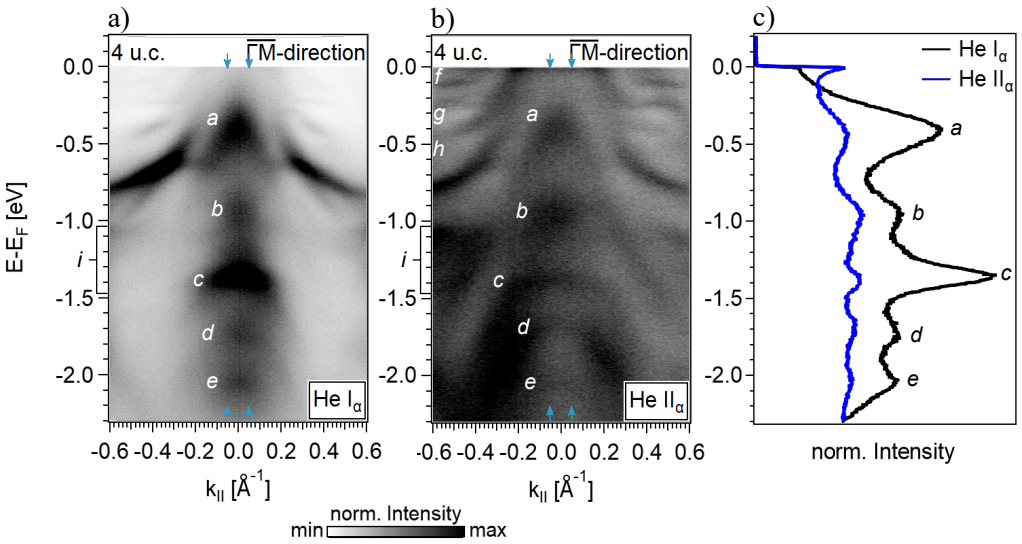

Figure 5.13: Valence band structure of CePt$_5$/Pt(111). a) and b) show the bandstructure of a thin film of CePt$_5$/Pt(111) with 4 u.c. layer thickness in dependence of the excitation energy with $h\nu = 21.22\,\text{eV}$ (He I$_\alpha$) in a) and $h\nu = 40.81\,\text{eV}$ (He II$_\alpha$) in b). The spectra are recorded at a temperature of $T_s = 10\,\text{K}$ and with a resolution of $\Delta\text{E} = 5.18\,\text{meV}$. Prominent features are marked with letters $a-i$. c) shows EDCs of the bandstructures in a) and b) integrated over $\boldsymbol{k}_{||} = \pm 0.05\,\text{Å}^{-1}$ as marked by the blue arrows in a) and b).

However in total, the bandstructure recorded with He II_α displays a higher level of detail. This is visible for the bands *c* and *d*, that show dispersion also at larger $|\boldsymbol{k}_{||}|$, as well as in the area of $|\boldsymbol{k}_{||}| > 0.2\,\text{Å}^{-1}$ and $-0.5\,\text{eV} < E - E_\text{F} < 0\,\text{eV}$. In this area bands $f-h$ are clearly distinguishable in figure 5.13 b) whereas they vanish in the background in a). Furthermore, figure 5.13 b) exhibits an intense structure *i* at $-1.5\,\text{eV} < E - E_\text{F} < -1.0\,\text{eV}$, that is strongly damped in a). This structure has been identified as the ionization peak of the *f* level in subsection 5.4.1. This assumption is supported by figure 5.13, where structure *i* is more prominent when excited with He II_α.
Finally, the most interesting difference is the strong increase in intensity at the Fermi level in figure 5.13 b). It is clearly visible around $\boldsymbol{k}_{||} = 0\,\text{Å}^{-1}$ as emphasized by the EDCs in figure 5.13 c). Additionally it is discernible as well at larger $|\boldsymbol{k}_{||}|$, especially where bands cross the Fermi level for example at $|\boldsymbol{k}_{||}| = 0.37\,\text{Å}^{-1}$. This intensity constitutes the occupied part of the Kondo resonance, with its actual maximum a few meV above the Fermi level. The Kondo resonance and in particular its evolution with increasing sample temperature T_s allows for an estimation of the characteristic Kondo temperature T_K of the system. For that, the tail of the Kondo resonance is extrapolated, by a Lorentzian function situated at or slightly above the Fermi level, as described in subsection 3.4.
Figure 5.14 shows the evolution of the Kondo resonance of a $CePt_5$ surface alloy with 4 u.c. layer thickness over a temperature range of $T_s = 10\,\text{K}$ to $T_s = 64\,\text{K}$ in a)–e) and additionally the spectrum acquired at room temperature ($T_s = 300\,\text{K}$) in f). The depicted EDCs, shown in grey, result from angle-resolved valence band spectra similar to the one shown in figure 5.16 c) by integrating a $\boldsymbol{k}_{||}$–range of $\pm\,0.08\,\text{Å}^{-1}$. They are normalized to one at $E - E_\text{F} = -0.15\,\text{eV}$ and the background is treated as described in subsection 3.4. The resulting inelastic background is depicted in dashed-dotted black lines, whereas the Gaussian fit to the first band maximum *a* is shown in light blue. Note that the maximum of the Gaussian is out of the depicted energy rang for figures a)–e). The Lorentzian fit to the Kondo resonance is shown in dark blue. In order to obtain a proper total fit, shown in red, the Lorentzian is shifted to one as determined by the normalization of the

experimental data. Figure 5.14 a) – e) show the tail of the Kondo resonance significantly decreasing within the temperature range of $T_s = 10 - 64\,\mathrm{K}$ until at $T_s = 300$ in f) it is completely vanished. The Lorentzian fits to the tail of the Kondo resonance resemble this trend, as they broaden and shift to higher $E - E_\mathrm{F}$ for T_s =10 – 64 K until at T_s =300 K a Lorentzian peak at E_F can not be determined anymore.

Following equation 2.4 one can estimate T_K for each sample temperature T_s, which is shown in figure 5.15 a). Taking into account the increasing T_s, the analysis of the Lorentzian FWHM should result in a constant T_K over the whole temperature range. This is shown in figure 5.15 a). The errors are estimated according to subsection 3.4. The estimated T_K range from 244 K – 312 K, resulting in a mean value of $\bar{T_\mathrm{K}}(4\,\mathrm{u.c.}) = (284 \pm 26)$ K for a layer thickness of 4 u.c. $CePt_5$/Pt(111). The second data point (circle) at $T_s = 10\,\mathrm{K}$ stems from a comparable measurement of another preparation of a $CePt_5$ film of 4 u.c., indicating the reproducibility of the low temperature spectra.

Considering the results based on the Ce 3*d* spectra in subsection 5.3, a Kondo temperature of $\bar{T_\mathrm{K}}(4\,\mathrm{u.c.}) \approx 284\,\mathrm{K}$ seems plausible. The spectra of the Ce 3*d* levels suggest no major change in n_f between $T_s = 9\,\mathrm{K}$ and $T_s = 290\,\mathrm{K}$ as shown in figure 5.5 e). A significant increase in n_f however, is only expected for temperatures well above the Kondo temperature. Therefore, if T_K is in the range of $\bar{T_\mathrm{K}}(4\,\mathrm{u.c.}) \approx 284\,\mathrm{K}$ the data taken at $T_s = 290\,\mathrm{K}$ are still too close to the systems Kondo temperature to observe significant changes in n_f. Considering $\bar{T_\mathrm{K}}(4\,\mathrm{u.c.}) \approx 284\,\mathrm{K}$, it might be surprising, that no Kondo resonance is visible in the valence band spectrum at $T_s = 300\,\mathrm{K}$ in figure 5.14 f). However, at these temperatures the Fermi Dirac distribution is heavily broadened. This strongly suppresses any signal at or slightly above the Fermi edge, making it impossible to distinguish any weak resonance that might sill be present.

Praetorius et al. obtain a Kondo temperature of $T_\mathrm{K} \approx 200\,\mathrm{K}$ for a $CePt_5$ surface alloy of 4 u.c. layer thickness [135]. This is based on temperature dependent changes of n_f between <10 K and 275 K as determined by XAS.

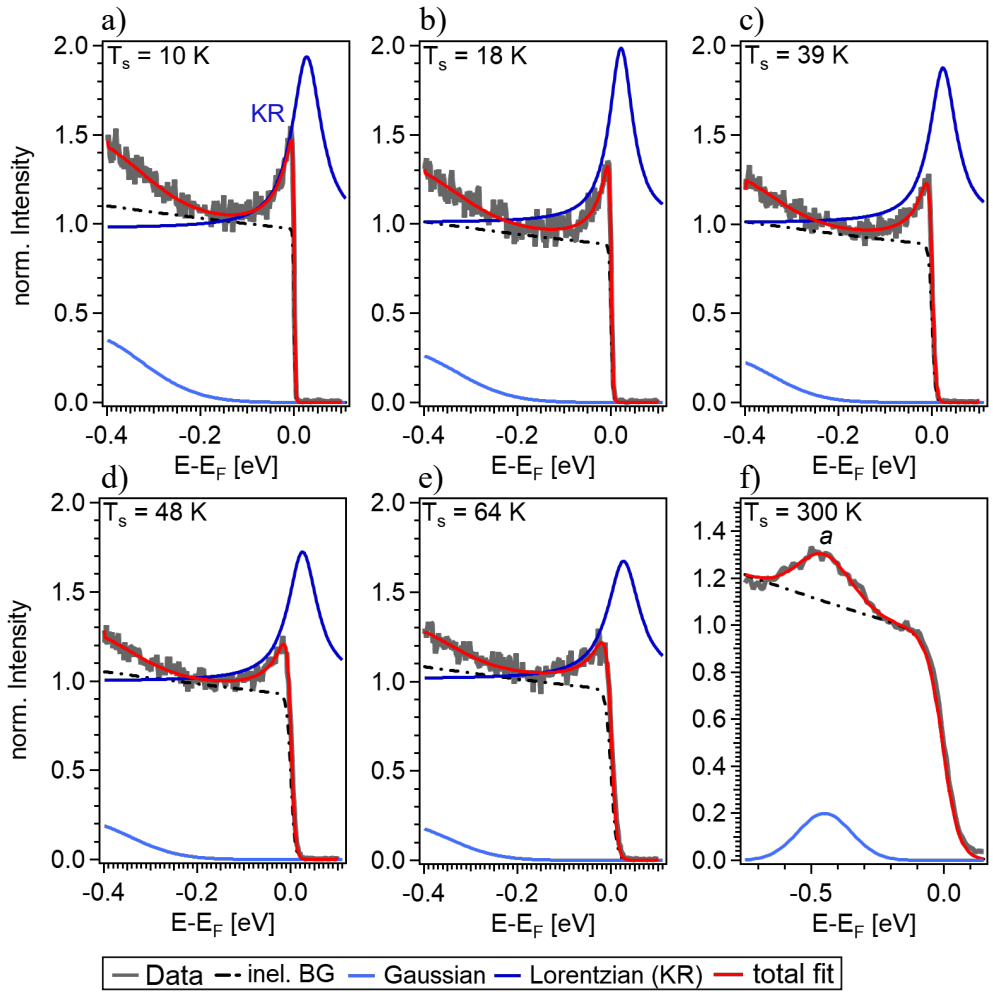

Figure 5.14: Temperature dependent Kondo resonance for 4 u.c. $CePt_5$/Pt(111). a) – f) show the evolution of the Kondo resonance with increasing sample temperature from $T_s = 10\,\mathrm{K}$ in a) to $T_s = 300\,\mathrm{K}$ in f). The experimental data shown in solid grey lines result from angle-resolved measurements similar to figure 5.16 c) by integrating the intensity between $\boldsymbol{k}_{||} = \pm 0.08\,\mathrm{Å}^{-1}$. They are normalized to one at $E - E_\mathrm{F} = -0.15\,\mathrm{eV}$. The inelastic background is shown in dashed-dotted black lines, the Gaussian fit to band a in light blue, the Lorentzian fit to the Kondo resonance in dark blue and the resulting total fit in red.

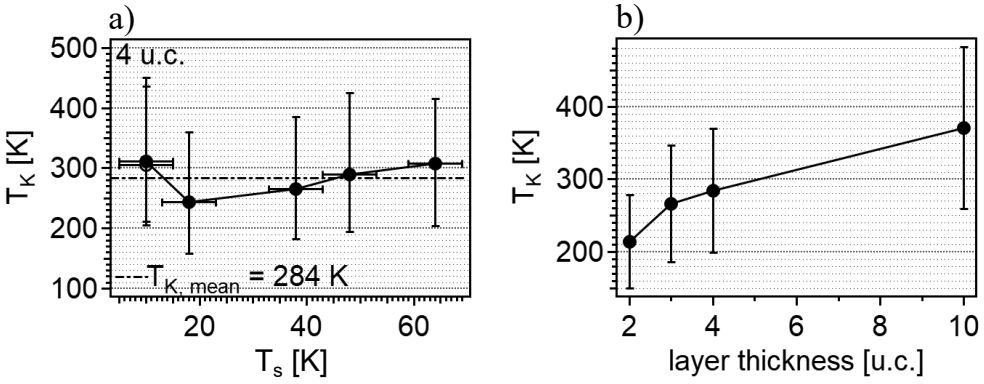

Figure 5.15: Kondo temperature in CePt$_5$/Pt(111). a) shows the Kondo temperature estimated on basis of equation 2.4 for a layer thickness of 4 u.c. CePt$_5$/Pt(111) for increasing sample temperatures. The resulting mean Kondo temperature is $\bar{T_K}(4\,\text{u.c.}) = 284\,\text{K}$. b) shows the Kondo temperatures estimated on the basis of equation 2.4 and figure 5.16 for 2, 3, 4 and >10 u.c..

However the saturation of n_f in the temperature range above $T_s > 250\,\text{K}$ is not very pronounced in the presented data in [135]. This at least allows for the possibility of a higher Kondo temperature also in the measurements presented in [135].

Figure 5.16 a) – d) show the valence band structure of 2, 3, 4, and >10 u.c. CePt$_5$/Pt(111) in a small $\boldsymbol{k}_{||}$-range around the $\overline{\Gamma}$-point of the surface Brillouin zone and close to E_F. The spectra are all acquired using an excitation energy of $h\nu = 40.81\,\text{eV}$. a) and b) are recorded with an experimental resolution of $\Delta\text{E} = 5.18\,\text{meV}$, whereas c) and d) have a resolution of $\Delta\text{E} = 7.58\,\text{meV}$. The sample temperature for all layer thicknesses is $T_s < 16\,\text{K}$ and the spectra are normalized in intensity at $\boldsymbol{k}_{||} = 0\,\text{Å}^{-1}$ and $E - E_\text{F} = -150\,\text{meV}$.

Although recorded with better energy resolution the bandstructure of 2 and 3 u.c. in a) and b) is significantly less intense, compared to the higher layer thicknesses of 4 and >10 u.c. in c) and d). However, all spectra exhibit an increase in intensity around $\boldsymbol{k}_{||} = 0\,\text{Å}^{-1}$, between the two conduction bands that cross the Fermi level at $\boldsymbol{k}_{||} = \pm\,0.19\,\text{Å}^{-1}$. At 2 and 3 u.c. one observes a lot more intensity from the two conduction bands reaching towards $\boldsymbol{k}_{||} = 0\,\text{Å}^{-1}$

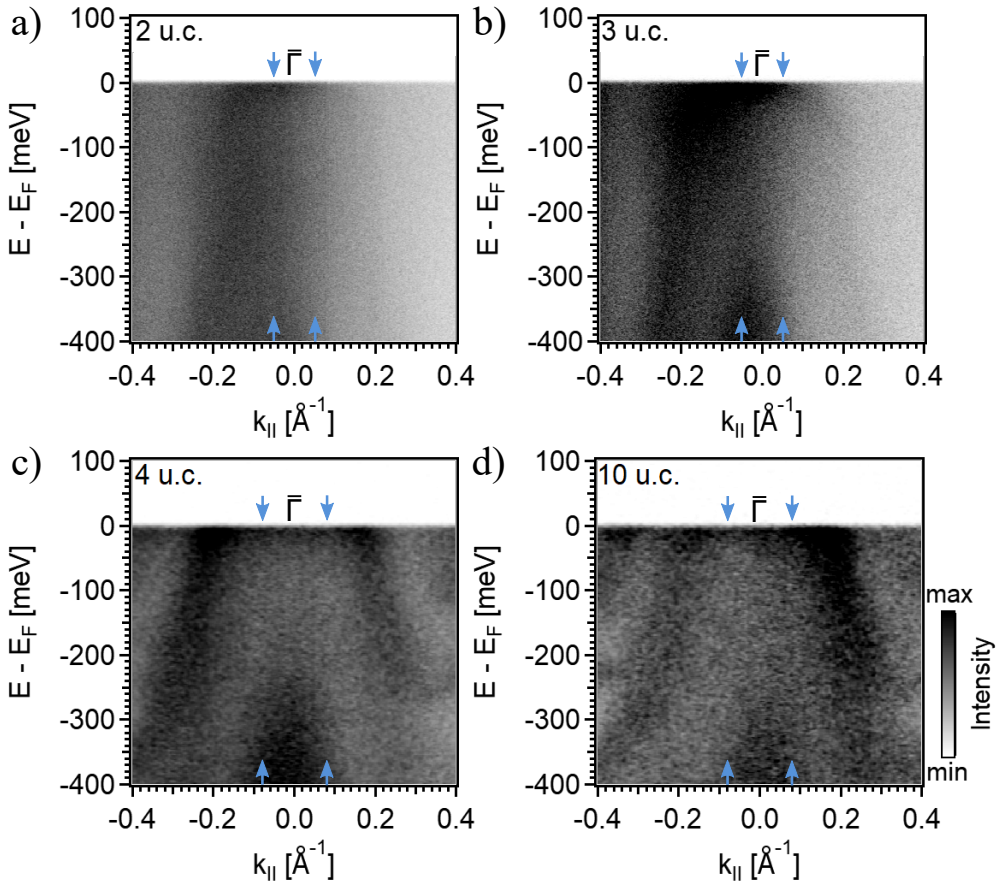

Figure 5.16: Valence band structure of different film thicknesses of CePt$_5$/Pt(111). a) and b) show the valence band structure of 2 and 3 u.c. CePt$_5$/Pt(111) recorded with $h\nu = 40.81$ eV, an energy resolution of $\Delta E = 5.18$ meV at temperatures of $T_s(2\,\text{u.c.}) = 15.4$ K and $T_s(3\,\text{u.c.}) = 9.8$ K respectively. c) and d) show the bandstructure of 4 and >10 u.c. CePt$_5$/Pt(111) recorded as well with $h\nu = 40.81$ eV, an energy resolution of $\Delta E = 7.58$ meV at temperatures of $T_s(4\,\text{u.c.}) = 10$ K and $T_s(<10\,\text{u.c.}) = 15.2$ K.

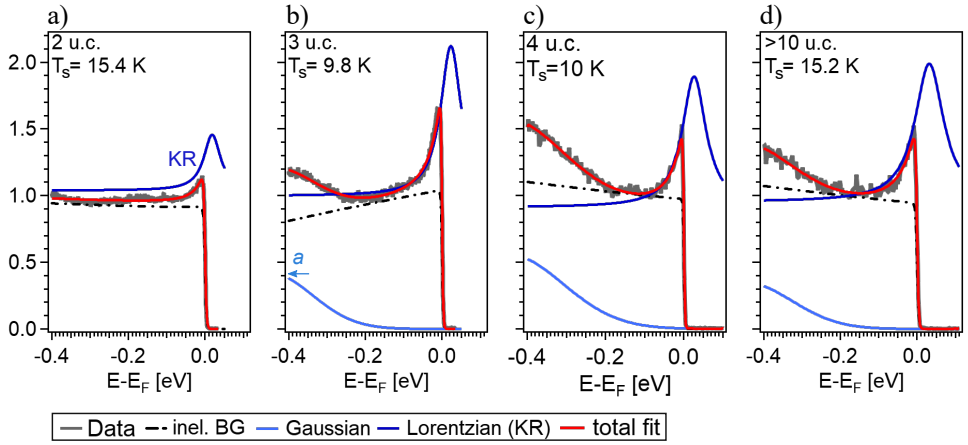

Figure 5.17: Layer thickness dependent Kondo resonance of $CePt_5$/Pt(111). a) – d) show the integrated EDCs according to figure 5.16 for 2, 3, 4, and >10 u.c.. The experimental data is shown in grey, the inelastic background in black, the Gaussian fit to band a in light blue, the Loretzian fit to the Kondo resonance in dark blue and the resulting total fit in red.

at E_F. In order to investigate the layer thickness dependent Kondo resonance, EDCs around the $\overline{\Gamma}$-point are shown in figure 5.17 a) – d) for each layer thickness. The intensity contribution from the respective conduction bands is taken into account, by integrating over smaller $\boldsymbol{k}_{||}$-ranges for 2 and 3 u.c. as compared to 4 and >10 u.c. This is illustrated by the blue arrows in figure 5.16 respectively.

The resulting EDCs in figure 5.17 a) – d) show an increase in intensity at E_F for all layer thicknesses. This is the occupied part of the Kondo resonance. However, the Kondo resonance is a lot sharper in 3 – >10 u.c. in b) – d) as compared to 2 u.c. in a). Furthermore, a strong variation in the inelastic background as well as the intensity of the first band maximum a is observed throughout the different layer thicknesses. At 2 u.c. in a) neither a rising inelastic background nor a structure similar to band a is observed. Therefore the Gaussian function is removed from the background treatment and the inelastic background, shown as a dashed-dotted black line, is modelled by a Fermi-Dirac distribution without slope.

For a layer thickness of 3 u.c. in b) the band maximum a becomes apparent and is modelled by a Gaussian as described in subsection 3.4, shown in light blue. However, the inelastic background increases between $-250\,\text{meV} \leq E - E_\text{F} \leq -100\,\text{meV}$ when approaching E_F. To account for this rise in the background towards E_F, the inelastic background is modelled by a Fermi Dirac distribution with a positive slope superimposed by a polynomial of 4th order. The background for layer thicknesses of 4 and >10 u.c. in c) and d) is treated as described in subsection 3.4, with a Gaussian reproducing the band maximum a and a constant Fermi-Dirac distribution superimposed by a polynomial of 4th order.
On the basis of this background treatment, the tail of the Kondo resonance is fitted by a Lorentzian function, shown in dark blue. Finally the total fit of the respective EDC is shown in red. The resulting Lorentzian peaks underline the observation, that 3 – >10 u.c. show a sharp Kondo resonance, whereas it is strongly reduced at a layer thickness of 2 u.c..
On the basis of the Lorentzian FWHM and the determined sample temperature T_s a Kondo temperature T_K is estimated for each layer thickness. The results are shown in figure 5.15 b). The Kondo temperatures estimated for 2 and 3 u.c. are $T_\text{K}(2\,\text{u.c.}) = 214\,\text{K}$ and $T_\text{K}(3\,\text{u.c.}) = 267\,\text{K}$. For 4 u.c. the mean value of $T_{\text{K, mean}}(4\,\text{u.c.}) = 284\,\text{K}$, as estimated above is shown. At a layer thickness of >10 u.c., the Lorentzian FWHM results in a Kondo temperature of $T_\text{K}(>10\,\text{u.c.}) = 371\,\text{K}$.

The T_K estimated for 2 and 3 u.c. are in good agreement with the conclusions made in subsection 5.3. On the basis of the final state structure of the Ce $3d$ core levels one observes a significant change in n_f between $\text{T} = 150\,\text{K}$ and $\text{T} = 290\,\text{K}$. This change in n_f occurs when going from well below the systems Kondo temperature to well above [26, 48, 135]. The estimated T_K for 2 and 3 u.c. match this temperature range of $150\,\text{K} - 290\,\text{K}$ very well.
At a layer thickness of >10 u.c. a higher Kondo temperature is estimated as compared to 4 u.c. This might be surprising at first, since the lattice parameters of >10 u.c. $CePt_5$/Pt(111) indicate a relaxation towards the bulk lattice structure of $CePt_5$, which is magnetically ordered at low temperatures [128].

However, the valence band spectrum in figure 5.16 d) clearly shows a sharp intensity at the Fermi edge for a $CePt_5$ layer thickness >10 u.c.. This can be understood in terms of the strong surface sensitivity of measurements with low excitation energies. The probing depth in ARPES is only of the order of 5 Å. Therefore, only the electronic structure of the topmost layer at the sample surface is accessible. The sample surface, however, presents a different chemical environment to the Ce atoms, as compared to the bulk structure. In particular in $CePt_5$, the sample surface is reported to be Pt terminated, providing an increased number of coordination partners for the Ce atom at the surface, leading to an increased hybridization, as discussed already in subsection 5.2. This is in good agreement with the effective occupancy n_f determined for >10 u.c. in subsection 5.2 as well. First, n_f determined for >10 u.c. at $T_s = 9\,\mathrm{K}$ is still well below one with $n_{f9\mathrm{K}}^{0^\circ} = (0.873 \pm 0.013)$. Although XPS is a lot more bulk sensitive than ARPES, the probing depth of $\lambda = 13.56\,\text{Å}$ still only amounts to ≈1/3 of the whole alloy thickness at >10 u.c. of approximatly 43.91 Å. Therefore, also XPS is rather surface sensitive in this large layer thickness regime. Second, the n_f determined for an emission angle of 60° off normal, which is even more surface sensitive, are lower than their equivalents determined for normal emission, especially in the large layer thickness regime (see figure 5.4 b)). Both results from the XPS spectra therefore support that the Kondo resonance observed at >10 u.c., is strongly driven by the enhanced hybridization at the sample surface. Hence this observation is not necessarily a contradiction to the assumption that bulk $CePt_5$ is no Kondo system, but shows magnetic order at low temperatures [128].

In summary this section provides a detailed overview over the manifestation of strong correlation in the surface alloy $CePt_5$/Pt(111). The first part extensively covers, how the high energy probe XPS provides valuable access to the low energy excitations governed by strong correlation in the valence band. The combined analysis of the relative final state spectroscopic weights in the Ce 3*d* core level spectra as well as simulations of the core levels using the Gunnarsson-Schönhammer formalism allows for a quantitative

determination of decisive parameters such as the $c-f$ hybridization Δ and the effective occupancy n_f of the f level. A determination of the systems Kondo temperature T_K is possible on the basis of a temperature dependent study of the Ce 3d core levels.
The second part eventually focuses on the actual low energy excitations in the valence band caused by strong correlation. Determining the FWHM of the Kondo resonance and its temperature dependence allows for an estimation of T_K as well.
Both methods paint the same picture for the manifestation of strong correlation throughout the different layer thicknesses of $CePt_5$ on Pt(111). First it is shown, that the layer thickness of the intermetallic thin film strongly influences the low temperature properties causing the system to assume two different ground states. That is a rather intermediate or mixed valent state at thin layer thicknesses with "α-like" Ce characterized by low n_f, and a Kondo ground state with "γ-like" Ce and $n_f \gtrapprox 0.9$ for layer thicknesses $\geqq$4 u.c.. Furthermore the temperature dependence of these different ground state regimes is analysed. In the low layer thickness regime n_f significantly increases between $T_s = 150\,\mathrm{K}$- $290\,\mathrm{K}$ suggesting a Kondo temperature somewhere inbetween. For layer thicknesses $\geqq$4 u.c. no comparable increase is observed suggesting larger T_K. Both results were obtained on the basis of the Ce 3d core level spectra in the first part of this section and are supported by the valence band spectra in the second part. The respective T_K are estimated as $T_\mathrm{K}(2\,\mathrm{u.c.}) = 214\,\mathrm{K}$, $T_\mathrm{K}(3\,\mathrm{u.c.}) = 267\,\mathrm{K}$, $T_\mathrm{K}(4\,\mathrm{u.c.}) = 284\,\mathrm{K}$ and $T_\mathrm{K}(>10\,\mathrm{u.c.}) = 371\,\mathrm{K}$
Furthermore it was possible to differentiate between surface and bulk contributions to n_f showing smaller n_f at the surface for the larger layer thicknesses but the opposite with lower n_f at the surface for the lower layer thicknesses. All of this is summarized schematically in figure 5.18. The increasing $CePt_5$ layer thickness is illustrated by more and more grey rectangles, set on the Pt(111) substrate, shown in blue. Lower n_f are symbolized by darker shades of grey, whereas lighter shades of grey depict larger n_f. The different regimes of T_K are marked by a border line between 3 and 4 u.c. layer thickness.
Additionally the analysis of the final state weights in the Ce 3d core levels

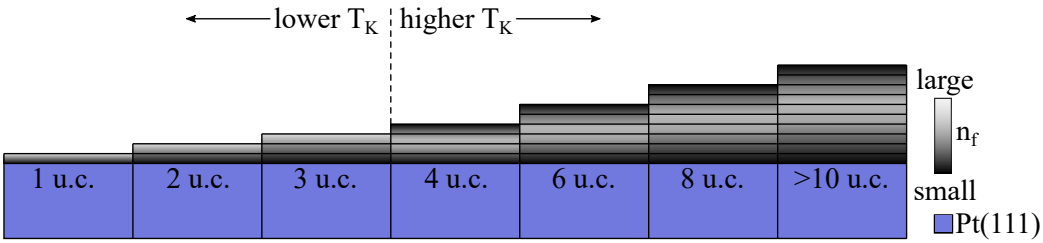

Figure 5.18: Schematic illustration of n_f for increasing layer thicknesses. From left to right increasing layer thicknesses of $CePt_5$ are depicted as grey rectangles on the blue Pt(111) substrate. Darker shades of grey correspond to lower n_f whereas lighter shades of grey stand for larger n_f.

underline the importance of taking into account the hybridization Δ, which is expressed by the f^2 contribution to the spectrum. By neglecting the influence of Δ, n_f might be overestimated up to 50 % [26, 30, 135].

This section conclusively shows how the structural changes accompanying the increasing surface alloy film thickness strongly affect the manifestation of strong correlation in $CePt_5$/Pt(111). Therefore controlling the film thicknesses of correlated systems by growing them epitaxially, provides a versatile way of influencing their electronic structure.
The following section is dedicated to a different system based on a $CeAg_x$ surface alloy. $CeAg_x$ is known to be only weakly correlated. The insights in manipulating strong correlation gained in this section are transferred to $CeAg_x$, in order to enhance correlation effects by varying the layer thickness or by adding a different element to the surface alloy.

6

Tunability of the electronic structure in $CeAg_x$/Ag(111)

A systems dimensionality, for example in form of a surface alloy's layer thickness, heavily influences the electronic structure in strongly correlated systems. As shown in the previous section for $CePt_5$/Pt(111), the ground state occupancy of the f level as well as the Kondo temperature vary with the $CePt_5$ film thickness. Especially at the interface between substrate and thin film as well as at the alloys surface the $c-f$ hybridization is considerably changed with respect to its values in the bulk. In this section dimensionality, as a tuning parameter for strong correlation is applied to $CeAg_x$/Ag(111). The surface alloy $CeAg_x$ is known to be only weakly correlated (see subsection 4.2). However, the influence of layer thickness is not studied with photoemission spectroscopy yet. On the basis of previous studies on $CePt_5$/Pt(111), as presented in this work, one expects a reduction of the low temperature ground state n_f in the thinner layer thickness regime. Especially at the transition between 3 and 4 u.c. $CePt_5$/Pt(111), where the moiré pattern, that is characteristic for the thin layer thicknesses, relaxes, n_f significantly increases. Hence, for $CeAg_x$ two film thicknesses are investigated, that show a similar succession of diffraction patterns upon increasing layer thickness.

Additionally the influence of adding Bi to the surface alloy will be discussed, in terms of affecting strong correlation through increased spin-orbit coupling. The first part presents the surface lattice structure of $CeAg_x$/Ag(111) of two different layer thickness as well as of Bi:$CeAg_x$/Ag(111). The second part focuses on the electronic structure of all three surface alloys as accessible by ARPES and XPS and in particular on the spectroscopic features that attest strong correlation. These are the Kondo resonance and its spin-orbit partner in the valence band as well as the characteristic f level final state multiplet in the Ce $3d$ core levels.

6.1 Lattice structure of $CeAg_x$ and Bi:$CeAg_x$ on Ag(111)

$CeAg_x$ surface alloys of two different thicknesses are prepared according to subsection 3.5. The tuning parameter for the film thickness is thereby the evaporation time t_e of Ce, determining the initial Ce coverage. The thin $CeAg_x$ surface alloy is prepared with $t_e = 60\,s$ whereas the thick film occurs after an evaporation time of $t_e = 120\,s$. However, $CeAg_x$/Ag(111) shows a peculiarity during preparation. After removing an aged film of $CeAg_x$ from the Ag(111) substrate by Ar^+-ion sputtering and subsequent annealing, the supposedly clean substrate shows a clear $CeAg_x$ diffraction pattern in LEED as well as a considerable amount of Ce on the surface, as determined by XPS. This is in strong contrast to $CePt_5$/Pt(111), where Ar^+-ion sputtering and subsequent annealing always result in a clean Pt(111) substrate with the characteristic threefold symmetric hexagonal diffraction pattern (see subsection 4.1.1). The resulting diffraction patterns of all $CeAg_x$/Ag(111) surface alloys are recorded with LEED and shown in figure 6.1 a) – d). The clean Ag(111) substrate is shown in a) whereas the self organized (so) $CeAg_x$ film ($CeAg_x^{so}$) is shown in b), both at $E_0 = 58\,eV$. The diffraction pattern of the clean Ag(111) substrate consists of six hexagonally ordered diffraction spots, that show a threefold symmetric intensity modulation upon varying the elec-

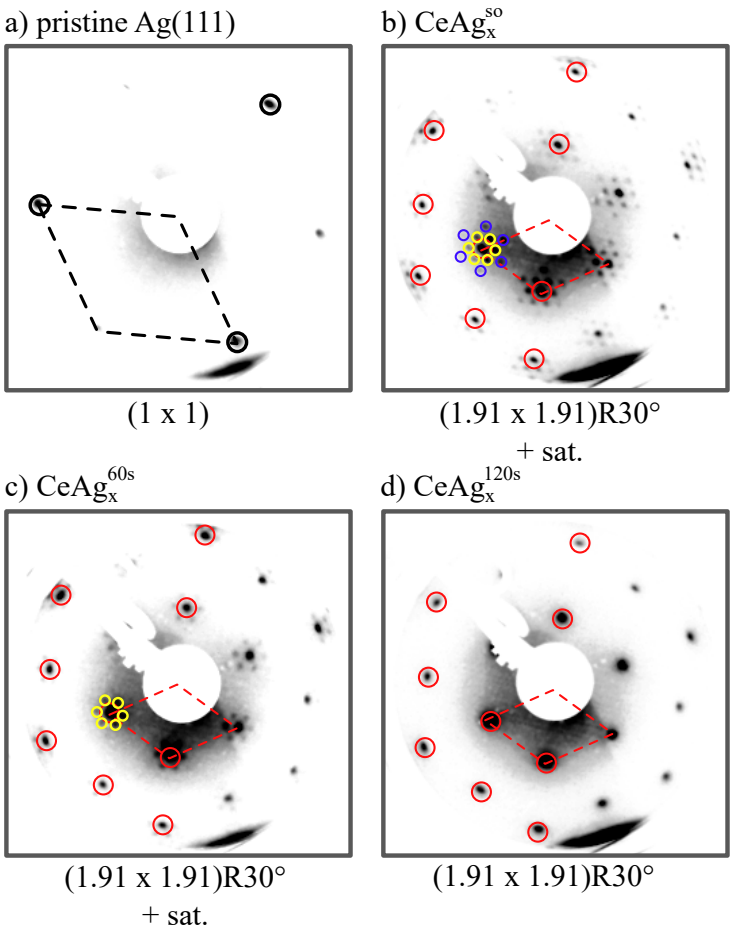

Figure 6.1: Layer thickness dependent surface reconstruction of CeAg$_x$/Ag(111). a) – d) subsequently show the diffraction patterns of pristine Ag(111), self organized CeAg$_x$/Ag(111) (CeAg$_x^{so}$), a thin CeAg$_x$ surface alloy with $t_e = 60$ s (CeAg$_x^{60s}$) and a thick CeAg$_x$ surface alloy with $t_e = 120$ s (CeAg$_x^{120s}$). All LEED patterns are recorded with an incident electron beam energy of $E_0 = 58$ eV. The main diffraction spots for Ag(111) in a) are partly highlighted in black, the ones for CeAg$_x$ in b) – d) in red. Additionally the satellite spots in b) and c) for CeAg$_x^{so}$ and CeAg$_x^{60s}$ are marked in yellow and blue. The primitive surface unit cell is shown in dashed lines respectively.

tron beam energy as highlighted by black circles. The primitive surface unit cell is marked in black. The $CeAg_x^{so}$ surface alloy in b) constitutes of a main $(1.91\,\mathrm{x}\,1.91)R30°$ reconstruction (red circles) as well as additional satellite spots with a reconstruction of $(10.65\,\mathrm{x}\,10.65)$ (yellow circles) with respect to the Ag $(1\,\mathrm{x}\,1)$ pattern. The primitive unit cell of the main reconstruction is marked in red. The intensity of the satellite spots is enhanced around the main spots but they extend also inbetween, as indicated by the blue circled spots in figure 6.1 b). The threefold symmetric intensity variation of the Ag substrate spots is not visible anymore in the $CeAg_x^{so}$ diffraction pattern. The lattice constant of the Ag substrate as estimated according to subsection 3.2 amounts to $a(Ag) = (4.153 \pm 0.071)$ Å and thus a nearest neighbour distance of $a_{NN}(Ag) = (2.94 \pm 0.050)$ Å. The nearest neighbour distance of the main diffraction pattern (red) in $CeAg_x^{so}$ is estimated to $a_{NN}^{so} = (5.605 \pm 0.095)$ Å with respect to the Ag(111) reconstruction, whereas the satellite spots (yellow, blue) exhibit a nearest neighbour distance of $a_{NN,\,sat.}^{so} = (31.25 \pm 0.53)$ Å. The lattice plane distance is $d_{hkl}^{so} = (4.580 \pm 0.054)$ Å.

After depositing Ce for $t_e = 60$ s either on the $CeAg_x^{so}$ reconstruction or the pristine Ag(111) substrate and subsequent annealing, a diffraction pattern as shown in figure 6.1 c) is observed. The pattern is very similar to the one of $CeAg_x^{so}$. The main spots, highlighted by red circles, are hexagonally ordered and exhibit a sixfold symmetric intensity distribution. The orientation of the hexagon is rotated by 30° with respect to the Ag(111) substrate. The satellite spots surrounding the main spots exhibit a hexagonal, sixfold symmetric diffraction pattern as well. However, their orientation is along the Ag(111) substrate, indicated by yellow circles. The main spots result in a $(1.91\,\mathrm{x}\,1.91)R30°$ reconstruction with a nearest neighbour distance of $a_{NN}^{60s} = (5.605 \pm 0.095)$ Å with respect to the Ag(111) substrate and a lattice plane distance of $d_{hkl}^{60s} = (4.580 \pm 0.054)$ Å. The primitive unit cell is again marked in red. The satellite spots exhibit the same periodicity as seen in $CeAg_x^{so}$, which is $(10.65\,\mathrm{x}\,10.65)$ with $a_{NN,\,sat.}^{60s} = (31.25 \pm 0.53)$ Å with respect to the Ag(111) substrate. However, only the satellite spots closest to the main spots, are visible for $CeAg_x^{60s}$ in figure 6.1 c). The second order as indicated by blue circles in figure 6.1 b) is not distinguishable.

After an initial Ce deposition of $t_e = 120\,s$ either on the pristine Ag substrate or the self organized $CeAg_x^{so}$ film the diffraction pattern slightly changes as shown in figure 6.1 d). The main pattern is still similar to the thinner layer thicknesses forming a sixfold symmetric $(1.91\,x\,1.91)R30°$ reconstruction with a nearest neighbour distance of $a_{NN}^{120s} = (5.605 \pm 0.095)\,Å$ and a lattice plane distance of $d_{hkl}^{60s} = (4.580 \pm 0.054)\,Å$, as compared to the Ag substrate. However the satellite spots vanish at this film thickness. The primitive unit cell is marked in red.

In general all three $CeAg_x$ diffraction patterns in figure 6.1 b) – d) show a slightly compresses $(2\,x\,2)$ reconstruction that is rotated by 30° with respect to the Ag(111) pattern as shown in a). However the thin layer thicknesses in b) and c) exhibit additional satellite spots, mainly visible around the main spots, that are again oriented along the Ag(111) substrate. This behaviour is very similar to the thin layer thicknesses of $CePt_5$/Pt(111) as described in subsection 4.1.1. At a layer thickness of 3 u.c. this intermetallic forms a compressed $(2\,x\,2)R30°$ reconstruction with additional non-rotated satellite spots that vanish at a layer thickness of 4 u.c., where only a compressed $(2\,x\,2)R30°$ reconstruction is observed (see subsection 4.1.1 and figure 4.2 d) and e)). In $CePt_5$ the satellite spots are the result of a long range moiré pattern, that develops from periodic height modulations in the $CePt_5$ surface alloy [27]. Since the nearest neighbour distance of Pt and Ag atoms in the respective (111) direction differs only by 0.11 Å, which is $\approx 4\,\%$, it is likely that the same mechanism also leads to the formation of a moiré pattern in $CeAg_x^{60s}$, resulting in the satellite spots observed in the diffraction patterns in figure 6.1 b) and d).

Both diffraction patterns of $CeAg_x^{60s}$ and $CeAg_x^{120s}$ have been observed in literature [28, 144]. For $CeAg_x^{60s}$ a reconstruction of $(1.1\sqrt{3}\,x\,1.1\sqrt{3})R30° + (3\sqrt{3}\,x\,3\sqrt{3})R30° = (1.91\,x\,1.91)R30° + (5.2\,x\,5.2)R30°$ satellites is estimated in [144]. Note that the satellite reconstruction in [144] is given with respect to the $CeAg_x$ main spots. Taking into account the factor of 1.91 of the $CeAg_x$ reconstruction this amounts to a $(9.92\,x\,9.92)$ periodicity with respect to the Ag(111) substrate. Considering that the satellite spots are very weak and an exact determination of their position is difficult this is in fairly good agree-

ment with the (10.65 x 10.65) reconstruction estimated in this work.
Schwab et al. determine a $(2\,\mathrm{x}\,2)R30°$ reconstruction without satellite spots for 2 monolayers of $CeAg_x$/Ag(111). This as well is in good agreement with the slightly compressed $(2\,\mathrm{x}\,2)R30°$ reconstruction observed in this work for $CeAg_x^{120s}$.
There are several binary Ce – Ag compounds listed in literature [142]. Of the truly hexagonal ones $CeAg_3$ with lattice constants of $a = b = 6.56$ Å and $c = 4.898$Å is a possible candidate for the observed surface reconstructions, since $c(CeAg_3)$ and $d_{hkl}(CeAg_x) = (4.580 \pm 0.054)$ Å are similar [142]. However, the Ag(111) substrate still has strong influence on the lattice parameters of the $CeAg_x$ thin film. Therefore a comparison with relaxed bulk values for $CeAg_3$ can only be a first estimation.
The self organized phase of figure 6.1 b) has not been reported in literature. However, it is known that Ce atoms might diffuse up to 150 Å deep into the bulk of the substrate upon annealing [152]. Therefore, evaporated Ce might diffuse into the bulk of the Ag crystal and resurface by the sputtering and annealing cycle, employed to remove aged $CeAg_x$ films. Since the electronic structure of $CeAg_x^{so}$ and $CeAg_x^{60s}$ does not differ (not shown) it will not be treated seperatly in the following sections, but only the electronic structure of $CeAg_x^{60s}$ and $CeAg_x^{120s}$ will be discussed.

Another way to influence the electronic structure of $CeAg_x$ pursued during the course of this work, was to add small amounts of Bi to the $CeAg_x$ surface alloy. To produce the Bi:$CeAg_x$ surface alloy, first Ce is evaporated for $t_e = 120$ s onto the clean Ag(111) substrate. During the annealing process of the $CeAg_x$ film at $T_{CeAg_x} = 600$ °C, Bi is evaporated on the sample for $t_e = 4$ min 10 s. This amount of Bi corresponds to 1/3 of a monolayer of Bi on Ag(111), forming the characteristic $BiAg_2$/Ag(111) surface alloy, with a reconstruction of $(\sqrt{3}\,\mathrm{x}\,\sqrt{3})R30°$, a well known Rashba – system [69]. After the Bi deposition, the alloying process is continued for 5 min at $T_{CeAg_x} = 600$ °C. This results in a reproducible surface reconstruction as shown in figure 6.2 c). For better comparability with the Ag(111) substrate as well as the bare $CeAg_x^{120s}$ film, their respective diffraction patterns are shown again in a) and

b), all recorded at an electron beam energy of $E_0 = 48\,\text{eV}$. Figure 6.2 d) shows the diffraction pattern of the Bi:CeAg$_x^{120s}$ surface alloy recorded at a lower energy of $E_0 = 28\,\text{eV}$ for better distinguishability of the lower order diffraction spots. Characteristic reflexes are highlighted by coloured circles and the primitive surface unit cells are marked by dashed lines respectively.

As discussed above, the CeAg$_x^{120s}$ surface alloy is characterized by a hexagonal $(1.91\,\text{x}\,1.91)R30°$ reconstruction with sixfold rotational symmetry. Part of the characteristic diffraction spots are highlighted with red circles and the respective primitive unit cell is marked by dashed red lines.

The Bi:CeAg$_x^{120s}$ surface alloy exhibits additional diffraction spots emphasized by yellow circles in figure 6.2 c) and d). They amount to a $(3.8\,\text{x}\,3.8)$ reconstruction with respect to the Ag(111) substrate which corresponds to a $(1.99\,\text{x}\,1.99)R30°$ reconstruction with respect to the CeAg$_x$ pattern. Accordingly the second and fourth order diffraction spots of Bi:CeAg$_x^{120s}$ coincide accuratly with the first and second order of CeAg$_x$. This is marked by half red and yellow circles in figure 6.2 c) and d). The nearest neighbour distance estimated on the basis of the additional $(3.8\,\text{x}\,3.8)$ reconstruction, observed for Bi:CeAg$_x^{120s}$, is $a_{NN}(\text{Bi:CeAg}_x^{120s}) = (11.15 \pm 0.19)\,\text{Å}$ with respect to the Ag(111) substrate.

The XPS spectra of Ce and Bi core levels presented in subsection 6.2.2 suggest a Ce and Bi rich surface. The low amount of Bi of about 1/3 of a monolayer on Ag(111), however, allows no meaningful comparison of the estimated Bi:CeAg$_x^{120s}$ lattice parameters with binary Ce – Bi bulk compounds. Nevertheless, it should be mentioned that there are two Ce – Bi compounds that exhibit a hexagonal or pseudo hexagonal lattice structure [142]. This is the hexagonal Ce_5Bi_3, which decomposes into Ce_2Bi and Ce_4Bi_3 layers with lattice constants of $a = b = 9.527\,\text{Å}$ and $c = 6{,}488\,\text{Å}$ and CeBi, that crystalizes in a NaCl-type *fcc* structure with lattice constants $a = b = c = 4.612\,\text{Å}$, exhibiting hexagonal symmetry along the (111) direction [142].

Concludingly the lattice structure of the surface alloy CeAg$_x$ is influenced both by its film thickness as well as by the adsorption of Bi, as shown by the structural investigation presented above. Thin films of CeAg$_x$/Ag(111)

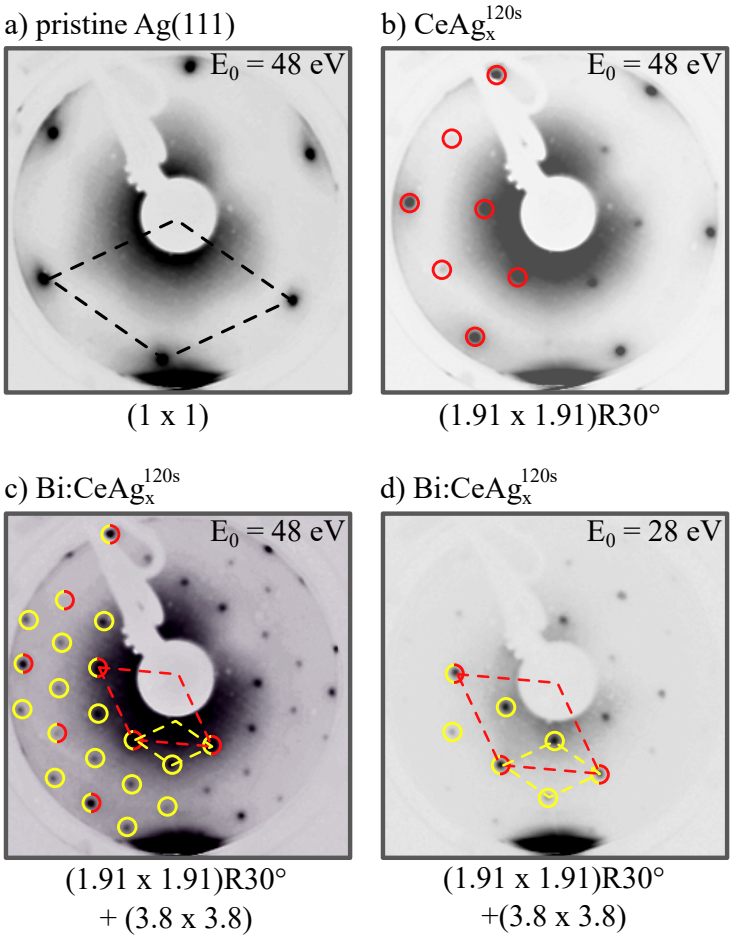

Figure 6.2: Surface reconstruction of Bi:CeAg$_x$/Ag(111). a) and b) show the diffraction pattern of pristine Ag(111) and CeAg$_x^{120s}$ at $E_0 = 48$ eV. c) and d) depict the surface reconstruction of Bi:CeAg$_x^{120s}$ at $E_0 = 48$ eV and $E_0 = 28$ eV respectively. Characteristic diffraction spots are marked with coloured circles and the respective primitive surface unit cells are shown in dashed lines.

exhibit a compressed $(2\,\mathrm{x}\,2)R30°$ diffraction pattern with respect to the Ag $(1\,\mathrm{x}\,1)$ surface. At very low initial Ce coverages this main pattern is accompanied by satellite spots of a $(10.68\,\mathrm{x}\,10.68)$ periodicity. Similar to thin films of $CePt_5$/Pt(111) these might arise from a long range morié pattern resulting from different Ce adsorption sites on the Ag(111) substrate.
Adding small amounts of Bi to the $CeAg_x^{120s}$ surface alloy results in a $(3.8\,\mathrm{x}\,3.8)$ reconstruction with respect to the Ag $(1\,\mathrm{x}\,1)$ substrate. In the following subsections it will be discussed to what extend these structural chances or the adsorption of Bi influence the electronic structure of $CeAg_x$/Ag(111).

6.2 Electronic structure of $CeAg_x$/Ag(111)

6.2.1 Layer thickness dependence

An impression of the core level electronic structure of the $CeAg_x$ alloys prepared by different Ce evaporation times of $t_e = 60\,\mathrm{s}$ and $t_e = 120\,\mathrm{s}$ is given in figure 6.3. An exemplary overview spectrum recorded on $CeAg_x^{120s}$ at $T_s = 11\,\mathrm{K}$ and normal emission with a resolution of $\Delta\mathrm{E} = 750\,\mathrm{meV}$ is shown in a). All expected core levels are present and no contaminations with carbon or oxygen are visible. Figure 6.3 b) shows a detailed spectrum of the Ce $3d$ core levels of both layer thicknesses and for emission angels of 0° and 60°. As discussed in section 2.1.2 the low energy Kondo physics in the valence band is reflected in the core level structure leading to a splitting of each Ce $3d$ spin-orbit channel into three final state components. This, however, is not observed in figure 6.3 b). Neither $CeAg_x^{120s}$ (black line) nor $CeAg_x^{60s}$ (blue line) show a multiplet structure as observed in section 5 for $CePt_5$/Pt(111). The visible peaks at $E_{bin} = 885\,\mathrm{eV}$ and $E_{bin} = 905\,\mathrm{eV}$, therefore, point towards an f^1 dominated initial configuration of the f level. At both emission angles one observes less total Ce $3d$ intensity for $CeAg_x^{60s}$ as compared to $CeAg_x^{120s}$. However, both layer thicknesses show a depletion of Ce at the surface indi-

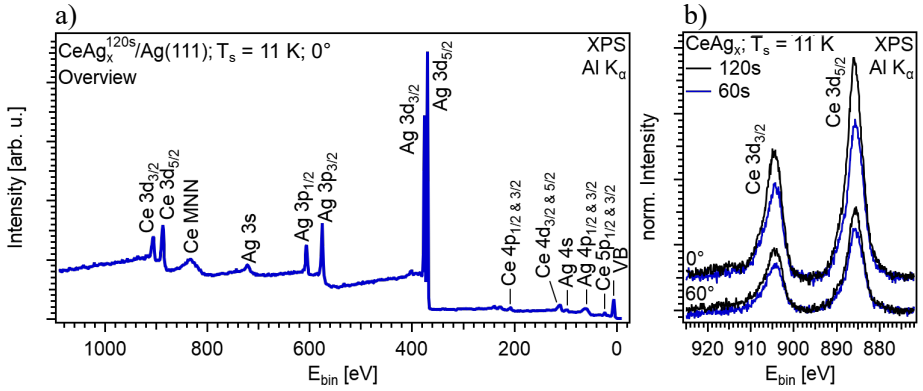

Figure 6.3: Core level electronic structure of CeAg$_x^{120s}$ and CeAg$_x^{60s}$. a) exemplarily shows and overview spectrum of CeAg$_x^{120s}$ recorded at at $T_s = 11\,\mathrm{K}$ and normal emission with a resolution of $\Delta\mathrm{E} = 750\,\mathrm{meV}$. The Ce $3d$ core levels for normal emission (0°) and 60° off normal emission are shown in more detail in b). The black spectrum corresponds to CeAg$_x^{120s}$ and the blue spectrum to CeAg$_x^{60s}$. No final state multiplet structure is visible in either CeAg$_x$ layer thickness.

cated by the loss of total intensity in the 60° spectra.

Figures 6.4 and 6.5 depict the valence band structure of both layer thicknesses of CeAg$_x$/Ag(111). The left column of figure 6.4 shows the Fermi surface as well as selected constant energy cuts at increasing binding energies of CeAg$_x^{120s}$ in a) – d). The right column depicts the respective constant energy cuts for CeAg$_x^{60s}$ in a$_\mathrm{i}$) – d$_\mathrm{i}$). Figure 6.5 shows the electronic structure along the high-symmetry directions $\overline{\Gamma\mathrm{K}}$ and $\overline{\Gamma\mathrm{M}}$ for CeAg$_x^{120s}$ in a) and a$_\mathrm{i}$) and CeAg$_x^{60s}$ in b) and b$_\mathrm{i}$). All ARPES spectra have been recorded at $T_s = 20\,\mathrm{K}$ with an excitation energy of $\mathrm{h}\nu(\mathrm{He\ I}_\alpha) = 21.22\,\mathrm{eV}$ and an energy resolution of $\Delta\mathrm{E} = 7.97\,\mathrm{meV}$. The momentum distribution maps have been recorded on differently mounted samples, therefore the constant energy cuts of CeAg$_x^{120s}$ in figure 6.4 a) – d) are rotated by 15° to allow for a better comparability of the band dispersion between the two surface alloys.

The Fermi surfaces of both film thicknesses, as shown in figures 6.4 a) and a$_\mathrm{i}$), reflect the hexagonal symmetry of the lattice structure and show a highly anisotropic bandstructure along the two high-symmetry directions.

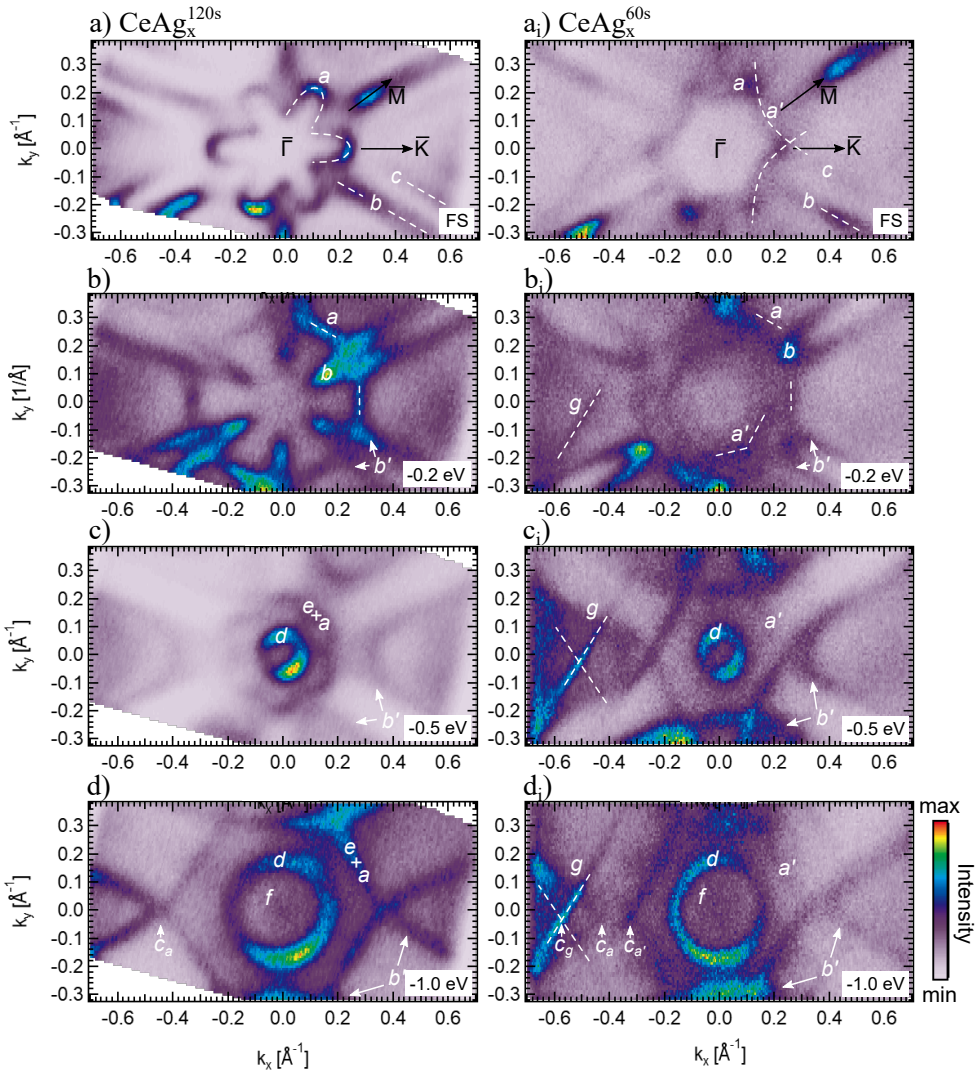

Figure 6.4: Constant Energy cuts of CeAg$_x^{120s}$ and CeAg$_x^{60s}$. a) – d) and a$_i$) – d$_i$) show the Fermi surface as well as selected constant energy cuts at increasing binding energies for CeAg$_x^{120s}$ and CeAg$_x^{60s}$. All spectra have been recorded at $T_s = 20\,\mathrm{K}$ with hν(He I$_\alpha$) = 21.22 eV and $\Delta E = 7.97\,\mathrm{meV}$. The momentum maps of CeAg$_x^{120s}$ in a) – d) are rotated by $\approx 15°$. The high-symmetry points and directions are marked in black, whereas interesting features in the bandstructure are labeled by white letters and dashed lines.

$CeAg_x^{120s}$ is characterized by a flower-like structure *a* around the $\overline{\Gamma}$-point with flower petals aligned along the $\overline{\Gamma K}$-direction. The flower shape is the constant energy contour of the weakly dispersing band *a* as marked in figure 6.5 a) and a_i). It crosses the Fermi level at $\boldsymbol{k}_{||} = \pm 0.25\,\text{Å}$ and $\boldsymbol{k}_{||} = \pm 0.125\,\text{Å}$ in $\overline{\Gamma K}$- and $\overline{\Gamma M}$-direction respectively. Additional stripe-like features *b* and *c* are visible along the $\overline{\Gamma M}$-direction or parallel to it. Feature *b* results from three electron-like parabolic bands that cross the Fermi level at increasing $\boldsymbol{k}_{||}$-values as visible in figure 6.5 a_i).
Towards higher binding energies, band *a* assumes larger $\boldsymbol{k}_{||}$-values as indicated by dashed lines in figure 6.4 b). The stripe like features *b* move towards $\overline{\Gamma}$, as the minimum of the three parabolas is approached. Next to the $\overline{\Gamma M}$-direction two new features *b'* appear, that form a wedge-like structure at $E - E_F = -0.2\,\text{eV}$ and split up further towards higher binding energies. At $E - E_F = -0.5\,\text{eV}$ two additional structures emerge in the center of the surface Brillouine zone. With a radius of $\boldsymbol{k}_x = \boldsymbol{k}_y = 0.07\,\text{Å}^{-1}$, the hole-like parabolic band *d* forms a circular structure around the $\overline{\Gamma}$-point. At larger $\boldsymbol{k}_{||}$-values a hexagonal contour is visible which is a result of band *a* in $\overline{\Gamma M}$-direction but also of a hole-like band *e* in $\overline{\Gamma K}$-direction as visible in figure 6.5 a). The corners of the hexagon are oriented along $\overline{\Gamma M}$-direction whereas the edges are visible along $\overline{\Gamma K}$.
At larger binding energies of $E - E_F = -1.0\,\text{eV}$ in figure 6.4 d), the diameter of structure *d* increases and an additional intensity *f* becomes apparent at the $\overline{\Gamma}$-point. The hexagonal structure $e + a$ persists at higher binding energies. However, at $E - E_F \leqq -1.0\,\text{eV}$ band *e* crosses band *a* in $\overline{\Gamma K}$-direction, leading to a change of the orientation of the hexagon, with corners now along $\overline{\Gamma K}$- and edges along $\overline{\Gamma M}$-direction.

The overall hexagonal symmetry is observed as well in the bandstructure of $CeAg_x^{60s}$ in figure 6.4 $a_i) - d_i)$. However the flower-like structure *a* seems strongly hexagonally deformed as indicated by the dashed white lines in figure 6.4 a_i). The reason is an additional band *a'* that crosses the Fermi level at slightly smaller $|\boldsymbol{k}_{||}|$-values as compared to band *a*. This is visible in the bandstructure along $\overline{\Gamma K}$-direction in figure 6.5 b) where both bands *a* and *a'* are distinguishable. The flower-like character of band *a* is partly conserved

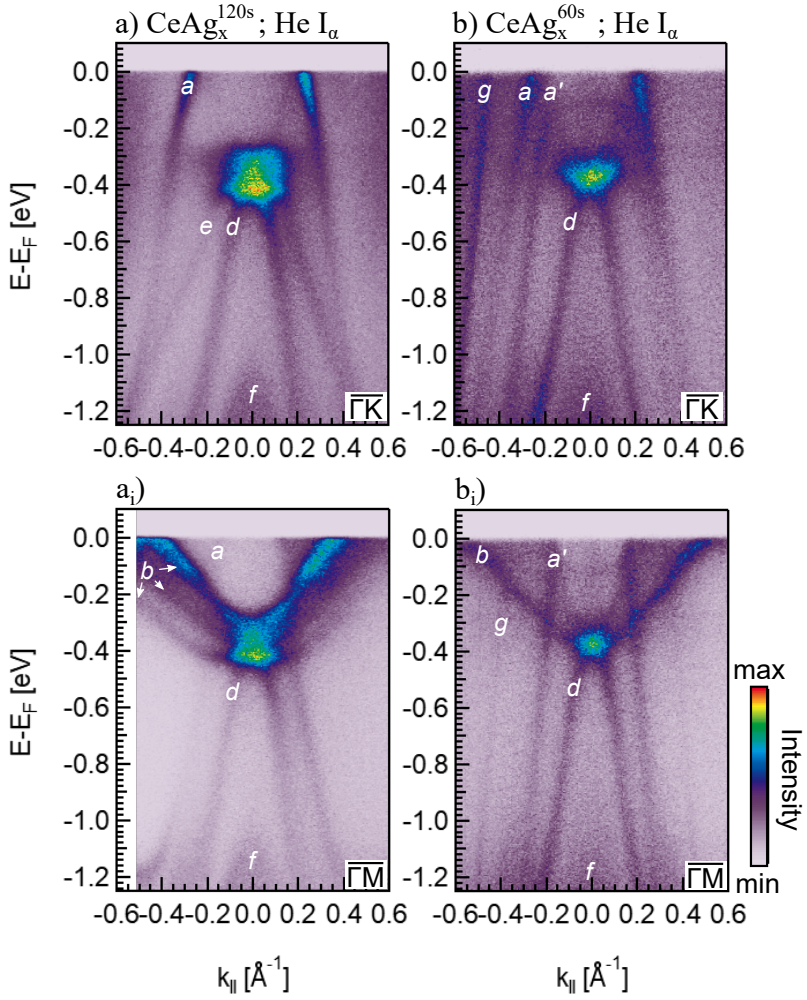

Figure 6.5: Bandstructure of CeAg$_x^{120s}$ and CeAg$_x^{60s}$. a) and a$_i$) show the bandstructure of CeAg$_x^{120s}$ along $\overline{\Gamma K}$- and $\overline{\Gamma M}$-direction, whereas b) and b$_i$) show the same for CeAg$_x^{60s}$. All spectra are recorded at $T_s = 20\,\mathrm{K}$ with with hν(He I$_\alpha$) = 21.22 eV and $\Delta E = 7.97\,\mathrm{meV}$. Characteristic bands are marked with letters $a - g$.

in $\overline{\Gamma K}$-direction where the intensity of structure *a'* is enhanced by a superposition with the curves of the flower petals.
Furthermore, the stripe-like features *b* and *c* are present as well for $CeAg_x^{60s}$ as visible in figure 6.4 a_i). Yet, structure *b* crosses the Fermi level at larger $|\boldsymbol{k}_{||}|$-values as compared to $CeAg_x^{120s}$ in a). The bandstructure along $\overline{\Gamma M}$-direction in figure 6.5 b_i) reveals, that structure *b*, consisting of three bands in $CeAg_x^{120s}$, now is the result of only one parabolic band. It crosses the Fermi level at $\boldsymbol{k}_{||} = \pm\, 0.5\,\text{Å}$ and has its minimum at $E - E_F = -0.5\,\text{eV}$. These values coincide with the middle parabola of band *b* in $CeAg_x^{120s}$ as depicted in figure 6.5 a_i).
Towards higher binding energies both structures *a* and *a'* split up leading to an inner hexagon at smaller $|\boldsymbol{k}_{||}|$-values labeled *a'* and an outer structure *a* that is identical with *a* in figure 6.4 b). Band *b* approaches the $\overline{\Gamma}$-point towards increasing binding energies, similar to *b* in $CeAg_x^{120s}$. A wedge-like structure *b'* appears as well at $E - E_F = -0.2\,\text{eV}$ that splits up further towards higher binding energies, as is in good agreement with band *b'* in $CeAg_x^{120s}$.
At $E - E_F = -0.5\,\text{eV}$ the circular contour of band *d* emerges similarly as in $CeAg_x^{120s}$. However, the hexagonal structure $e + a$ is not distinguishable for $CeAg_x^{60s}$. In fact a hexagonal structure is visible for $CeAg_x^{60s}$ in figure 6.4 c_i) but this is the contour of band *a'* as supported by the bandstructure shown in figure 6.5 b) and b_i): Whereas band *d* is clearly visible as the innermost hole-like parabola, the next structure towards larger $|\boldsymbol{k}_{||}|$-values is identified as band *a'*. No additional structure similar to band *e* is visible in $CeAg_x^{60s}$.
At $E - E_F = -1.0\,\text{eV}$ in figure 6.4 d_i) the constant energy contours of bands *d* and *a'* increase towards larger $|\boldsymbol{k}_{||}|$-values and an additional structure *f* emerges at the $\overline{\Gamma}$-point similar to $CeAg_x^{120s}$ in d).
Another feature of $CeAg_x^{60s}$ that has no equivalent in $CeAg_x^{120s}$ is the hexagonal structure *g*. It is best visible at higher binding energies of $E - E_F = -1.0\,\text{eV}$ and $E - E_F = -0.5\,\text{eV}$ but looses intensity on approaching E_F. It is distinguishable as well in the band structure of $CeAg_x^{60s}$ in figure 6.5 b) and b_i) as a weakly dispersing band crossing E_F at $\boldsymbol{k}_{||} = \pm\, 0.45\,\text{Å}$ and $\boldsymbol{k}_{||} = \pm\, 0.35\,\text{Å}$ in $\overline{\Gamma K}$- and $\overline{\Gamma M}$-direction respectively.

To investigate the origin of structures *a'* and *g* in $CeAg_x^{60s}$, figure 6.6 shows the Fermi surface of $CeAg_x^{60s}$ recorded in a larger $|\boldsymbol{k}_y|$-range including the second Brillouin zone as indicated by white dashed lines. Additionally, the Brillouin zone of the Ag(111) substrate as well as the Ag *sp*-bulk band is indicated in solid and dashed black lines respectively [74]. The dashed-dotted black lines are constructed around the adjoining Brillouin zones of $CeAg_x^{60s}$ and represent the backscattering of the Ag *sp*-band. The backscattered Ag *sp*-bulk band as well as the actual band at $\boldsymbol{k}_y \approx 1\,\text{Å}^{-1}$ match very well with band *a'* of $CeAg_x^{60s}$. Furthermore, the splitting of the wedge-like band *b'* towards higher binding energies, as described above, is likely to be caused by the backscattering as well. This is supported by the course of bands at higher binding energies of $E - E_\text{F} = -1.0\,\text{eV}$ in figure 6.4 d_i) where band *b'* merges with band *a'* forming a warped hexagon, similar to the contour of the backscattered Ag *sp*-band. Although similar at first glance, this course of bands can not be transferred easily to the structure of $CeAg_x^{120s}$. As indicated in figure 6.4 d_i) there are three band crossings along $\overline{\Gamma\text{K}}$-direction, highlighted by the three crossing points c_g, c_a and $c_{a'}$. In figure 6.4 d), however, the bandstructure of $CeAg_x^{120s}$ exhibits only one crossing point c_a in $\overline{\Gamma\text{K}}$-direction. This emphasizes again, that there are two distinct bands *a* and *a'* of which only band *a'* can be attributed to a backscattering of the Ag *sp*-bulk band.

Still unclear, however, is the origin of band *g*. Figure 6.6 shows, that it is not caused by the Ag *sp*-band or its backscattering. Also the (10.65 x 10.65) periodicity of the moiré pattern is not suitable for explaining band *g*. A (10.65 x 10.65) reconstruction would result in a ten times smaller Brillouin zone causing a multitude of backscattered *sp*-bands. This is not observed in figures 6.4 or 6.5.

In summary the bandstructure of both layer thicknesses is very complex and highly anisotropic along the two high-symmetry directions. The lower film thickness of $CeAg_x^{60s}$ shows some similarities to the larger layer thickness as for example bands *b*, *d* and *f*, whereas other bands, like *a*, *e*, and the side bands of band *b*, are heavily suppressed. In addition one observes a

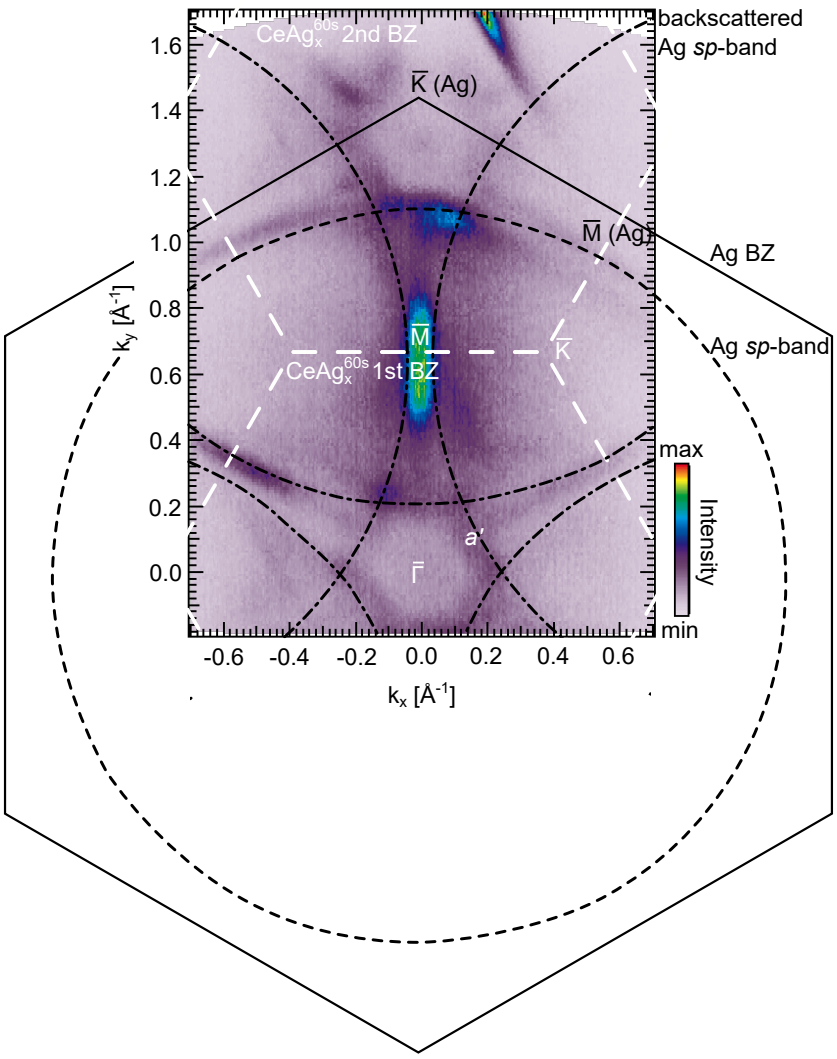

Figure 6.6: Large Fermi surface map of CeAg$_x^{60s}$. Fermi surface map of CeAg$_x^{60s}$ recorded at $T_s = 20\,\mathrm{K}$ with hν(He I$_\alpha$) = 21.22 eV and $\Delta E = 7.97\,\mathrm{meV}$. The first and second Brillouin zones (BZ) of CeAg$_x^{60s}$ are shown in white whereas the Brillouin zone of the Ag(111) substrate is shown in black. The Ag *sp*-bulk band is schematically indicated by dashed black lines, whereas the dashed-dotted black lines correspond to the backscattered Ag *sp*-bulk band. The latter coincides with band *a'* of CeAg$_x^{60s}$.

backscattering of the Ag *sp*-band at the adjoining $CeAg_x^{60s}$ Brillouin zones. This backscattered band causes the warped hexagonal structure *a'* at the Fermi surface of $CeAg_x^{60s}$. Whether these changes in the valence band structure affect the manifestation of Kondo physics in $CeAg_x$ will be discussed in the following part. However, the Ce 3*d* core levels shown in figure 6.3 b) point towards a predominantly f^1-like initial state.

Figure 6.7 shows the bandstructure of both $CeAg_x$ film thicknesses, recorded in a larger binding energy range and with two different excitation energies of $h\nu(\text{He I}_\alpha) = 21.22\,\text{eV}$ in a) and a_i) and $h\nu(\text{He II}_\alpha) = 40.81\,\text{eV}$ in b) and b_i). The top row depicts the spectra of $CeAg_x^{120s}$, whereas the bottom row shows the spectra for $CeAg_x^{60s}$. Note that the spectra are recorded at different temperatures. Whereas the bandstructure of $CeAg_x^{120s}$ is shown at $T_s = 7\,\text{K}$ the one of $CeAg_x^{60s}$ was measured at room temperature (RT). Furthermore the spectra are recorded slightly off $\overline{\Gamma\text{K}}$-direction, due to the fixed azimuthal sample orientation. This, however, is tolerated for the sake of better statistics. The intensity of the spectra is normalized at $E - E_\text{F} = -0.8\,\text{eV}$ and $\boldsymbol{k}_{||} = 0\,\text{Å}^{-1}$ where no band is visible in either layer thickness.

First of all the two bands *a'* and *g* are again clearly visible in $CeAg_x^{60s}$ as can be seen in figure 6.7 a_i). However, they are not present in the spectrum recorded with $h\nu(\text{He II}_\alpha)$ in b_i). The increased signal to noise ratio in these spectra as opposed to the momentum maps in figure 6.4 reveals, that the hole-like band *e* is present as well in $CeAg_x^{60s}$, with its maximum at $E - E_\text{F} = -0.25\,\text{eV}$. At $E - E_\text{F} = -0.7\,\text{eV}$ it intersects with the backscattered *sp*-band *a'*. It is still distinguishable when excited with $h\nu(\text{He II}_\alpha)$ in figure 6.7 b_i), similar to $CeAg_x^{120s}$ in b).

For both layer thicknesses the spectra shown in figure 6.7 reveal, that band *d* splits up at higher binding energies in *d* and *d'* and the contour of the hole-like band *f* is now clearly visible.

In addition the bandstructure of $CeAg_x^{120s}$ shows two intensities *h* at the Fermi level at high $|\boldsymbol{k}_{||}|$-values for both excitation energies in figure 6.7 a) and b). These features are not visible for $CeAg_x^{60s}$. When changing the excitation energy from He I_α to He II_α most bands remain visible, except band

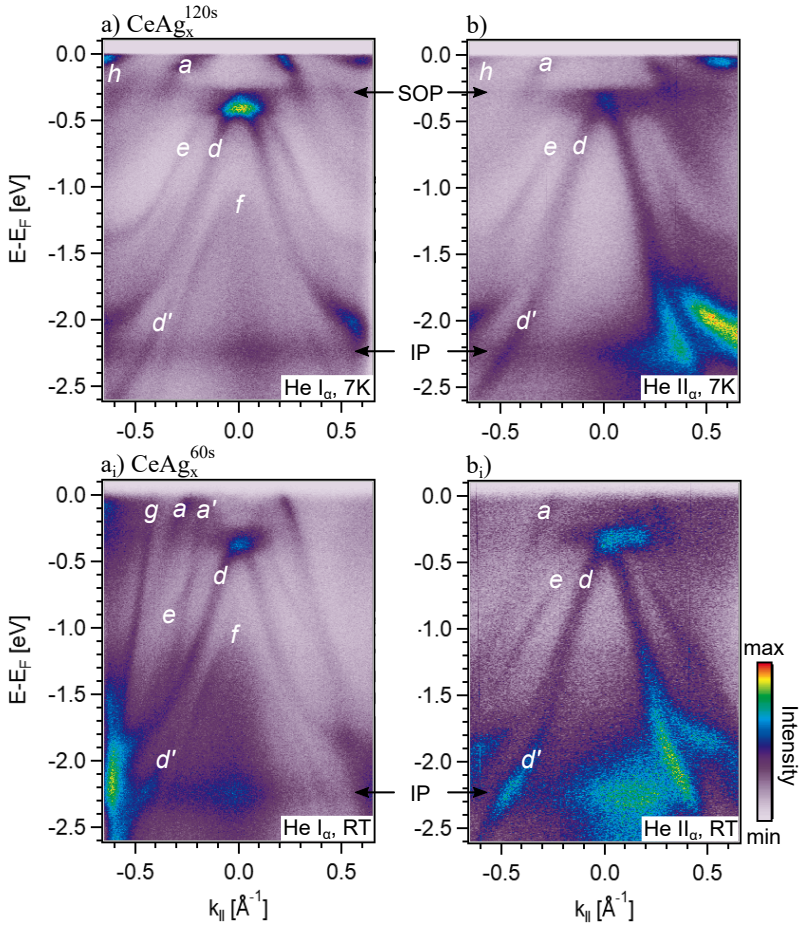

Figure 6.7: Excitation energy dependent bandstructure of CeAg$_x^{120s}$ and CeAg$_x^{60s}$. a) and b) show the electronic structure of CeAg$_x^{120s}$ with hν(He I$_\alpha$) = 21.22 eV and hν(He II$_\alpha$) = 40.81 eV recorded at $T_s = 5$ K with ΔE = 7.97 meV. a$_i$) and b$_i$) show the respective data for CeAg$_x^{60s}$ but recorded at room temperature (RT). All spectra are normalized in intensity at $E - E_F = -0.8$ eV and $\boldsymbol{k}_{||} = 0$ Å^{-1}. The direction of the bandstructre is slightly off $\overline{\Gamma K}$ as predetermined by the fixed azimuthal sample position.

f, which vanishes completely when excited with He II$_\alpha$.
The spectra of CeAg$_x^{120s}$ in figure 6.7 a) and b) exhibit two non-dispersive structures at $E - E_F = -0.275\,\text{eV}$ and $E - E_F = -2.25\,\text{eV}$. The energetic position and the lack of dispersion suggest that these structures are the spin-orbit partner (SOP) of the Kondo resonance and the *f* level ionization peak (IP). Furthermore both structures are enhanced in intensity when increasing the *f* electron cross section by switching from He I$_\alpha$ to He II$_\alpha$. For CeAg$_x^{60s}$, in figure 6.7 b$_i$), only the IP is clearly visible. The SOP at $E - E_F = -0.275\,\text{eV}$ is not discernible amongst the dispersive bands. However, this might be due to the higher sample temperature. Whereas the IP resembles bare photoemission from the *f* level, the SOP is a result from the low energetic Kondo ground state. Whereas photoemission from the *f* level is possible at any temperature, the formation of the Kondo ground state is highly temperature dependent. Therefore, the SOP is only visible in the low temperature spectra of CeAg$_x^{120s}$ in figure 6.7 a) and b).

For a close investigation of the Kondo resonance in both CeAg$_x$ layer thicknesses the bandstructure close to E_F is shown again in figure 6.8 a) and b) for temperatures $T_s \approx 9\,\text{K}$ and $T_s \approx 15\,\text{K}$ respectively. The spectrum of CeAg$_x^{60s}$ in b) thereby exhibits a peculiar structure at small $|\boldsymbol{k}_{||}|$-values that is not visible for CeAg$_x^{120s}$ in a). However, none of the two layer thicknesses shows an increase in intensity at E_F, that is characteristic for the Kondo resonance. The weak, non dispersive feature at $E - E_F = -0.275\,\text{eV}$ is now visible for both CeAg$_x$ films. This is emphasized by figure 6.8 c) where EDCs for both layer thicknesses are shown around $\boldsymbol{k}_{||} = 0\,\text{Å}^{-1}$ (in, bottom part) and around $\boldsymbol{k}_{||} = -0.75\,\text{Å}^{-1}$ (out, top part). The inner EDC of CeAg$_x^{60s}$, depicted in blue, emphasizes again the complex bandstructure of CeAg$_x^{60s}$, close to E_F as opposed to CeAg$_x^{120s}$ shown in black. However, none of the EDCs shows a Kondo resonance tail below E_F. The outer EDCs in the upper part of figure 6.8 c) are taken in a $\boldsymbol{k}_{||}$-range with less bandstructure, except for band *h* of CeAg$_x^{120s}$. They clearly show a peak at $E - E_F = -0.275\,\text{eV}$ for both layer thicknesses, confirming the impression of a non dispersive feature that might be the spin-orbit partner of the Kondo resonance.

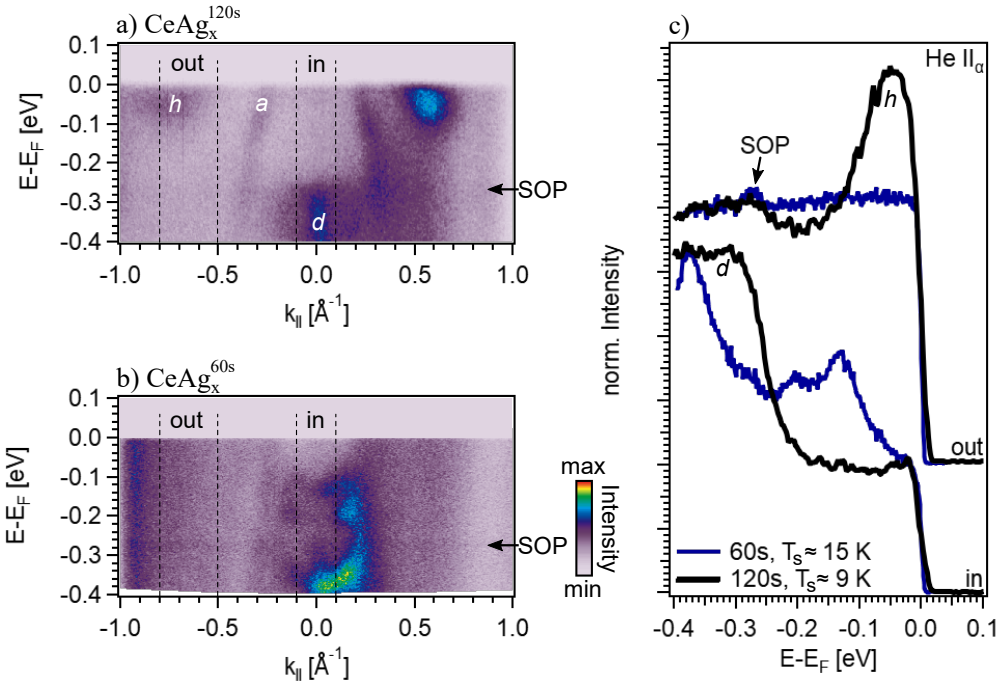

Figure 6.8: Kondo resonance of CeAg$_x^{120s}$ and CeAg$_x^{60s}$. a) and b) show the bandstructure close to E_F for CeAg$_x^{120s}$ and CeAg$_x^{60s}$ respectively, recorded with hν(He II$_\alpha$) and an energy resolution of $\Delta\mathrm{E} = 6.97\,\mathrm{meV}$ at $T_s \approx 9\,\mathrm{K}$ and $T_s \approx 15\,\mathrm{K}$. c) shows EDCs for CeAg$_x^{120s}$ in black and CeAg$_x^{60s}$ in blue around $\boldsymbol{k}_{||} = 0\,\mathrm{Å}^{-1}$ (in, bottom part) and $\boldsymbol{k}_{||} = -0.75\,\mathrm{Å}^{-1}$ (out, top part).

In summary this part shows that it is possible to grow ordered films of $CeAg_x$ on Ag(111) of two different layer thickness. For thin layer thicknesses, represented by $CeAg_x^{60s}$, one observes a compressed $(2\,x\,2)R30°$ reconstruction that is modulated by a long range moiré pattern with a periodicity of $(10.65\,x\,10.65)$ with respect to the Ag(111) substrate. At higher initial Ce coverages in $CeAg_x^{120s}$, the moiré pattern vanishes, resulting in a single diffraction pattern with a compressed $(2\,x\,2)R30°$ reconstruction. The electronic structure as investigated by ARPES and XPS to some extend exhibits a dependency on the varying $CeAg_x$ layer thickness as shown in figures 6.4 – 6.6. In general, the electronic structure of $CeAg_x$ resembles the hexagonal symmetry of the lattice, regardless of the layer thickness, and is highly anisotropic along the two high-symmetry directions $\overline{\Gamma K}$ and $\overline{\Gamma M}$. Whereas the bandstructure of $CeAg_x^{120s}$ has a very high signal to noise ratio and shows no features of the Ag(111) substrate, the electronic structure of $CeAg_x^{60s}$ is less clear. The characteristic features of $CeAg_x^{120s}$, for example the flower-like structure *a* at the Fermi surface and the three parabolic bands *b* along the $\overline{\Gamma M}$-direction, subside and are superimposed by the backscattered Ag(111) *sp*-bulk band.

By increasing the *f* electron cross section it is possible to enhance the signal of the SOP of the Kondo resonance as well as the IP. As discussed in subsection 2.1.2, the spectral feature of the SOP emerges as a result of a Kondo screened state, forming in the $j = \frac{7}{2}$ spin-orbit branch of the Ce $4f$ level. Since the $j = \frac{7}{2}$ state is the first excited state after the $j = \frac{5}{2}$ Kondo ground state, its binding energy is larger than that of the true, $j = \frac{5}{2}$ Kondo resonance. Thus, its spectral feature is located at higher binding energies of $E - E_F = -0.275\,\text{eV}$ and more robust against increasing temperatures. It is therefore possible, that the SOP is detected in the presented spectra taken at $T_s \approx 9 - 15\,\text{K}$, whereas the temperature is too high to resolve the $j = \frac{5}{2}$ Kondo resonance at the Fermi level [48, 54].

Another indication, that the Kondo ground state is not fully separated at temperatures of $T_s \approx 9 - 15\,\text{K}$ is the large spectroscopic weight in the IP at $E - E_F = -2.25\,\text{eV}$. The IP is the spectroscopic representation of a final state

with predominantly f^0 character. It resembles pure photoemission from the atomic like f level with an occupation change from $f^1 \rightarrow f^0$. Large spectroscopic weight in the IP, automatically implies little deviation from the f^1 occupancy in the ground state i.e. weak Kondo coupling.
This impression of $CeAg_x$ being in the weak Kondo coupling regime, is supported by the high energetic spectroscopy of the Ce $3d$ core levels. A strong Kondo coupling of the f level to the surrounding conduction band electrons results in an f^0, f^1 and f^2 multiplet structure of the f level. As discussed in subsection 3.1.3, this f multiplet in the valence band is reflected in the Ce $3d$ core levels, leading to a multiplet splitting of both Ce $3d$ spin-orbit partners as well. This characteristic splitting, as discussed in section 5 for $CePt_5$/Pt(111), is not observed for $CeAg_x$ regardless of the layer thickness. These findings are in good agreement with literature [28, 144]. *Praetorius et al.* study a $CeAg_x$ layer thickness similar to $CeAg_x^{60s}$ with XAS and XMCD and confirm a very small Kondo temperature [144]. *Schwab et al.* investigate a $CeAg_x$ surface alloy resembling $CeAg_x^{120s}$ with on and off resonant photoelectron spectroscopy on the Ce $4d-4f$ resonance. There, also a strong IP and SOP partner, but no Kondo resonance is observed.
Consequently the electronic structure itself can be influenced by the variation of the $CeAg_x$ layer thickness, however, an effect on the Kondo coupling could not be detected on the basis of the presented data.

6.2.2 Bi doped $CeAg_x$/Ag(111)

Another attempt to influence the manifestation of strong correlation in $CeAg_x$ was made by adding Bi to the surface alloy. As described above it was possible to grow an ordered Bi:$CeAg_x^{120s}$ film, resulting in a diffraction pattern of a compressed $(2\,\mathrm{x}\,2)R30°$ reconstruction as observed for pure $CeAg_x^{120s}$ superimposed by additional compressed $(4\,\mathrm{x}\,4)$ diffraction spots as a result of the Bi deposition. Figure 6.9 shows the Ce $3d$ and Bi $4f$ core levels for $CeAg_x^{120s}$ in a) and Bi:$CeAg_x^{120s}$ in b) and c). All spectra are recorded at $T_s = 11\,\mathrm{K}$ and with an energy resolution of $\Delta\mathrm{E} = 750\,\mathrm{meV}$. The black lines

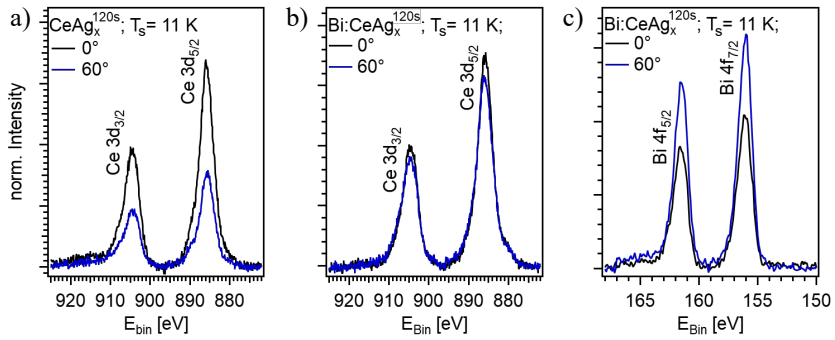

Figure 6.9: Ce 3*d* and Bi 4*f* core levels in CeAg$_x^{120s}$ and Bi:CeAg$_x^{120s}$. a) shows the Ce 3*d* core levels of pure CeAg$_x^{120s}$ at normal emission (0°, black line) and 60° off normal emission (60°, blue line). b) and c) show the Ce 3*d* and Bi 4*f* core levels for Bi:CeAg$_x^{120s}$ again for normal emission (0°, black lines) and 60° off normal emission (60°, blue lines). All spectra are recorded at $T_s = 11\,\mathrm{K}$, with an excitation energy of hν(Al K$_\alpha$) = 1486.6 eV with an energy resolution of $\Delta\mathrm{E} = 750\,\mathrm{meV}$.

correspond to the spectra recorded at normal emission (0°), whereas the blue lines show the data recorded at 60° off normal emission. For pure CeAg$_x^{120s}$, figure 6.9 a) shows a significant decrease in the Ce 3*d* intensity when going from normal emission to 60° off normal emission. When Bi is added to the CeAg$_x^{120s}$ thin film, this decrease of Ce 3*d* intensity is clearly lessened as can be seen in figure 6.9 b). The Bi 4*f* intensity in Bi:CeAg$_x^{120s}$, shown in c), even increases when going from 0° to 60°. This points towards a Ce and Bi rich surface as discussed in subsection 6.1.

However, the addition of Bi to the CeAg$_x$ surface alloy does not lead to a splitting of the Ce 3*d* core levels into the characteristic f^0, f^1 and f^2 final state multiplet as observed for CePt$_5$/Pt(111) in section 5. The observed Ce 3*d* peaks of Bi:CeAg$_x^{120s}$ in figure 6.9 b) represent a predominantly f^1-like initial state of the Ce 4*f* level.

The changes in the valence band structure upon Bi deposition are shown in figure 6.10. Figure 6.10 b) and b$_i$) show the electronic structure of Bi:CeAg$_x^{120s}$ in the high-symmetry directions $\overline{\Gamma\mathrm{K}}$ and $\overline{\Gamma\mathrm{M}}$ compared to the respective

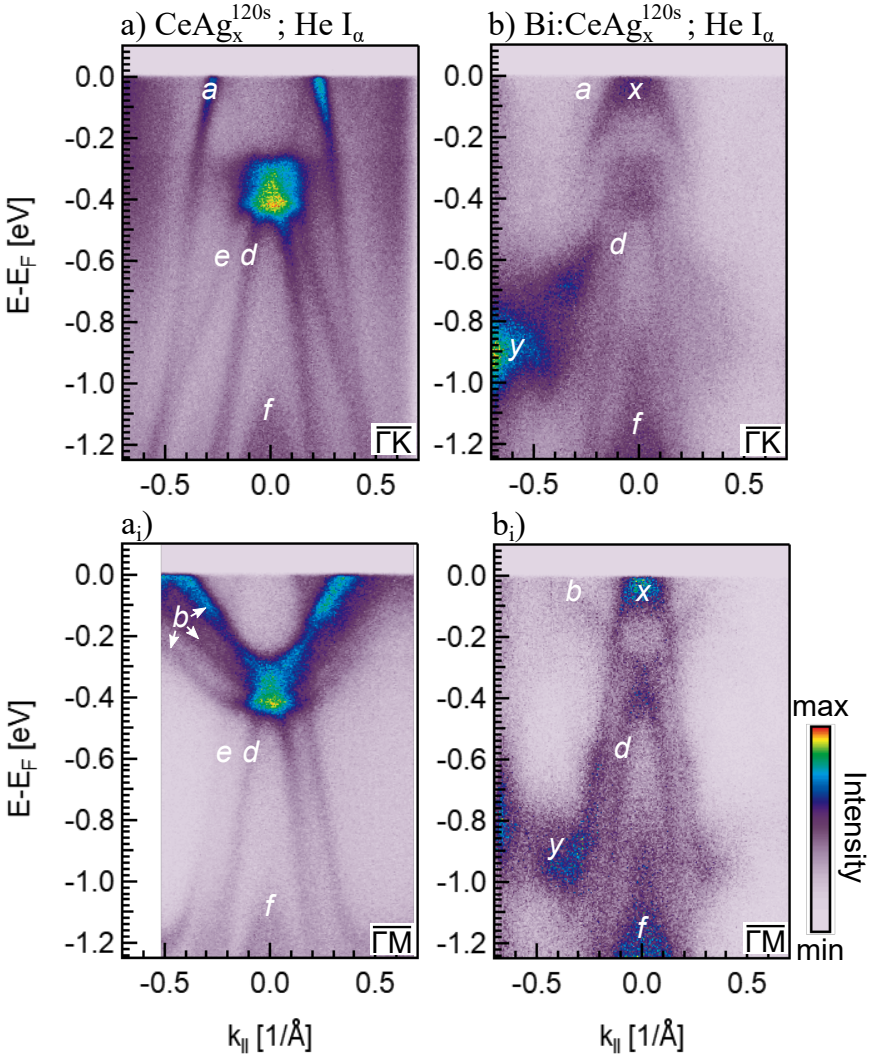

Figure 6.10: Bandstructure of CeAg$_x^{120s}$ and Bi:CeAg$_x^{120s}$. a) and a$_i$) show the bandstructure of CeAg$_x^{120s}$ in $\overline{\Gamma K}$- and $\overline{\Gamma M}$-direction, whereas b) and b$_i$) show the respective spectra of Bi:CeAg$_x^{120s}$. Characteristic features are labeled with letters $a-f$ according to figures 6.4 and 6.5 as well as x and y for Bi:CeAg$_x^{120s}$. All spectra are recorded with hν(He I$_\alpha$) = 21.22 eV with an energy resolution of ΔE = 7.97 meV at T_s = 7 K.

bandstructure of $CeAg_x^{120s}$ in a) and a_i). The spectra have been recorded at $T_s = 7\,\mathrm{K}$ with an energy resolution of $\Delta E = 7.97\,\mathrm{meV}$ and an excitation energy of $h\nu(\mathrm{He\ I}_\alpha) = 21.22\,\mathrm{eV}$. Characteristic bands are labeled according to figure 6.5 with letters *a – f*.

The bandstructure of Bi:$CeAg_x^{120s}$ in b) and b_i) exhibits two distinct differences when compared to $CeAg_x^{120s}$ in a) and a_i). First, Bi:$CeAg_x^{120s}$ shows a strong intensity *x* at the Fermi level around $\boldsymbol{k}_{||} = 0\,\mathrm{Å}^{-1}$. It is observed in both high-symmetry directions at $E - E_F = 0\,\mathrm{eV}$. For higher binding energies it looses intensity in $\overline{\Gamma K}$-direction, but continues in $\overline{\Gamma M}$-direction towards a structure *y*. At *y* the dispersion changes and the structure propagates towards higher $|\boldsymbol{k}_{||}|$-values at a constant energy of $E - E_F = -0.9\,\mathrm{eV}$. In $\overline{\Gamma K}$-direction in figure 6.10 b) this intensity *y* is also observed at $E - E_F = -0.9\,\mathrm{eV}$ and larger $|\boldsymbol{k}_{||}|$, however, a connection between *x* and *y* is not obvious. Furthermore, whereas bands *a*, *b* and *d* seem to be less pronounced in Bi:$CeAg_x^{120s}$, the intensity of structure *f* is enhanced.

Figure 6.11 emphasizes these differences by showing three constant energy cuts for $CeAg_x^{120s}$ in a) – a_{ii}), Bi:$CeAg_x^{120s}$ in b) – b_{ii}) as well as second derivatives of the constant energy cuts of Bi:$CeAg_x^{120s}$ in c) – c_{ii}). All spectra are rotated in the process of data evaluation so that the $\overline{\Gamma M}$-direction is oriented vertically, to ensure better comparability of the visible features. The second derivative is obtained by convoluting the spectrum with the second derivative of a two dimensional Gaussian. This emphasizes areas with strong intensity gradients and is therefore used for tracking the course of bands when the signal to noise ratio is low. The high intensity at the edges of the spectra, hence, is simply caused by the contrast between the data in purple and the background in white. They have no physical meaning.

The Fermi surfaces in figures 6.11 a), b) and c) clearly show, that Bi:$CeAg_x^{120s}$ in contrast to $CeAg_x^{120s}$ has a feature *x* of high intensity at the $\overline{\Gamma}$-point. Band *a*, that causes the flower-like structure in $CeAg_x^{120s}$ is hardly discernible in Bi:$CeAg_x^{120s}$ in b) and c). However, especially the second derivative in c) shows, that band *a* is still present. Also band *b*, that causes the stripe-like structures in the Fermi surface of $CeAg_x^{120s}$ persists in Bi:$CeAg_x^{120s}$.

Towards lower binding energies in figures 6.11 a_i), b_i) and c_i) the detailed

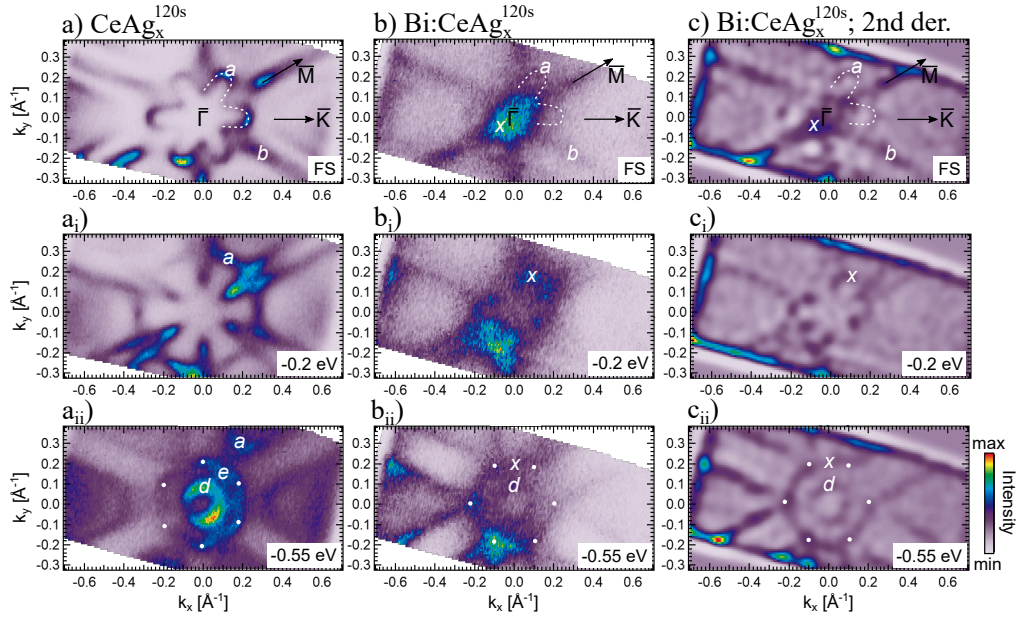

Figure 6.11: Constant energy cuts of CeAg$_x^{120s}$ and Bi:CeAg$_x^{120s}$. a) – a$_{ii}$) and b) – b$_{ii}$) show constant energy cuts of CeAg$_x^{120s}$ and Bi:CeAg$_x^{120s}$ at the Fermi level as well as higher binding energies. c) – c$_{ii}$) depict second derivatives of the constant energy cuts of Bi:CeAg$_x^{120s}$, shown in b) – b$_{ii}$). Characteristic bands are labeled with letters $a - y$ according to figure 6.10.

structure of band x becomes visible. Especially the second derivative in c$_\mathrm{i}$) exposes a flower-like structure of band x with flower petals oriented in $\overline{\Gamma\mathrm{K}}$-direction. Despite the strong similarity this is not caused by band a. Band a runs at larger $|\boldsymbol{k}_{||}|$-values at this binding energy. For example it crosses the $\boldsymbol{k}_y = 0\,\text{Å}^{-1}$-axes at $\boldsymbol{k}_x = \pm\,0.3\,\text{Å}^{-1}$. In contrast the flower petals of band x only at $\boldsymbol{k}_x = \pm\,0.2\,\text{Å}^{-1}$.
At binding energies of $E - E_\mathrm{F} = -0.55\,\mathrm{eV}$ in a$_\mathrm{ii}$), b$_\mathrm{ii}$) and c$_\mathrm{ii}$) finally, the difference between structure e of CeAg$_x^{120\mathrm{s}}$ and x of Bi:CeAg$_x^{120\mathrm{s}}$ is discernible. Whereas the constant energy contour of band e is a hexagon with corners along $\overline{\Gamma\mathrm{M}}$-direction, the contour of band x resembles a hexagon that is rotated by 30° putting the corners along $\overline{\Gamma\mathrm{K}}$-direction. This is illustrated by white dots in the corners of the respective hexagons. The stripe like feature b, however, seems to follow a similar course in Bi:CeAg$_x^{120\mathrm{s}}$ and CeAg$_x^{120\mathrm{s}}$. At the Fermi level its constant energy contours are stripes along the $\overline{\Gamma\mathrm{M}}$-direction, that close in towards $\overline{\Gamma}$ at increasing binding energies.
In summary the addition of Bi causes two new features to appear in the electronic structure of CeAg$_x^{120\mathrm{s}}$. First, at the Fermi level, there is an intensive, electron-like band x at the $\overline{\Gamma}$-point. Second, at $E - E_\mathrm{F} = -0.9\,\mathrm{eV}$ either band x takes a turn towards a flatter dispersion or a new structure y emerges. In any case this intensity y at $E - E_\mathrm{F} = -0.9\,\mathrm{eV}$ and large $|\boldsymbol{k}_{||}|$-values is not observed for pure CeAg$_x^{120\mathrm{s}}$.

Figure 6.12 illustrates the differences between CeAg$_x^{120\mathrm{s}}$ and Bi:CeAg$_x^{120\mathrm{s}}$ when excited with two different photon energies. a) and b) show the bandstructure of CeAg$_x^{120\mathrm{s}}$, roughly along $\overline{\Gamma\mathrm{K}}$ – direction, recorded with hν(He I$_\alpha$) and hν(He II$_\alpha$), respectively. The spectra are taken at $T_s = 7\,\mathrm{K}$ and with $\Delta\mathrm{E} = 7.97\,\mathrm{meV}$. a$_\mathrm{i}$) and b$_\mathrm{i}$) show the equivalent spectra of Bi:CeAg$_x^{120\mathrm{s}}$. Bands a, d, d', e, f and h show the same tendency as described in connection with figure 6.7. That is a decrease of intensity for bands a and f, whereas bands d, d', e and h are not affected by the excitation energy change. The Bi:CeAg$_x^{120\mathrm{s}}$ bands x and y in a$_\mathrm{i}$) and b$_\mathrm{i}$) loose intensity when excited with He II$_\alpha$. Structure y even vanishes completely. However, at larger binding energies of $E - E_\mathrm{F} = -1.35\,\mathrm{eV}$ another band z is observed in figures 6.12 a$_\mathrm{i}$)

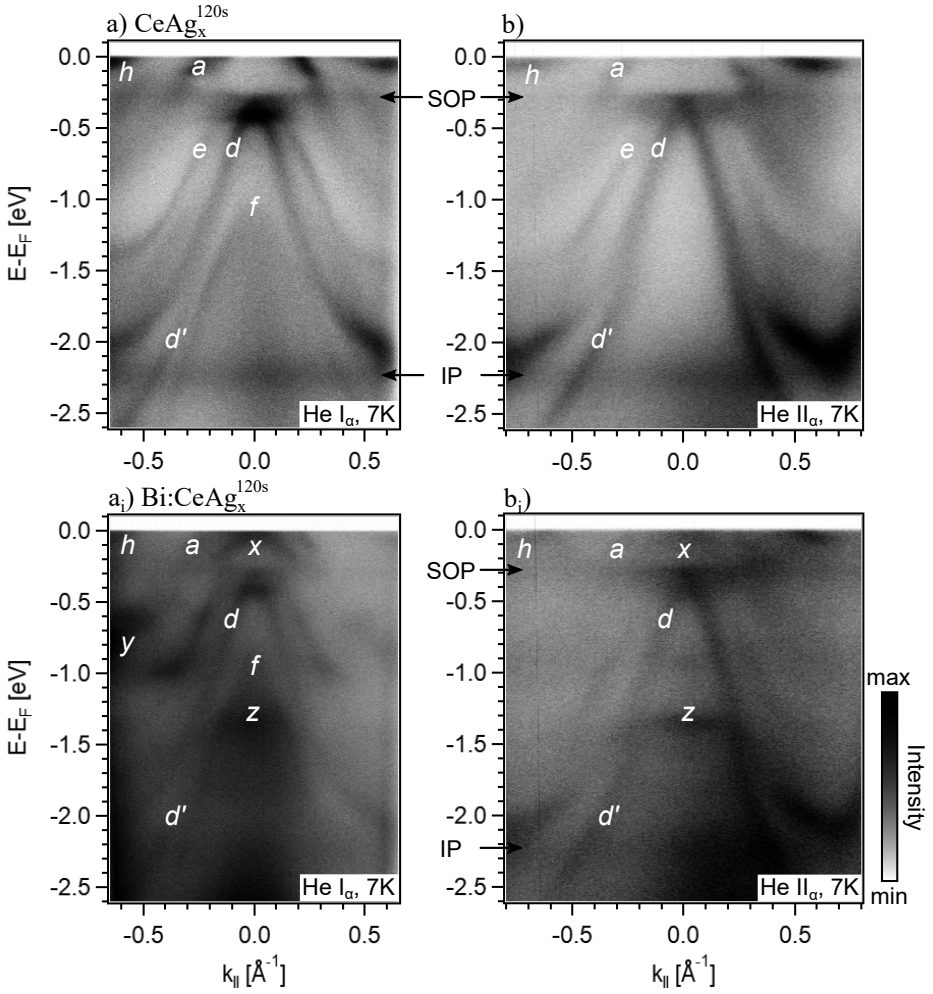

Figure 6.12: Excitation energy dependent bandstructure of $\mathbf{CeAg_x^{120s}}$ and Bi:$\mathbf{CeAg_x^{120s}}$. a) and b) show the bandstructure of $CeAg_x^{120s}$ excited with hν(He I$_\alpha$) = 21.22 eV and hν(He II$_\alpha$) = 40.81 eV. The spectra are recorded at $T_s = 7$ K with an energy resolution of $\Delta E = 7.97$ meV. a$_i$) and b$_i$) show the respective spectra of Bi:$CeAg_x^{120s}$. All spectra are normalized in intensity at $E - E_F = -0.8$ eV and $\boldsymbol{k}_{||} = 0$ Å^{-1}. Characteristic bands are labeled with letters $a - z$.

and b$_\mathrm{i}$) that has no match in CeAg$_x^{120\mathrm{s}}$ in a) and b). Band z superimposes band f and causes the observed increase in intensity of band f in figures 6.10 b) and b$_\mathrm{i}$).
The change of excitation energy to He II$_\alpha$ enhances the f electron cross section and therefore enhances features with predominantly f character in the valence band spectra. In case of CeAg$_x^{120\mathrm{s}}$ this affects in particular the SOP of the Kondo resonance at $E - E_\mathrm{F} = -0.275\,\mathrm{eV}$ and the IP at $E - E_\mathrm{F} = -2.25\,\mathrm{eV}$ that are clearly visible in a) and b). For Bi:CeAg$_x^{120\mathrm{s}}$ those features are hardly discernible in figure 6.12 c) when excited with He I$_\alpha$, but are emphasized by using hν(He II$_\alpha$) in d). However, the Kondo resonance that is expected to cause an increase in intensity at the Fermi level is observed for neither of the two compounds.

The XPS data shown at the beginning of this part, suggest a Ce and Bi rich surface of Bi:CeAg$_x^{120\mathrm{s}}$. This is based on the observation, that the Ce $3d$ intensity decreases significantly less when going from normal emission to the more surface sensitive 60° off normal emission in Bi:CeAg$_x^{120\mathrm{s}}$ as compared to CeAg$_x^{120\mathrm{s}}$ in figures 6.9 b) and a) respectively. Furthermore the Bi $4f$ intensity is larger for the more surface sensitive 60° spectra as seen in figure 6.9 c). Therefore binary Ce – Bi compounds are examined for similarities in the electronic structure.
The analysis of the surface lattice structure of Bi:CeAg$_x^{120\mathrm{s}}$ in connection with figure 6.2 suggests a hexagonal symmetry. The only binary Ce – Bi compound with a hexagonal symmetry is Ce_5Bi_3 [153]. However, there is no electronic structure reported for this compound, known to the author.
Another option would be to consider stoichiometric CeBi. It crystalizes in the *fcc* NaCl-structure and therefore exhibits a hexagonal symmetry along the (111)-direction [154–156]. The bulk bandstructure of CeBi along $\overline{\Gamma\mathrm{X}}$-direction consists of three hole-like bands. The maxima of the two bands at lower binding energies lie in the unoccupied part of the spectrum. Their branches cross the Fermi level at $|\boldsymbol{k}_{||}| = \pm\,0.2\text{Å}^{-1}$ and $|\boldsymbol{k}_{||}| = \pm\,0.35\text{Å}^{-1}$ and flatten towards larger $|\boldsymbol{k}_{||}|$-values at $E - E_\mathrm{F} = -1.6\,\mathrm{eV}$ and $E - E_\mathrm{F} = -0.4\,\mathrm{eV}$ respectively [155]. The third band has its maximum in the occupied part, at

$E - E_\mathrm{F} = -1.6\,\mathrm{eV}$ [155]. Furthermore at $E - E_\mathrm{F} = -2.9\,\mathrm{eV}$ one observes an intense non-dispersive feature over the whole $\boldsymbol{k}_{||}$-range. This is not discussed in [155] but has been identified as the f^0 ionization peak of the Ce $4f$ level in other works [156, 157]. *Kuroda et al.* investigate a substitutional series of CeX, with X being As, Sb or Bi [155]. The electronic structure of all three compounds consists of three hole-like bands $\mathrm{p}_{3/2}$, split into X1 and X2, and $\mathrm{p}_{1/2}$. $\mathrm{p}_{3/2}$ and $\mathrm{p}_{1/2}$ are separated by spin orbit splitting, which increases when going from As to Bi. This drives $\mathrm{p}_{3/2}$ towards the Fermi level and $\mathrm{p}_{1/2}$ down towards higher binding energies. The splitting between the two bands ranges from $\mathrm{SOC} = 0.4\,\mathrm{eV}$ in CeAs to $\mathrm{SOC} = 2\,\mathrm{eV}$ in CeBi. In this work a splitting between band x and z of $\Delta\mathrm{E} \approx 1.35\,\mathrm{eV}$ is observed. However, a clear assignment of bands x and y to $\mathrm{p}_{3/2}$ and z to $\mathrm{p}_{1/2}$ is of course far fetched, since the data presented in [155] correspond to the (001) plane and the bulk electronic structure of CeBi, whereas the data presented in this work show the projected surface band structure. However, bands x, y and z, identified in this work as arising due to the Bi deposition, to some extend resemble the courses of the three parabolas of CeBi as reported in [155]. Furthermore the ionization peak is observed both in literature [155–157] and the presented data in figure 6.12 d), however, with an energy difference of $\Delta\mathrm{E} = 0.65\,\mathrm{eV}$.
In any way, neither the valence band electronic structure nor the Ce $3d$ core levels show any sign of increased c–f hybridization in relation to the Bi deposition in Bi:CeAg$_x^{120\mathrm{s}}$.

Concludingly this section presents a detailed investigation of the lattice and electronic structure of CeAg$_x$. It is possible to grow ordered surface alloys of CeAg$_x$ with different layer thicknesses as well as a Bi doped CeAg$_x$ surface alloy. Whereas changes in the electronic structure related to both varying layer thickness and Bi adsorption are observed, the strength of electronic correlation could not be enhanced with either approach.
Nevertheless, at $E - E_\mathrm{F} = -0.275\,\mathrm{eV}$ the spin-orbit partner of the Kondo resonance is observed for all investigated CeAg$_x$ specimen. This suggests that Kondo coupling in fact defines the low temperature ground state in CeAg$_x$/Ag(111). The pronounced ionization peak at $E - E_\mathrm{F} = -2.25\,\mathrm{eV}$,

however, points towards a small deviation from the f^1-like ground state, i.e. only weak Kondo coupling. Due to the small energy scale of the Kondo screening in $CeAg_x$ the sample temperatures reached in the presented valence band measurements of $T_s = 7\,\mathrm{K}$ might not be low enough to probe the spectroscopic manifestation of the actual Kondo ground state singlet.
XPS spectra of Ce $3d$ core levels are known to serve as a high energy probe for the low energy excitations in the valence band caused by Kondo screening. However, also XPS could not reveal any signs for strong correlation in $CeAg_x$ in the presented spectra.
The cause of the very low correlation energy scale might be the lattice structure of $CeAg_x$. All known Ce – Ag compounds offer at most 12 nearest neighbours to the Ce atoms. This is considerably lower than in $CePt_5$, where there are 18 nearest Pt neighbours to each Ce atom. This reduced number of neighbouring Ag atoms might not exhibit enough orbital overlap to significantly reduce the Ce f level occupation to $n_f < 1$. However, to gain certainty in this line of argument a determination of the exact $CeAg_x$ thin film stoichiometry and bulk lattice structure is necessary.
The same holds true for Bi doped $CeAg_x$. In order to fully understand the changes in the electronic structure it is inevitable to gain more insight into the exact lattice structure and the location of the Bi adsorption sites, by for example scanning tunneling microscopy (STM). Furthermore the proposition of a CeBi-rich surface could be investigated by transmission electron microscopy (TEM).

7

Concluding discussion

The strength of electronic correlation in a given material system eventually comes down to the local environment of the respective lanthanide or actinide. Actively influencing the electronic structure of strongly correlated systems was the main task in this work. On the one hand this was persued by varying the binding partner of the lanthanide from Pt to Ag as well as by Bi doping. On the other hand given a set material composition, the electron-electron correlation was influenced by varying the layer thickness of the surface intermetallic. A change in layer thickness has multiple effects: It might lead to variations in the surface alloy lattice structure that again influence the local environment of the lanthanide. Furthermore by changing the intermetallic film thickness one obtains different relative contributions of the substrate-film interface, intermetallic bulk and surface. The larger the layer thickness, the more dominant are the materials bulk properties, whereas the electronic structure of lower layer thicknesses is dominated by interface and surface effects.

Ce-based materials often serve as prototype Kondo systems, since Ce features exactly one $4f$ electron, rendering the theoretical description rather manageable compared to systems with larger f electron count. Therefore, in this work, epitaxially grown thin films of $CePt_5$/Pt(111) and $CeAg_x$/Ag(111) are

chosen as a basis to unvail the influence of different tuning parameters.
X-ray and angle-resolved photoelectron spectroscopy are able to directly probe the high and low binding energy electronic structure of a system. In particular, PES measures the spectral function including all possible excitations in the system, real and virtual alike. In the low binding energy regime ARPES allows direct access to the low energy excitations in Kondo systems like the Kondo resonance slightly above the Fermi level and its spin-orbit partner at 200 – 300 meV binding energy. XPS on the other hand serves as a high energy probe for these low energy valence band excitations. Due to the Coulomb coupling between the core hole, created in the photoemission process, and the f level, the Ce $3d$ core level spectra exhibit a characteristic final state multiplet, reflecting the different f level occupations f^n (with $n = 0, 1, 2$) in the valence band.
Both energy regimes of PES are used in section 5 to unravel the manifestation of strong correlation in $CePt_5$/Pt(111) and to trace the changes occuring due to different layer thicknesses, interface, bulk and surface contributions as well as temperature. A systematic study of Ce $3d$ core level spectra paints the following picture: In the low layer thickness regime between 1 – 3 u.c. the Pt(111) substrate exercises strong influence on the $CePt_5$ surface alloy. This manifests on the one hand in the $CePt_5$ lattice structure that develops a moiré pattern for 2 and 3 u.c.. On the other hand the f^n final states in the Ce $3d$ spectra reveal a strong $c-f$ hybridization with low f level occupancies of $n_f \approx 0.8$. However, temperature dependent studies of the Ce $3d$ core levels exhibit a change of n_f between $T_s = 150\,\mathrm{K}$ and room temperature, leading to an estimated Kondo temperature $150\,\mathrm{K} < T_\mathrm{K} < 290\,\mathrm{K}$ for 1 – 3 u.c. of $CePt_5$/Pt(111).
For the larger layer thickness regime > 4 u.c. the evaluation of the f^n weights in the Ce $3d$ core levels result in a slightly lower hybridization as well as higher $n_f \approx 0.9$. Still, n_f exhibits no change between $T_s < 10\,\mathrm{K}$ and room temperature. The Kondo temperature in the larger layer thickness regime therefore is higher compared to lower layer thicknesses, with $T_\mathrm{K}(> 4\,\mathrm{u.c.}) \gtrapprox 290\,\mathrm{K}$.
This estimation was eventually confirmed by temperature and layer thickness dependent ARPES studies of the valence band of $CePt_5$/Pt(111). The tem-

perature dependent evolution of the FWHM of the Kondo resonance yields $200\,\mathrm{K} < T_\mathrm{K} < 270\,\mathrm{K}$ for $1-3$ u.c. and $T_\mathrm{K} > 280\,\mathrm{K}$ for > 4 u.c..
The angle dependent core level studies furthermore point towards a higher hybridization and therefore lower n_f at the $CePt_5$ surface as compared to its bulk value for layer thicknesses > 4 u.c.. At first this seems to be in contradiction to literature, that proposes a lower hybridization at the sample surface due to the lack of binding partners. In $CePt_5$, however, the sample surface is known to be Pt terminated [122]. Next to the remarkable inertness of the intermetallic, this excess of Pt atoms at the surface leads to a higher hybridization, comparable to the effects seen at the substrate – thin film interface in the thinner layer thickness regime.
Additionally the determination of n_f by Ce $3d$ XPS core level spectra reveals the importance of taking into account the hybridization Δ as determined by the relative f^2 weight to the spectrum. Neglecting Δ, underestimates the f^0 weight c_0 to the ground state up to 50 %, causing increased values of n_f.
Moreover, it was possible to determine the layer thickness dependent f level – core hole Coulomb attraction $U_{fc} = 12\,\mathrm{eV}$ and the $f-f$ Coulomb repulsion $U_{ff} = 8.5-9.5\,\mathrm{eV}$ by reproducing the Ce $3d$ core level spectra with the Gunnars-son-Schönhammer model for core level spectroscopy. The trends for n_f throughout the increasing layer thicknesses could be confirmed with the GS-model fits as well.

In section 6 the metallic host for the Ce based intermetallic is changed. It was possible to grow ordered thin fims of $CeAg_x$/Ag(111) with two different layer thicknesses and therefore lattice structures, as well as Bi doped $CeAg_x$/Ag(111). For all three compounds the $c-f$ hybridization was found to decrease comapred to $CePt_5$/Pt(111). Neither a Kondo resonance at the Fermi level nor a Ce $3d$ core level final state multiplet was observed for any $CeAg_x$ based compound in the accessible temperature range of $T_s \geqq 7\,\mathrm{K}$. However, all systems show large spectral weight in the spin-orbit partner of the Kondo resonance at $E - E_\mathrm{F} = -0.275\,\mathrm{eV}$ as well as in the ionization peak at $E - E_\mathrm{F} = -2.25\,\mathrm{eV}$.
Although the exact stoichiometry of the $CeAg_x$ thin film is still unknown it

is most likely that the coordination of the Ce ions in $CeAg_x$ is lower as compared to $CePt_5$, leading to less f electron delocalization an therefore $n_f \approx 1$ and very small T_K.
To settle the debate around topological surface states in Kondo insulators it is worth considering the epitaxial growth of Kondo insulating systems. This provides access to the desired high-symmetry directions in which topological surface states are proposed, as well as tuning parameters for influencing the energy scales of electronic correlation and spin-orbit coupling.

In summary the manifestation of strong correlation in Ce-based surface alloys is very sensitive to external parameters like lattice structure, layer thickness and interface, bulk and surface contributions, as well as to the specific binding partner of the Ce ion. X-ray and angle-resolved photoelectron spectroscopy proof as a reliable tool to identify even small changes in the f electron distribution. However, the results obtained from Ce $3d$ core level spectra by XPS and the Kondo resonance by ARPES are highly sensitive to the evaluation procedure. Therefore, the most trustworthy results are shurely obtained by a combination of both, high and low energetic spectroscopies. For the first time XPS was used in a wide parameter range of layer thickness, temperature and surface versus bulk sensitivity, to paint a complete picture of the manifestation of strong correlation in the surface alloy $CePt_5$/Pt(111). It is shown that XPS, by probing the systems final state, is highly sensitive to the f electron count in the valence band. A careful evaluation of the different f^n weights in the Ce $3d$ core level spectra allows for tracking the f level occupation throughout the whole parameter range. Monitoring the change of f^n weight with temperature gives access to the systems Kondo energy scale. This is even possible in a temperature range where the decisive features in the valence band, like the Kondo resonance, already vanish in the temperature broadening of the Fermi level.
These results show, that PES is a powerful technique for the investigation of systems, where the spectral function significantly deviates from the one-particle picture. Only PES can lastly settle the debate around the alleged topological Kondo insulators SmB_6 or $Ce_3Bi_4Pt_3$ or around the proposed transition between the topological Kondo insulating state in $Ce_3Bi_4Pt_3$ to

the Weyl Kondo semimetal $Ce_3Bi_4Pd_3$. This thesis demonstrates how different energy regimes of photoemission spectroscopy allow access to the low energy excitations in strongly correlated material systems, and how the correlation energy scale is driven by a multitude of external parameters.

Appendix

A.1 Experimental setup

Figure A.1 shows the main views of the preparation chamber designed during the course of this work. It is connected to the exisiting chamber via a DN100CF flange (Port 03) and features a DN150CF flange (Port 01) on the opposite side for attaching the manipulator. Ports $02, 05, 07$ and $10-16$ all aim towards the same spot in the middle of the chamber, that serves as the main preparation position. However, ports 02 and 07 are not used at the beginning and serve as view ports. Ports 04 and 09 are reserved for pumping, whereas port 17 is equipped with a needle valve conntected to the Ar gas line for sputtering. Port 08 is equipped with a Bayard-Alpert ion gauge sensitive to preassures between $10^{-4} - 10^{-11}$ mbar. Port 06 is not used at the moment and serves as a view port.
Figure A.2 depicts all port positions and angles in detail, to the aid of future users.
Figure A.3 shows the detailed design of the heating stage attached to the manipulator in the new preparation chamber. It is equipped with a thoriated W-filament of 0.2 mm diameter. The filament is situated inside a Wehnelt-

cylinder that focuses the electron beam, which is again set in a ceramics pod, isolating the filament from the remaining sample stage. The sample stage itself is made by Mo and is electronically isolated from the gold coated stage body via a saphire plate (blue). The heating stage is equipped with two Type-K thermocouples, enabeling temperature measurement on the Cu block (pos. 1) and on the head of the sample holder (pos. 2). Additionally, the sample stage features a contact for a quartz micro balance (pos. 3), that is used for determining evaporation rates.

Figure A.4 illustrates the technical drawings of the new main chamber cryostat head and cooling shield developed in this work. The head is manufactured from oxygen free copper (OFHC). It is fixed onto the cryostat ending by an M6 screw. The sample holder is held by two spring bronze plates as well as two M4 screws, that can be tightened for higher cooling efficiency and lower temperatures. The cooling shield is made from a copper tube and is fixed onto the cryostat end by a copper clamp. It is designed to tightly fit the cryostat head, but must not contact it in any place, to enshure the shielding effect.

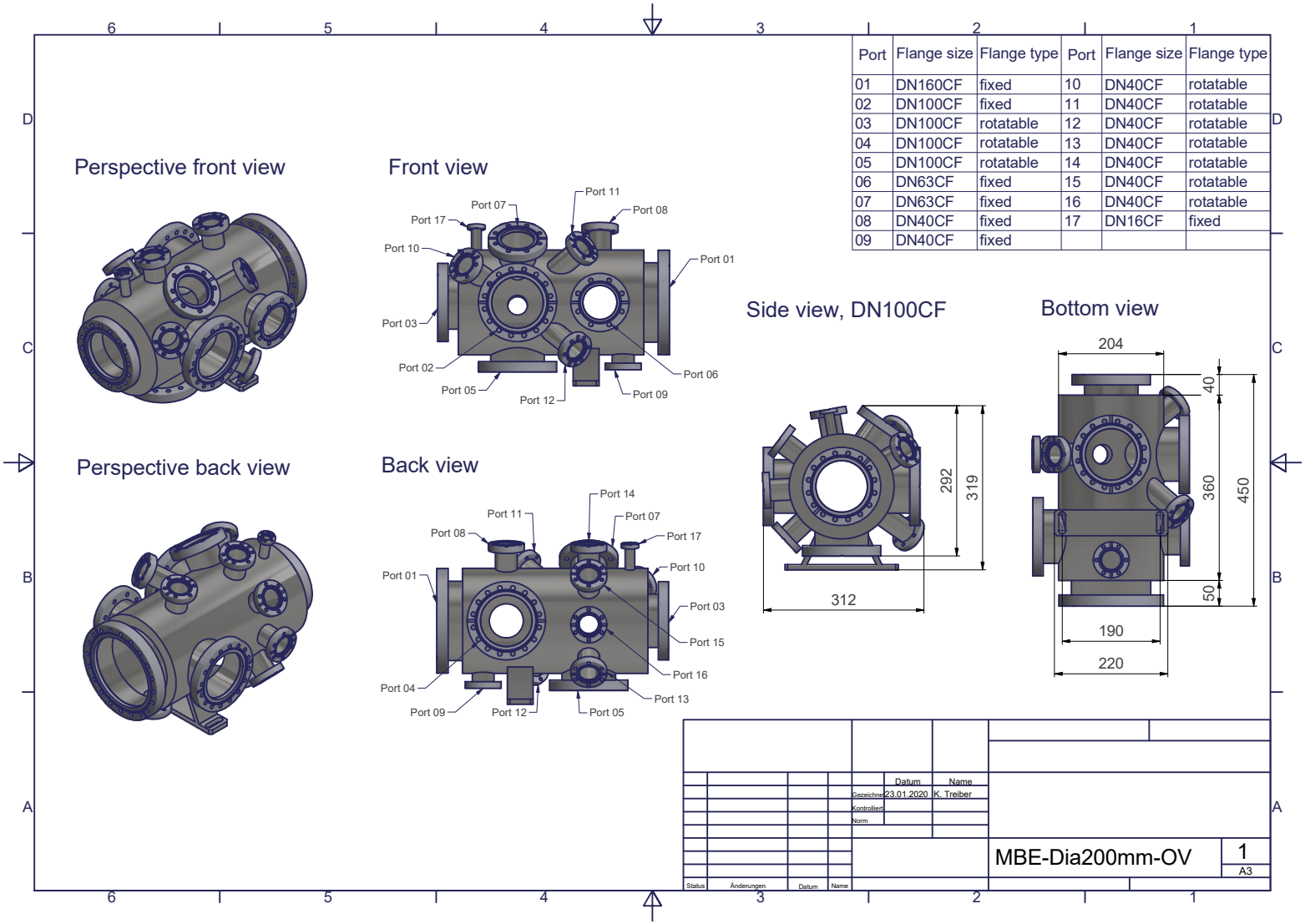

Port	Flange size	Flange type	Port	Flange size	Flange type
01	DN160CF	fixed	10	DN40CF	rotatable
02	DN100CF	fixed	11	DN40CF	rotatable
03	DN100CF	rotatable	12	DN40CF	rotatable
04	DN100CF	rotatable	13	DN40CF	rotatable
05	DN100CF	rotatable	14	DN40CF	rotatable
06	DN63CF	fixed	15	DN40CF	rotatable
07	DN63CF	fixed	16	DN40CF	rotatable
08	DN40CF	fixed	17	DN16CF	fixed
09	DN40CF	fixed			

Figure A.1: Technical drawing of the new preparation chamber – Overview

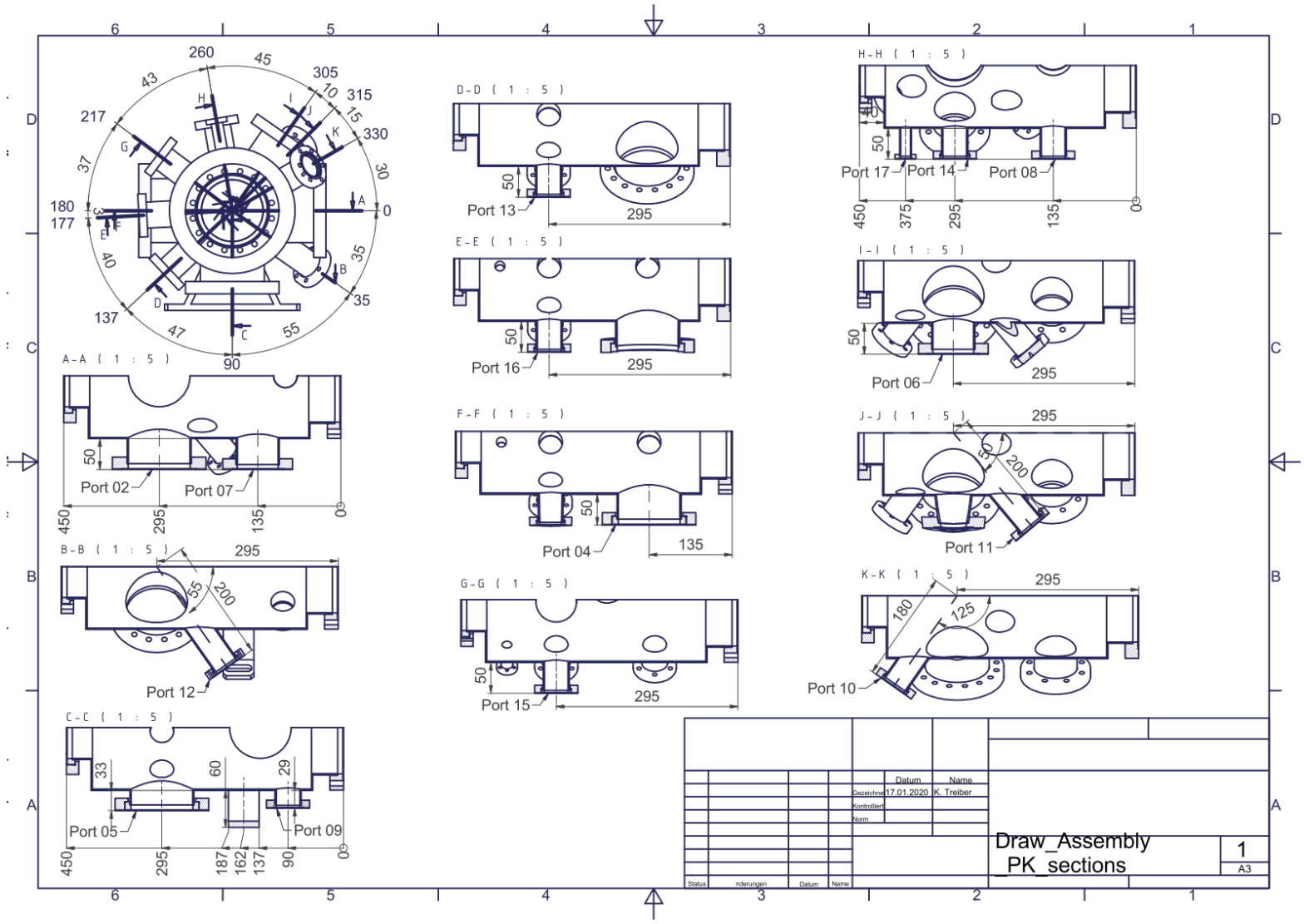

Figure A.2: Sectional views of all ports on the new preparation chamber.

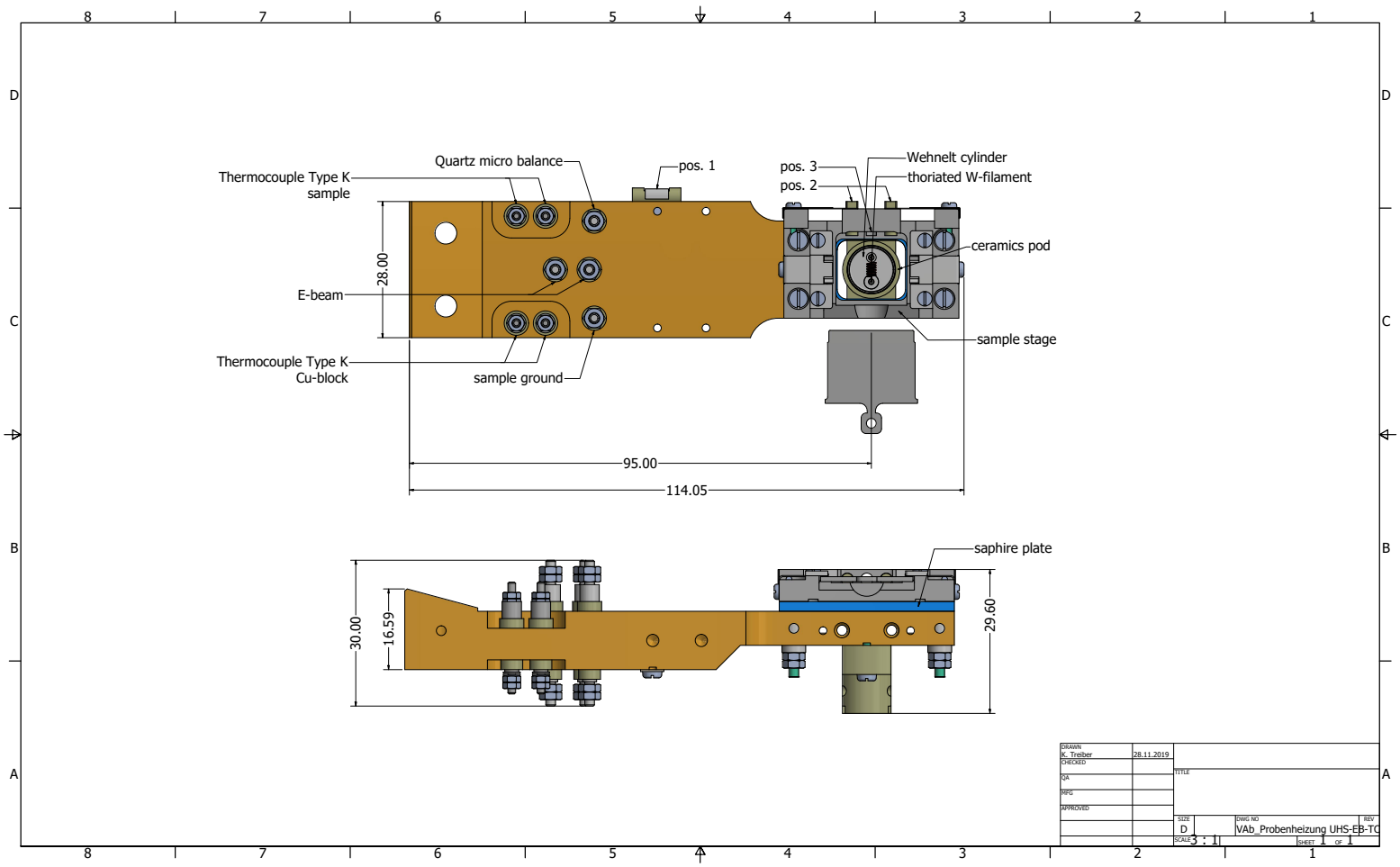

Figure A.3: Preparation chamber heating stage.

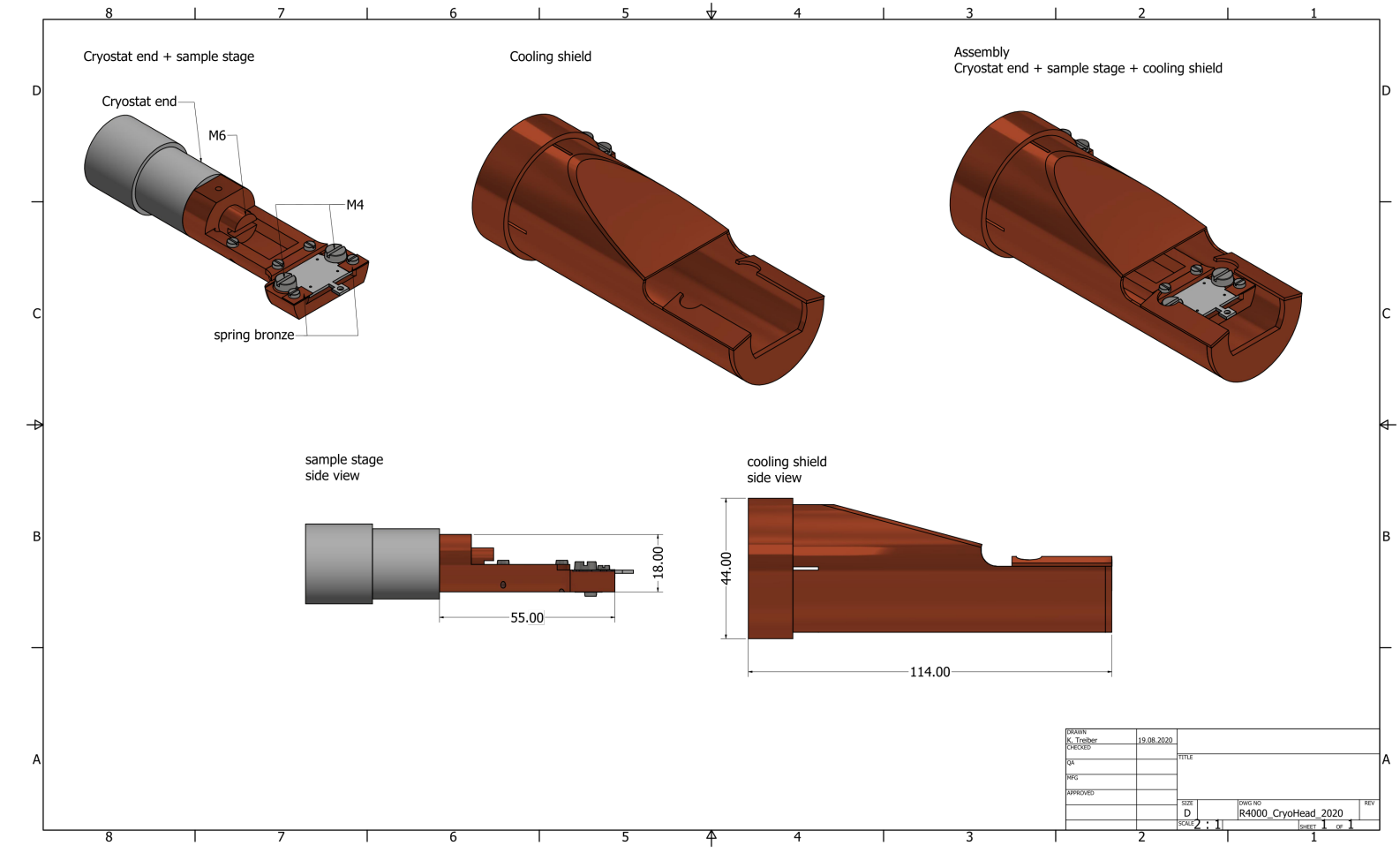

Figure A.4: Cryostat head and cooling shield.

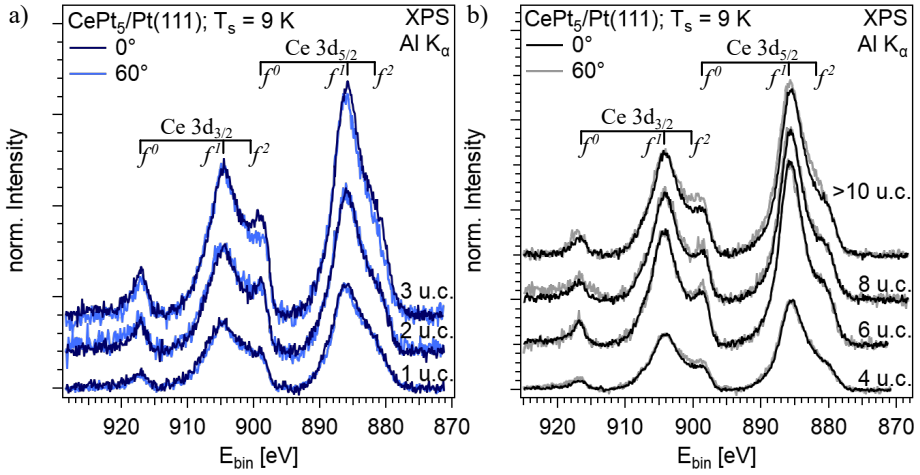

Figure A.5: Emission angle dependence of the Ce 3*d* multiplet structure at $T_s = 9\,\mathrm{K}$.

A.2 Angle-dependent Ce 3*d* multiplet structure in CePt$_5$/Pt(111)

The n_f estimated for different layer thicknesses of $CePt_5$ on Pt(111) as discussed in subsection 5.2 show a characteristic dependence on the emission angle. According to subsection 5.2 at $T_s = 9\,\mathrm{K}$ n_f is higher (lower) for layer thicknesses of $1-3\,$u.c. ($4->10\,$u.c.) for emission angles of 60° as compared to normal emission. At $T_s = 290\,\mathrm{K}$ the n_f for 60° are lower than for 0° for layer thicknesses of $2-10\,$u.c.. At $1\,$u.c. n_f is estimated slightly larger for 60° compared to 0°.

This observation is supported when considering the bare background corrected Ce 3*d* spectra as shown in figures A.5 and A.6 for $T_s = 9\,\mathrm{K}$ and $T_s = 290\,\mathrm{K}$ respectively. Figure A.5 a) shows layer thicknesses of $1-3\,$u.c., whereas figure A.5 b) shows $4->10\,$u.c.. The spectra are normalized to the intensity of the Ce $3d_{3/2}$ f^1 peak respectively and larger layer thicknesses are artificially shifted to higher intensities for better comparability.

For $2->10\,$u.c. the calculated n_f match very well with the weights of the f^0 peaks of both spin-orbit partners. For $2\,$u.c. the f^0 weights for 0° and 60°

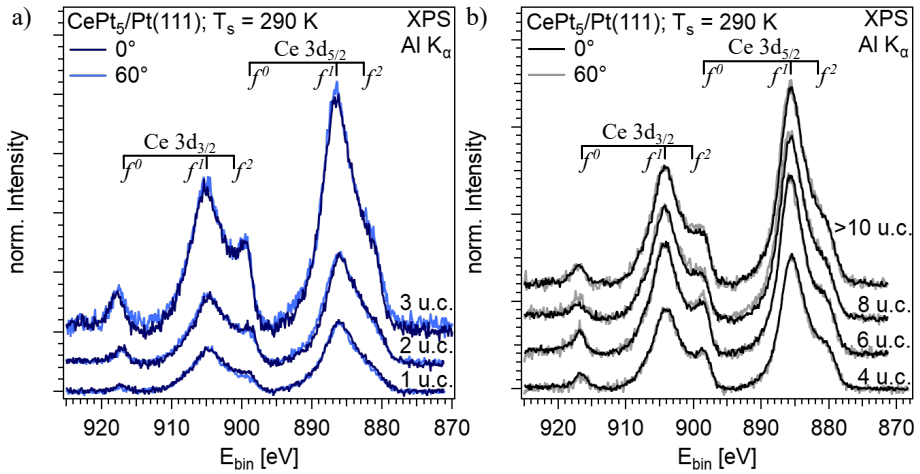

Figure A.6: Emission angle dependence of the Ce 3*d* multiplet structure at $T_s = 290\,\mathrm{K}$.

are similar as is n_f. For 3 u.c. the f^0 weight is smaller for 60° as for 0°. This is also reflected in the calculated n_f. For layer thicknesses of 4 –>10 u.c. the f^0 weight at 60° is always higher than at 0°, which is again reflected in the calculated n_f. At a layer thickness of 1 u.c. the large difference in n_f as shown in figure 5.4 b) is hard to observe in the bare spectra. At close look the f^0 shares at 60° seem indeed to be slightly lower than for 0°. Since the overall intensity at a layer thickness of 1 u.c. is very low compared to larger layer thicknesses, this small reduction already leads to a large difference in the calculated n_f.

In figure A.6 all Ce 3*d* spectra recorded at $T_s = 290\,\mathrm{K}$ are compared regarding the emission angle. Figure A.6 a) again shows the spectra for layer thicknesses of 1 – 3 u.c., b) the ones for 4 – >10 u.c.. In the higher layer thickness regime (> 4 u.c.) the f^0 shares of the data recorded at 60° off normal emission (grey lines) are always higher than their counterparts in the 0° spectra. This is also visible for a layer thickness of 3 u.c. in figure A.6 a). At a layer thickness of 2 u.c. the f^0 weights for 0° (dark blue lines) and 60° (light blue lines) are comparable, whereas they are lower as their 0° counterparts for 1 u.c. layer thickness. This is in agreement with the course of n_f shown in figure 5.4 b).

A.3 GS-model fits of Ce 3*d* spectra in $CePt_5$/Pt(111) at $T_s = 290\,K$

Figure A.7 and **figure A.8** show the Ce 3*d* spectra (grey data points) of increasing layer thicknesses of $CePt_5$/Pt(111) recorded at $T_s = 290\,K$ for normal emission and 60° off normal emission respectively. The spectra were acquired with $h\nu(Al\ K_\alpha) = 1486.6\,eV$ and with an energy resolution of $\Delta E = 750\,meV$. All spectra are modeled with calculations based on the Gunnarsson-Schönhammer model for core level spectroscopy according to sections 3.1.4 and 5.4. The blue GS-model fits correspond to the respective fits to the data acquired at $T_s = 9\,K$ and normal emission, whereas the red fits emphasize when parameters of the $T_s = 9\,K$-fit were changed to achieve the best replica of the $T_s = 290\,K$ data. The modified parameters are listed in the respective graphs.

A.4 Δ^{GS} determined from the relative f^2 weight

Figure A.9 shows the hybridization strength Δ^{GS} determined from the relative weights of the Ce $3d_{5/2}$ f^2 peaks according to subsection 3.1.3 and equation 3.17. The spectral weight of the f^1 and f^2 peak is determined by the area of a Voigt fit. The observed trend is still similar to Δ^{GS} as determined with equation 3.19, however, the absolute values are in better agreement with Δ estimated purely on the basis of the experimental spectra in subsection 5.2.

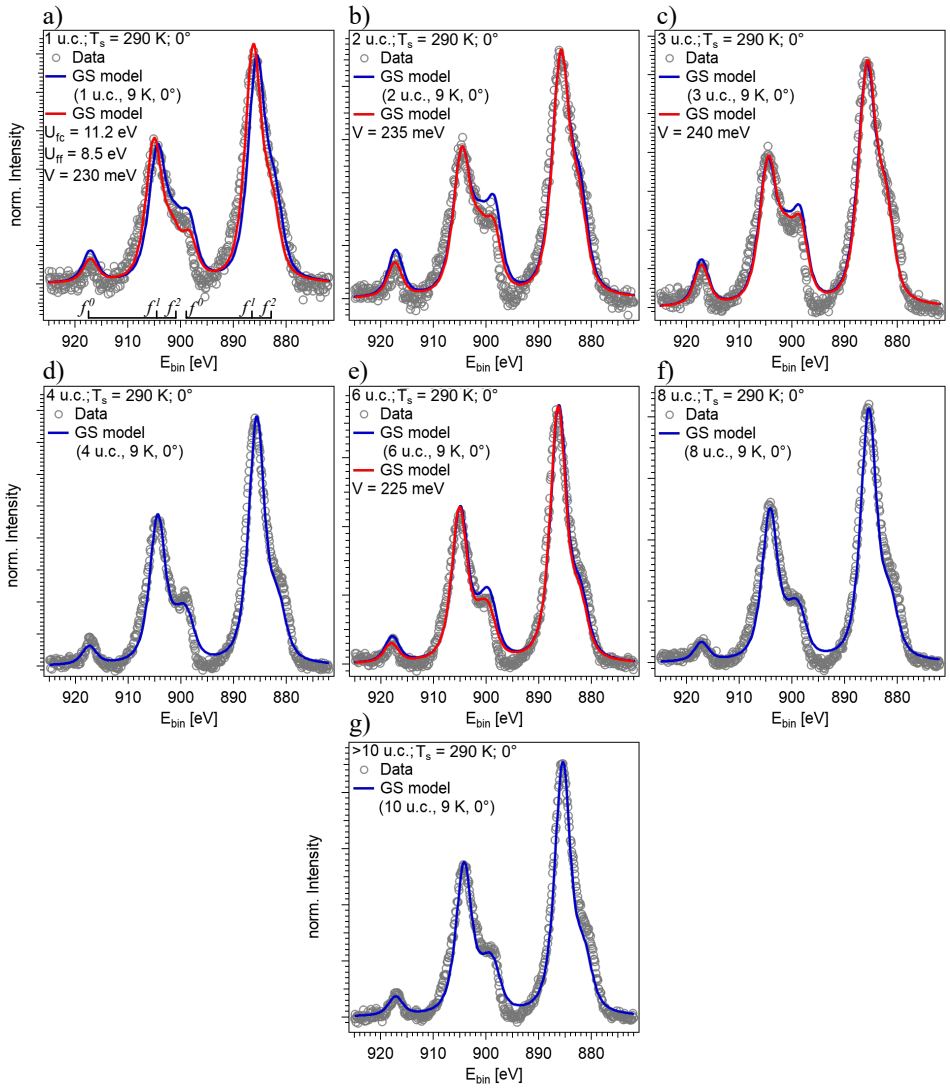

Figure A.7: GS-model fits to the Ce 3*d* spectra acquired at $T_s = 290\,\mathrm{K}$ and normal emission. a) – g) show the GS-model fits to increasing layer thicknesses of $CePt_5$/Pt(111). Grey points represent the spectra, measured with an excitation energy of $h\nu(Al\ K_\alpha) = 1486.6\,eV$ and an energy resolution of $\Delta E = 750\,meV$. Blue and red lines show the respective GS-model fits.

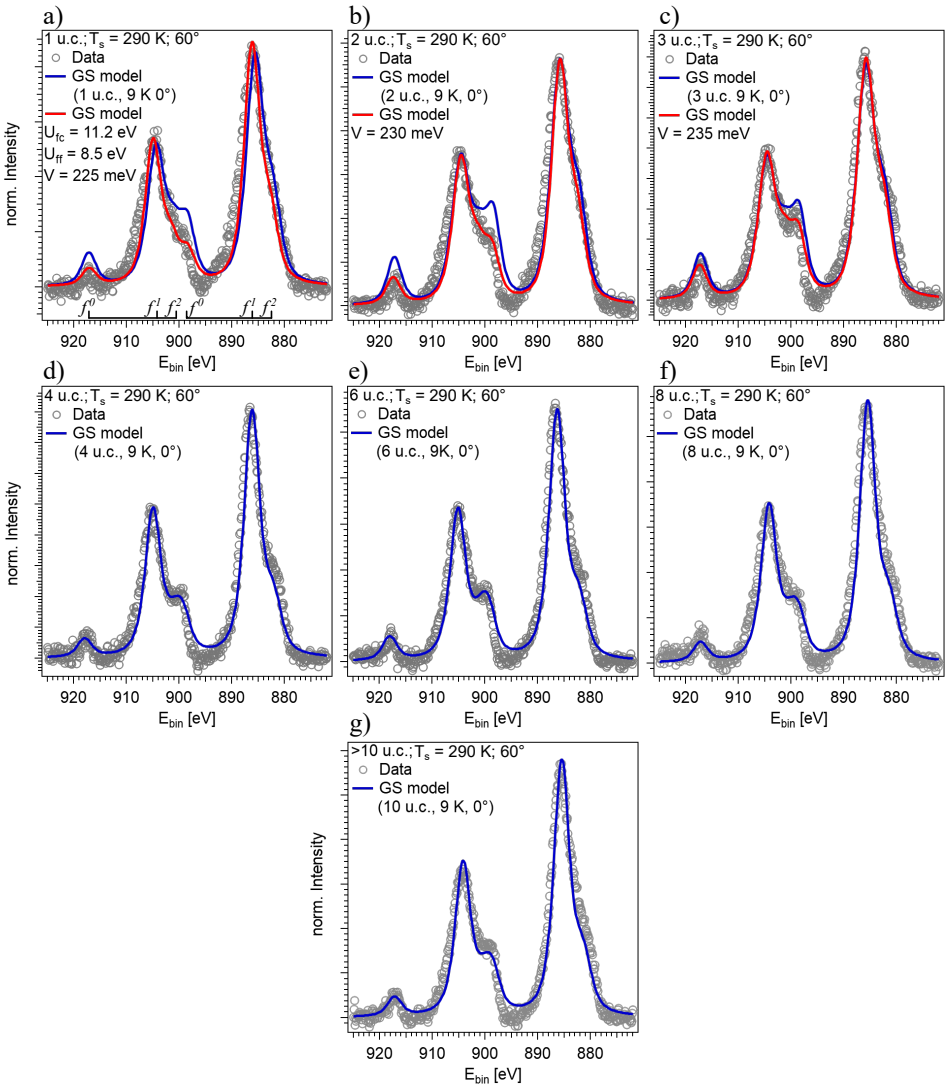

Figure A.8: GS-model fits to the Ce 3*d* spectra acquired at $T_s = 290\,\mathrm{K}$ and 60° off normal emission. a) – g) show the GS-model fits to increasing layer thicknesses of $CePt_5$/Pt(111). Grey points represent the spectra, measured with an excitation energy of $h\nu(Al\ K_\alpha) = 1486.6\,eV$ and an energy resolution of $\Delta E = 750\,meV$. Blue and red lines show the respective GS-model fits.

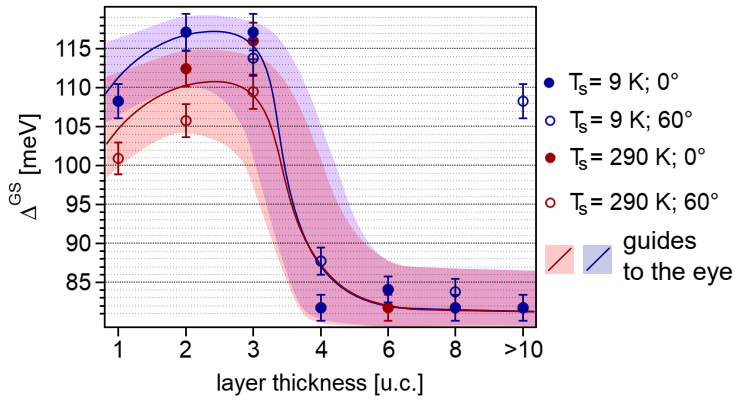

Figure A.9: Δ^{GS} determined on the basis of the relative f^2 weight to the GS-model fit. Δ^{GS} determined according to equation 3.17 based on the GS-model fits to the respective Ce 3*d* spectra.

Bibliography

[1] M. Dzero, K. Sun, V. Galitski, and P. Coleman. Topological Kondo Insulators. *Phys. Rev. Lett.,* ***104****, p. 106408*, 2010.

[2] M. Dzero, K. Sum, P. Coleman, and V. Galitski. Theory of Topological Kondo Insulators. *Phys. Rev. B.,* ***85****, p. 045130*, 2012.

[3] M. Dzero, J. Xia, V. Galitski, and P. Coleman. Topological Kondo Insulators. *Annu. Rev. Condens. Matter Phys.* ***7****, p. 249–280*, 2016.

[4] M. Z. Hasan and C. L. Kane. Colloquium: Topological insulators. *Rev. Mod. Phys.,* ***82****, p. 3045*, 2010.

[5] X.-L. Qi and S.-C. Zhang. Topological Insulators and Superconductors. *Rev. Mod. Phys.,* ***83****, p. 1057*, 2011.

[6] D. Hsieh, D. Qian, L. Wray, Y. Xia, Y. S. Hor, R. J. Cava, and M. Z. Hasan. A topological Dirac insulator in a quantum spin Hall phase. *Nature,* ***452****, pp. 970–974*, 2008.

[7] Y. Xia, D. Qian, D. Hsieh, L. Wray, A. Pal, H. Linv, A. Bansil, D. Grauer, Y. S. Hor, R. J. Cava, and M. Z. Hasan. Observation of a large-gap topological-insulator class with a single Dirac cone on the surface. *Nature Physics,* ***5****, pp. 398–402*, 2009.

[8] Y. L. Chen, J. G. Analytis, J.-H. Chu, Z. K. Liu, S.-K. Mo, X. L. Qi, H. J. Zhang, D. H. Lu, X. Dai, Z. Fang, S. C. Zhang, I. R. Fisher, Z. Hussain, and Z.-X. Shen. Experimental Realization of a Three-Dimensional Topological Insulator, Bi_2Te_3. *Science,* ***325****, pp. 178-181*, 2009.

[9] A. C. Hewson. *The Kondo Problem to Heavy Fermions.* Cambridge University Press, 1993.

[10] W.J. de Haas, J. dë Boer, and G.J. van dën Berg. The electrical resistance of gold, copper and lead at low temperatures. *Physica* ***1****, pp. 1115-1124*, 1934.

[11] B. Knook and G. J. Van dën Berg. The electrical resistance of pure Au and Ag at low temperatures. *Physica,* ***26****, pp. 505-512*, 1960.

[12] G. S. Knapp and M. P. Sarachik. Resistivity and Susceptibility of Rh-Ru Alloys Containing Fe. *J. Appl. Phys.,* ***40****, p. 1474*, 1969.

[13] J. Kondo. Resistance Minimum in Dilute Magnetic Alloys. *Progress of Theoretical Physics,* ***32****, pp. 37–49*, 1964.

[14] P.W. Anderson. Localized Magnetic States in Metals. *Phys. Rev.,* ***124****, p. 41*, 1961.

[15] K. G. Wilson. The renormalization group: Critical phenomena and the Kondo problem. *Rev. Mod. Phys.* ***47****, p. 773*, 1975.

[16] A. Menth, E. Buehler, and T. H. Geballe. Magnetic and Semiconducting Properties of SmB_6. *Phys. Rev. Lett.,* ***22****, p. 295*, 1969.

[17] M. F. Hundley, P. C. Canfield, J. D. Thompson, Z. Fisk, and J. M. Lawrence. Hybridization gap in $Ce_3Bi_4Pt_3$. *Phys. Rev. B,* ***42****, p. 6842(R)*, 1990.

[18] A. Severing, J. D. Thompson, P. C. Canfield, Z. Fisk, and P. Riseborough. Gap in the magnetic excitation spectrum of $Ce_3Bi_4Pt_3$. *Phys. Rev. B,* ***44****, p. 6832*, 1991.

[19] B. Bucher, Z. Schlesinger, P. C. Canfield, and Z. Fisk. Kondo coupling induced charge gap in $Ce_3Bi_4Pt_3$. *Phys. Rev. Lett.,* ***72****, p. 522*, 1994.

[20] P.-Y. Chang, O. Erten, and P. Coleman. Möbius Kondo Insulators. *Nat. Phys.,* ***13****, pp. 794-798*, 2017.

[21] J. W. Allan, B. Batlogg, and P. Wachter. Large low-temperature Hall effect and resistivity in mixed-valent SmB_6. *Phys. Rev. B,* ***20*** *p. 4807*, 1979.

[22] M. Neupane, N. Alidoust, S.-Y. Xu, T. Kondo, Y. Ishida, D. J. Kim, Chang Liu, I. Belopolski, Y. J. Jo, T.-R. Chang, H.-T. Jeng, T. Durakiewicz, L. Balicas, H. Lin, A. Bansil, S. Shin, Z. Fisk, and M. Z. Hasan. Surface electronic structure of the topological Kondo-insulator candidate correlated electron system SmB_6. *Nat. Commun.,* ***4****, p. 2991: 1-7*, 2013.

[23] N. Xu, X. Shi, P. K. Biswas, C. E. Matt, R. S. Dhaka, Y. Huang, N. C. Plumb, M. Radović, J. H. Dil, E. Pomjakushina, K. Conder, A. Amato, Z. Salman, D. McK. Paul, J. Mesot, H. Ding, and M. Shi. Surface and bulk electronic structure of the strongly correlated system SmB_6 and implications for a topological Kondo insulator. *Phys. Rev. B,* ***88****, p. 121102(R)*, 2013.

[24] J. Jiang, S. Li, T. Zhang, Z. Sun, F. Chen, Z.R. Ye, M. Xu, Q.Q. Ge, S.Y. Tan, X.H. Niu, M. Xia, B.P. Xie, Y.F. Li, X.H. Chen, H.H. Wen, and D.L. Feng. Observation of possible topological in-gap surface states in the Kondo insulator SmB_6 by photoemission. *Nat. Commun.,* ***4****, p. 3010: 1-8*, 2013.

[25] P. Hlawenka, K. Siemensmeyer, E. Weschke, A. Varykhalov, J. Sánchez-Barriga, N. Y. Shitsevalova, A. V. Dukhnenko, V. B. Filipov, S. Gabáni, K. Flachbart, O. Rader, and E. D. L. Rienks. Samarium hexaboride is a trivial surface conductor. *Nat. Commun.,* ***9****, p. 517: 1-7*, 2018.

[26] J. Tang, J. M. Lawrence, and J. C. Hemminger. Structure and valence of the Ce/Pt(111) system. *Phys. Rev. B,* ***48****, p. 15342*, 1993.

[27] J. Kemmer, C. Praetorius, A. Krönlein, P.-J. Hsu, K. Fauth, and M. Bode. Structural analysis of the intermetallic surface compound $CePt_5$/Pt(111). *Phys. Rev. B* ***90****, p. 195401*, 2014.

[28] H. Schwab, M. Mulazzi, J. Jiang, H. Hayashi, T. Habuchi, D. Hirayama, H. Iwasawa, K. Shimada, and F. Reinert. Character of valence-band

states in the kondo surface alloys $CeAg_x$/Ag(111) and $CePt_5$/Pt(111). *Phys. Rev. B,* ***85****, p. 125130*, 2012.

[29] M. Mulazzi, K. Shimada, J. Jiang, H. Iwasawa, and F. Reinert. Evidence of coexisting Kondo screening and valence fluctuations in the $CePd_7$/Pd(001) surface alloy. *Phys. Rev. B,* ***89****, p. 205134*, 2014.

[30] Christian M. Praetorius. *Ce M4,5 XAS and XMCD as Local Probes for Kondo and Heavy Fermion Materials - A Study of $CePt_5$/Pt(111) Surface Intermetallics.* PhD thesis, Julius-Maximilians University of Würzburg, 2015.

[31] Stefan Hüfner. *Photoelectron Spectroscopy - Principles and Application.* Springer Series in Solid-State Sciences, 2nd edition, 1996.

[32] S. Hüfner. Valence band photoemission on metallic Ce systems. *Z. Phys. B,* ***86****, pp. 241–246*, Condensed Matter 86:241–246, 1992.

[33] L. Duò. Surface effects in the spectroscopy of mixed-valent Ce compounds. *Surf. Sci. Rep.,* ***32****, pp. 233-289*, 1998.

[34] Neil W. Ashcroft and N. David Mermin. *Festkörperphysik.* De Gruyter Oldenbourg, 9th edition, 2007.

[35] Charles Kittel. *Einführung in die Festkörperphysik.* R. Oldenburg Verlag GmbH, 6th edition, 1983.

[36] F. Bloch. *Über die Quantenmechanik der Elektronen in Kristallgittern.* PhD thesis, University of Leipzig, 1928.

[37] F. Bloch. Über die Quantenmechanik der Elektronen in Kristallgittern. *Z. Phys.,* ***52****, pp. 555–600*, 52(7):555–600, 1929.

[38] J. Hubbard. Electron correlations in narrow energy bands. *Proc. R. Soc. A,* ***276****, pp. 238-257*, 1963.

[39] J. Hubbard. Electron correlations in narrow energy bands II. The degenerate band case. *Proc. R. Soc. A* ***277****, pp. 237-259*, 1964.

[40] B. H. Brandow. Electronic Structure of Mott insulators. *Adv. Phys.* ***25****, pp. 651-808*, 26:651–808, 1977.

[41] S. Hüfner, J. Ostenwalder, T. Riesterer, and F. Hulliger. Photoemission and Inverse Photoemission Spectroscopy of NiO. *Solid State Commun.,* ***52****, pp. 793-796*, 52(9):793–796, 1984.

[42] O. Gunnarsson and K. Schönhammer. *Handbook on the Physics and Chemistry of Rare Earths - Many-body formulation of spectra of mixed valence systems.* Volume 10, Chapter 64,103, Elsevier, 1987.

[43] L. Kouwenhoven and L. Glazman. Revival of the Kondo effect. *Phys. World,* ***14****, pp. 33-38*, 2001.

[44] C. Zener. Interaction between the *d* shells in the Transition Metals. *Phys. Rev.* ***81****, p. 440*, 1951.

[45] T. Kasuya. A Theory of Metallic Ferro- and Antiferromagnetism on Zener's Model. *Prog. Theor. Phys.,* ***16(1)****, pp. 45-57*, 1956.

[46] K. Yosida. Magnetic Properties of Cu-Mn Alloys. *Phys. Rev.* ***106****, pp. 893-898*, 1957.

[47] K. Yosida. Anomalous Electrical Resistivity and Magnetoresistance due to an *s-d* Interaction in Cu-Mn alloys. *Phys. Rev.,* ***107****, p. 396*, 1957.

[48] N. E. Bickers, D. L. Cox, and J. W. Wilkins. Self-consistent large-N expansion for normal-state properties of dilute magnetic alloys. *Phys. Rev. B,* ***36****, p. 2036*, 1987.

[49] O. Gunnarsson and K. Schönhammer. Electron Spectroscopies for Ce Compounds in the Impurity Model. *Phys. Rev. B,* ***28****, p. 4315*, 1983.

[50] J. R. Schrieffer and P. A. Wolff. Relation between the Anderson and Kondo Hamiltonians. *Phys. Rev.* ***149****, p. 491*, 1966.

[51] Jonas Sweep. The s-d exchange model. Master's thesis, Radboud University of Nijmegen, 2012.

[52] V. Y. Irkhin and A. V. Zarubin. Metal-insulator transition in the Hubbard model: a simple description including the Kondo effect. *Europ. Phys. J. B.* ***38****, pp. 563-570*, 2004.

[53] O. Gunnarsson and K. Schönhammer. Photoemission from Ce Compounds: Exact model calculation in the Limit of Large Degeneracy. *Phys. Rev. Lett.,* ***50****, p. 604*, 1983.

[54] F. Patthey, J.-M. Imer, W.-D. Schneider, H. Beck, and Y. Baer. High-resolution photoemission study of the low-energy excitations in 4f-electron systems. *Phys. Rev. B,* ***42****, pp. 8864-8881*, 1990.

[55] D. Malterre, M. Grioni, and Y. Baer. Recent developments in high-energy spectroscopies of Kondo systems. *Adv. Phys.,* ***45****, pp. 299-348*, 1996.

[56] K. Nagaoka, T. Jamneala, M. Grobis, and M. F. Crommie. Temperature Dependence of a Single Kondo Impurity. *Phys. Rev. Lett.,* ***88****, p. 077205*, 2002.

[57] M. A. Ruderman and C. Kittel. Indirect Exchange Coupling of Nuclear Magnetic Moments by Conduction Electrons. *Phys. Rev.,* ***96****, pp. 99-102*, 1954.

[58] S. Doniach. The Kondo lattice and weak antiferromagnetsim. *Physica B, C,* ***91****, pp. 231-234*, 1977.

[59] J. R. Iglesias, C. Lacroix, and B. Coqblin. Revisited Doniach diagram: Influence of short-range antiferromagnetic correlations in the Kondo lattice. *Phys. Rev. B,* ***56****, p. 11820*, 1997.

[60] M. Klein, A. Nuber, H. Schwab, N. Tobita, M. Higashiguchi, J. Jiang, S. Fukuda, K. Tanaka, K. Shimada, M. Mulazzi, F. F. Assaad, and F. Reinert. Coherent heavy quasiparticles in $CePt_5$ surface alloy. *Phys. Rev. Lett.,* ***106(13)****, p. 186407*, 2011.

[61] M. Klein. *Starke Korrelation in Festkörpern: von lokalisierten zu itineranten Elektronen*. PhD thesis, Julius-Maximilians University of Würzburg, 2009.

[62] J. J. Sakurai. *Advanced Quantum Mechanics*. Addison-Wesley Publishing Company, 1967.

[63] J. F. Moudler, W. F. Stickle, P. E. Sobol, and K. D. Bomben. *Handbook of X-Ray Photoelectron Spectroscopy*. Eden Prairie: Perkin-Elemer, 1992.

[64] E. I. Rashba and Y. A. Bychkov. Oscillatory effects and the magnetic susceptibility of carriers in inversion layers. *J. Phys. C. Solid State Phys., **17**, p. 6039*, 1984.

[65] S. LaShell, B. A. McDougall, and E. Jensen. Spin Splitting of an Au(111) Surface State Band Observed with Angle Resolved Photoelectron Spectroscopy. *Phys. Rev. Lett., **77**, p. 3419*, 1996.

[66] G. Nicolay, F. Reinert, S. Hüfner, and P. Blaha. Spin-orbit splitting of the L-gap surface state on Au(111) and Ag(111). *Phys. Rev. B, **65**, p. 033407*, 2001.

[67] J. Henk, A. Ernst, and P. Bruno. Spin polarization of the L-gap surface states on Au(111). *Phys. Rev. B, **68**, p. 165416*, 2003.

[68] Yu. M. Koroteev, G. Bihlmayer, J. E. Gayone, E.V. Chulkov, P. M. Echenique S. Blügel and, and Ph. Hofmann. Strong Spin-Orbit Splitting on Bi Surfaces. *Phys. Rev. Lett., **93**, p. 046403*, 2004.

[69] C. R. Ast, J. Henk, A. Ernst, L. Moreschini, M. C. Falub, D. Pacile P. Bruno, K. Kern, and M. Grioni. Giant Spin Splitting through Surface Alloying. *Phys. Rev. Lett., **98**, p. 186807*, 2007.

[70] H. Bentmann, F. Forster, G. Bihlmayer, E. V. Chulkov, L. Moreschini, M. Grioni, and F. Reinert. Origin and manipulation of the Rashba splitting in surface alloys. *Europhys. Lett., **87**, p. 37003*, 2009.

[71] F. Meier, H. Dil, J. Lobo-Checa, L. Patthey, and J. Osterwalder. Quantitative vectorial spin analysis in angle-resolved photoemission: Bi/Ag(111) and Pb/Ag(111). *Phys. Rev. B,* ***77****, p. 165431*, 2008.

[72] L. El-Kareh, P. Sessi, T. Bathon, and M. Bode. Quantum Interference Mapping of Rashba Split Bloch States in Bi/Ag(111). *Phys. Rev. Lett.,* ***110****, p. 176803*, 2013.

[73] G. Bihlmayer, S. Blügel, and E. V. Chulkov. Enhanced Rashba spin-orbit splitting in Bi/Ag(111) and Pb/Ag(111) surface alloys from first principles. *Phys. Rev. B,* ***75****, p.195414*, 2007.

[74] D. Pacilé, C. R. Ast, M. Papagno, C. Da Silva, L. Moreschini, M. Falub, Ari P. Seitsonen, and M. Grioni. Electronic structure of an ordered Pb/Ag(111) surface alloy: Theory and experiment. *Phys. Rev. B,* ***73****, p. 245429*, 2006.

[75] L. Fu and C. Kane. Topological insulators with inversion symmetry. *Phys. Rev. B,* ***76****, p. 045302*, 2007.

[76] L. Isaev, Y. H. Moon, and G. Ortiz. Bulk-boundary correspondence in three-dimensional topological insulators. *Phys. Rev. B,* ***84****, p. 075444*, 2011.

[77] M. König, S. Wiedmann, C. Brüne, A. Roth, H. Buhmann, L. W. Molenkamp, X.-L. Qi, and S.-C. Zhang. Quantum Spin Hall Insulator State in HgTe Quantum Wells. *Science,* ***318****, pp. 766–770*, 2007.

[78] C.-Z. Chang, J. Zhang, X. Feng, J. Shen, Z. Zhang, M. Guo, K.Li, Y. Ou, P. Wei, L.-L. Wang, Z.-Q. Ji, Y. Feng, S. Ji, X. Chen, J. Jia, X. Dai, Z. Fang, S.-C. Zhang, K. He, Y. Wang, L. Lu, X.-C. Ma, and Q.-K. Xue. Experimental Observation of the Quantum Anomalous Hall Effect in a Magnetic Topological Insulator. *Science,* ***3400****, pp. 167-170*, 2013.

[79] M. M. Otrokov, I. I. Klimovskikh, H. Bentmann, D. Estyunin, A. Zeugner, Z. S. Aliev, S. Gaß, A. U. B. Wolter, A. V. Koroleva,

A. M. Shikin, M. Blanco-Rey, M. Hoffmann, I. P. Rusinov, A. Yu. Vyazovskaya, S. V. Eremeev, Yu. M. Koroteev, V. M. Kuznetsov, F. Freyse, J. Sánchez-Barriga, I. R. Amiraslanov, M. B. Babanly, N. T. Mamedov, N. A. Abdullayev, V. N. Zverev, V. Kataev A. Alfonsov, B. Büchner, E. F. Schwier, S. Kumar, A. Kimura, L. Petaccia, G. Di Santo, R. C. Vidal, S. Schatz, K. Kißner, M. Ünzelmann, C. H. Min, S. Moser, T. R. F. Peixoto, F. Reinert, A. Ernst, P. M. Echenique, A. Isaeva, and E. V. Chulkov. Prediction and observation of an antiferromagnetic topological insulator. *Nature,* ***576****, pp. 416-422*, 2019.

[80] A. Zeugner, F. Nietschke, A. U. B. Wolter, S. Gaß, R. C. Vidal, T. R. F. Peixoto, D. Pohl, C. Damm, A. Lubk, R. Hentrich, S. K. Moser, C. Fornari, C. H. Min, S. Schatz, K. Kißner, M. Ünzelmann, M. Kaiser, F. Scaravaggi, B. Rellinghaus, K. Nielsch, C. Hess, B. Büchner, F. Reinert, H. Bentmann, O. Oeckler, T. Doert, M. Ruck, and A. Isaeva. Chemical Aspects of the Candidate Antiferromagnetic Topological Insulator $MnBi_2Te_4$. *Chem. Mater.,* ***31, 8****, pp. 2795-2806*, 2019.

[81] Y. Ando and L. Fu. Topological Crystalline Insulators and Topological Superconductors: From Concepts to Materials. *Annu. Rev. Condens. Matter Phys.* ***6****, pp. 361-381*, 2015.

[82] Y. Tanaka, Z. Ren, T. Sato, K. Nakayama, S. Souma, T. Takahashi, K. Segawa, and Y. Ando. Experimantal realization of a topological crystalline insulator in SnTe. *Nature Physics* ***8****, pp. 800-803*, 2012.

[83] P. Dziawa, B. J. Kowalski, K. Dybko, R. Buczko, A. Szczerbakow, M. Szot, E. Lusakowska, T. Balasubramanian, B. M. Wojek, M. H. Berntsen, O. Tjernberg, and T. Story. Topologial crystalline insulator states in Pb(1-x)Sn(x)Se. *Nat. Mater.* ***11****, pp. 1023-1027*, 2012.

[84] X. Wan, A. M. Turner, A. Vishwanath, and S. Y. Savrasov. Topological semimetal and Fermi-arc surface states in the electronic structure of pyrochlore iridates. *Phys. Rev. B* ***83****, p. 205101*, 2011.

[85] A. A. Burkov and L. Balents. Weyl Semimetal in a Topological Insulator Multilayer. *Phys. Rev. Lett.* ***107****, p. 127205*, 2011.

[86] B. Bradlyn, J. Cano, Z. Wang, M. G. Vergniory, C. Felser, R. J. Cava, and B. A. Bernevig. Beyond Dirac and Weyl fermions: Unconventional quasiparticles in conventional crystals. *Science* ***353****, p. 558*, 2016.

[87] N. P. Armitage, E. J. Mele, and A. Vishwanath. Weyl and Dirac semimetals in three-dimensional solids. *Rev. Mod. Phys.* ***90****, p. 015001*, 2018.

[88] H.-H. Lai, S. E. Grefe, S. Paschen, and Q. Si. Weyl-Kondo semimetal in a heavy fermion system. *PNAS* ***115****, pp. 93-97*, 2018.

[89] X.-Y. Feng, J. Dai, C.-H. Chung, and Q. Si. Competing Topological and Kondo Insulator Phases on a Honeycomb Lattice. *Phys. Rev. Lett.,* ***111****, p. 016402*, 2013.

[90] X.-Y. Feng, H. Zhong, J. Dai, and Q. Si. Dirac-kondo semimetals and topological Kondo insulators in the dilute carrier limit. *arXiv:1605.02380 [cond-mat.str-el]*, 2016.

[91] S. Dzsaber, L. Prochaska, A. Sidorenko, G. Eguchi, R. Svagera, M. Waas, A. Prokofiev, Q. Si, and S. Paschen. Kondo insulator to semimetal transformation tuned by spin-orbit coupling. *Phys. Rev. Lett.,* ***118****, p. 246601*, 2017.

[92] P. Hlawenka, K. Siemensmeyer, E. Weschke, A. Varykhalov, J. Sánchez-Barriga, N. Y. Shitsevalova, A. V. Dukhnenko, V. B. Filipov, S. Gabáni, K. Flachbart, O. Rader, and E. D. L. Rienks. Samarium hexaboride: A trivial surface conductor. *Nat. Commun.* ***9****, p. 517*, 2018.

[93] L. Moreschini, A. Bendounan, H. Bentmann, M. Assig, K. Kern, F. Reinert, J. Henk, C. R. Ast, and M. Grioni. Influence of the substrate on the spin-orbit splitting in surface alloys on (111) noble-metal surfaces. *Phys. Rev. B,* ***80****, p. 035438*, 2009.

[94] H. Hertz. Über einen Einfluss des ultravioletten Lichtes auf die electrische Entladung. *Ann. Phys.* ***267****, pp. 983–1000*, 1887.

[95] A. Einstein. Über einen die Erzeugung und Verwandlung des Lichtes betreffenden heuristischen Gesichtspunkt. *Ann. Phys.* ***322****, pp. 132–148*, 1905.

[96] A. Tejeda and D. Malterre. *A Primer in Photoemission: Concepts and Applications*. EDP SCIENCES, 2019.

[97] S. Moser. An experimentalist's guide to the matrix element in angle resolved photoemission. *J. Electron. Spectrosc.,* ***214****, pp. 29-52*, 2017.

[98] A. Damascelli, Z. Hussain, and Z.-X. Shen. Angle-resolved photoemission studies of the cuprate superconductors. *Rev. Mod. Phys.,* ***75****, p. 473*, 2003.

[99] L. D. Landau. The Theory of a Fermi Liquid. *Sov. Phys. JETP,* ***3****, pp. 920-925*, 1957.

[100] L. D. Landau. On the Theory of the Fermi Liquid. *Sov. Phys. JETP,* ***35****, pp. 70-74*, 1959.

[101] P. Auger. Sur l'effet photoélectrique composé. *J. Phys. Radium* ***6****, p. 205-208*, 1925.

[102] J. C. Fuggle, F. U. Hillebrecht, Z. Zolnierek, R. Lässer, Ch. Freiburg, O. Gunnarsson, and K. Schönhammer. Electronic structure of Ce and its intermetallic compounds. *Phys. Rev. B,* ***27****, p. 7330*, 1983.

[103] O. Gunnarsson and K. Schönhammer. Double occupancy of the f orbital in the Anderson model for Ce compounds. *Phys. Rev. B,* ***31****, pp. 4815-4834*, 1985.

[104] Martin G. Zinner. *Adsorbat-induzierte Oberflächensysteme und ultradünne intermetallische Legierungsfilme im Fokus der niederenergetischen Elektronenbeugung und spektroskopischer Analysemethoden.* PhD thesis, Julius-Maximilians University of Würzburg, 2019.

[105] Katharina Treiber. Manipulation der elektronischen Struktur in epitaktischem $CePt_5$/Pt(111). Master's thesis, University of Wuerzburg, 2016.

[106] T. Fauster, L. Hammer, K. Heinz, and M.A. Schneider. *Oberflächenphysik - Grundlagen und Methoden*. Oldengourg-Verlag, 2013.

[107] R. Gross and A. Marx. *Festkörperphysik*. DeGruyter Studium, 2018.

[108] L. de Broglie. A Tentative Theory of Light Quanta. *Philos. Mag.,* ***6****, pp. 446-458*, 1924.

[109] M. P. Seah and W. A. Dench. Quantitative Electron Spectroscopy of Surfaces: A Standard Data Base for Electron Inelastic Mean Free Paths in Solids. *Surf. Interface Anal.,* ***1****, pp. 2-11*, 1979.

[110] M. Horn von Hoegen. Growth of semiconductor layers studied by spot-profile analysing low energy electron diffraction. *Z. Kristallogr.,* ***214****, pp. 591-629 and pp. 684-721*, 1999.

[111] P.J. Estrup and E.G. McRae. Surface Studies by Electron Diffraction. *Surf. Sci.* ***25****, pp. 1-52*, 1971.

[112] J. Merino and O. Gunnarsson. Role of Surface States in Scanning Tunneling Spectroscopy of (111) Metal Surfaces with Kondo Adsorbates. *Phys. Rev. Lett.,* ***93****, p. 156601*, 2004.

[113] M. P. Marder. *Condensed Matter Physics*. John Wiley & Sons, 2000.

[114] *Manual: Intense VUV Photon Source - MBScientific AB*.

[115] A. Nuber. *Intrinsische und extrinsische Einflüsse auf zweidimensionale elektronische Zustände*. PhD thesis, Julius – Maximilians University Würzburg, 2011.

[116] Gammadata Scienta AB, editor. *User Manual SCIENTA R4000*. Gammadata Scienta AB, 2004.

[117] *NIST X-ray Photoelectron Spectroscopy (XPS) Database - url: https://srdata.nist.gov/xps/main_search_menu.aspx year: 2021 (accessed: February 15, 2021).*

[118] János Végh. The shirley background revised. *J. Electron Spectrosc. Relat. Phenom., **46**, pp. 411-417*, 1988.

[119] Felix Schmitt. Hochaufgelöste PES an $CeSi_2$ nahe E_F und Auswertung der Kondo-Resonanz. Master's thesis, Julius-Maximilians University of Würzburg, 2005.

[120] Focus Omicron NanoTechnology. *Instruction Manual - UHV Evaporator EFM 3/4.* Focus - Omicron NanoTechnology, 2008, Version 3.9.

[121] C. J. Baddeley, A. W. Stephenson, C. Hardacre, M. Tikhov, and R. M. Lambert. Structural and electronic properties of Ce overlayers and low-dimensional Pt-Ce alloys on Pt(111). *Phys. Rev. B, **56**, pp. 12589-12598*, 1997.

[122] C. Praetorius, M. Zinner, G. Held, and K. Fauth. Surface termination of $CePt_5$/Pt(111): the key to chemical inertness. *Phys. Rev. B, **92**, p. 195427*, 2015.

[123] H. H. Binder. *Lexikon der chemischen Elemente: Das Periodensystem in Fakten, Daten und Zahlen.* S. Hirzel Verlag, Stuttgart, 1999.

[124] C. G. Mosander. Über Cer, Lanthan und Didym, sowie über Yttererde, Erbium und Terbium. *Justus Liebigs Ann. Chem, **48**, pp. 210-223*, 1843.

[125] K. Reinhardt and H. Winkler. Cerium Mischmetal, Cerium Alloys and Cerium Compounds. *Ullmann's Encyclopedia of Industrial Chemistry, **8**, pp.41-56*, 2000.

[126] J. W. Allan and R. M. Martin. Kondo Volume Collapse and the γ - α Transition in Cerium. *Phys. Rev. Lett., **49**, p. 1106*, 1982.

[127] P. Coleman. *Heavy Fermions and the Kondo Lattice: A 21st Century Perspective*. Forschungszentrum Jülich, 2015.

[128] A. Schröder, G. Aeppli, R. Coldea, M. Adams, O. Strockert, H. v. Löhneysen, E. Bucher, R. Ramazashvili, and P. Coleman. Onset of antriferromagnetism in heavy-fermion metals. *nature* ***407****, pp. 351-355*, 2000.

[129] R. R. Joseph, K. A. Gschneider Jr, and R. E. Hungsberg. Low-Temperature Heat Capacity of $LaPt_2$ and $CePt_2$ and the Magnetic Susceptibility of $CePt_2$. *Phys. Rev. B,* ***5****, p.1878*, 1972.

[130] A. Schröder, R. van den Berg, H. v. Löhneysen, W. Paul, and H. Lueken. Magnetic ordering of $CePt_5$. *Solid State Commun.,* ***65****, pp. 99-101*, 1988.

[131] H. Lueken, M. Meier, G. Klessen, W. Bronger, and J. Fleischhauer. Magnetische Eigenschaften von $CePt_5$ zwischen 4.2 und 295 K. *J. Less-Common Met.,* ***63****, pp. 35-44*, 1979.

[132] A. Janghorban, M. Lomello-Tafin, J. M. Moreau, and Ph. Galez. The phase diragram of the Ce-Pt system. *Intermetallics,* ***18****, pp. 2208-2218*, 2010.

[133] J. Essen, C. Becker, and K. Wandelt. Pt_xce_{1-x} surface alloys on pt(111): Structure and adsorption. *e-J. Surf. Sci. Nanotech.,* ***7****, pp. 421-428*, 2009.

[134] J. W. Arblaster. Crystallographic Properties of Platinum. *Platinum Metals Rev.,* ***41****, pp. 12-21*, 1997.

[135] C. Praetorius, M. Zinner, A. Köhl, H. Kießling, S. Brück, B. Muenzing, M. Kamp, T. Kachel, F. Choueikani, P. Ohresser, F. Wilhelm, A. Rogalev, and K. Fauth. Electronic tunability of a structurally rigid surface intemetallic and Kondo lattice: $CePt_5$/Pt(111). *Phys. Rev. B,* ***92****, p. 045116*, 2015.

[136] P. Weibel, D. Malterre, M. Grioni, B. Dardel, and Y. Baer. Spectroscopic investigation of 4f correlations in CeAg; comparison between LDA and many-body descriptions. *Z. Phys. B - Condensed Matter* ***87****, pp. 165-168*, 1992.

[137] P. Monachesi, S. Fraizzoli, and E. G. Moroni. Electronic structure calculations for CeAg. *J. Magn. Magn. Mater.,* ***98****, pp. 130-140*, 1991.

[138] K. Persson. Materials Data on CeAg (SG:123) by Materials Project (Computed materials data using density functional theory calculations. These calculations determine the electronic structure of bulk materials by solving approximations to the Schrodinger equation. For more information, see https://materialsproject.org/docs/calculations). 2014.

[139] *$CeAg_2$: url: https://materialsproject.org/materials/mp-1206322/, year: 2021 (accessed: May 10, 2021).*

[140] K. Persson. Materials Data on $CeAg_3$ (SG:194) by materials project (Computed materials data using density functional theory calculations. These calculations determine the electronic structure of bulk materials by solving approximations to the Schrodinger equation. For more information, see https://materialsproject.org/docs/calculations). 2016.

[141] *Ce_3Ag url: https://materialsproject.org/materials/mp-1183754/ (accessed May 10, 2021).*

[142] A. Jain, S. Ping Ong, G. Hautier, W. Chen, W. Davidson Richards, S. Dacek, S. Cholia, D. Gunter, D. Skinner, G. Ceder, and K. A. Persson. The Materials Project: A materials genomeapproach to accelerating materials innovation. *APL Materials,* ***1****, p. 011002*, 2013.

[143] P. Morin. Quadrupolar ordering in CeAg. *J. Magn. Magn. Mater.* ***71****, pp. 151-164*, 1988.

[144] C. Praetorius, M. Zinner, P. Hansmann, M. W. Haverkort, and K. Fauth. Exploring small energy scales with x-ray absorption and dichroism. *Phys. Rev. B* ***93****, p. 165107*, 2016.

[145] P. Link and D. Jaccard. Pressure induced heavy-fermion behaviour of $CeAu_2Si_2$ near 17 GPa. *Physica B,* ***230-232****, pp. 31-34*, 1997.

[146] D. Jaccard, P. Link, E. Vargoz, and K. Alami-Yadri. Pressure effects in Ce and Yb-based HF compounds. *Physica B,* ***230-232****, pp. 297-300*, 1997.

[147] F.M. Grosche an S.R. Julian, N.D. Mathur, and G.G. Lonzarich. Magnetic and superconducting phases of $CePd_2Si_2$. *Physica B,* ***223-224****, pp. 50-52*, 1996.

[148] R. Movshovich, T. Graf, D. Mandrus, M.F. Hundley, J.D. Thompson, R.A. Fisher, N.E. Phillips, and J.L. Smith. Response of $CeRh_2Si_2$ to pressure. *Physica B,* ***223-224****, pp. 126-130*, 1996.

[149] A. B. Andrews, J. J. Joyce, A. J. Arko, J. D. Thompson, J. Tang, J. M. Lawrence, and J. C. Hemminger. Evidence for possible $4f$ bands at $T \gg t_k$ in the heavy – fermion single crystal $CePt_{2+x}$. *Phys. Rev. B* ***51****, pp. 3277-3280*, 1995.

[150] J.J. Yeh and I.Lindau. Atomic subshell photoionization cross sections and asymmetry parameters: $1 \leq Z \leq 103$. *Atomic Data and Nuclear Data Tables,* ***32, 1****, pp. 1-155*, 1985.

[151] O. Gunnarsson, K. Schönhammer, J. C. Fuggle, F. U. Hillebrecht, J.-M. Esteva, R. C. Karnatak, and B. Hillebrand. Occupancy and hybridization of the f level in Ce compounds. *Phys. Rev. B,* ***28****, p. 7330*, 1983.

[152] T. Okane, M. Yamada, S. Suzuki, S. Sato, A. Kakizaki, T. Kobayashi, S. Shimoda, M. Iwaki, and M. Aono. Atomic Diffusion and Electronic Structures of Ce/Ni(110) and Ce/Cu(110) Systems. *J. Phys. Soc. Jpn.* ***67****, pp. 264-271*, 1998.

[153] *Ce_5Bi_3: url: https://materialsproject.org/materials/mp-1188996/#snl (accessed: May 13, 2021).*

[154] *Ce – Bi compounds: url: https://materialsproject.org/ (accessed: May 13, 2021).*

[155] K. Kuroda, M. Ochi, H. S. Suzuki, M. Hirayama, M. Nakayama, R. Noguchi, C. Bareille, S. Akebi, S. Kunisada, T. Muro, M. D. Watson, H. Kitazawa, Y. Haga, T. K. Kim, M. Hoesch, S. Shin, R. Arita, and Takeshi Kondo. Experimental determination of the topological phase diagram in Cerium monopnictides. *Phys. Rev. Lett.* ***120*** *p. 086402*, 2018.

[156] H. Oinuma, S. Souma, K. Nakayama, K. Horiba, H. Kumigashira, M. Yoshida, A. Ochiai, T. Takahashi, and T. Sato. Unusual change in the Dirac-cone energy band upon two-step magnetic transition in CeBi. *Phys. Rev. B,* ***100****, p. 125122*, 2019.

[157] N. Alidoust, A. Alexandradinata, S.-Y. Xu, I. Belopolski, S. K. Kushwaha, M. Zeng, M. Neupane, G. Bian, C. Liu, D. S. Sanchez, P. P. Shibayev, H. Zheng, L. Fu, A. Bansil, H. Lin, R. J. Cava, and M. Z. Hasan. A new form of (unexpected) Dirac fermions in thestrongly-correlated cerium monopnictides. *arXiv:1604.08571 [cond-mat.str-el]*, 2016.

Own publications

- R. Kurleto, M. Fidrysiak, L. Nicolaï, J. Minár, M. Rosmus, Ł. Walczak, A. Tejeda, J. E. Rault, F. Bertran, A. P. Kądzielawa, D. Legut, D. Gnida, D. Kaczorowski, **K. Kissner**, F. Reinert, J. Spałek and P. Starowicz, "Photoemission signature of momentum dependent hybridization in $CeCoIn_5$", arXiv:2101.05761 [cond-mat.str-el].

- M. Ünzelmann, H. Bentmann, P. Eck, T. Kißlinger, B. Geldiyev, J. Rieger, S. Moser, R. C. Vidal, **K. Kißner**, L. Hammer, M. A. Schneider, T. Fauster, G. Sangiovanni, D. Di Sante, and F. Reinert."Orbital-Driven Rashba Effect in a Binary Honeycomb Monolayer AgTe". *Phys. Rev. Lett.* **124** (2020), p. 176401

- M. M. Otrokov, I. I. Klimovskikh, H. Bentmann, D. Estyunin, A. Zeugner, Z. S. Aliev, S. Gaß, A. U. B. Wolter, A. V. Koroleva, A. M. Shikin, M. Blanco-Rey, M. Hoffmann, I. P. Rusinov, A. Yu. Vyazovskaya, S. V. Eremeev, Yu. M. Koroteev, V. M. Kuznetsov, F. Freyse, J. Sánchez-Barriga, I. R. Amiraslanov, M. B. Babanly, N. T. Mamedov, N. A. Abdullayev, V. N. Zverev, A. Alfonsov, V. Kataev, B. Büchner, E. F. Schwier, S. Kumar, A. Kimura, L. Petaccia, G. Di Santo, R. C. Vidal, S. Schatz, **K. Kißner**, M. Ünzelmann, C. H. Min, S. Moser, T. R. F. Peixoto, F. Reinert, A. Ernst, P. M. Echenique, A. Isaeva and E. V. Chulkov. "Prediction and observation of an antiferromagnetic topological insulator". *Nature* **576** (2019), p. 416–422

- R. C. Vidal, H. Bentmann, T. R. F. Peixoto, A. Zeugner, S. Moser, C. H. Min, S. Schatz, **K. Kißner**, M. Ünzelmann, C. I. Fornari, H. B. Vasili, M. Valvidares, K. Sakamoto, D. Mondal, J. Fujii, I. Vobornik, S. Jung, C. Cacho, T. K. Kim, R. J. Koch, C. Jozwiak, A. Bostowick,

J. D. Denlinger, E. Rotenberg, J. Buck, M. Hoesch, F. Diekmann, S. Rohlf, M. Kalläne, K. Rossnagel, M. M. Otrokov, E. V. Chulkov, M. Ruck, A. Isaeva and F. Reinert. "Surface states and Rashba – type spin polarization in antiferromagnetic $MnBi_2Te_4(0001)$". *Phys. Rev. B* **100** (2019), p. 121104(R)

- A. Zeugner, F. Nietschke, A. U. B. Wolter, S. Gaß, R. C. Vidal, T. R. F. Peixoto, D. Pohl, C. Damm, A. Lubk, R. Hentrich, S. K. Moser, C. Fornari, C. H. Min, S. Schatz, **K. Kißner**, M. Ünzelmann, M. Kaiser, F. Scaravaggi, B. Rellinghaus, K. Nielsch, C. Hess, B. Büchner, F. Reinert, H. Bentmann, O. Oeckler, T. Doert, M. Ruck, and A. Isaeva. "Chemical Aspects of the Candidate Antiferromagnetic Topological Insulator $MnBi_2Te_4$". *Chem. Mater* **31,8** (2019), p. 2795 – 2806

- C. H. Min, H. Bentmann, J. N. Neu, P. Eck, S. Moser, T. Figgemeier, M. Ünzelmann, **K. Kißner**, P. Lutz, R. J. Koch, C. Jozwiak, A. Bostwick, E. Rotenberg, R. Thomale, G. Sangiovanni, T. Siegrist, D. Di Sante and F. Reinert."Orbital Fingerprint of Topological Fermi Arcs in the Weyl Semimetal TaP". *Phys. Rev. Lett.* **122** (2019), p. 116402

- V. B. Zabolotnyy, K. Fürsich, R. J. Green, P. Lutz, **K. Treiber**, C.-H. Min, A. V. Dukhnenko, N. Y. Shitsevalova, V. B. Filipov, B. Y. Kang, B. K. Cho, R. Sutarto, F. He, F. Reinert, D. S. Inosov and V. Hinkov. "Chemical and valence reconstruction at the surface of SmB_6 revealed by means of resonant soft x-ray reflectometry". *Phys. Rev. B* **97** (2018), p. 205416

- T. R. F. Peixoto, H. Bentmann, S. Schreyeck, M. Winnerlein, C. Seibel, H. Maaß, M. Al-Baidhani, **K. Treiber**, S. Schatz, S. Grauer, C. Gould, K. Brunner, A. Ernst, L. W. Molenkamp, F. Reinert."Impurity states in the magnetic topological insulator $V:(Bi,Sb)_2Te_3$". *Phys. Rev. B* **94** (2016), p. 195140

Danksagung

Am Ende einer solchen Arbeit gilt es natürlich einigen Leuten meinen Dank auszusprechen.

Zuallererst möchte ich mich bei meinem Doktorvater Prof. Friedrich Reinert bedanken, der es mir ermöglicht hat diese Doktorarbeit an seinem Lehrstuhl durchzuführen. Er konnte mich an der ein oder anderen kritischen Stelle während der Doktorarbeit abholen und mich die Arbeit wieder mit neuem Mut aufnehmen lassen. Im Speziellen möchte ich mich für die kontinuierliche Unterstützung während der Planungsphase der neuen Präparationskammer bedanken, in der durch annähernd wöchentliche Treffen, nach und nach das neue Kammer-layout entstanden ist. Besonders hervorheben möchte ich auch das "correlation-meeting" gegen Ende meiner Doktorarbeit. Im Rahmen dieses wöchentlichen Treffens konnten wir alle aus der "correlation-community" der EP VII in langen, fruchtbaren Diskussionen unser Wissen über korrelierte Elektronensysteme grundlegend vertiefen. Für diese Zeit möchte ich dir, Friedel, nochmals ausgesprochen danken und hoffe für alle correlation-guys, dass das meeting in irgendeiner Form weiter bestehen bleibt.

Zudem wurde ich während meiner Arbeit von zwei Post-docs unterstützt. Zuerst möchte ich mich bei Dr. Chul-Hee Min bedanken, der mich vor Allem in der Anfangszeit unterstützt hat. Durch ihn konnte ich im Rahmen einiger Messzeiten verschiedenste Forschungseinrichtungen auf der ganzen Welt kennenlernen. Dies hat mich nicht nur im wissenschaftlichen Sinne, sonder auch persönlich sehr bereichert. Gegen Ende meiner Arbeit erfuhr ich dann noch große Unterstützung durch Dr. Eike Schwier, der auch der Initiator des "correlation-meetings" war. Anfangs war ich zwar so viel Betreuung gar

nicht gewohnt, aber schlussendlich haben sein Input, seine anhaltenden kritischen Nachfragen und nicht zuletzt die ein oder andere softwaretechnische Unterstützung meine Arbeit sehr bereichert. Vielen Dank Eike!

Herzlich bedanken möchte ich mich auch bei Herrn Prof. Vladimir Hinkov für das Erstellen des Zweitgutachtens dieser Arbeit.

Ein sehr sehr sehr großes Dankeschön geht nun auch an meine Bürokollegen Max Ünzelmann, Can Raphael Crespo Vidal und Tim Figgemeier. Mir fehlen fast ein bisschen die Worte um auszudrücken wie dankbar ich euch bin, dass ihr immer für mich da wart, auch in schweren Zeiten der Doktorarbeit immer an mich geglaubt habt und mir immer positive Seiten aufzeigen konntet. Mit eurer einzigartigen Art wart ihr einfach eine unschätzbare Bereicherung während meiner ganzen Doktorarbeit. Die Pandemie hat uns zwar das letzte Jahr gemeinsamen Bürospaß ein bisschen genommen, aber ich hoffe dennoch, dass es uns auch in Zukunft gelingt in Kontakt zu bleiben.
Bevor sich dieses quartetto infernale gefunden hat, wurde unser Büro noch einige Zeit noch von Dr. Henriette Maaß bereichert. Auch bei dir möchte ich mich herzlich bedanken, denn deine hervorragende Betreuung während der Masterarbeit hat mich überhaupt erst davon überzeugt die Doktorarbeit in Angriff zu nehmen.

Ein herzlicher Dank geht auch an meine beiden Korrekturleser Dr. Eike Schwier und Max Ünzelmann, die die Arbeit sicherlich um einige Fehler ärmer gemacht haben.

Für die Phase des Kammerumbaus möchte ich mich außerdem für die tatkräftige Unterstützung von Max Ünzelmann, Can Raphael Crespo Vidal, Tim Figgemeier, Philipp Kagerer, Johannes Heßdörfer, Lukas Simon, Dr. Hendrik Bentmann und für die kleineren Reparaturen danach auch bei Begmuhammet Geldiyev herzlichst bedanken.
Ein großes Dankeschön geht in diesem Zusammenhang auch an die Mitarbeiter der wissenschaftlichen Werkstatt, Herrn Brauner, Herrn Grünebaum, Herrn Krause und Herrn Ochmann, ohne deren geduldige Unterstützung einige Bestandteile des neuen setups nicht hätten entstehen können. Auch

Herrn Ziga aus der He-Verflüssigung möchte ich für die manchmal auch sehr spontane Versorgung mit LHe danken.

Während meiner Doktorarbeit durfte ich zudem drei Masterarbeiten betreuen. Mit Philipp Eirich sind einige der Daten zu $CePt_5$ entstanden, wohingegen Hendrik Bostelmann-Arp und Lukas Simon vor allem am Projekt $CeAg_x$ beteiligt waren. Vielen Dank für eure Zeit und Arbeit und auch viel Erfolg bei den zum Teil eigens angestrebten Doktorarbeiten.

Neben all diesen wissenschaftlichen Beiträgen zu meiner Arbeit möchte ich mich auch bei allen anderen Kollegen der EP VII für die gute Zeit bedanken. Es hat mich besonders gefreut, dass in prä-Corona Zeiten unsere mittägliche Essensrunde über die Jahre kontinuierlich gewachsen ist, bis schließlich unser Kaffeezimmer fast zu klein war für die versammelten Lidl-Gänger und Selbstkocher. Diese gemeinsame Pause hat den Arbeitsalltag wirklich immer ungemein bereichert.

Auch durch meine Familie und Freunde habe ich während der gesamten Zeit nichts als Unterstützung erfahren. Vielen Dank Jani, Martin und Flo für die vielen schönen Abende bei denen die Physik einmal nicht so wichtig war.

Auch meine Eltern Anita und Fritz Treiber haben mich über all die Jahre wissenschaftlicher Ausbildung immer gefördert, mich nie unter Druck gesetzt und jede meiner Entscheidungen respektiert und unterstützt. Vielen Dank für diesen Rückhalt, ohne den diese Arbeit nicht hätte entstehen können.

Zuletzt gilt mein Dank meinem (mittlerweile) Mann Max Kißner. Auch wenn das Fachliche dieser Arbeit vielleicht nicht zu deiner ausgesprochenen Expertise gehört, weiß ich nicht wie ich diese Arbeit ohne dich hätte abschließen können. Es bedeutet mir unheimlich viel, dass du meine Entscheidung zur Promotion nie in Frage gestellt hast und mich während dieser Zeit immer nur unterstützt hast. Vielen Dank, dass du mich zwingst in den Urlaub zu fahren, neue Dinge auszuprobieren und mir generell die Augen öffnest, dass nicht immer alles im Leben bis später irgendwann warten muss. Danke, dass du mein Leben bereicherst. P.S.: Du glaubst gar nicht, wie glücklich mich die fast tägliche Frage “Was essen wir heut?” immer macht.